




**Università
degli Studi
di Palermo**

Engineering Department
Ph.D. Course in Chemical, Environmental, Biomedical,
Hydraulic and Materials Engineering

Climate Change and extreme precipitation events: from observation to projections

Ph.D. Candidate:
Dario Treppiedi

Advisor: Prof. Leonardo Valerio Noto 
Co-advisors: Prof. Gabriele Villarini
Ph.D. Course Coordinator: Prof. Giorgio Micale

Graduation Year 2024 - XXXVI Cycle



Contents

Contents	i
List of Figures	v
Introduction	1
1 Chapter one	3
1.1 5W1H for Climate Change	3
1.1.1 What	4
1.1.2 Why	7
1.1.3 Where	10
1.1.4 When	13
1.1.5 Who	17
1.1.6 How	20
1.2 Extreme precipitation in a climate change context	25
1.2.1 Observed changes in precipitation extremes	27
1.2.2 Projected changes in precipitation extremes	33
2 Chapter two	39
2.1 The Mediterranean area: a climate change hot spot	39
2.2 Insight for a semi-arid region: Sicily	43
2.2.1 Area of study and dataset	43
2.2.2 Asymmetric changes in the rainfall extremes magnitude with duration	48
2.2.2.1 Quantile regression vs. Mann-Kendall trend test	49
2.2.2.2 Pre-processing of the SIAS data	51
2.2.2.3 Precipitation trends through the QR method at the gauge level	53
2.2.2.4 Effects of duration and quantile on precipitation trends . .	56
2.2.2.5 Spatial analysis of precipitation trends	61
2.2.2.6 Mann–Kendall test for rainfall annual maxima trends . . .	67

2.2.3	Larger and more frequent extremes affect the reliability of design rainfall	69
2.2.3.1	Regional Depth Duration Frequency curves for Sicily . . .	70
2.2.3.2	Regional Quantile Exceedance Detection	72
2.2.3.3	Revision of the return periods defined with the regional approach	77
2.2.4	Convective or stratiform? A partitioning algorithm to separate the rainfall regimes	83
2.2.4.1	The partitioning framework	85
2.2.4.2	Data pre-processing and total precipitation distribution . .	90
2.2.4.3	Partitioning procedure	96
2.2.4.4	Detection of convective events	99
2.2.4.5	At-site and regional trend analysis	106
3	Chapter three	109
3.1	A global perspective on past and future changes in rainfall characteristics .	109
3.1.1	Magnitude or seasonality: why choose one?	109
3.2	A joint projected change in magnitude and seasonality of extreme precipitation events	112
3.2.1	How to model the bivariate dependence	114
3.2.1.1	Circular statistics for periodic variables	115
3.2.1.2	Circular-linear copulae	120
3.2.2	Precipitation datasets and data pre-processing	126
3.2.3	GCMs validation and statistical framework	130
3.2.4	Future changes in the bivariate dependence	134
3.2.5	Final considerations on the changes in the characteristics of precipitation extremes	141
4	Chapter four	143
4.1	Compound events for an improved risk assessment	143
4.2	Climate change exacerbates the compounding of heat stress and flood . . .	151
4.2.1	How to compound heat stress and flooding: data, methods and remarks	155
4.2.2	Historical response and GCMs validation	163
4.2.3	Future evolution of the compounding	166
4.2.4	A growing risk to the future population	173
4.2.5	Final considerations on the heat stress - flooding compound events .	175

Conclusion	177
A Appendix: supplementary material for Chapter two	181
B Appendix: supplementary material for Chapter three	199
C Appendix: supplementary material for Chapter four	201
Bibliography	205



List of Figures

1.1	From NOAA Climate.gov: Yearly temperature compared to the 20 th -century average (red bars mean warmer than average, blue bars mean colder than average) from 1850–2022 and atmospheric CO ₂ amounts (gray line): 1850–1958 from IAC, 1959–2019 from NOAA ESRL. Original graph by Dr. Howard Diamond (NOAA ARL), and adapted by NOAA Climate.gov.	6
1.2	From MrGeogWagg: Representation of natural (a) and human enhanced greenhouse effect (b)	8
1.3	Modified from (Houghton et al., 2001): schematic showing the effect on extreme temperatures when (b) the mean temperature increases, (c) the variance increases, and (d) when both the mean and variance increase for a normal distribution of temperature (a)	9
1.4	From NOAA Climate.gov: trends in global average surface temperature between 1993 and 2022 in degrees Fahrenheit per decade. The map is based on data from NOAA Centers for Environmental Information	10
1.5	From (Masson-Delmotte et al., 2021): synthesis of assessed observed and attributable regional changes for hot extremes (a), heavy precipitation (b) and agricultural and ecological drought (c). The hexagons correspond to each one of the IPCC AR6 WGI reference regions	12
1.6	Schematic of a Global Circulation Model (a, from Balaji et al. (2022)) and the projected trajectories of Representative Concentration Pathways (b, from Wikipedia), Shared Socioeconomic Pathways (c, from Deutsches Klimarechenzentrum), and their combination (d, from Government of Canada website)	15
1.7	From IPCC AR6: global surface temperature changes in °C relative to 1850–1900. These changes were obtained by combining CMIP6 model simulations with observational constraints based on past simulated warming, as well as an updated assessment of equilibrium climate sensitivity. Very likely ranges are shown for the low and high GHG emissions scenarios (SSP1-2.6 and SSP3-7.0)	17

- 1.8 From IPCC AR6: Observed (1900–2020) and projected (2021–2100) changes in global surface temperature (relative to 1850-1900), which are linked to changes in climate conditions and impacts, illustrate how the climate has already changed and will change along the lifespan of three representative generations (born in 1950, 1980 and 2020). Future projections (2021–2100) of changes in global surface temperature are shown for very low (SSP1-1.9), low (SSP1-2.6), intermediate (SSP2-4.5), high (SSP3-7.0) and very high (SSP5-8.5) GHG emissions scenarios. Changes in annual global surface temperatures are presented as ‘climate stripes’, with future projections showing the human-caused long-term trends and continuing modulation by natural variability (represented here using observed levels of past natural variability). Colours on the generational icons correspond to the global surface temperature stripes for each year, with segments on future icons differentiating possible future experiences. 18
- 1.9 From IPCC AR6: risks of species losses as indicated by the percentage of assessed species exposed to potentially dangerous temperature conditions, as defined by conditions beyond the estimated historical (1850–2005) maximum mean annual temperature experienced by each species, at global warming levels of 1.5°C, 2°C, 3°C and 4°C 20
- 1.10 Major climate negotiations timeline 21
- 1.11 From Sun et al. (2021): summary of Mann–Kendall trend analyses for the period 1950–2018 for 7293 stations with trends for Rx1day (a) and Rx5day (b), respectively. Light blue open dots indicate non-significant increasing trends and light red open dots mark non-significant decreasing trends. Dark blue and red filled dots indicate statistically significant trends as determined by a two-sided test conducted at the 5% level 29
- 1.12 From Ali et al. (2021): scaling rates (%K⁻¹) estimated using hourly precipitation from the global subdaily rainfall (GSDR) data set (Lewis et al., 2019) and daily dew point temperature from the HadISD data set (Dunn, 2019). Scaling is estimated using the binning method (BM) at the 99th percentile for 7,088 gauges, which have at least 12 years of hourly precipitation data. The number in blue indicates the number of gauges (NS) in each region and the number in black indicates the median scaling (%K⁻¹) for each region. The numbers below each panel indicate the percentage of gauges within each region, which show scaling rates ranging from 0-0.5CC (green), 0.5CC-CC (yellow), CC-1.5CC (orange), 1.5CC-2CC (pink), and greater than 2CC (red) respectively, where CC is 6.5%K⁻¹ 31

1.13 From Pal et al. (2013): trends of Julian days count from 1 January to the center of the (a) wettest and (b) driest 91 day period in a given year (“shift in seasons”). Wettest (driest) period is defined as the center of the 91 day period with the maximum (minimum) number of precipitating days, allowing for overlap with the preceding/following year. Color bubbles indicate location of the stations, sign, and significance of the trend estimates. The size (as well as the shading) of the bubble is proportional to the magnitude of the trend. The percentages in parentheses indicate fraction of the total number of stations having such trend category 32

1.14 From Persiano et al. (2020): mean date of occurrence of rainfall annual maxima for durations $d = 1, 3, 6, 12, 24$ h and time periods 1961–1989 and 1990–2015. Direction and colour of the arrows indicate the average timing, while their length reflects the regularity of the dates of occurrence within the year. Black-contoured arrows indicate stations where statistically significant trends have been detected in the Julian date of occurrence over the period 1961–2015 33

1.15 From Morrison et al. (2019): median maximum 3-hourly precipitation (mm) based on an ensemble that includes CNRM-CM5, FGOALS-g2, MRI-CGCM3 and MRI-ESM1. The results for the RCPs 2.6, 4.5 and 8.5 (Columns 2–4) represent the percentage differences between the projected changes (2081–2100) and the historical period (1986–2005), normalized by the historical period (1986–2005). Results are for annual precipitation (Row 1), DJF (Row 2), MAM (Row 3), JJA (Row 4), and SON (Row 5) 35

1.16 From Marelle et al. (2018): (a) Season of the multimodel median day of year of extreme daily precipitation in the CMIP5 ensemble for 1976–2005. (b) Multimodeled median change in the median day of year of extreme daily precipitation between 1976–2005 and 2071–2100 (RCP8.5 scenario). On panel (b), black boxes indicate the location of the regions selected for further analysis, and stippling indicates that more than 66% of models agree on the sign of change. DJF = December–February; JJA = June–August; MAM = March–May; SON = September–November 36

2.1 From Ali et al. (2022): Topography and bathymetry (colour bar in metres), main urban areas (population in thousands of people for 2020), container ports (millions of TEU [twenty-foot container equivalent units] in 2017) and borders of the Mediterranean region 40

2.2	Area of study overlaid on the digital elevation model	44
2.3	Spatial distribution of SIAS rain gauges	45
2.4	Completeness of the SIAS rain gauge network. Panel A shows the % of missing data in each station (rows) for each year (column). In panel B the red cells represent all those years for each station where the % of missing values is lower than 30%	46
2.5	Spatial distribution of the number of valid years for the SIAS rain gauges .	47
2.6	Spatial distribution of the mean annual precipitation values computed from the SIAS network	47
2.7	Example of the aggregation procedure for 20 and 30-minute duration . . .	52
2.8	Graphic representation of QR lines (coloured-solid) and OLS line (black-dashed) for the station of ‘Palermo’ at (a) 10-min, (b) 1-hr, and (c) 24-hr durations. In the lower right panel, it is reported an exemplification of the annual increment of hourly intensity to compare slopes of rainfall intensity at different durations	54
2.9	Slope of the regression lines versus quantile level for the station of ‘Palermo’ at (a) 10-min, (b) 1-hr, (c) 24-hr durations. Black points are representative of the slopes for various quantiles, while the grey bands stand for the 90% confidence intervals. The figure also displays the slope of the OLS regression line (red-solid line) and the related confidence intervals (red-dashed lines) at the three considered durations	56
2.10	Percentage of rain gauges characterized by a positive (red), negative (green), and non-significant (grey) trend coming out from QR procedure at 0.2, 0.5, 0.9, 0.95, and 0.99 quantiles at all durations	58
2.11	ECDF of the trend magnitude for 10, 30min and 1, 6, and 24hr at (a) 0.2, (b) 0.95 and (c) 0.99 quantile. ECDFs are representative of the positive and negative trend magnitude with a significance level of .1. The sample size for any quantile-duration combination is reported in the legend	60
2.12	Spatial distribution of the gauges under study and magnitude (colour), expressed in $mm \cdot h^{-1} \cdot year^{-1}$, direction (triangles orientation) and significance (triangle size, large for $\alpha_{sig} \leq 0.05$, medium for $0.05 < \alpha_{sig} \leq 0.1$ and small for $\alpha_{sig} > 0.1$) from QR at 0.2, 0.5, 0.9, 0.95, 0.99 quantiles for 10-min, 1- and 24-hr durations. The bold letters, A-E, stand for the quantiles, while the bold numbers 1–3, denote the durations	62

2.13	Local Moran analysis for the 0.95 quantile at (a) 10-min, (b) 1-hr, and (c) 24-hr duration. The LISA is applied to both the positive and negative trend magnitudes with a significance level of 0.1. Red and blue circles are relative to high-high (HH) and low-low (LL) clustering cases, respectively, and characterized by a p -value lower than 0.1. The significant outliers are marked with light blue and pink diamonds for low-high (LH) and high-low (HL) clustering cases, respectively. The crosses represent those locations in which the significance exceed the level of 0.1	66
2.14	Annual maxima for the rain gauge of ‘Palermo’ of the SIAS data set at 10-min, 1-hr, 24-hr duration (a), spatial distribution of magnitude, direction and significance of trends (b), and percentage of stations having a negative (green), positive (red), or non-significant (grey) trend obtained through the MK test (c)	68
2.15	Homogeneous regions (a) and spatial distribution of values of the parameter a_{24} (b) and n (c) from Forestieri et al. (2018)	72
2.16	At-site comparison between the hreg for the 1 h duration and the 5-year return period and the aggregated data series of the SIAS rain gauge named ‘Palermo’ (upper panel) and spatial distribution of the number of exceedances for different durations (rows) and return periods (columns) over the entire region (lower panel)	74
2.17	Probability density functions of the binomial statistical distribution, in blue, and of the number of h_{reg} exceedances, in red, for the reference durations (rows) and return periods (columns). The small panels represent the respective cumulative distribution function	76
2.18	Spatial distribution of p -value for the K–S test for the reference durations. High p -values indicate greater significance in not rejecting the null hypothesis that the sample belongs to the theoretical EV1 distribution	78
2.19	Empirical density distribution of the T_{SIAS} of all 72 considered SIAS rain gauges, compared to the corresponding T_{reg} (red dashed line). Results are expressed for all the reference durations (rows) and the return periods of 5, 10, and 20 years (columns)	80
2.20	Spatial representations of the T_{SIAS} for the 72 considered SIAS rain gauges. Results are expressed for all reference durations (rows) and the T_{reg} of 5, 10, and 20 years (columns)	81

- 2.21 Precipitation intensity heatmap for a) February and b) September of the year 2006 at 1) $\Delta I=0.6 \text{ mm}\cdot 20\text{min}^{-1}$ and 3) $\Delta I=1.8 \text{ mm}\cdot 20\text{min}^{-1}$. The colorbar indicates the total precipitation values, while black color indicates no rainfall records. The sub-panels inside each heatmap provide a zoom for 23rd Feb. 2006 and 15th Sep. 2006 for 2) $\Delta I=0.6 \text{ mm}\cdot 20\text{min}^{-1}$ and 4) $\Delta I=1.8 \text{ mm}\cdot 20\text{min}^{-1}$. The 20-minute precipitation distribution related to the 15:00 of the 15th Sep. 2006 (black curve) and to the 17:00 of the 23rd Feb. 2006 (red curve) are depicted for c) $\Delta I=0.6 \text{ mm}\cdot 20\text{min}^{-1}$ and d) $\Delta I=1.8 \text{ mm}\cdot 20\text{min}^{-1}$. 92
- 2.22 Precipitation intensity heatmap for the year 2006 at the 5-day scale a) $\Delta I = 0.6 \text{ mm}\cdot 20\text{min}^{-1}$ and c) $\Delta I = 1.8 \text{ mm}\cdot 20\text{min}^{-1}$. The colorbar indicates the total precipitation values, while black color indicates no rainfall records. The remaining panels show the $P_T(I)$ for 1) 21-25 January, 2) 11-15 June, 3) 26-31 August, and 4) 21-25 November combined with a) $\Delta I = 0.6 \text{ mm}\cdot 20\text{min}^{-1}$, b) $\Delta I = 1 \text{ mm}\cdot 20\text{min}^{-1}$, and c) $\Delta I = 1.8 \text{ mm}\cdot 20\text{min}^{-1}$. 95
- 2.23 Results from the application of the partitioning procedure for the same combinations between 5-day interval and ΔI depicted in Figure 2.22. The black lines represent the 5-day total precipitation distribution, while the red lines stand for the stratiform component (i.e., the negative exponential curve). The gray bars, instead, quantify the convective amount of rainfall for each class of intensity 96
- 2.24 Median percentage of convective rainfall with respect to the intensity class, as a function of the month (e.g., the panels) and the ΔI (e.g., the colors). In particular, red, green, blue and purple curve stands for 0.6, 1, 1.4 and, 1.8 $\text{mm}\cdot 20\text{min}^{-1}$, respectively 99
- 2.25 Monthly median critical intensity threshold I_{cr} values for a) $\lambda=50\%$ and b) $\lambda=75\%$ considering 1) $\Delta I=0.6 \text{ mm}\cdot 20\text{min}^{-1}$, 2) $\Delta I=1 \text{ mm}\cdot 20\text{min}^{-1}$, 3) $\Delta I=1.4 \text{ mm}\cdot 20\text{min}^{-1}$ and, 4) $\Delta I=1.8 \text{ mm}\cdot 20\text{min}^{-1}$ 101
- 2.26 Example of the aggregation procedure (panel a) related to 16th of November 2018 for Catania rain gauge considering the I_{cr} value for $\lambda=50\%$, $\Delta I=0.6 \text{ mm}\cdot 20\text{min}^{-1}$ and November. The other panels show the spatial distribution of b) the average annual occurrence of convective events and c) the average annual percentage of convective rainfall for 1) $\lambda=50\%$ and 2) $\lambda=75\%$, obtained by considering the monthly median I_{cr} related to $0.6 \text{ mm}\cdot 20\text{min}^{-1}$ 103
- 2.27 Representation of the orographic effect that generates convective rainfall in the northeastern area of Sicily 104

2.28 Comparison between a) the monthly absolute number of convective events and b) the monthly percentage of convective precipitation using $\lambda=50\%$ and $\lambda=75\%$ (i.e., the red and green curve, respectively) and the outcomes obtained from Sottile et al. (2022) (i.e., the blue curve). The gray shaded area represents the differences between the two λ 106

2.29 Trend analysis results for a) the peak of convective events and b) the total convective precipitation for 1) $\lambda=50\%$ and 2) $\lambda=75\%$. The cross symbol stands for the gauges where no significant trend has been detected, while the colored triangles pointing up (pointing down) represents the gauges interested by a significant increasing (decreasing) trend. The p-value from the Regional Kendall test is shown in the bottom-left corner of each panel 108

3.1 Example of time series for daily rainfall precipitation (a). Exceedances of the 99th percentile (red points) represented as function of time (b) and as day of occurrence of the events(c) 110

3.2 Bivariate representation of the magnitude (i.e., position along the radius) and the seasonality (i.e., position on the circle) for the precipitation POT in Figure 3.1 111

3.3 Bivariate representation of the monthly correlation between the percentages of events that exceed the 99th percentile of the at-site distribution and their median value at a global scale over the 1979-2014 period. The white-to-purple scale represents the percentage of events in the month, while the white-to-green characterizes the magnitude of the median of the events exceeding the threshold. Hence, the greener (more purple) the color, the greater (lower) the magnitude of the precipitation event in a given month, and at the same time, the lower (higher) the number of extreme events that characterize it. Dark colors represent high percentages and high magnitudes of these events, while totally white pixels indicate that no events occurred during the study period 113

3.4 Example of circularized data with the length and the direction of the sample mean (blue) and sample median (red) vectors. The wind dataset is available in the `circular` package (Agostinelli and Lund, 2023) in R 117

3.5 Example of empirical probability density function for wind directions treated as a linear (red line) and circular (blue line) variable. The wind dataset is available in the `circular` package (Agostinelli and Lund, 2023) in R 118

3.6 Example of Gumbel (a), Clayton (b) and Frank (c) copula generated with random parameter 121

- 3.7 Example of rotated circular-linear copulae. The PDFs of the rotated Clayton and Gumbel copula is shown in a 2-D and 3-D visualization 124
- 3.8 Example of rectangular patchwork of copulae. The PDFs of the rotated Clayton, Frank and Gumbel copula is shown in a 2-D and 3-D visualization 125
- 3.9 From Beck et al. (2018): Present-day (1980–2016) (a) and future (2071–2100) (b) Köppen-Geiger climate classification maps. The acronyms stand for: Tropical rainforest (Af), monsoon (Am), savannah (Aw); Arid desert - hot (Bwh), desert-cold (BWk), steppe-hot (BSh), steppe-cold (BSk); Temperate dry summer - hot summer (Csa), dry summer - warm summer (Csb), dry summer - cold summer (Csc), dry winter - hot summer (Cwa), dry winter - warm summer (Cwb), dry winter - cold summer (Cwc), no dry season - hot summer (Cfa), no dry season - warm summer (Cfb), no dry season - cold summer (Cfc); Cold dry summer - hot summer (Dsa), dry summer - warm summer (Dsb), dry summer - cold summer (Dsc), dry summer - very cold winter (Dsd), dry winter - hot summer (Dwa), dry winter - warm summer (Dwb), dry winter - cold summer (Dwc), dry winter - very cold winter (Dwd), no dry season - hot summer (Dfa), no dry season - warm summer (Dfb), no dry season - cold summer (Dfc) no dry season - very cold winter (Dfd); Polar tundra (ET), Polar frost (EF) 127
- 3.10 Value of the 99th percentile of the precipitation distribution for different climates according to a future Köppen – Geiger climate classification map (Beck et al., 2018). Rows are representative of Arid, Tropical, Temperate, Cold, and Polar classification, while the sub-climate spatial distributions are depicted on the left together with the box plots of the corresponding threshold values in the right column 129
- 3.11 Empirical (u,v) points overlayed to the best selected copula according to the Akaike Information Criterion. u refers to the circular variable, while v to the linear one. The viridis colors represent the copula density. In particular the density decreases as the colors change from yellow to purple 130
- 3.12 Outline of the AIC bootstrap approach 131
- 3.13 Results of the AIC bootstrap approach for the validation of the GCMs. The panels indicate the IPCC zones, while the bars refer to the nine GCMs analyzed. The red color indicates the percentage of pixels where there is not enough evidence to reject the null hypothesis that the GCM outputs can be extracted from the same copula as the reference data 133

3.14 Example of the procedure followed to derive the bivariate dependence between magnitude and occurrence of precipitation extremes. In the top right panel, the empirical (u,v) points are overlaid to a circular-linear copula. The other panels show the linear (bottom-right) and the circular (top-left) marginal distribution. The empirical CDF is depicted in black, while the theoretical GPD and vMD with red color 134

3.15 Example of exceedances of the 2-D density generated from the selected copula and marginal distributions. As for Figure 3.11, the density decreases as the colors change from yellow to purple. The red line indicates the median daily extreme precipitation depth $h_{50}(d)$. The red dot corresponds to the maximum of the $h_{50}(d)$ and represents the reference precipitation depth (H_{50}) that is projected to occur on a specific day ($D(H_{50})$) of the year according to the developed bivariate model 136

3.16 Example of how $\Delta\bar{R}_{i,SSP}$ and $\Delta\bar{S}_{i,SSP}$ are derived, starting from the historical and SSP average values (blue dots) 137

3.17 Average projected changes in the characteristics of the extreme precipitation for the 2065- 2100 period with respect to the historical baseline (1979 – 2014) under four difference scenarios (SSP1-RCP2.6, SSP2-RCP4.5, SSP3-RCP7.0, and SSP5-RCP8.5). The bivariate circular palette is here used to concurrently display the shift in the seasonality (i.e., $\Delta\bar{S}$ change in color) and the changes in the magnitude (i.e., $\Delta\bar{R}$ change in brightness). Positive (negative) percentages for the $\Delta\bar{R}$ indicate an increase (decrease) in the intensity of the future extreme events compared to the past, while positive (negative) values for the $\Delta\bar{S}$ indicate a backward (forward) potential shift in the seasonality. The scatterplot inside each panel shows where the pixel values are located within the bivariate circular plane 139

3.18 Projected changes in seasonality as a function of seasonal components. Percentage of pixels characterized by one, two or more than three von Mises distributions per discrete values of $\Delta\bar{S}$ (in months) for SSP1-RCP2.6, SSP2-RCP4.5, SSP3-RCP7.0, and SSP5-RCP8.5 scenario. 141

4.1 From app.dimensions.ai: Number of publications per year on the topic of compound events. The number of publications was filtered considering only those in the following macro areas: *Earth Sciences, Environmental Sciences, Atmospheric Sciences, Engineering* 144

4.2 From Zscheischler et al. (2020): Overview of elements in the climate and weather domain that make up a compound event 145

- 4.3 From Zscheischler et al. (2020): Hypothetical responses in the probability of compound events (shift of the bivariate distribution from grey to red) arising from a shift in the mean of driver or hazard 2 (panel a), an increase in the variability of driver or hazard 2 while holding correlation between the variables constant (panel b) and an increase in the strength of the dependence between driver or hazards 1 and 2 (panel c). The dashed line represents a moderate impact threshold, assumed constant for both present and future climates. The dotted line represents a threshold surpassed only under altered climate conditions. The colored areas indicate events with moderate (light shading) and substantial (darker shading) impacts 146
- 4.4 Modified from Zscheischler et al. (2018): The hypothetical distribution of temperature and humidity in the present climate (green), a future climate with a shift in mean, variability and correlation between the drivers (Future 1, blue) and a future climate with an increase in dependence in the upper tail of both drivers (Future 2, purple). The intensity of Hazard 1 increases towards the upper right of the climate space (a). The same climate distributions as in a for Hazard 2, which increases towards the lower right of the climate space (b) 147
- 4.5 From Zscheischler et al. (2020): Typologies of compound events: a) preconditioned event, b) multivariate event, c) temporally compounding event, d) spatially compounding event 149
- 4.6 From Our World in Data: Global deaths from disasters over the period 1900 - 2020. The size of the bubble represents the estimated annual death toll 151
- 4.7 Physical mechanism behind the compounding of heat stress and flood . . . 154
- 4.8 Characteristics (e.g., source, spatial resolution, and analysis period) for both reference dataset and GCMs 156
- 4.9 Example of peak-over-threshold to extract heat stress (a) and extreme runoff (b) events from the reference datasets and the historical experiments of GCMs 158
- 4.10 Spatial distribution for the 95th percentile of the wet bulb temperature. The colorbar is related to those area in which the 95th percentile is greater than 20°C, while the light grey area represents the pixels in which this threshold is not exceeded. The present and future Köppen - Geiger arid desert/steppe zones are shown in gray and dark gray, respectively 159

4.11 Spatial variability of the percentage of summer heat stress events (a) and extreme runoff (b). The summer period includes June, July, and August (December, January, and February) for the northern (southern) hemisphere. The percentage is computed as the ratio between the number of heat stress/extreme runoff events that occurred during the summer and the total number of events 161

4.12 Representation of the criterion to compound heat stress and flooding events for the reference (a) and the GCMs experiments (b) 162

4.13 Spatial distribution of the percentage of compound heat stress – runoff based on the reference data. The study period is 1979-2014. The gray shaded areas represent “Arid desert” or “Arid steppe” zones (according to the global Köppen – Geiger classification) or the regions where the 95th percentile of the wet bulb temperature distribution does not exceed 20°C and, therefore, are excluded from the analyses 164

4.14 Spatial distribution of the percentage of compound heat stress – runoff. The results in the top-left panel are based on the reference data, while the remaining panels show the results for the historical runs of seven CMIP6 GCMs 165

4.15 Averaged percentage of compound heat stress – runoff for the GCMs historical experiments. The color transparency is used to distinguish those areas in which at least four GCMs agree with the presence of compounding (i.e., no transparency) from those where the response of GCMs is more uncertain (i.e., transparency) 166

4.16 Averaged percentage of compound heat stress – runoff for the GCMs historical experiments and the SSPs. The rows show the results for the different experiments, while the columns for the different regions. The historical simulations (top row) focus on the 1979-2014 period, while the future conditions on the 2065-2100 period. The color transparency is used to distinguish those areas in which at least four GCMs agree with the presence of compounding (i.e., no transparency) from those where the response of GCMs is more uncertain (i.e., transparency). The shaded gray areas are excluded because of future arid conditions based on the Köppen – Geiger zones or because the threshold for the wet bulb temperature is lower than 20°C 167

- 4.17 Averaged changes in the future frequency of heat stress events preceding floods compared with the historical experiments. The red color (i.e., increasing changes) indicates those areas where in the future there may be more heat stress events preceding floods, while the blue color (i.e., decreasing changes) represents a reduction in these changes. The rows show the results for all the SSPs considered, while the columns for the different regions 168
- 4.18 Distributions of the ratio between the number of events (heat stress in pink and extreme runoff in blue) in the future scenarios and in the historical experiment. The rows show the results for the different SSP scenarios . . . 170
- 4.19 Empirical cumulative distribution functions for the percentage of compounding heat stress – runoff. The results for the GCMs are summarized on the rows, while the regions are on the columns. The red line represents the historical experiments (1979 – 2014), while the other colors are related to the SSP projection (2065 – 2100) 172
- 4.20 GCMs outcomes in the compounding of heat stress – runoff for Europe and western Asia. The first column represents the historical experiment for the seven GCMs (one per row), while the other columns correspond to the future expansion of the affected areas according to the different SSPs. The shaded gray area represents what is described in Figure 4.13 173
- 4.21 Population exposed to the compounding of heat stress – runoff for the GCMs historical experiment and SSP scenarios. Colors from yellow to purple represent the number of people that might be exposed to a certain percentage of compound heat stress – runoff events, while dark gray is representative of no data values 174
- A.1 Empirical PDFs of rainfall intensity data for Palermo’s station at a) 10-minute, b) 1-hour and c) 24-hour durations 188
- A.2 Empirical CDFs of the trend magnitude for 10, 20, 30, 40 minutes and 1, 3, 6, 12 and 24 hours at a) 0.2, b) 0.5, c) 0.9, d) 0.95 and e) 0.99 quantile. ECDFs are representative of the positive and negative trend magnitude with a significance level of 0.1. The sample size for any quantile-duration combination is reported in the legend of each panel 189
- A.3 Spatial distribution of the gauges under study and magnitude (color), expressed in mm/h/y, direction (triangles orientation) and significance (triangle size) from QR at 0.2, 0.5, 0.9, 0.95, 0.99 quantiles for 20-minute, 30-minute and 40-minute durations. The bold letters, A-E, stand for the quantiles, while the bold numbers 4-6, indicate the durations 190

A.4 Spatial distribution of the gauges under study and magnitude (color), expressed in mm/h/y, direction (triangles orientation) and significance (triangle size) from QR at 0.2, 0.5, 0.9, 0.95, 0.99 quantiles for 3-hour, 6-hour and 12-hour durations. The bold letters, A-E, stand for the quantiles, while the bold numbers 7-9, indicate the durations 191

A.5 Local Moran analysis at 0.2, 0.5, 0.9, 0.95, 0.99 quantiles for 10-minute, 1-hour and 23-hour durations. The bold letters, A-E, stand for the quantiles, while the bold numbers 1-3, indicate the durations. The LISA is applied to both the positive and negative trend magnitudes with a significance level of 0.1. Red and blue circles are relative to High-High (HH) and Low-Low (LL) clustering cases, respectively, and characterized by a p -value lower than 0.1. The significant outliers are marked with light blue and pink diamonds for Low-High (LH) and High-Low (HL) clustering cases, respectively. The crosses represent those locations in which the significance exceed the level of 0.1 193

A.6 Spatial distribution of the occurrence of convective events (expressed as number of convective events in a year) extracted by using the monthly median I_{cr} for $0.6 \text{ mm}\cdot 20\text{min}^{-1}$ and considering $\lambda=50\%$. Each panel is representative of a different year in the period 2002 – 2020. The colored points depict the gauges interested by at least one convective event, the circle-cross symbol stands for the working gauges where no convective events have been detected, while the plus sign symbolizes the not working stations in that year 194

A.7 Same of Figure A.6 but for the annual percentage of convective rainfall . . 195

A.8 Spatial distribution of the occurrence of convective events (expressed as number of convective events in a year) extracted by using the monthly median I_{cr} for $0.6 \text{ mm}\cdot 20\text{min}^{-1}$ and considering $\lambda=75\%$. Each panel is representative of a different year in the period 2002 – 2020. The colored points depict the gauges interested by at least one convective event, the circle-cross symbol stands for the working gauges where no convective events have been detected, while the plus sign symbolizes the not working stations in that year 196

A.9 Same of Figure A.8 but for the annual percentage of convective rainfall . . 197

B.1 Intergovernmental Panel on Climate Change WGI reference regions from the Fifth Assessment Report (AR5) (Stocker et al., 2014) 199

C.1 From Kii (2021): Spatial distribution of urban agglomerations by the population scale for 2010 (a) and projections for 2100 under scenarios SSP1 (b) and SSP2 (c) respectively 202



Introduction

Climate change represents one of the greatest challenges humanity has ever faced. The unmistakable signs of climate change, such as global warming, rising sea and ocean temperatures, rising global sea levels, decreasing Arctic sea ice, and melting glaciers, pose a real and tangible risk to the future of the planet. The geographic extent of the problem requires a planetary effort by everyone: from governments, which should pursue climate policies in synergy with each other, to individuals who should respect the environment in which they live. The scientific community is called upon to help both sides, not only by bringing evidence of the changing climate, but also by supporting the processes of adaptation and resilience to climate change.

One of the consequences that is increasingly being blamed for the problem of climate change and global warming is the possible increase in the frequency and magnitude of extreme events, namely all those phenomena that, because of the statistical connotation of the term "extreme," should be marked by certain exceptionality. Among these phenomena, extreme precipitation events assume considerable importance, and it is particularly alarming what was reported in 2021 by the Intergovernmental Panel on Climate Change within the "Sixth Assessment Report": the frequency and intensity of extreme precipitation events are likely to have increased on a global scale in most regions, and it is likely that the 21st century will see an increase in the frequency of intense rainfall in many areas of the globe and, at the same time, a decrease in total rainfall. In light of this statement, moreover, it is possible to perceive how the risk of further unbalancing of the hydrological cycle is indeed possible. A decrease in total rainfall may lead to a further increase in surface and atmospheric temperatures and in the frequency of hot extremes, which, in turn, are among the causes of higher evaporative rates and increased relative humidity in the air; this may further enhance an increase in the intensity and frequency of extreme weather events, triggering floods and jeopardizing our society.

Given this premise, the research activity developed and presented in this doctoral thesis is framed within the context of studying the effects of climate change on the extreme precipitation regime. In particular, the thesis is divided into four chapters.

Chapter 1 will provide a description of climate change analyzed through the *Kipling method* (i.e., 5W1H questions); starting from general concepts related to climate change,

it will be examined more in detail what is changing and the physical reasons for these alterations; after this it will also be explored who and what is affected by these changes, how long the climate is likely to change under the effect of global warming and what policies have been undertaken to address this global issue. Finally, a more detailed description of the observed and projected changes in the extreme precipitation regime will be provided.

Chapter 2 will be devoted to analyzing the changes in the extreme precipitation regime for the Mediterranean area and, particularly, for Sicily. In particular a trend analysis based on quantile regression will be carried out, focusing especially on shorter duration extreme precipitation events, which are particularly relevant in the urban environment. The second part will focus on examining the potential consequences of the alterations in the extreme precipitation regime from an engineering perspective. In particular, it will be investigated how these potential changes affect the extreme value distributions used in the design of hydraulic structures. Finally, since these short-duration intense events are generally associated to convective systems, an algorithm for separating convective and stratiform regimes will be implemented and used.

Chapter 3 will focus on the analysis of the changes in two characteristics of extreme precipitation events, namely the magnitude and the seasonality. Since local changes are often influenced by changes in the large-scale regime, in this case the analysis will be conducted looking at the global scale, in order to provide a broader view of the state of the climate. Using the projections of different Global Circulation Models (GCMs) at different Shared Socioeconomic Pathways (SSPs) and Representative Concentration Pathways (RCPs), it will be analyzed how these characteristics of precipitation extremes might change at the end of the 21st century. Moreover, for the first time, changes in the intensity and seasonal occurrence of the extremes will be examined using a peculiar branch of copulae, namely bivariate statistical models capable of modeling the correlation between linear (the magnitude) and circular (the seasonality) variables.

Finally, Chapter 4 will delve into the study of compound hydro-meteorological events. It will be studied whether and how heat stress event can be a precursor of summer flooding across different areas of the globe. In this case, precipitation extremes will be considered as a "masked" element in the compounding between heat stress and flood events. Indeed, these two hazards are connected through atmospheric conditions leading to increased convective available potential energy (CAPE) and stormy weather. Moreover, by using the outcomes from several GCMs at different combination of SSPs and RCPs, it will be examined whether the strength of this compounding is projected to increase or decrease in the future, considering also the potential threats to society and the economy.

1 | Chapter one

1.1. 5W1H for Climate Change

Nowadays, there is probably no person in the world who has never heard of *climate change*. This expression has entered in our everyday life through newspapers, television, networks and so on, triggering completely different reactions, from fear (the so-called *eco-anxiety*) to negationism. Regardless of individual's point of view, some of the world's largest organizations have no doubt in defining what climate change is. During the 2021 United Nations Security Council, David Attenborough, who is among the world's most famous biologist and natural historian, defined climate changes as "*the biggest threat to security that modern humans have ever faced*", pointing out that continuing in this direction is likely to see a collapse in global food security, in the availability of fresh water and so on. In this case, it will be the poorest who will suffer first. This latter topic is particularly relevant to the Food and Agriculture Organization (FAO), which in the report "Strategy on Climate Change 2022-2031" stressed the urgency of addressing climate change, given the 720-811 million of people facing hunger in 2020 and the increasing impacts of extreme weather events on food security, nutrition and poverty. Last but not least, in the report "Climate Change 2013: The Physical Science Basis" the Intergovernmental Panel on Climate Change (IPCC) stated that "*the scientific evidence is unequivocal: climate change is a threat to human wellbeing and the health of the planet. Any further delay in concerted global action will miss the brief, rapidly closing window to secure a liveable future*". More recently, the findings from IPCC Working Group I in the Sixth Assessment Report (AR6) (Masson-Delmotte et al., 2021) underline the unequivocal climate crisis the planet is currently facing and will continue to face in the coming decades. This crisis includes the increasing risk in the occurrence of unprecedented heatwaves, intense precipitation, prolonged droughts, wildfires, and tropical cyclones, with impacts projected to rise in all regions across the globe. What is certain is that if no action will be taken to face climate change, some climate tipping points might be reached (Lenton, 2011), resulting in strong consequences for Earth, difficult or even impossible to revert (e.g., the ice melt in the poles).

However, it is undeniable that addressing climate change issues in a comprehensive

and precise manner poses significant challenges. Indeed, the intricate nature of the climate system, coupled with the interdisciplinary range of topics and variables to be considered, enhances the complexity of the subject even further. In this context, it may be useful to draw inspiration from the methods used in problem-solving or project management, such as the *Kipling method*. This method, also known as *5W1H*, is a questioning approach that answers all the basic elements within a problem (i.e., What, Who, When, Where, Why, and How), providing a structured way to gather information, analyze situations, and communicate effectively. Thus, applying it to the topic of climate change could provide a clearer overall picture compared to a classical bottom-up or top-down approach, which may be more useful in understanding the effects of climate change at a more detailed scale.

Therefore, in the next paragraphs, the *5W1H* method will be applied to climate change. It is worth to emphasized that, due to the vastness of the topic, it is not possible to encapsulate all the advances achieved over time. As much as possible, however, this section will aim to be as clear and comprehensive as possible. Finally, the ultimate goal will be a focus on extreme precipitation events in the context of climate change, as will be seen in section 1.2.

1.1.1. What

Obviously, the first question worth answering is "**what is climate change?**". As defined from the National Aeronautics and Space Administration (NASA), climate change is "*a long-term change in the average weather patterns that have come to define Earth's local, regional and global climates*".

The first key information that can be extracted from this definition is inherent to the difference between climate and weather. Indeed, while "weather" refers to short-term atmospheric conditions at a given location, which may change daily or even hourly, "climate" represents the long-term behavior of the (averaged) weather conditions in a certain geographic area. Mark Twain's famous quote is often used (even if de-contextualized from the original meaning) to provide a glaring example of how time is a key variable in distinguishing the two concepts: "*if you don't like the weather in New England now, just wait a few minutes*". According to the World Meteorological Organization (WMO), the length of the reference period to asses changes in climate should be 30 consecutive years, and the organization also recommends to update the "Standard Normals" (i.e., a suite of data products that provide information about typical climate conditions for thousands of locations throughout the world) every 10 years. The term "Normals" also introduces a fundamental notion in climate change-related studies, namely statistics. Although the

term "change" inherently contains the concept of departing from something usual (or normal), it is essential for this concept to have universal consensus. Thus, statistics offers the required level of objectivity to achieve agreement on the presence of a genuine change. Moreover, the use of the 30-year window allows to introduce an additional concept about the nature of climate change. Indeed, if on the one hand it ensures that changes in weather are not mistaken for significant changes in climate, on the other it implies that climate is not static but has always been changing, not allowing to define an absolute mutation in its status. The glacial periods cyclically experienced by Earth represent a clear example of this dynamism. Thus, the aspect that distinguishes the natural changes from what is observed today is our presence, namely the human impacts. To be more specific, it is possible to consider climate change as the resultant of two components: the *natural* and the *anthropogenic* climate change. The first component refers to all the natural phenomena that contribute and have contributed to modify the Earth's climate (such as volcanic eruptions, Earth's orbital changes, solar variations and so on), while the second one is directly linked to the human-induced impacts, such as the emission of greenhouse gases, land alteration, deforestation and so on.

From what has been seen so far, "time" has been the main subject in defining climate change. However, the last piece of information in the definition of climate change is related to the geographic scale of change, i.e., "space". Indeed, these changes may affect not only the global climate, but can also be identified at smaller scales, such as regional or local. However, these aspects will be explored in the *where* paragraph.

Once defined what climate change is, a second question that may arise is "**what is changing?**". When considering this question, the first variable that typically comes to mind is temperature. As stated by the IPCC AR6, the emission of greenhouse gases (GHGs) induced by human activities, have unequivocally exacerbated global warming, resulting in a 1.1°C rise in global surface temperatures in 2011-2022, compared with the 1850-1900 baseline. This correlation is evident in Figure 1.1, where the differences in the global surface temperature are represented together with the global atmospheric concentration of carbon dioxide (CO₂).

The consequences of this global temperature increase are several and affect different components of the Earth's climate system, such as the atmosphere, ocean, cryosphere and biosphere. Anthropogenic global warming is the main driver of the global retreat of glaciers since the 1990s and the decrease in Arctic sea ice area between 1979–1988 and 2010–2019. Between 2010 and 2016, grounding lines in West Antarctica, East Antarctica, and the Antarctic Peninsula retreated at rates faster than 25 m·yr⁻¹ in 22%, 3%, and 10% of surveyed cases, respectively (Konrad et al., 2018). Regarding the mountain glaciers, it has been observed a rapid glacier retreat across the European Alps, estimated in a loss

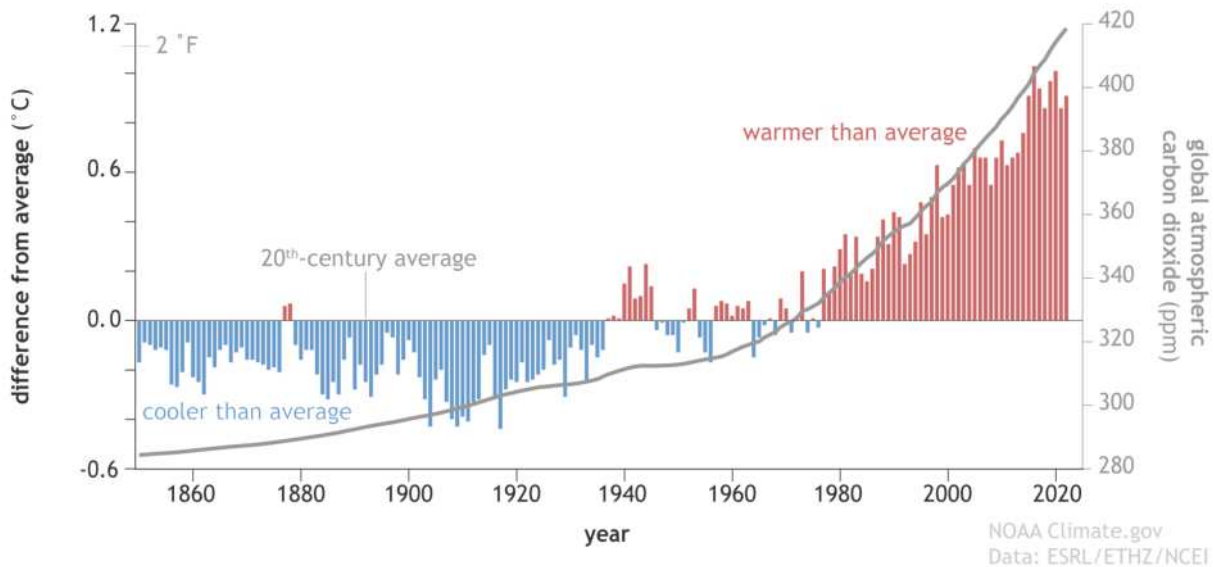


Figure 1.1: From NOAA Climate.gov: Yearly temperature compared to the 20th-century average (red bars mean warmer than average, blue bars mean colder than average) from 1850–2022 and atmospheric CO₂ amounts (gray line): 1850-1958 from IAC, 1959-2019 from NOAA ESRL. Original graph by Dr. Howard Diamond (NOAA ARL), and adapted by NOAA Climate.gov.

of $39 \text{ km}^2 \cdot \text{yr}^{-1}$ during the period 2000-2014 (Sommer et al., 2020). The loss of mass from glaciers together with the ocean thermal expansion are the primarily responsible for the global mean sea level rise, which has increased from $2.2 \pm 0.3 \text{ mm} \cdot \text{yr}^{-1}$ in 1993 to $3.3 \pm 0.3 \text{ mm} \cdot \text{yr}^{-1}$ in 2014 (Chen et al., 2017). The increasing concentration of CO₂ in the atmosphere enhance its absorption by the oceans, leading to a decrease in pH levels and, in turn, their acidification. This process can have significant effects on marine ecosystems, disrupting the balance of marine food chains and impact the overall health of the oceans (Doney et al., 2020). It has been demonstrated that human activities are undermining about 75% of the world’s reefs (Spalding and Brown, 2015).

Anthropogenic climate change is also affecting the magnitude and the frequency of many weather and climate extremes worldwide. Since 1950, rising global temperatures have lead to more frequent and severe heat extremes, such as heatwaves (Perkins-Kirkpatrick and Lewis, 2020) and heat stress events (Chen et al., 2020). Hot and dry conditions have exacerbated the risk of wildfires, lengthening the fire weather season on a large portion of the Earth’s surface (Jolly et al., 2015). The 2023 Canadian wildfires began in March, and by October more than 6,500 fires had burned about 5% of Canada’s entire forest area. As the planet warms, an imbalance in the hydrological cycle is becoming increasingly evident. Higher temperatures are leading to greater evaporation rate from land and oceans, exasperating the *DIDWIW* (i.e., *Drier In Dry, Wetter In Wet*) paradigm (Feng and Zhang, 2015). Indeed, drying trends generally occur in arid regions, where the

reduction of soil moisture increases the risk of more prolonged and severe drought conditions (Trenberth et al., 2014). At the same time, a warmer atmosphere can hold more water vapor, changing the heavy rainfall characteristics (i.e., frequency, intensity, duration and so on) and increasing wetter trends especially in humid regions (Fowler et al., 2021). These changes in intense rainfall are hardly compatible with the capacity of natural and urban drainage systems, increasing the risk of catastrophic floods (Milly et al., 2002).

However, this is just a small part of what is changing due to climate change. Other signatures of climate change are related to intensification of tropical cyclones (Emanuel, 2005), worsening air and water quality (Delpla et al., 2009), erosion of coastal areas (Toimil et al., 2017), and so on.

1.1.2. Why

If paragraph 1.1.1 analyzes what is changing in the climate, it is now appropriate to explore "**why is the climate changing?**". From what has emerged previously, one of the major players is the rise in temperatures, which has been found to be highly correlated with CO₂ emissions (but also other GHGs have to be considered, such as water vapor, H₂O and methane, CH₄). So the starting point needs to be the physical mechanism that links these GHGs to temperature, namely the greenhouse effect. This phenomenon is a natural process that has allowed the proliferation of life on our planet. Solar radiation from the sun reaches the Earth and warms its surface. In response, the Earth emits heat in the form of infrared radiation. Here is where GHGs come into play. These gases absorb the outgoing infrared radiation and re-radiate it in all directions, including back toward the Earth's surface (Figure 1.2a). This action effectively traps heat within the Earth's atmosphere, slowing the loss of heat to space and maintaining temperatures at a level suitable for life.

Starting from the Industrial Revolution in the late 18th century, human activities have been altering the composition of Earth's atmosphere, giving rise to the enhanced greenhouse effect (Figure 1.2b). This phenomenon is driven by the excessive accumulation of GHGs, primarily due to human activities. The most significant contributor to this increase is the burning of fossil fuels for energy, industry, and transportation. Also deforestation results in the increased release of GHGs into the atmosphere. Healthy forests play a crucial role in absorbing CO₂ from the atmosphere, effectively serving as valuable carbon sinks. However, when forests are cleared and subjected to deforestation, they lose this crucial capacity, leading to the release of higher volumes of carbon into the atmosphere. As a result, the concentration of CO₂ in the atmosphere has risen to levels not seen in hundreds of thousands of years. With more CO₂ (and GHGs) in the air,

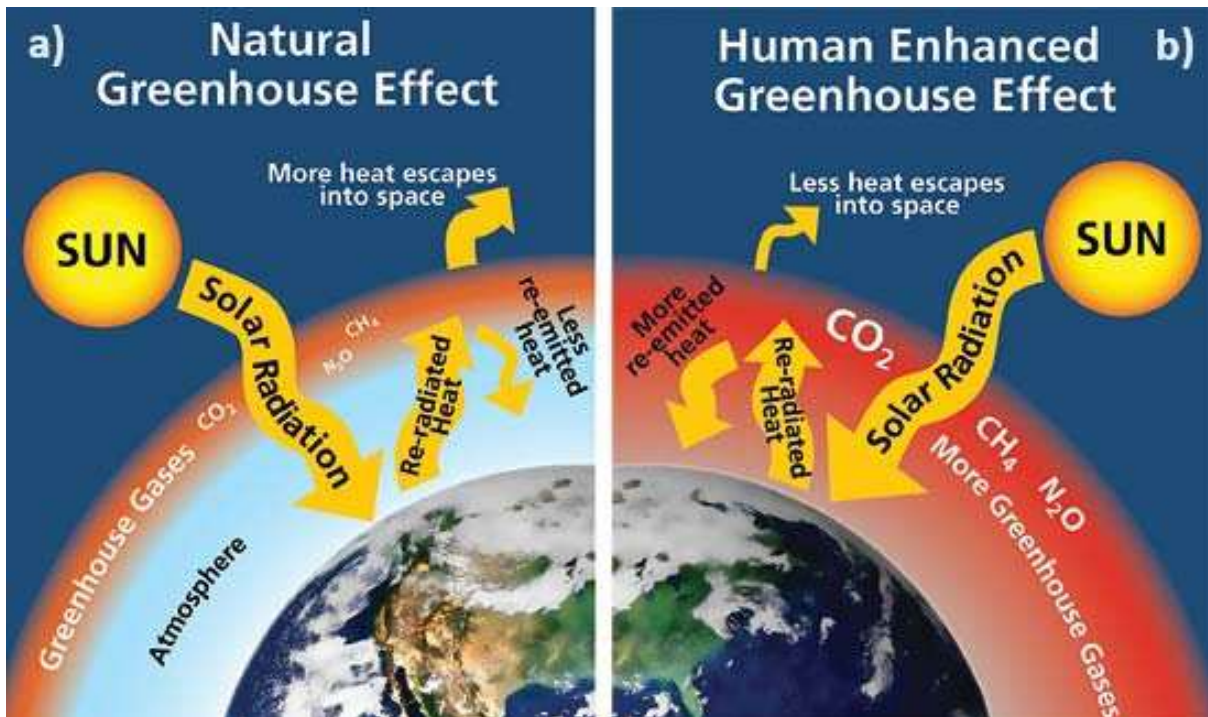


Figure 1.2: From MrGeogWagg: Representation of natural (a) and human enhanced greenhouse effect (b)

heat passing through on its way out is more likely to be stopped, increasing the surface temperature of Earth.

In paragraph 1.1.1 it has also been seen that the occurrence and intensity of extreme events are changing. So it is reasonable to ask: **"why are extremes becoming more extreme and frequent?"** Although this question may seem obvious, nevertheless it is useful to examine it from a statistical point of view. As an example, the distribution of the temperatures related to a certain period generally takes the form of a normal distribution. For instance, the distribution shown in Figure 1.3a can be derived by considering the daily temperatures for a 30-year window at a certain location. Moreover, if these observed temperatures refer to a period in the middle of the 20th, it is possible to conclude that this distribution is representative for the past climate. In this case, the probability to have cold or hot weather is described by the left and right tail of the distribution, respectively.

When this distribution is non-stationary or, in other words, when global warming has a relevant effect on temperature, it implies alterations in either the mean and/or variance of the resulting curve. Comparing the previous with the current temperature distribution (which could be, for example, derived from the observations in the past 30 years at the same location), an increase in the mean temperature of the planet could lead to a rightward shift in the distribution (Figure 1.3b). The effects of this shift may result in a strong reduction in cold events and, at the same time, an increase in the frequency of

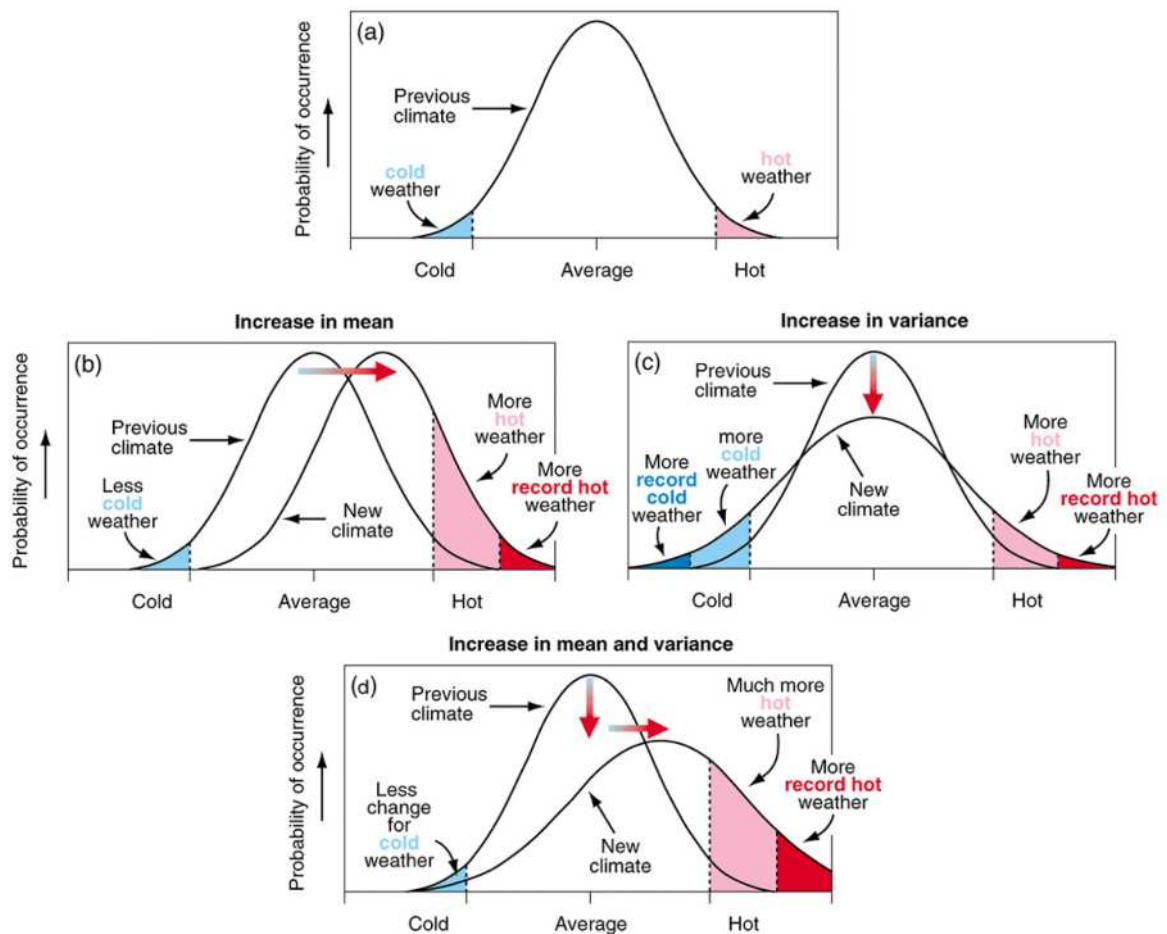


Figure 1.3: Modified from (Houghton et al., 2001): schematic showing the effect on extreme temperatures when (b) the mean temperature increases, (c) the variance increases, and (d) when both the mean and variance increase for a normal distribution of temperature (a)

hot weather (pink shaded area) and in the probability of recording even more extreme hot events (red shaded area), that are not consistent with the previous climate distribution.

An alteration in the mean does not necessarily correspond to a change in variability (or variance), despite the resulting impact may still be dangerous. Indeed, an increase in variability without a change in the mean implies an increase in the probability of both hot and cold extremes as well as the absolute value of the extremes (Figure 1.3c).

However, climate change hardly affect only one of these two parameters. Instead, it is highly likely that alterations could manifest in both mean and variance. When both these characteristics change (Figure 1.3d), this leads to more frequent hot events with even more extreme high temperatures and fewer occurrences of cold events.

1.1.3. Where

What one can reasonably ask is "**where is the climate changing?**". Although climate change is an issue that the entire globe is experiencing, in fact, the greatest impacts may affect a certain area more than another. This greatly depends on which variable is being considered.

Considering the spatial trends in global average surface temperature between 1993 and 2022 (Figure 1.4), is it possible to observe that most of the planet is warming, except for a few locations in the Southern Hemisphere oceans. To be more detailed, the Northern Hemisphere is heating up at a faster rate than the Southern and this is primarily due to the distribution of land and oceans in our planet. Indeed, the Northern Hemisphere has a greater proportion of landmasses compared to the Southern Hemisphere, which has more oceans. Due to their relevant heat capacity (i.e., thermal inertia), the oceans warm and cool more slowly than landmasses and, as a result, the Northern Hemisphere experiences more significant temperature variations, leading to more rapid warming trends.

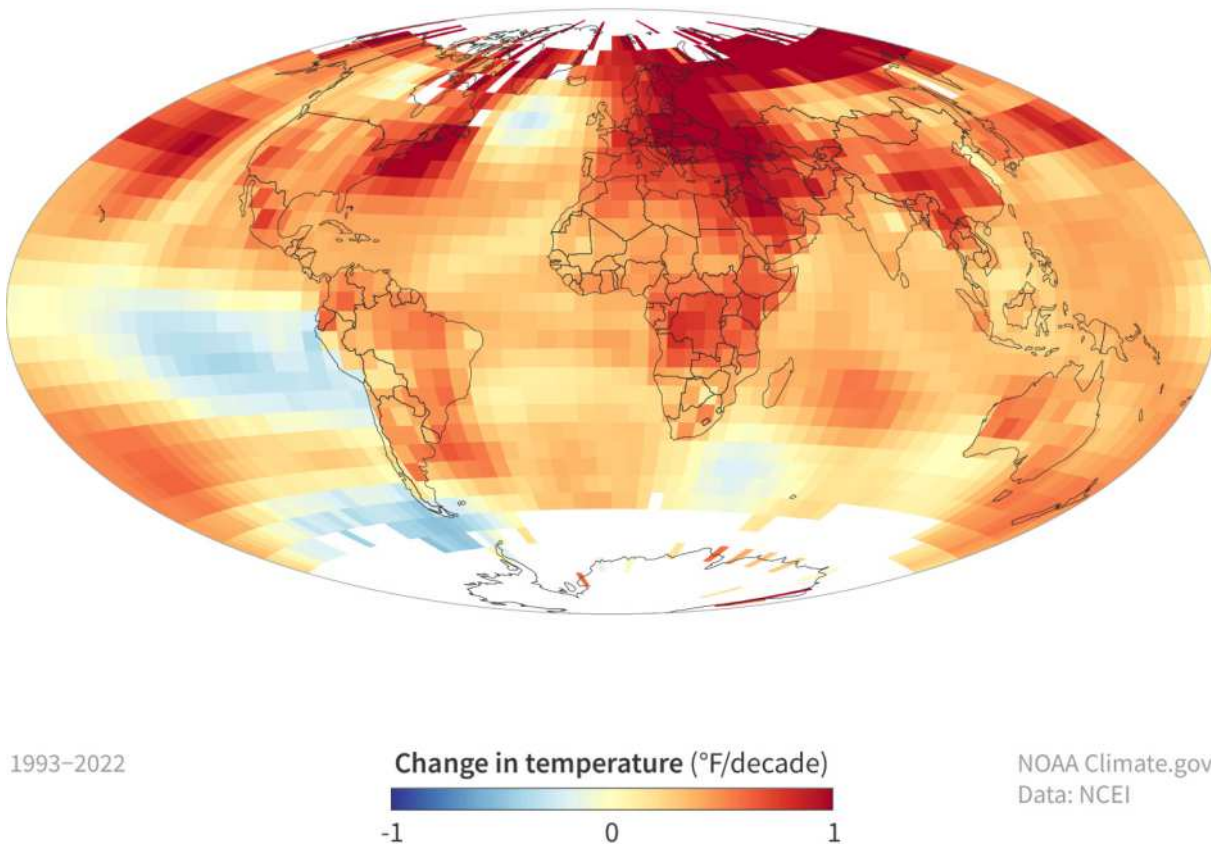


Figure 1.4: From NOAA Climate.gov: trends in global average surface temperature between 1993 and 2022 in degrees Fahrenheit per decade. The map is based on data from NOAA Centers for Environmental Information

However oceans also play a more active and dynamic role in redistributing the heat absorbed by the sun. Ocean currents, such as the Gulf Stream, move vast amounts of heat across the planet and transport warm water from the equator toward the Northern Hemisphere. Since the oceans are confined by land masses, their heat transport is more localized and channelled into specific regions, influencing regional climate patterns and contribute to warming.

Focusing on the extremes and, particularly, on hot extremes, heavy precipitation and agricultural and ecological drought, the Working Group I in the AR6 (Masson-Delmotte et al., 2021) collected what the scientific community has produced over the years to provide a comprehensive picture of the observed changes and the human contribution to these alterations (Figure 1.5). Regarding hot extremes (Figure 1.5a), the report states that average and extreme heat events are increasing in every region of the world and that it is very likely that human activities have contributed on these trends. Regional increases in hot extremes have been found in China (Sun et al., 2014; Chen and Sun, 2021) and India (Kothawale et al., 2010; Joshi et al., 2020). Chen and Sun (2021) explored the changes in two climate extreme indices that together measure hot and cold events (i.e., hottest day, TXx, the coldest night, TNn) over China. Both TXx and TNn respond strongly to the rapid warming, being characterized by an increasing rate of 0.17 and 0.52 °C/10 years during 1961–2014, respectively. Joshi et al. (2020) showed that India has witnessed an increase in the occurrences of hot days with higher temperatures in the recent period (1976–2018) compared to the past (1951–1975). The study identifies robust positive geopotential height anomalies at 500 hPa over northern India as crucial factors, dynamically leading to subsidence, clear sky conditions, reduced precipitable water, and depleted soil moisture, contributing to the heightened occurrence of hot extremes in recent decades. Also United States (Smith et al., 2013; Mutiibwa et al., 2015), Europe (Stott et al., 2016; Rousi et al., 2022), Africa (Vizy and Cook, 2012; Ceccherini et al., 2017) and Australia (Perkins-Kirkpatrick et al., 2016) has been characterized by rises in the occurrence and magnitude of hot extremes. Rousi et al. (2022) identified Europe as a hotspot for heatwaves, experiencing trends that are three to four times faster than the rest of the northern mid-latitudes over the past 42 years. This accelerated trend is associated with changes in atmospheric dynamics, specifically an increase in the frequency and persistence of double jet stream states over Eurasia. Over Africa, Ceccherini et al. (2017) quantified heatwaves using the Heat Wave Magnitude Index daily (HWMId), which combines the duration and intensity of extreme temperature events into a single numerical index. They have found that HWMId related to maximum temperatures had the most significant presence during 2006–2015. In this period, the frequency of extreme heatwaves increased to 24.5 observations per year compared to 12.3 per year in the period from 1981

to 2005.

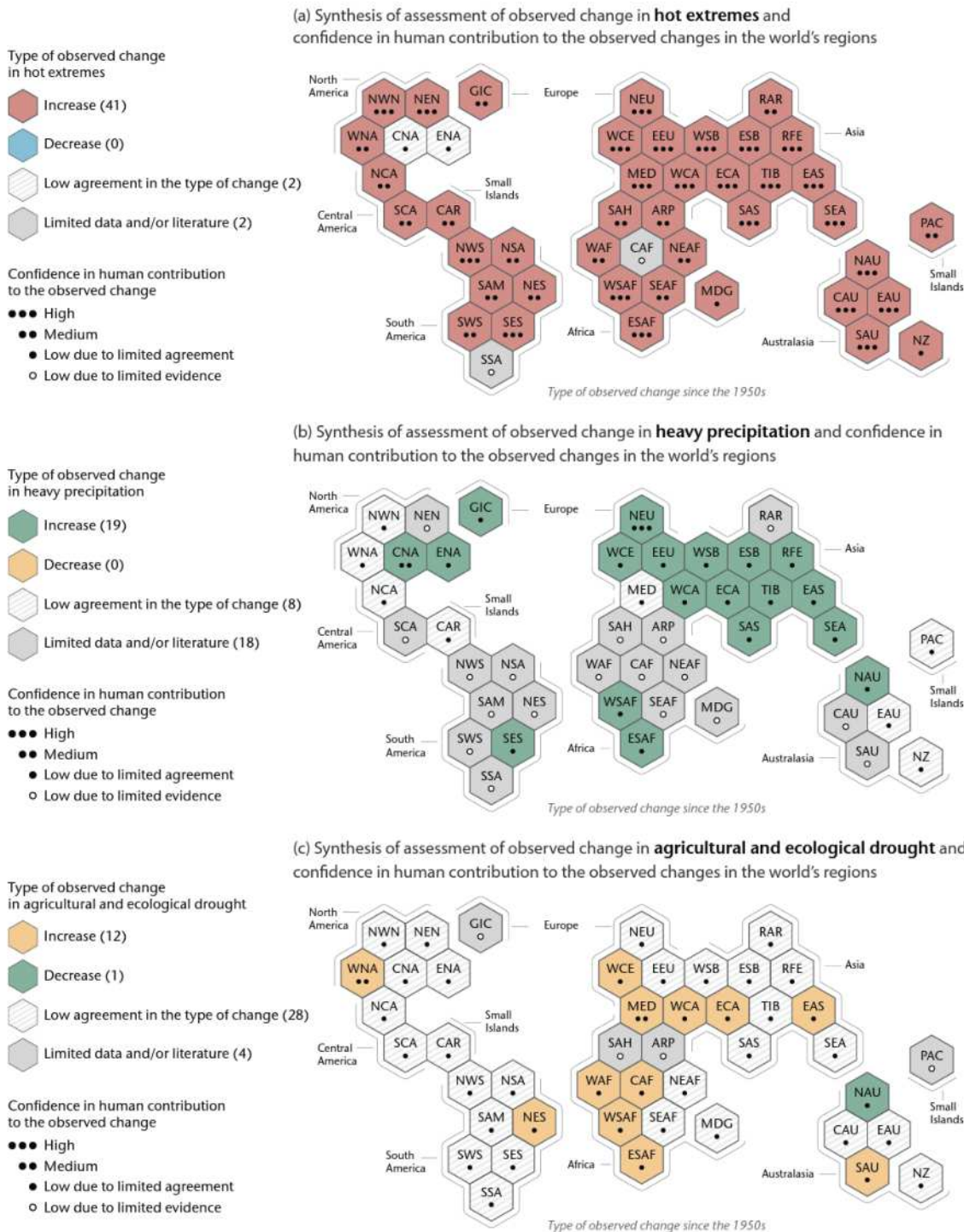


Figure 1.5: From (Masson-Delmotte et al., 2021): synthesis of assessed observed and attributable regional changes for hot extremes (a), heavy precipitation (b) and agricultural and ecological drought (c). The hexagons correspond to each one of the IPCC AR6 WGI reference regions

Differently from the hot extremes, changes in the pattern of heavy precipitation (Fig-

ure 1.5b) and agricultural and ecological drought (Figure 1.5c), do not show a clear global trend, but uncertainties are present for some regions, as well as low agreements in the type of change (mainly due to differences in the methodology to define the heaviness of the events, dataset and extension of the analysis). However, where present, trends always manifest a sign of growth, that is, intensification of extreme events and worsening of drought conditions. Regarding extreme precipitation, especially the Northern Europe (Cioffi et al., 2015; Zeder and Fischer, 2020), the central and eastern United States (East-erling et al., 2017) and Asia (Chen and Sun, 2021) have experienced changes in the usual patterns, despite the confidence in human contribution to the observed changes is not always certain. A more detailed discussion on changes in precipitation extremes will be addressed in the section 1.2.

1.1.4. When

From what has been seen so far, our planet has experienced significant changes in its climate since the 1800s, with an acceleration especially in the last 50 years. Looking to the future, "**until when will climate change be something we have to worry about?**". To answer this question, it is first necessary to introduce the instruments that allow to examine the projected state of the climate, namely Global (or General) Circulation Models (GCMs, Figure 1.6a). GCMs are numerical models that describe the interactions among the major components of the climate system (atmosphere, land surface, oceans, etc...) through quantitative methods based on solving differential equations. These equations are similar to the one used in Numerical Weather Prediction (NWP) models, including terms for the conservation of mass, equations governing fluid flow and thermodynamic. However, NWP models are used for weather prediction (namely for short-term prediction, according to what has been explained in section 1.1.1), since they use high resolution spatial grids and temporal time step and this would require huge computing resources in order to be applied at the global scale.

In GCMs, the equations are numerically solved in a three dimensional grid over the entire globe, typically characterized by a horizontal resolution that can reach 100 km (i.e., $\simeq 1^\circ$) and by several layers in the atmosphere and in the oceans. The temporal resolution is generally daily, although some models are able to achieve sub-daily resolutions, such as 6 or 3 hours. Having these coarse spatial and temporal resolutions, GCMs usually contain parameterizations (i.e., simplifications) for processes that occur on scales too small to be resolved directly (i.e., convection).

These models are forced with scenarios that quantify the trajectory of the GHGs concentration up to 2100. In particular, the IPCC AR5 introduced the Representative

Concentration Pathways (RCPs), which consider the GHG concentrations in terms of radiative forcing potentially reached in 2100, i.e., the warming effect on the Earth caused by these concentrations (Figure 1.6b). The RCPs introduced are four, namely RCP2.6, RCP4.5, RCP6, and RCP8.5, corresponding to a radiative forcing of 2.6, 4.5, 6, and 8.5 W/m^2 in 2100. In addition to RCPs, the IPCC AR6 introduced the Shared Socioeconomic Pathways (SSPs), that estimate GHG trajectories according to different climate policies (Figure Figure 1.6c). Hence, SSPs are useful for understanding how human activities and socioeconomic policies might influence GHG concentrations and, consequently, climate change up to 2100. The five scenarios introduced by the IPCC AR6 are SSP1 (Sustainability - "Taking the Green Road"), SSP2 ("Middle of the Road"), SSP3 (Regional Rivalry - "A Rocky Road"), SSP4 (Inequality - "A Road divided") and SSP5 (Fossil-fueled development - "Taking the Highway"). By combining the radiative forcing levels and SSPs (Figure 1.6d), GCM models are able to provide a more comprehensive view of how climate might respond in different socio-economic and emission situations. From the latter panel it is also possible to observe that four scenarios are considered the top priority in the experimental design (i.e., Tier 1), since they serve as a good comparison to RCPs established in AR5. Moreover, the modelling centres are eventually allowed to explore other scenarios (i.e., Tier 2), in order to range over other potential pathways. However, it is worth mentioning that not all the combinations between radiative forcing levels and SSPs are plausible (i.e., the white boxes). As an example, it would not be realistic to combine SSP5, which favors the fossil-fuel development, with the low forcing scenario (e.g., $1.9 \text{ W}/\text{m}^2$), which would require stricter climate policies and strong mitigation measures, resulting in reduced greenhouse gas emissions.

Finally, before answering the question raised at the beginning of the paragraph, it is worth mentioning two important concepts in using these models, namely potential biases and uncertainties in their climate projections. Being models, GCMs can be affected by systematic errors in their output, mainly due to their limited spatial resolution, simplified thermodynamic processes and physics or incomplete understanding of the global climate system. Indeed, the atmosphere is a very complex system to model, as the interactions that occur with the other components. To reduce these biases, two procedures are generally employed: the first one is based on correcting the outputs relative to the historical baseline through observations (i.e., bias-correction methods), and the second one is based on averaging the response of multiple GCMs, namely by creating an ensemble of GCMs. Although these two procedures can be used together, it is clear that the former is much more challenging and often struggles with the availability of sufficient recorded data. The second, on the contrary, is always carried out and, as demonstrated by a large number of scientific publications, is often enough to return a signal consistent with the one

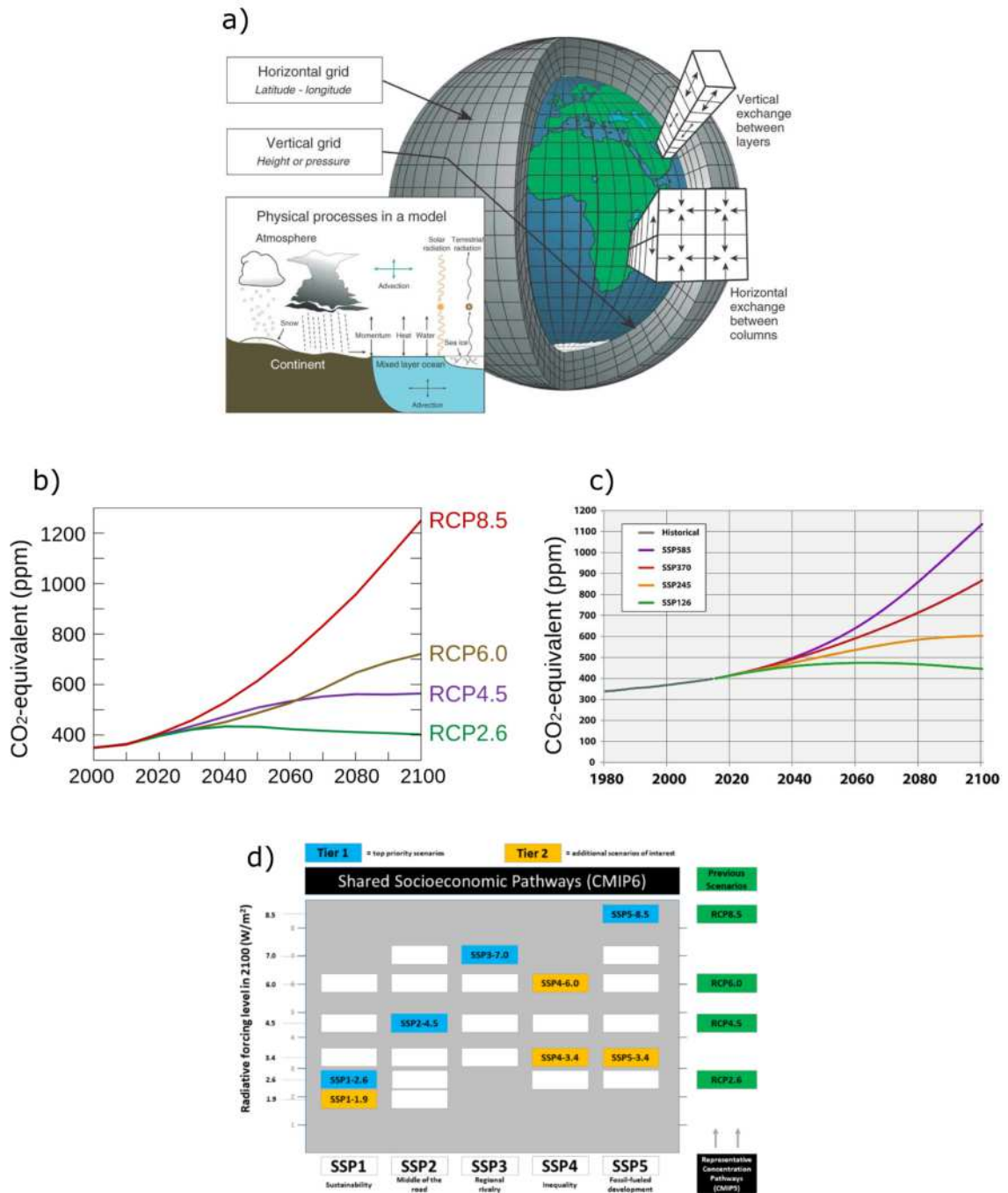


Figure 1.6: Schematic of a Global Circulation Model (a, from Balaji et al. (2022)) and the projected trajectories of Representative Concentration Pathways (b, from Wikipedia), Shared Socioeconomic Pathways (c, from Deutsches Klimarechenzentrum), and their combination (d, from Government of Canada website)

observed. In addition to models error, a significant factor contributing to uncertainty in long-term climate projections is the radiative forcing resulting from human-induced emissions of GHGs. If on the one hand this uncertainty is partially coped by the different combinations of RCPs and SSPs that can be used, on the other it remains the uncertainty dependent on how quickly each component responds (e.g., the atmosphere responds quickly to various forcing conditions, the ocean takes much longer). This issue is generally solved by performing more than one simulation, i.e., by creating different realizations (e.g., simulations that differ only in their initial conditions) with different initialization (e.g., simulations performed under the same conditions but with different initialization procedures). These simulations are generally referred to as "variant" of a certain GCM and denoted by abbreviation; such an example, in the GCMs included in the Coupled Model Intercomparison Project Phase 6 (CMIP6), each individual variant is characterized by four indices: r for the realization, i for the initialization, p for the physics (i.e., identifying the physics version used by the model) and, f for the forcing (i.e., distinguishing runs conforming to the protocol of a single CMIP6 experiment, but with different variants of forcing applied).

By using GCMs projection at different SSP-RCP scenarios, it is possible to obtain the projected changes in the state of climate. Figure 1.7 depicts the future changes in global surface temperature in comparison to the period 1850-1900. The horizontal gray line represents the mean surface temperature observed during the period 2011-2020, which is 1.1°C warmer than 1850-1900. The colored lines, on the other hand, show the potential trajectories for temperature changes based on different scenarios. What emerges from the figure is a clear distinction between changes related to worst-case and best-case scenarios. For the scenarios with lower GHGs concentrations (i.e., blue lines) there could be a slowdown in the temperature growth trend starting around 2030 and a subsequent stabilization about $+1.5^{\circ}\text{C}$ with a small decrease until 2100. Completely different is the trend expected in the worst-case scenarios (including even the intermediate one): in these cases a maximum point in temperature changes might not be reached by 2100, with projected increases up to 4°C in the very high emission scenario.

What is worth noting is that even by curbing GHG emissions into the atmosphere today, the planet could suffer from what has already been produced for hundreds of years. For this reason, as strongly urged by different research organizations, it is essential that climate policies are swiftly implemented to mitigate the ongoing impacts of global warming and pave the way for a sustainable and resilient future.

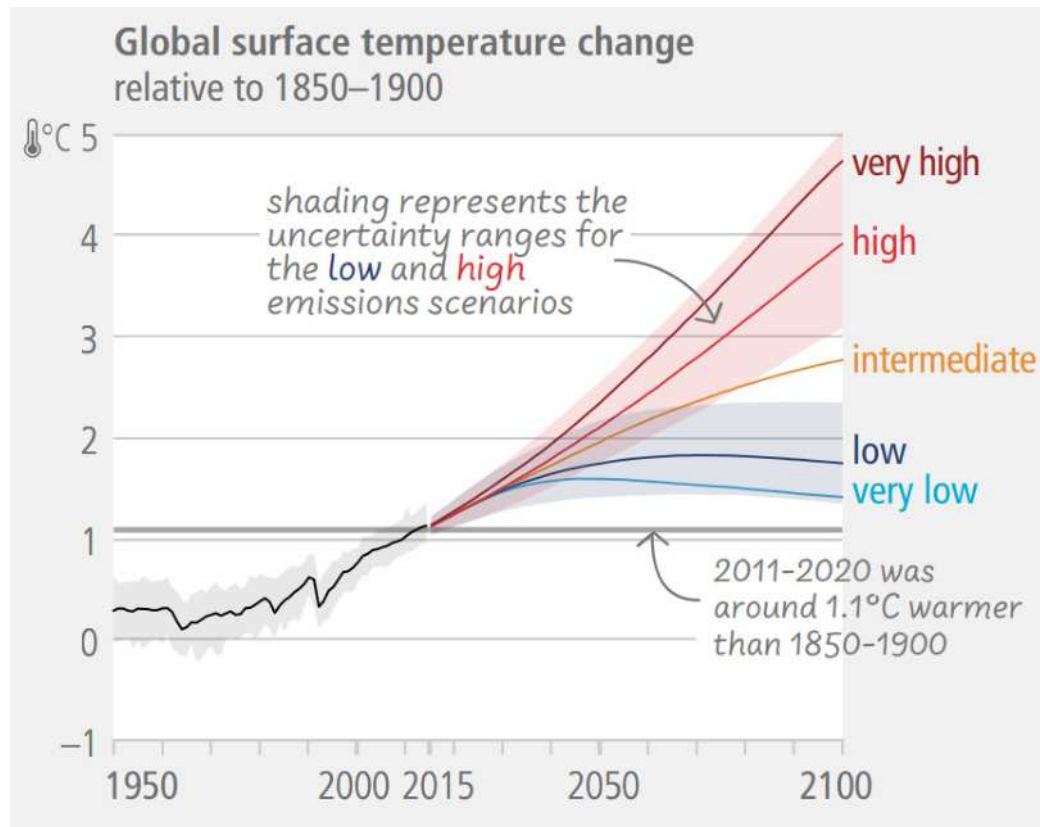


Figure 1.7: From IPCC AR6: global surface temperature changes in °C relative to 1850–1900. These changes were obtained by combining CMIP6 model simulations with observational constraints based on past simulated warming, as well as an updated assessment of equilibrium climate sensitivity. Very likely ranges are shown for the low and high GHG emissions scenarios (SSP1-2.6 and SSP3-7.0)

1.1.5. Who

Throughout the previous paragraphs, some of the impacts related to climate change have been analyzed, as well as how the changing climate is projected to be an even more serious issue for years to come. What has not been still explored is: **who (entity/factor) is affected by climate change impacts?**

Of course, climate change poses a range of threats to human health, affecting various aspects of life. Rising average temperatures and the resulting increase in the frequency and duration of heat waves will increase the risk of heat-related deaths (Zhao et al., 2016; Im et al., 2018). Mora et al. (2017) identified a global threshold beyond which daily mean surface air temperature and relative humidity become lethal. They found this deadly threshold is currently exceeded for more than 20 days in a year in large area, jeopardizing about the 30% of the global population. By the year 2100, this percentage is projected to rise to around 48% under a low-concentration scenario, while 74% under a scenario of

rising emissions.

In this light, Figure 1.8 from IPCC AR6 is meaningful, since it shows how the climate has already changed and will change along the lifespan of three representative generations (born in 1950, 1980 and 2020). A person born in 1950 entered a world that had seen approximately 0.25°C of warming compared to the late 1800s. Today, a 70-year-old has witnessed an increase of 0.85°C in temperature during its lifetime, that means approximately 0.12°C per decade. For someone born in 1980, the initial condition was already worse, since the starting exposure was to approximately 0.4°C of warming above pre-industrial levels. Over the last 40 years, someone from this latter generation experienced 0.75°C of warming, equivalent to an average rate of almost 0.19°C per decade.

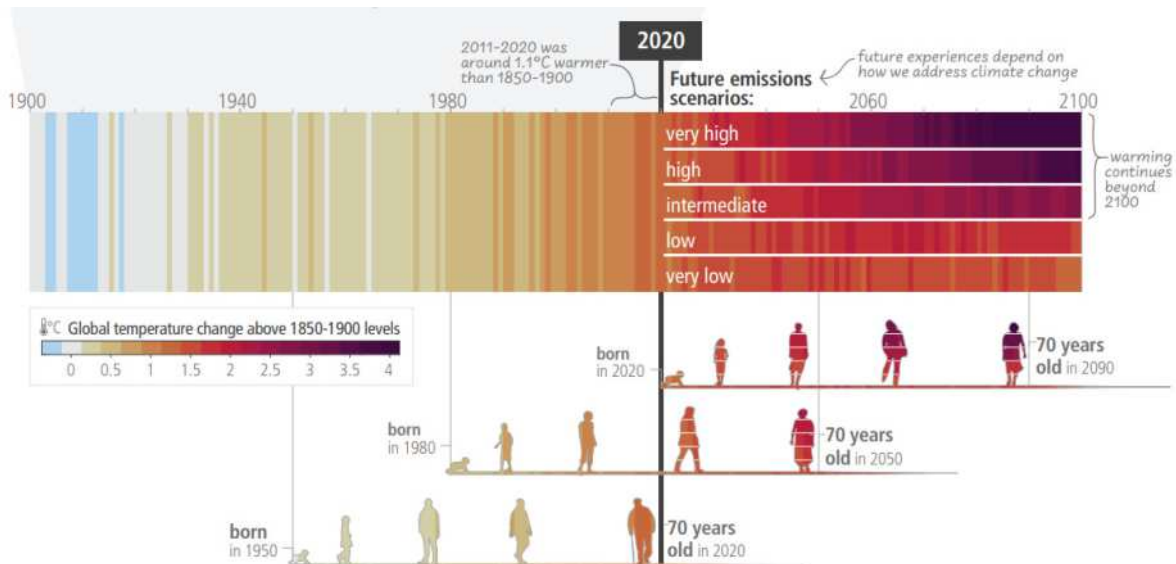


Figure 1.8: From IPCC AR6: Observed (1900–2020) and projected (2021–2100) changes in global surface temperature (relative to 1850–1900), which are linked to changes in climate conditions and impacts, illustrate how the climate has already changed and will change along the lifespan of three representative generations (born in 1950, 1980 and 2020). Future projections (2021–2100) of changes in global surface temperature are shown for very low (SSP1-1.9), low (SSP1-2.6), intermediate (SSP2-4.5), high (SSP3-7.0) and very high (SSP5-8.5) GHG emissions scenarios. Changes in annual global surface temperatures are presented as ‘climate stripes’, with future projections showing the human-caused long-term trends and continuing modulation by natural variability (represented here using observed levels of past natural variability). Colours on the generational icons correspond to the global surface temperature stripes for each year, with segments on future icons differentiating possible future experiences.

Notably, the rate of warming for those born in 1980 was nearly 50% faster than for those born in 1950. What is even more dramatic is that the last generation considered, namely those born in 2020, have seen an average temperature already 1.1°C higher than pre-industrial levels. Under higher emission scenarios, these individuals might experience

average decadal warming rates about three times higher than those born in 1950 by the time they reach the age of 70. However, in scenarios where warming is limited below 2°C or 1.5°C, as seen in low and very low emission scenarios, the generation of the 2020s could witness climate stabilization before reaching 30 years of age.

Although Figure 1.8 implies equality in exposure to global warming, different studies have shown that certain segments of the population will suffer more from the climate crisis (King and Harrington, 2018; Ahmadalipour et al., 2019). This is a reflection not only of the asymmetric distribution of climate change impacts at the regional scale (as shown in paragraph 1.1.3), but also of existing social inequalities that could be exacerbated under the stress of climate change. As an example, by assessing the mortality risk related to extreme heat stress for individuals aged over 65 across the Middle East and North Africa region, Ahmadalipour et al. (2019) found that the poorest countries might experience higher mortality risks compared to wealthier nations, even if their contribution to global climate change is considerably lower.

Not only hot extremes, but also the increases in frequency and magnitude of other extreme phenomena (i.e., heavy precipitation, drought, floods, and so on) might pose a serious risk for human life. An increasingly warm climate could result in an increase of the occurrence of longer and more intense droughts in the 21st century with relevant implications in water availability for humans (but also for vegetation and agriculture, which will be discussed later on) (Mosley, 2015). A growing body of evidence suggests that climate change may alter the incidence of waterborne diseases, undermining the gains made in public health and development during the past half-century (Levy et al., 2018). Moreover, more extreme rainfall events could lead to severe floods, resulting in fatalities, spreading the waterborne disease, disrupting access to hospitals and so on (Funari et al., 2012; Tabari, 2020). All these aspects, in the long-term, could produce social and economic frictions between population, leading to a growth of future risk of conflicts (Mach et al., 2019).

However, humans are not the only ones affected. Climate change also poses a threat to various ecosystems and the species that inhabit them. Indeed, climate change may have an interaction with land-cover changes, exacerbating the risk of habitat loss and fragmentation on biodiversity (Jetz et al., 2007; Mantyka-Pringle et al., 2015). Segan et al. (2016) found that it is likely that climate change has influenced habitat losses in more than 19% of ecoregions worldwide, and this number is projected to increase up to 44% under the worst-case scenario during the 21st century. Figure 1.9 (Pörtner et al., 2022) depicts the risks of an increasingly irreversible losses, in terrestrial, freshwater, cryospheric, coastal and open ocean ecosystems at different global warming levels. Under the SSP5-8.5 scenario, these losses might also reach values higher than 90% for several

species of birds, mammals, reptiles, amphibians, marine fish, and so on, especially located in the equatorial and tropical areas.

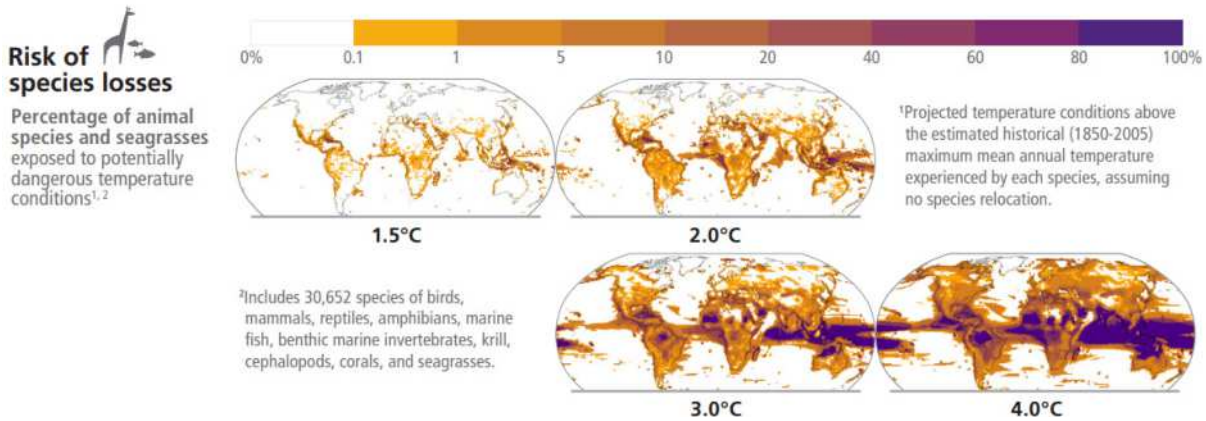


Figure 1.9: From IPCC AR6: risks of species losses as indicated by the percentage of assessed species exposed to potentially dangerous temperature conditions, as defined by conditions beyond the estimated historical (1850–2005) maximum mean annual temperature experienced by each species, at global warming levels of 1.5°C, 2°C, 3°C and 4°C

Climate and weather extremes may also undermine agriculture, threatening food security. Indeed, agricultural yield strongly depends on weather conditions, crop and soil management practices, the presence of pathogens and pests, and the occurrence of extreme weather events. All these elements might be impacted by climate change. As an example, high temperature can suppress plant immunity, leading to increased pathogen infections (Singh et al., 2023). Lesk et al. (2016) quantify the global losses in cereal production resulting from reported extreme weather disasters during 1964–2007. The authors showed that droughts and extreme heat significantly reduced national cereal production by 9–10%. Moreover, they showed that production losses from droughts were linked to decreases in both harvested area and yields, while extreme heat primarily led to reductions in cereal yields. Looking at the future, Asseng et al. (2015) estimated that the global wheat production might decrease by 6% for each °C of further temperature increase, becoming more variable both in space and time.

1.1.6. How

Only one question in this paragraph, "**how have we faced and how are we facing climate change?**". As awareness of anthropogenic influences on climate has increased, so the need for policies to mitigate these effects and adapt to the changing environment. There is a long history on the evolution of climate policies, full of milestones, international agreements, and changes in public perception. In the following, the major

climate negotiations will be briefly described, along with the main points introduced in each of them. Additionally, a summarized chronological scheme is presented in Figure 1.10.

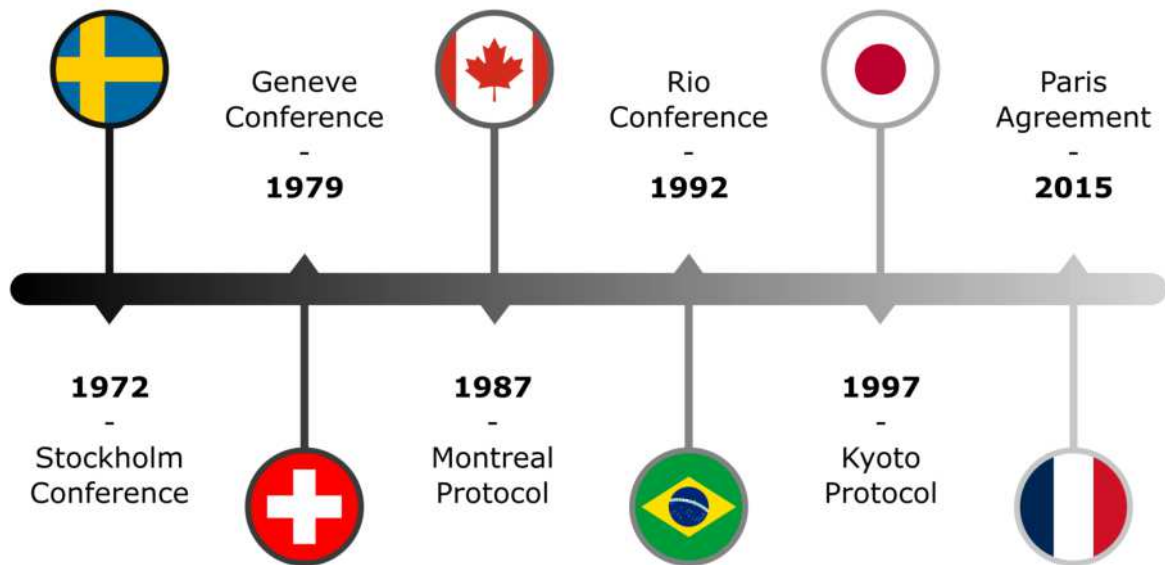


Figure 1.10: Major climate negotiations timeline

Stockholm Conference (1972) Although several climate change issues had already emerged during the 20th century, the first real effort at the international level was the 1972 UN Scientific Conference, also known as the First Earth Summit, held in Stockholm. During this conference, a Declaration containing 26 principles concerning the environment and development was adopted, delineating principles for the preservation and improvement of the human environment. It is worth mentioning Principle 6 of the Declaration, which states that: "*The discharge of toxic substances or of other substances and the release of heat, in such quantities or concentrations as to exceed the capacity of the environment to render them harmless, must be halted in order to ensure that serious or irreversible damage is not inflicted upon ecosystems. [...]*", pointing out the capacity of the environment to remediate to only part of the pollution (of any kind) produced by humans.

Moreover, The UN Scientific Conference also emphasized the importance of climate observations in order to gain insight into real changes in the environment, Indeed, as stated by the 79th recommendation (out of 109) of the Action Plan, the WMO was responsible to guide and coordinate the States involved in setting up a large global network (not less than 100 stations) for "*monitoring properties and constituents of the atmosphere on a regional basis and especially changes in the distribution and*

concentration of contaminants".

Geneve Conference (1979) The World Climate Conference in Geneva was one of the first major meetings on climate change and it was sponsored by the WMO. This Conference led to the establishment of the World Climate Programme, which was characterized by four main milestones:

- research into the mechanisms of climate with the aim to clarify the relative roles of natural and anthropogenic influences thanks to the development of mathematical models for simulating the climate system;
- improving the acquisition and availability of a vast amount of meteorological, hydrological oceanographic and pertinent geophysical data;
- application of knowledge of climate in planning, development and management;
- study of the impact of climate variability and change on human activities, requiring the improvements in the understanding of the relationships between climate and human society.

This Conference also set the stage for the establishment of the IPCC in 1988 through the effort of the WMO and the United Nations Environment Programme (UNEP).

Montreal Protocol (1987) The Montreal Protocol stands as a landmark international treaty designed to address the depletion of the ozone layer. It represents a collaborative global effort to mitigate the impact of human activities on the Earth's stratospheric ozone. The core objective was to control and eventually eliminate the production and consumption of substances identified as Ozone-Depleting Substances (ODS). Chlorofluorocarbons (CFCs), halons, carbon tetrachloride, and other chemicals detrimental to the ozone layer were targeted, and due to its extensive adoption and execution, it has often been hailed as a paradigm of successful international collaboration. This aspect has also been proven by different modeling studies, which have suggested that, if the Montreal Protocol had not been implemented, the global mean temperatures would have raised by over 2°C by 2070 solely due to the warming effects caused by ozone-depleting substances (Garcia et al., 2012; Barnes et al., 2019).

Rio Conference (1992) On the 20th anniversary of the Stockholm conference, a second Earth Summit (officially known as the United Nations Conference on Environment and Development, UNCED) was held in Rio de Janeiro. The summit brought together heads of state, government officials, and representatives from various sectors to discuss pressing issues related to sustainable development. The summit sought to establish international agreements that would serve as the basis for global efforts toward sustainable development. Among the most significant outcomes was the Rio Declaration on Environment and Development (27 Principles), which articulated

the basic principles guiding sustainable development initiatives. Among the central points of this summit, there was also the formulation a comprehensive agenda (i.e., the "Agenda 21") to outlines global strategies for sustainable development. It addresses a wide range of environmental and social issues, emphasizing the need for international cooperation to achieve sustainable development. The agenda includes commitments not only to address climate change, but also to combat poverty, promote health and preserve biodiversity. It encourages the integration of environmental considerations into development planning at all levels and underscores the role of various stakeholders, including governments, businesses, and citizens, in fostering sustainability.

Kyoto Protocol (1997) The Kyoto Protocol implemented the objectives defined in 1992 by the United Nations Framework Convention on Climate Change (UNFCCC) on reducing the greenhouse gas concentrations in the atmosphere. In particular, all the industrialized countries that were members of the OECD (Organisation for Economic Co-operation and Development) in 1992 should have "*individually or jointly, ensured that their aggregate anthropogenic carbon dioxide equivalent emissions greenhouse gases (carbon dioxide, methane, nitrous oxide, hydrofluorocarbons, perfluorocarbons and sulphur hexafluoride) did not exceed their assigned amounts reduction commitments[...] with a view to reducing their overall emissions of such gases by at least 5 per cent below 1990 levels in the commitment period 2008 to 2012.*" To facilitate compliance, the Kyoto Protocol incorporated flexibility mechanisms. Emission trading allowed participating countries to trade emission allowances, fostering cost-effective reductions. The Clean Development Mechanism (CDM) enabled developed nations to invest in emission reduction projects in developing countries, earning certified emission reduction credits. Joint Implementation (JI) permitted collaborative emission reduction projects among the industrialized countries of the OECD. Moreover, while developing countries were not assigned specific emission reduction targets, the Protocol encouraged their voluntary mitigation actions. Financial assistance and technology transfer were recognized as crucial for helping developing nations adapt to climate change and reduce emissions. However, the Protocol's first commitment period (2008 - 2012) did not have the desired effects. Indeed, the emissions of GHG dramatically increased between 1997 and 2012 (Rosen, 2015), mainly driven by countries not bound by the Protocol (e.g., China, who was considered a developing country, and United States, who did not ratify the Protocol). Also, the European Union ability to meet its target was not due entirely to an effective community policy, but more on the massive cuts by Germany and the United Kingdom together with the absorption of low-emission territories in

Eastern Europe (that reduce the EU overall emissions due to the flexible mechanisms within the Protocol).

A second commitment period was agreed in 2012 to extend the agreement to 2020. (i.e., the Doha Amendment to the Kyoto Protocol), setting a goal of reducing GHG emissions by 18% compared to 1990 levels for participating countries. However, it entered into force only in 31 December 2020, following its acceptance by the mandated minimum of at least 144 states, although the second commitment period ended on the same day.

Paris Agreement (2015) The Paris Agreement, adopted in 2015 during the 21st Conference of the Parties (COP21) to the UNFCCC, sought to unite nations in a collective effort to limit global temperature increase, adapt to the impacts of climate change, and foster climate resilience. The heart of the Agreement is to keep the global average temperature well below 2°C above pre-industrial levels. This ambitious target recognizes the severe consequences of exceeding the 2 °C threshold, particularly for vulnerable countries and ecosystems. In addition to this, the Paris Agreement promoted climate change adaptation and resilience themes, aligning financial flows with low-emission and climate-resilient development.

Unlike the Kyoto Protocol, the Paris Agreement adopts a bottom-up approach, encouraging countries to set their own Nationally Determined Contributions (NDCs) to emission reduction. This approach is designed for a more inclusive participation, especially involving the developing countries, recognizing the different contributions of each nations in assessing the global warming issue. Another crucial point in the Paris Agreement is the transparency framework for achieving the goals: each country is required to report regularly on its emission and progress against the NDCs. This transparency should increase accountability and facilitates a global assessment process every five years to evaluate collective progress toward the Agreement's goals. The first assessment took place in 2018 during COP24 in Katowice (Poland), while COP26 in Glasgow (UK) was anticipated as one of the most crucial conferences, as many countries were expected to present new climate objectives following the first five-year review cycle outlined in the Paris Agreement.

About eight years after the Paris Agreement, around 107 of the 177 countries (80.6% of global emissions) have submitted a new or updated NDC with reduced total emissions compared to their initial NDC.

1.2. Extreme precipitation in a climate change context

Defining an extreme event is not as simple as it would sound. From a terminology perspective, the word "extreme" does not have an unambiguous definition, but other words (e.g., "severe", "intense", "rare", "high-impact", and so on) are often used interchangeably (Stephenson et al., 2008). For example, Camuffo et al. (2020) drew on the different meanings of "extreme" that can be found in the Oxford Dictionary. In this case, four definitions are reported:

- *Very great.* This definition is "quantitative", being based on the intensity, or the amount, i.e., a very high threshold.
- *Not ordinary or usual.* This definition is "frequency or time related", being based on the fact that the event, or its intensity, is rare and may occur again after a long (return) period.
- *Serious or severe.* This definition might be interpreted in terms of "effectiveness and impact", i.e., leaving a dramatic impact on the society or the landscape. From this point of view, every natural disaster is also an extreme event. However, this definition might also be interpreted in terms of the quantitative concept (*Very great*).
- *Far from moderate.* This definition is "relative" to the normal occurrence, as it indicates an event that departs from the normal distribution, and may be interpreted as exceeding a certain percentile threshold, or departing from a typical distribution.

Although it may seem that these meanings can be universally comprehensive, Stephenson et al. (2008) states that the definition of "extreme" cannot have an absolute meaning, but that its relativity is highly context-dependent. Referring to the "hydrological extreme events", for instance, Morbidelli (2022) define them as "*natural events that have the potential for a significant adverse impact on lives, infrastructure, or the environment*". This definition, in fact, appears to be perfect when referring to extremes in the hydrological field, since the concepts of hazard and risk of potential impacts turn out to be of central importance. In other words, even a flood characterized by a low return period (i.e., not exceptional from a statistical point of view) can be defined as extreme when it exposes society to a major risk. Moving to the meteorological field, the IPCC (Seneviratne et al., 2012) defines an "extreme climate or weather event" as "*the occurrence of a value of a weather or climate variable above (or below) a threshold value near the upper (or lower) ends of the range of observed values of the variable*". Thus, in this case more emphasis is placed on the magnitude of these events, which is also often related to a certain rarity in the occurrence (as shown by the temperature distribution in Figure 1.3a).

The definition provided by Seneviratne et al. (2012) also adds a second ambiguity, more related to a methodological aspect: there is no unique threshold from which an event can be defined as extreme or not. Obviously considering the probability distribution of a generic variable, the smaller the portion of the tails that is considered, the more "extremes" are the selected values. However, this often clashes with the availability of long series of observations.

Focusing on precipitation, different methods can be used to define extreme events and to study observed and projected changes in their characteristics, such as the Block-Maxima (Pujol et al., 2007; Villarini, 2012; Westra et al., 2013; Wi et al., 2016), the Peak Over Threshold (POT) (Villarini et al., 2011a; Trambly et al., 2012; Wi et al., 2016) and the indices developed by the Expert Team on Climate Change Detection and Indices (ETCCDI) (Song et al., 2015; Panda et al., 2016; Gentilucci et al., 2020). It is clear that each of these methods has strengths and weaknesses, and the choice of one or the other method depends on the ultimate goal of the study. As an example, while block-maxima consists of dividing the observation period into non-overlapping periods of equal size and restricts attention to the maximum observation in each period, POT is based on selecting all the values that exceeds a certain threshold (i.e., generally a certain high percentile). When applied to extreme value theory, the block-maxima ensures that each selected event is statistically independent from the others, while other conditions need to be defined for this property to be respected in the POT, especially as the temporal resolution of the series increases. On the other hand, POT returns larger sample size and, at the same time, prevents that severe events are discarded just because they are contained in the same block. The ETCCDI indices are mainly based on daily data and serve as a valuable tool for comparing diverse regional studies worldwide, offering a seamless integration of index data on a global scale (Morbidelli, 2022). However, some complications may arise when dealing with sub-daily durations. Indeed, the physical phenomena that may generate sub-daily extreme precipitation may be completely different, requiring other indices to be analyzed (e.g., the sub-daily rainfall indices that Blenkinsop et al. (2018) defined within the *INTElligent use of climate models for adaptatioN to non-Stationary hydrological Extremes - INTENSE* project).

In addition to the different methodologies that can be used to extract precipitation extremes, these events have a variety of different attributes that can be examined (Stephenson et al., 2008). In other words, it is challenging to fully characterize changes in the precipitation extremes using a single numerical value, since they can be defined by a variety of different characteristics, such as magnitude, rate of occurrence, timing, temporal duration, spatial scale and so on. As an example, over the years several scientific papers have focused on extreme precipitation magnitude, exploring potential changes

and dwelling on the physical explanation behind these. Other studies have focused more on other aspects, such as changes in the occurrence and/or seasonality. Moreover, also thanks to climate projections (see paragraph 1.1.4) an increasing number of publications are examining potential future changes in these features due to the stress induced by climate change and global warming.

Therefore, the following paragraphs will be devoted in analyzing the main works based on the study of observed (paragraph 1.2.1) and projected (paragraph 1.2.2) changes in the characteristics of extreme precipitation events.

1.2.1. Observed changes in precipitation extremes

From what has been observed in section 1.1, climate change and global warming have a major effect on alterations in the characteristics of precipitation extremes. Different areas of the globe have experienced an increase in the magnitude of extreme rainfall both at daily (Donat et al., 2013; Westra et al., 2013; Sun et al., 2014) and sub-daily (Fowler et al., 2021) duration, and there is growing evidence that the anthropogenic contribution has been relevant to these alterations (Fischer and Knutti, 2015). Indeed, a warmer atmosphere can induce higher evaporation rates (i.e., increasing the moisture availability) and, at the same time, contain more water vapor (Westra et al., 2014). These aspects necessarily increase the probability of having more severe rainfall events. The physical explanation for this statement has to be necessarily traced back to the relationship that scales water-holding capacity of a gas and its temperature, namely the Clausius-Clapeyron (CC) equation. In particular, the equation expresses the saturation pressure of water vapor as a function of absolute atmospheric temperature:

$$\frac{\partial e_s}{\partial T} = \frac{L_v(T)e_s}{R_v T^2} \quad (1.1)$$

where e_s is saturation vapor pressure, T is the temperature in Kelvin, $L_v(T)$ is the water specific latent heat of evaporation, and TR_v is the gas constant of water vapor. A good approximation of the CC equation, which unties the dependence of e_s on $L_v(T)$, is the August-Roche-Magnus equation:

$$e_s = 6.1094 \cdot \exp\left(\frac{17.625T}{T + 243.04}\right) \quad (1.2)$$

with T expressed in degrees Celsius. Equation 1.2 is useful to retrieve the specific humidity, q_v , i.e., the ratio between the mass of water vapor and the total mass of air (combination of dry air and water vapor), at the saturation condition:

$$q_{v,sat} \approx 0.622 \frac{e_s}{P} \quad (1.3)$$

where 0.622 is the ratio between the gas constant for dry air and the gas constant for water vapor, while P is the atmospheric pressure. Combining equation 1.2 and 1.3, it is possible to observe that the saturation vapor pressure increases exponentially with temperature. In particular, it increases by $\sim 7\%$ per degree at 0°C and $\sim 6\%$ per degree at 24°C (Westra et al., 2014).

Considering the global scale, Westra et al. (2014) analyzed a high-quality dataset (i.e., 8326 high-quality land-based observing stations with more than 30 years of record over the period from 1900 to 2009) of annual maximum daily precipitation to evaluate the presence of trends through a monotonic nonparametric test (i.e., the Mann-Kendall trend test, see section 2.2.2 for further details) and a nonstationary generalized extreme value analysis. The authors found that almost two-thirds of stations exhibited increasing trends. Moreover, the nonstationary analysis revealed a statistically significant positive association with near-surface atmospheric temperature, with a global median value ranging from 5.9% to $7.7\% \text{ K}^{-1}$.

More recently, Sun et al. (2021) analyzed trends in the annual maximum amount of precipitation accumulated in 1 day (Rx1day) and in 5 consecutive days (Rx5day) over almost 7500 stations from HadEX2 dataset. Over the 1950–2018 (i.e., the period with the best spatial coverage), the authors found out that the stations showing increasing trends (66%) are about twice as many as those showing decreasing trends (34%) for both the indices (Figure 1.11). However, only a portion of these stations, mainly concentrated in North America, Europe, and South Africa, showed a statistically significant increasing trend ($\sim 9.1\%$) and an even smaller portion ($\sim 2.1\%$) showed a significant decreasing trend. Moreover, following the framework provided by Westra et al. (2014), the authors used the global mean surface temperature as a covariate to verify the association between changes in extreme precipitation and temperature. Consistently with the previous work, the median estimated sensitivity of extreme precipitation to warming over the global land areas with station data is 6.6% and 5.7% per 1 K of temperature increase for Rx1day and Rx5day, respectively.

What is worth emphasizing is that both Westra et al. (2014) and Sun et al. (2014) have expressly stated to be careful in interpreting this results as solely a consequence of CC relationship. Indeed the CC equation would suggest that with 2°C of global warming, the world could expect 14% more moisture in the air and with 3°C of warming that would be 21% , and so on. However, as stated by Adam (2023), this is not so straightforward. The CC relationship only works fully over the oceans, where there is an unlimited supply

of water.

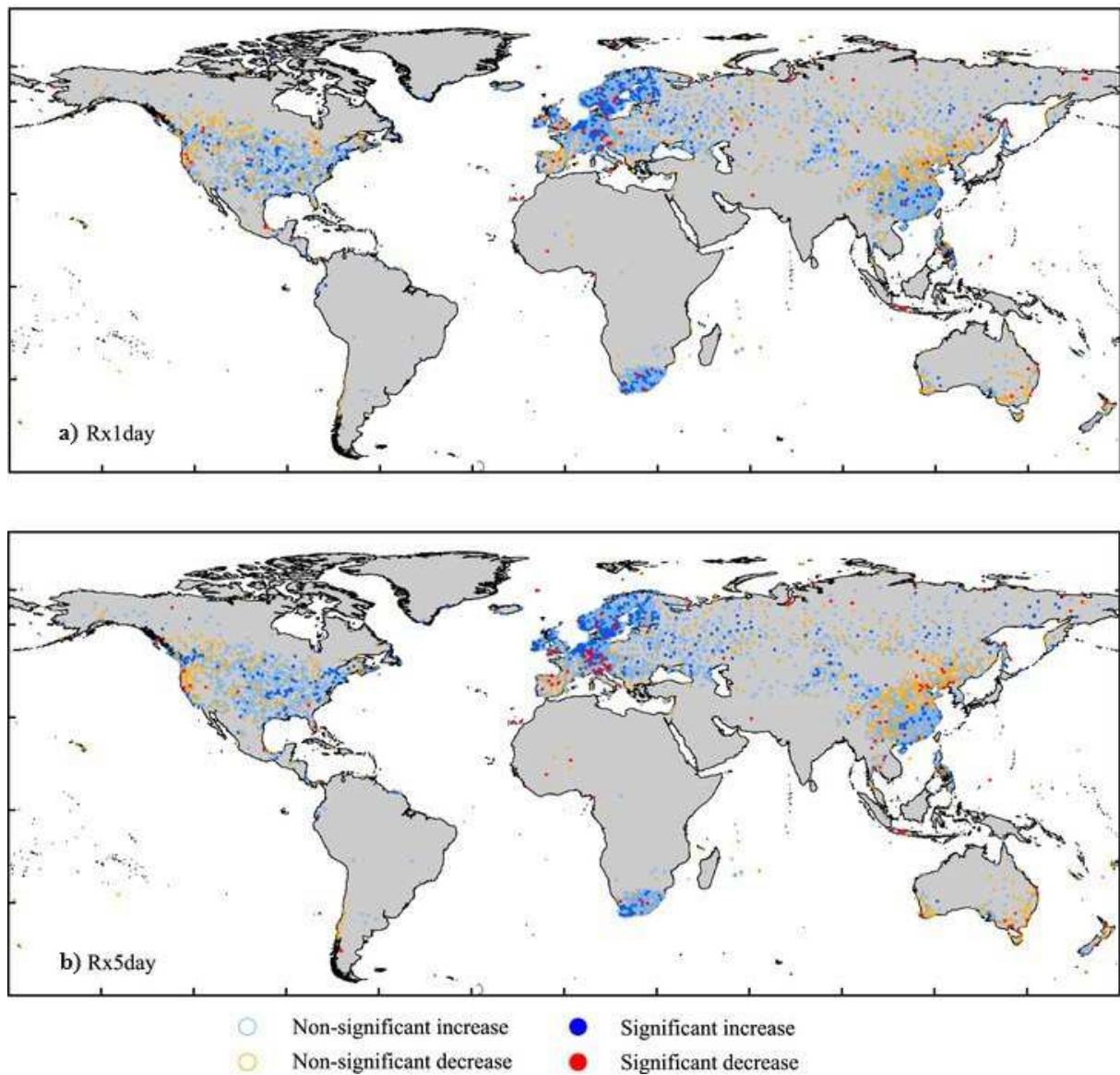


Figure 1.11: From Sun et al. (2021): summary of Mann–Kendall trend analyses for the period 1950–2018 for 7293 stations with trends for Rx1day (a) and Rx5day (b), respectively. Light blue open dots indicate non-significant increasing trends and light red open dots mark non-significant decreasing trends. Dark blue and red filled dots indicate statistically significant trends as determined by a two-sided test conducted at the 5% level

Over land, the scenario is different: if there is not 7% extra moisture available in the soil, the air above will not absorb and retain that quantity of water, regardless of temperature increase. Over land, the availability of water is finite, and for intense rain events, it necessitates an air mass originating from over the ocean. Hence, other factors has to be take into account, such as the atmospheric circulation, air instability, cloud size, storm type and vertical speed and directional wind shear, to fully understand the physical

phenomena underlying extreme precipitation. As an example, convective precipitation is associated with the convective movement of warm moist air masses towards the cold layers of the overlying atmosphere. It is also supported by contributions of energy and water vapour from limited areas, carried by a convergent flow of air masses. Consequently, increasing temperatures introduce more moisture into the air, amplifying the storm's intensity. This implies that the increase in rainfall from thunderstorms can often exceed the scaling rate of the Clausius–Clapeyron relationship (Adam, 2023).

This aspect has already been demonstrated in some parts of the globe, and, particularly, in Europe (Lenderink and Van Meijgaard, 2008; Ali et al., 2021; Fowler et al., 2021). Indeed, some studies have focused more on the *apparent* scaling (Bao et al., 2017; Lenderink et al., 2021), namely on estimating the scaling proportion between extreme rainfall and dry (or wet) bulb temperature observations. In doing so, the importance of event duration in this process has become evident: while daily extremes exhibit an apparent CC scaling of approximately 7%, intense hourly and sub-hourly rainfall are characterized by higher values, reaching also 2CC rate (i.e., 14% °C⁻¹, the so-called "super-CC") in some cases. For instance, by using a large dataset of hourly precipitation (i.e., about 7,000 hourly precipitation gauges over six global macro-regions), Ali et al. (2021) showed that the scaling of hourly extreme precipitation in more than 60% of gauges follows at least the CC rate at a regional scale, and often a super-CC rate at the gauge-level (Figure 1.12). This is especially true for Europe, where the authors found that the scaling curves follow 2-CC beyond 12°C, confirming what Lenderink and Van Meijgaard (2008) observed for Netherlands. However, also in this case, it is important to underline that these results may change when other dynamical processes (i.e., large-scale circulation, storm type or changes to long-term moisture transport patterns) are considered in the scaling approach (Pfahl et al., 2017; Morbidelli, 2022). In this context, (Fowler et al., 2021) recently summarized the new understanding of the feedback processes affecting rainfall extremes.

Despite changes in rainfall seasonality have not been explored as much as those related to magnitude, the effects of significant variations can have serious consequences. Substantial shifts in the timing of the wet season can have large impacts on plants and vegetation, especially in semi-arid areas. Weltzin et al. (2003) suggest that shifts in precipitation regimes may lead to severe impact to ecosystem dynamics, even stronger than the increase in temperature driven by CO₂. Ecosystems can be influenced by shifts in the onset of the rainy season, since this marks some fundamental moments in the biotic cycle (Feng et al., 2013). Potential changes in the timing of extreme precipitation are also important in terms of storm water management and preparation against these events (Li et al., 2021). For the generation of floods, a change to the frequency and timing of extreme rainfall events may be as important as changes in magnitude and duration (Fowler and

Kilsby, 2003).

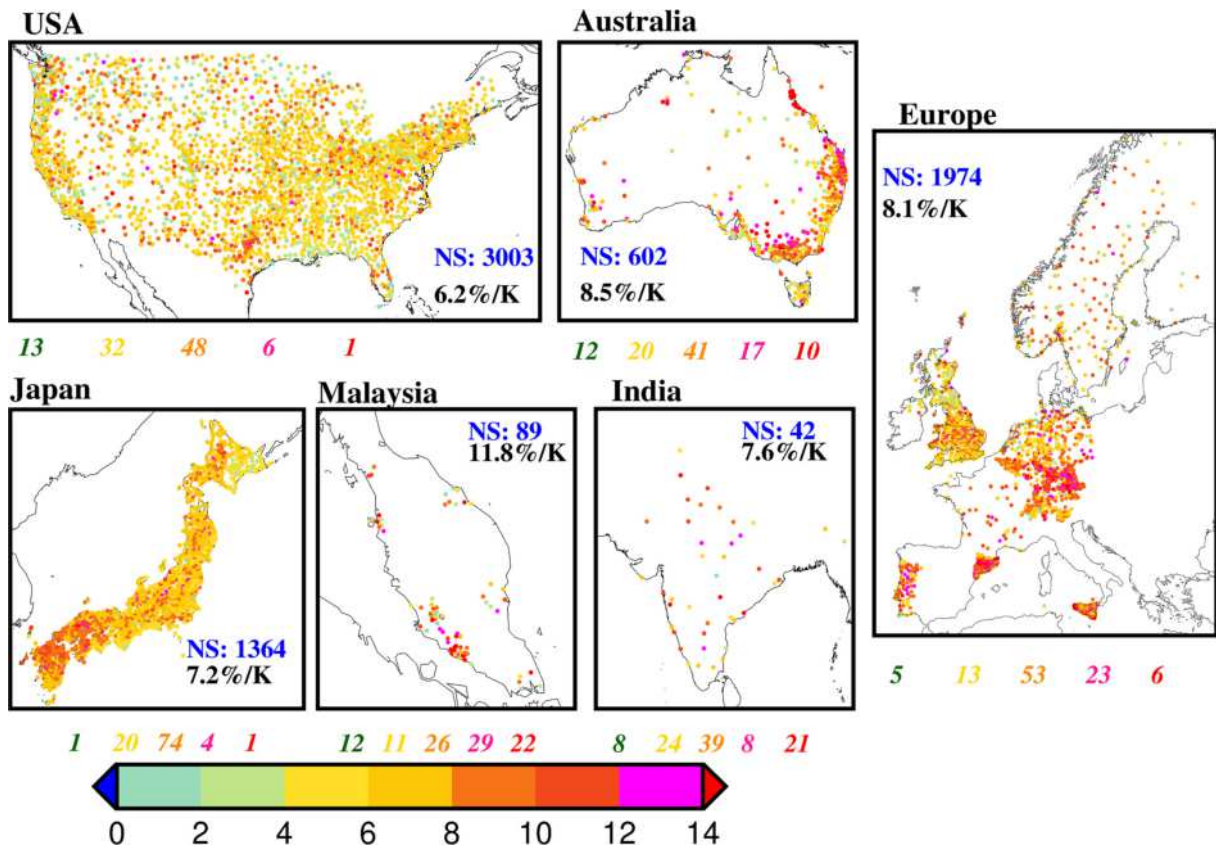


Figure 1.12: From Ali et al. (2021): scaling rates ($\%K^{-1}$) estimated using hourly precipitation from the global subdaily rainfall (GSDR) data set (Lewis et al., 2019) and daily dew point temperature from the HadISD data set (Dunn, 2019). Scaling is estimated using the binning method (BM) at the 99th percentile for 7,088 gauges, which have at least 12 years of hourly precipitation data. The number in blue indicates the number of gauges (NS) in each region and the number in black indicates the median scaling ($\%K^{-1}$) for each region. The numbers below each panel indicate the percentage of gauges within each region, which show scaling rates ranging from 0-0.5CC (green), 0.5CC-CC (yellow), CC-1.5CC (orange), 1.5CC-2CC (pink), and greater than 2CC (red) respectively, where CC is $6.5\%K^{-1}$

Unlike magnitude and frequency, there is a lack of studies on changes in the seasonality of extreme rainfall on a global scale. In addition, regional or local studies often focus on the entire precipitation regime rather than the extremes. As an example, Pal et al. (2013) identified a systematic shift in the year-to-year variations of the timing of these wet and dry season over the United States in the period 1930 - 2009 (Figure 1.13). The authors showed that the most significant shifts in timing occur in the Ohio River valleys where the onset of the dry period during fall arrived up to 2–3 weeks earlier. They also found contrasting shifts in the Southwest and the Northwest area. In particular, the first exhibited positive shifts in the timing of the wet season representative of a delayed summertime monsoon onset, while the second one showed a negative shift, representative

of an earlier onset of spring (early winter) precipitation.

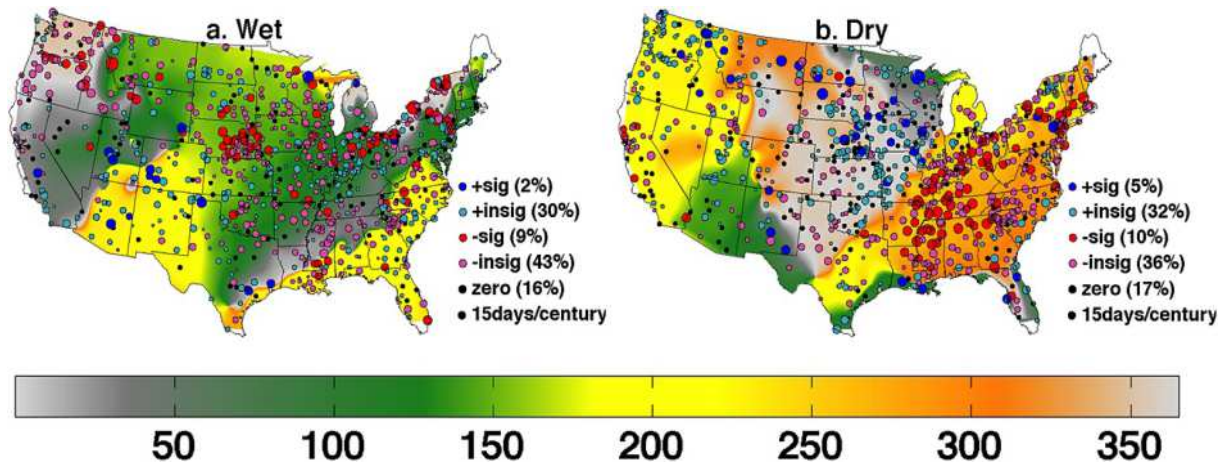


Figure 1.13: From Pal et al. (2013): trends of Julian days count from 1 January to the center of the (a) wettest and (b) driest 91 day period in a given year (“shift in seasons”). Wettest (driest) period is defined as the center of the 91 day period with the maximum (minimum) number of precipitating days, allowing for overlap with the preceding/following year. Color bubbles indicate location of the stations, sign, and significance of the trend estimates. The size (as well as the shading) of the bubble is proportional to the magnitude of the trend. The percentages in parentheses indicate fraction of the total number of stations having such trend category

Still focusing on the US, Mallakpour and Villarini (2017) examined the potential shifting in the seasonality of annual maximum precipitation in the period 1948 - 2012 by investigating whether the day of the year at which the maximum precipitation occurs has changed over time. However, the authors found out that only a small number of points revealed a statistically significant trend in the day in which maximum annual precipitation occurred, meaning that there is not enough evidence of any specific change in the seasonality of annual maximum precipitation for the period considered.

Moving to a smaller spatial scale, Persiano et al. (2020) performed a detailed analysis of possible changes in seasonality of sub-daily rainfall extremes in Emilia-Romagna region (Italy) (Figure 1.14). The authors considered a dataset of annual maximum series of sub-daily (1, 3, 6, 12 and 24 h) and sub-hourly (5, 10, 15, 20, 30, and 45 min) duration rainfall depths, collected at ~ 500 stations over the period 1931–2015. By applying a trend analysis on the date of occurrence (expressed in terms of Julian date) for each duration over two consecutive period (i.e., 1961-1989 and 1990-2015), the authors found out the presence of a generalized delay in the mean timing of extreme events from late summer to autumn for all the durations. This delay is more accentuated in the central-western part of the Apennine, while an opposite behaviour is locally observed for some stations in the same area for higher durations (i.e. 12 and 24 h).

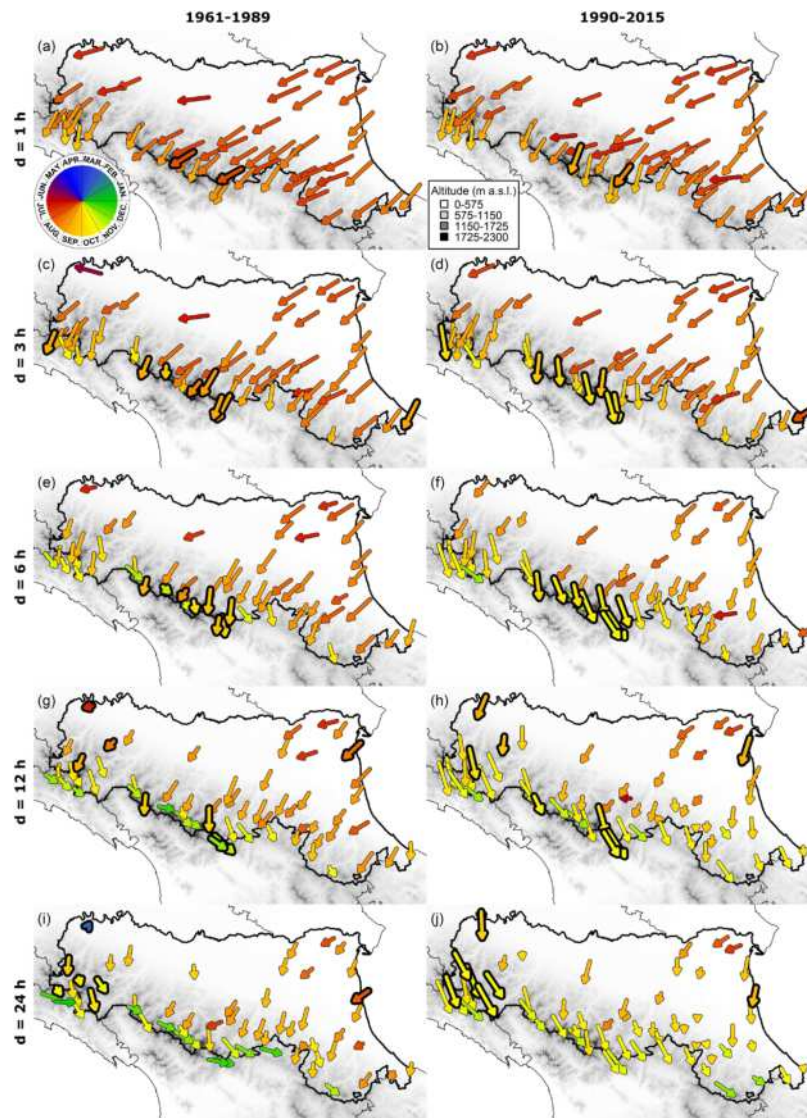


Figure 1.14: From Persiano et al. (2020): mean date of occurrence of rainfall annual maxima for durations $d = 1, 3, 6, 12, 24$ h and time periods 1961–1989 and 1990–2015. Direction and colour of the arrows indicate the average timing, while their length reflects the regularity of the dates of occurrence within the year. Black-contoured arrows indicate stations where statistically significant trends have been detected in the Julian date of occurrence over the period 1961–2015

The few studies on changes in the seasonality of extreme rainfall highlight how further research is needed to fill the knowledge gap on this topic.

1.2.2. Projected changes in precipitation extremes

As shown in paragraph 1.1.4, climate models are a fundamental tool to project the future response of the climate under the pressure of climate change and global warming. In this context, different studies have shown that what has been observed in the past regarding changes in extreme rainfall characteristics is likely to be projected into the

future, obviously with different signals depending on the scenarios considered.

Focusing on the daily scale, Giorgi et al. (2014) analyzed the projected changes in six hydroclimatic indices associated with different characteristics of the surface hydroclimatic regime, such as the mean daily precipitation intensity (SDII) or the heavy precipitation index (R95). All the indices for the 21st century projections show a clear picture of a predominant hydroclimatic response to global warming toward a regime of more intense, shorter, less frequent, and less widespread precipitation events. The authors also found out that this response is more pronounced and spatially consistent for tropical than extratropical regions, suggesting that tropical convection plays a critical role in this mechanism. Sillmann et al. (2013) provided an overview of projected changes in climate extremes ETCCDI indices computed using the CMIP5 multimodel ensemble. According to the authors, extreme precipitation exhibits a disproportionate increase compared to total wet-day precipitation (PRCPTOT). The analysis of changes in very wet days (R95p) indicates a relevant uptrend in extreme precipitation across most regions, especially under the RCP8.5 scenario. The Mediterranean region presents a slightly different behavior, suggesting a decrease in total precipitation and an increase in longer dry spells, confirming an intensification of drought conditions in this area (as already seen in Figure 1.5). A slight increase in the projected R95p for this region, however, suggests that although dry conditions become more severe, precipitation can be still extreme when it does occur.

There is a discrepancy between global-scale studies on future changes in daily and sub-daily precipitation. This is mainly due to the high computational costs involved in running GCMs at sub-daily time scales. This is reflected in not having a large number of models and, consequently, in higher uncertainties in evaluating the results. However, Morrison et al. (2019) evaluated projected changes in precipitation at both the daily and sub-daily time scales (i.e., 3-hour). Evaluating the model accuracy with respect to the observations over the historical period, the authors found the first difference between the two temporal resolutions: compared with the 3-hour resolution, the accuracy is greater for daily precipitation. This may arise from the fact that current GCMs do not explicitly resolve convective processes, which are a crucial information for the development of sub-daily extreme precipitation. However, by selecting the ensemble that includes the models with the best performances over the historical baseline, the authors showed that the median maximum 3-hourly precipitation are projected to increase in the future, especially moving towards the end of the 21st century (Figure 1.15).

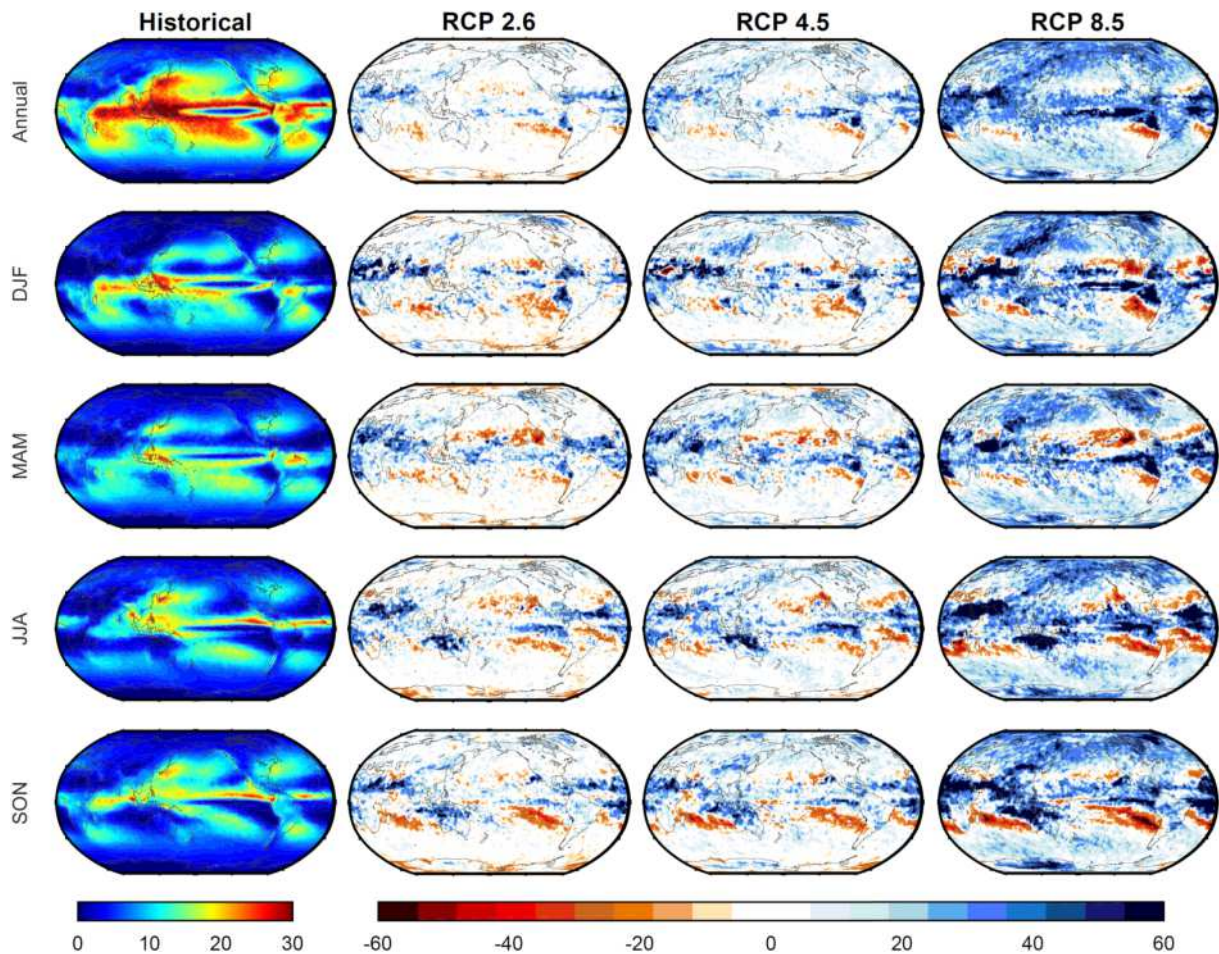


Figure 1.15: From Morrison et al. (2019): median maximum 3-hourly precipitation (mm) based on an ensemble that includes CNRM-CM5, FGOALS-g2, MRI-CGCM3 and MRI-ESM1. The results for the RCPs 2.6, 4.5 and 8.5 (Columns 2–4) represent the percentage differences between the projected changes (2081–2100) and the historical period (1986–2005), normalized by the historical period (1986–2005). Results are for annual precipitation (Row 1), DJF (Row 2), MAM (Row 3), JJA (Row 4), and SON (Row 5)

In particular, the results based on RCP8.5 point to an increase in extreme precipitation of more than 50%, especially around the equator, in the midlatitudes and polar regions. The stronger responses of precipitation extremes in the future at sub-daily scale are consistent with the super CC scaling identified in other studies at the sub-daily scale, compared with CC scaling at the daily scale (see paragraph 1.2.1).

If it is already difficult to find studies on observed changes in the seasonality of rainfall extremes, the gap is even more evident moving to future projections. Probably, one of the few studies is that of Marelle et al. (2018), who investigated changes in the seasonal timing of extreme precipitation using global climate models from the CMIP5, in 1871–1900, 1976–2005, and 2071–2100 for an extreme future emission scenario (RCP8.5). The authors showed that, while very little seasonality changes occurred during the past

hundred years, by the end of the 21st century, extreme precipitation (quantified using the Rx1d index) could substantially shift later in the year, in most regions from summer and early fall toward fall and winter (Figure 1.16). If on the one hand, precipitation extremes in the tropics and at middle and high latitudes tend to occur during summer and fall (JJA and SON in the Northern Hemisphere; DJF and MAM in the Southern Hemisphere) and in the Northern Hemisphere's subtropics, during winter and spring (DJF and MAM), on the other in the future this peak could change significantly in several regions, by up to more than a month.

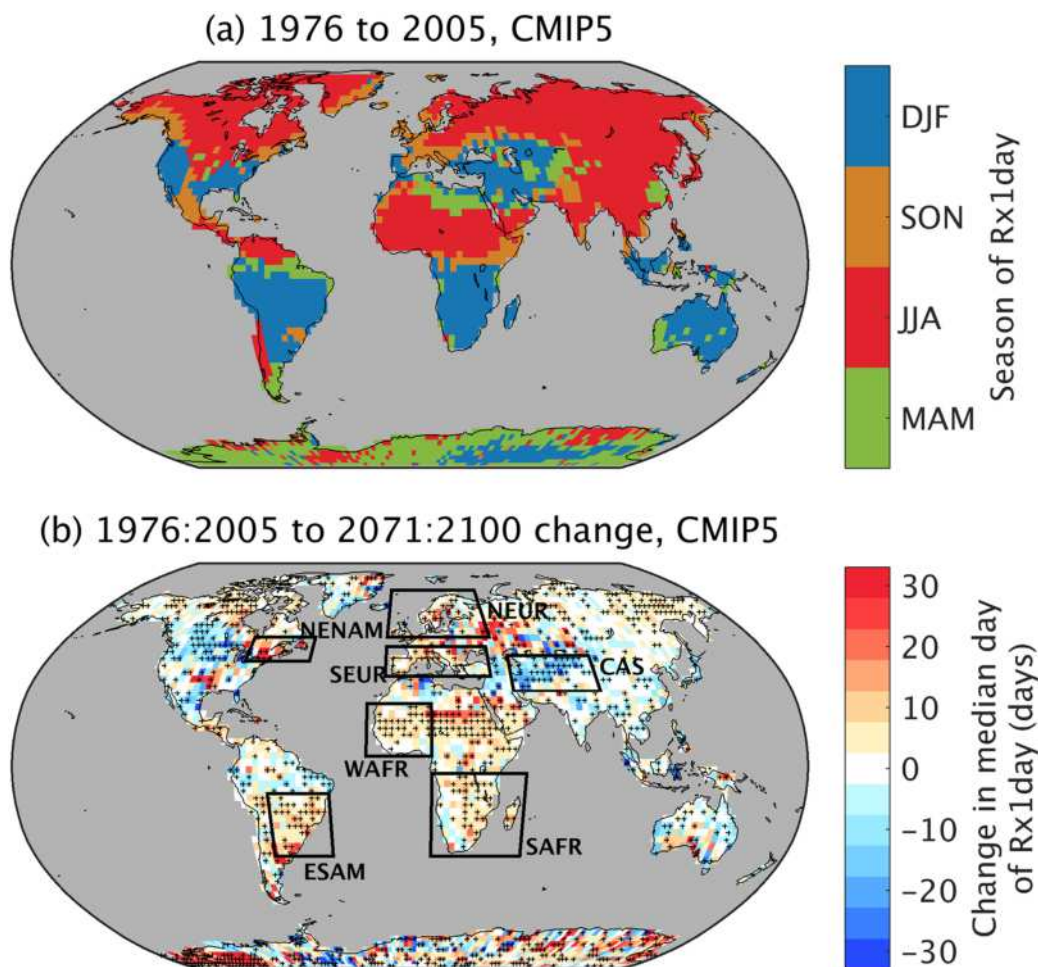


Figure 1.16: From Marelle et al. (2018): (a) Season of the multimodel median day of year of extreme daily precipitation in the CMIP5 ensemble for 1976–2005. (b) Multimodeled median change in the median day of year of extreme daily precipitation between 1976–2005 and 2071–2100 (RCP8.5 scenario). On panel (b), black boxes indicate the location of the regions selected for further analysis, and stippling indicates that more than 66% of models agree on the sign of change. DJF = December–February; JJA = June–August; MAM = March–May; SON = September–November

In particular, they found that extreme precipitation are projected to occur later in the year (from summer and early fall toward fall and winter) in most land regions, such

as the Northern Hemisphere's polar regions, Europe, Africa, Central America, and South America. On the contrary, Rx1day is projected to occur earlier in Central and Southwest Asia and in a large part of North America.



2 | Chapter two

2.1. The Mediterranean area: a climate change hot spot

Over the past years, the Mediterranean region (Figure 2.1) has been referenced as one of the most responsive regions to climate change, so much to be defined as a primary hotspot of climate change (Giorgi, 2006). Also, the Special Report on Climate Change and Land (SRCCL) from the Intergovernmental Panel on Climate Change (Shukla et al., 2019) has highlighted the Mediterranean as one of the most vulnerable regions in the world to the impacts of global warming, mainly because of the significant exposure and vulnerability of both human societies and ecosystems to these alterations. This is particularly evident in Figure 2.1, from which it is possible to quantify how many million people live in the Mediterranean basin, especially near the coasts. Moreover, due to its geographical location and configuration, the ecological and human factors interact significantly, presenting a relevant hazard for biodiversity, especially for the marine one (Coll et al., 2010).

One of the most evident consequences of climate change in the Mediterranean is the rise in temperatures. The region is warming 20% faster than the global average (Lionello and Scarascia, 2018), resulting in more frequent and severe heatwaves (Perkins-Kirkpatrick and Lewis, 2020). The implications of these events are dramatics, such as the 70k heat-related deaths during the summer of 2003 (Robine et al., 2008) and the 60k in 2022 (Ballester et al., 2023). The future could be even more alarming considering that the European population is increasingly aging (Harper, 2014), and it is precisely this segment of the population that often suffers the worst consequences during heatwaves.

Concerning the hydrological cycle, rising temperatures are exacerbating water scarcity issues in the Mediterranean area (Jiménez Cisneros et al., 2014; Noto et al., 2023b). The increase in temperatures, coupled with higher evaporation rates and a reduction in the annual total precipitation (Philandras et al., 2011; Mariotti et al., 2015), is impacting the surface water balance, thus generating a decrease in surface runoff and in groundwater levels (Noto et al., 2023a). The resulting reduction in water supply might lead to a decreasing in water availability for agriculture, industry, and households.

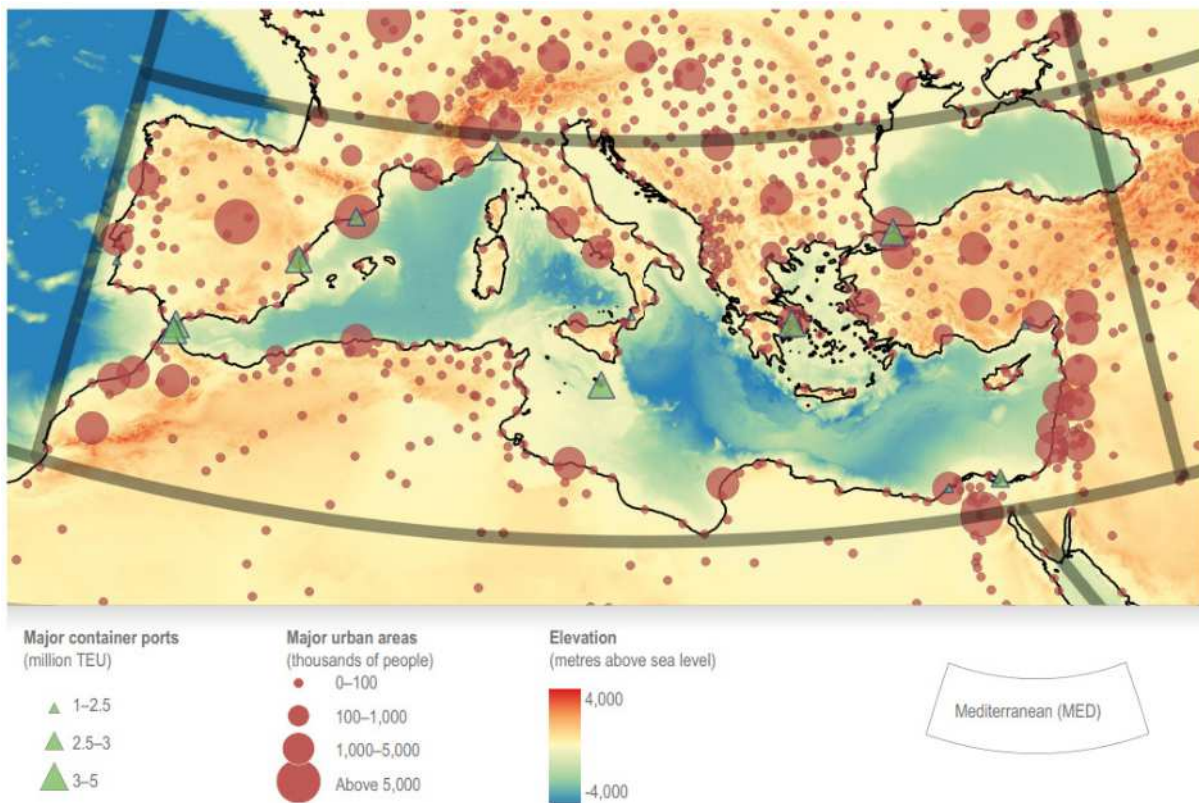


Figure 2.1: From Ali et al. (2022): Topography and bathymetry (colour bar in metres), main urban areas (population in thousands of people for 2020), container ports (millions of TEU [twenty-foot container equivalent units] in 2017) and borders of the Mediterranean region

While it has been shown that the Mediterranean area is highly prone to water scarcity and heat-related disasters, one of the most debated points is whether climate change is leading to an increase in frequency and magnitude of heavy rainfall events. The detection of significant trends in such a kind of events is crucial since, other than being an indicator of a climate alteration, it could support political decisions to mitigate their effects (Ingold and Fischer, 2014). For this reason, over the last decades, a great number of studies have been aimed to detect the presence of trends in precipitation time-series over the Mediterranean region. Although it would be highly important to study changes in the extreme characteristics across the entire Mediterranean basin, this is quite challenging for different reasons. First of all, the high geo-political fragmentation of the area makes retrieving regional datasets extremely difficult. The case of Italy serves as a paradigm, since each of the 20 regions (21 when considering the two autonomous provinces of Trentino-Alto Adige), independently manages its meteorological network. Another problem lies in the lack of consistency among the characteristics of different datasets, such as their length and temporal resolution, as well as their spatial distribution. For all these reasons, with the exception of a few studies that have attempted to gather data from multiple agencies

(Alpert et al., 2002; Karagiannidis et al., 2009) or others that use reanalysis data or regional climate ensemble simulations (Casanueva et al., 2014; Trambly and Somot, 2018), most of scientific literature is focused at a regional scale or at finer levels of detail (e.g., sub-region or basin scales).

Regarding the Iberian Peninsula, a great number of studies have been conducted to investigate changes in extreme precipitation and the potential presence of climatic trends. The overall signal for this area reveals a reduction in the precipitation extremes (Costa and Soares, 2009; Gonzalez-Hidalgo et al., 2010), despite this message is completely reversed in other works, mainly depending on the zone, the reference period and the methodologies used. As an example, Bartolomeu et al. (2016) perform a spatial and temporal analysis on some extreme precipitation indices (i.e., the precipitation fraction due to the 75th and 95th percentile of the precipitation distribution, R75pTOT and R95pTOT, respectively) over Portugal and Spain in the period 1986 - 2005. The authors used both the observational datasets from these nations and the results obtained from the Weather Research and Forecast (WRF) model forced by the ERA-Interim reanalysis data and the Max Planck Institute Earth System Model (MPI-ESM). Regarding the R95pTOT, the authors found positive statistical significant trends in the observational dataset, mainly located in the north area of Portugal and in the south and central part of Spain. However, these results are partially confirmed by the ERA-driven simulation results, while are completely reversed for the MPI-driven simulations, enhancing the difficulties in studying extreme precipitation changes over this geographic area.

Moving eastward, a relevant intensification of the extreme precipitation has been found by Ribes et al. (2019) in the Mediterranean France, regardless of the overall decreasing trends in total precipitation. The authors found a significant increase in the mean intensity of annual maxima, estimated in +22% over the period 1951-2015. Moreover, the non-linear upward trend exhibits a different behavior over time, with a faster change by the end of the 20th century. The identified changes are coherent with the expected increase suggested by the observed regional warming and Clausius–Clapeyron scaling. Focusing on the same area and considering the yearly maxima of daily rainfall at point and on a 8x8 km² regular grid, Blanchet et al. (2018) compare different non-stationary models to test the significance of trends. Also their results indicate an increasing tendency in the rainfall magnitude, with some local spot where the yearly maxima reached more than +62 mm/day of changes in 20 year.

Alterations in intense precipitation can exhibit different characteristics in the eastern Mediterranean, depending on the scale, severity, and region of interest (Hochman et al., 2022). By analyzing different extreme precipitation indices in the period 1974 - 2016 for the Gaza Strip, Ajjur and Riffi (2020) found out that the majority of indices exhibit

statistical significant trends. The trend directions align with those obtained by Nastos and Zerefos (2008) for Greece, although statistical significance is lacking in this case.

As well as the eastern Mediterranean, the North African region is characterized by significant uncertainties in the increase of extreme rainfall (Nouaceur, 2010; Nouaceur and Murărescu, 2016). For instance, Khomsi et al. (2015) found out that the majority of trends observed in heavy rainfall events show a positive direction with relatively weak magnitudes in Morocco. However, the authors did not find any statistical significance in the results obtained.

Regarding Italy, a great number of studies involving trend analysis have been applied over the peninsula (Buffoni et al., 1999; Crisci et al., 2002; Libertino et al., 2019), its southern part (Longobardi and Villani, 2010; Caloiero et al., 2019), and its main islands, i.e., Sardinia and Sicily (Bonaccorso et al., 2005; Cannarozzo et al., 2006; Arnone et al., 2013; Caloiero et al., 2019). The mechanisms that generate rainfall extremes can vary significantly from one region to another. While the northern regions are prone to intense convective storms enhanced by the orographic uplift of humid air masses (Abbate et al., 2022; Cassola et al., 2023), southern regions often experience heavy rainfall generated by multiple factors (orography, moist convection, large-scale uplift along fronts) (Caccamo et al., 2017; Lee et al., 2019).

Focusing on Sicily, which will be the region of interest of this Chapter, many studies have involved the use of trend test for detecting changes in the extremes at several durations and evaluating their significance. As an example, Bonaccorso et al. (2005) applied the Mann-Kendall trend test to Sicilian rainfall annual maxima at the canonical durations (i.e., 1, 3, 6, 12, and 24 hours) for those stations having more than 50 years of data. The authors found a relationship between the trend direction and duration, highlighting an increasing trend at the shortest time scale and an opposite behavior at the longest ones. Arnone et al. (2013) used the same test to determinate the magnitude of trends and thus identify changes in rainfall characteristics at the canonical durations for Sicily. The authors found out that the percentage of gauges showing a positive trend tends to decrease when duration increases, finding the maximum percentage at the 1-hour duration. For this reason, they guessed that a further increase in the percentage of stations showing a positive trend and, consequently, of extreme events could be extrapolated towards sub-hourly durations, enhancing the interest in studying the rainfall extremes in the region.

2.2. Insight for a semi-arid region: Sicily

Being the widest island of the Mediterranean area and lying in the heart of the Mediterranean Sea, Sicily has a climate that can be considered as representative of an area quite extensive of the Mediterranean. Moreover, due to its central position and representing a transition area between the arid climate in North Africa and the continental one that characterize Europe, Sicily might represent a *'laboratory'* to investigate changes in the rainfall regime.

In this section, after a brief description of the geomorphology and the meteo-climatic characteristics of Sicily, the framework used to verify changes in the extreme precipitation characteristics will be analyzed. The first part will be devoted to a trend analysis on extreme precipitation, especially those related to short-duration events, representing one of the few works on this subject. The second part will focus on examining the potential consequences of these alterations from a practitioner perspective. In particular, it will be investigated how these changes affect the extreme value distributions used to design hydraulic structures. Finally, since these short-duration intense events are generally associated to convective systems, an algorithm for separating convective and stratiform regimes will be carried out.

2.2.1. Area of study and dataset

Sicily island has an extension of about 25,700 km² and a morphology that is characterized by a mountain range along the longitudinal direction on the northern side (i.e., the Peloritani, Nebrodi and Madonie mountains) and the Etna volcano on the eastern side (Figure 2.2). Elevation ranges from 0 m a.s.l. to about 3,300 m a.s.l. in correspondence of the volcano Etna. Precipitation across the island has a significant spatio-temporal variability. The mean annual precipitation (MAP) over the whole island is about 715 mm, but it can significantly vary considering the southeast area (i.e., about 360 mm) and the volcano Etna in the northern side (i.e., 1,900 mm) (Di Piazza et al., 2011; Caracciolo et al., 2018). Concerning temporal variability, the greatest part of MAP occurs during the winter seasons, while the summers are generally drier, despite severe storms may sometimes occur in this season, such as the one that hit Palermo on 15th July 2020 (Francipane et al., 2021).

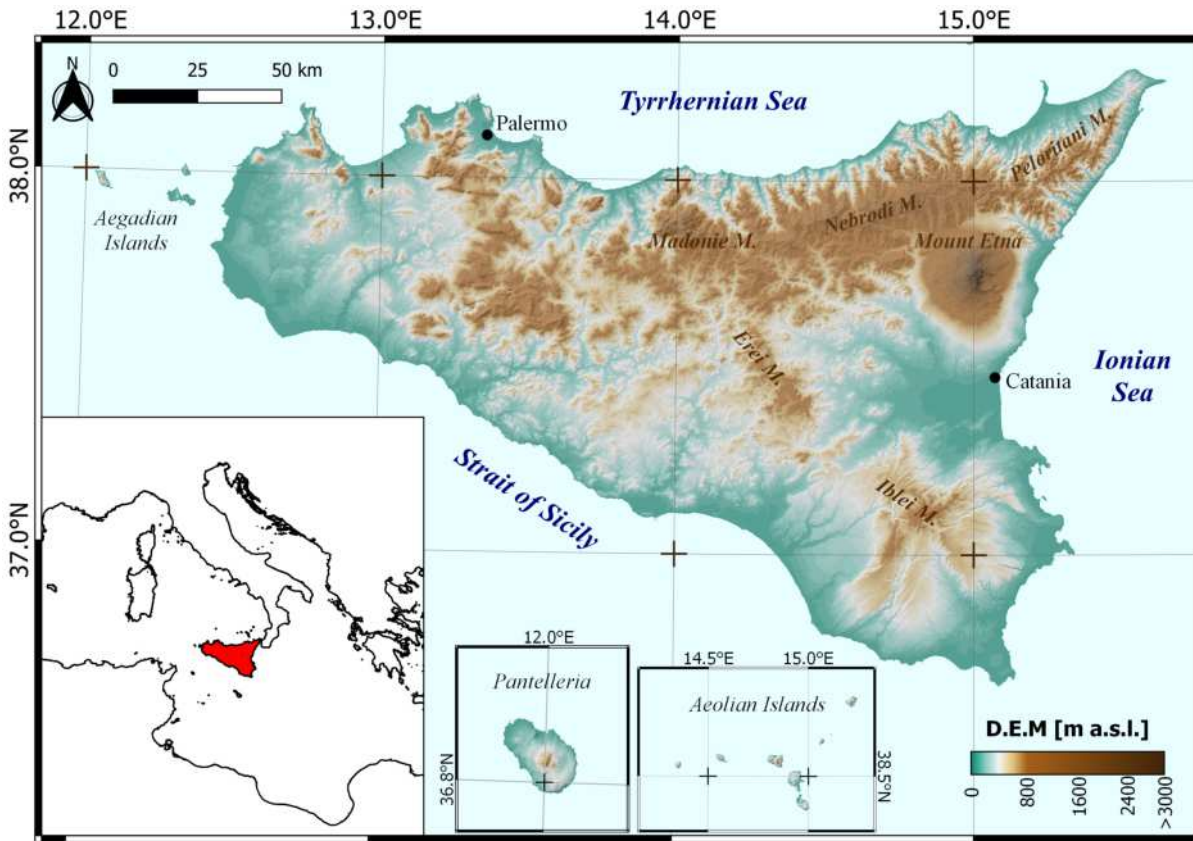


Figure 2.2: Area of study overlaid on the digital elevation model

Sicily has different rainfall datasets. The oldest one is the regional database collected by OA-ARRA (*Osservatorio delle Acque – Agenzia Regionale per i Rifuti e le Acque*), which consists of annual maxima (AMAX) rainfall for 1, 3, 6, 12 and 24 h duration, daily rainfall and AMAX daily rainfall for about 350 rain gauges within the period 1929–2014). In the past, these data have been largely used for analyzing the rainfall characteristics (Arnone et al., 2013; Caracciolo et al., 2018) or the design rainfall estimation (Cannarozzo et al., 1995; Noto and La Loggia, 2009; Forestieri et al., 2018). However, the temporal resolution of this dataset does not allow to investigate all those phenomena that develop and fade away rapidly. For this reason, the dataset used in this chapter is the one provided by the regional agency SIAS (*Servizio Informativo Agrometeorologico Siciliano; i.e., Agro-Meteorological Information Service of Sicily*). SIAS rain gauge network consists of 107 tipping bucket rain gauge stations rather homogeneously distributed across the island (Figure 2.3) with an average density equal to about 250 Km²/gauge and covers the period 2002-2023. In Table A.1 in the Appendix A the rain gauges names, IDs and coordinates are listed. Data are retrieved with high temporal resolution (10 minutes) allowing time aggregation when necessary. The time-series are characterized by a high level of homogeneity, as declared by the SIAS Agency. The survey sites were chosen

according to the WMO (World Meteorological Organization) standards and the strict criteria used in data detection, management and validation provide a high degree of uniformity over the whole island.

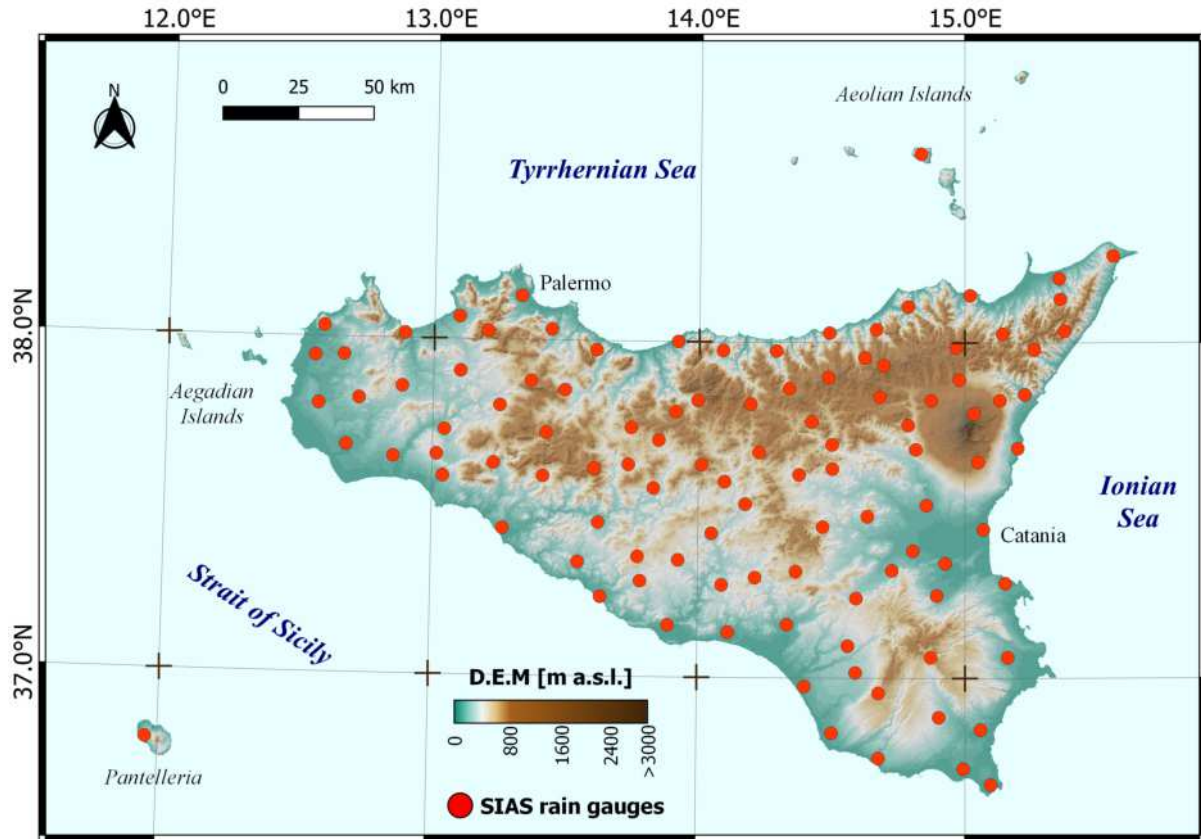


Figure 2.3: Spatial distribution of SIAS rain gauges

The SIAS rain gauges network has been firstly pre-processed in order to verify its completeness. For the i^{th} year, the percentage of missing data (Figure 2.4a) has been computed as in equation 2.1, considering the ratio between the number of recorded data and the number of expected data.

$$\%ofMissingData_i = \frac{\#ofRecordedData_i}{\#ofExpectedData_i} \cdot 100 \quad (2.1)$$

As it is possible to observe, with the exception of about 10 stations that have been in disuse since 2005 and about 10 other stations that were installed later, most of the rain gauges have low missing data. The threshold of 30% has been chosen as the value for considering as complete each year and Figure 2.4b shows the heatmap containing all the valid years for each station (i.e., the red cells). By observing Figure 2.4a, it is also possible to notice a constant percentage of missing data in 2011 (possibly due to a network upgrade in that period). However, this percentage never exceeds the 30%, as shown in

Figure 2.4b.

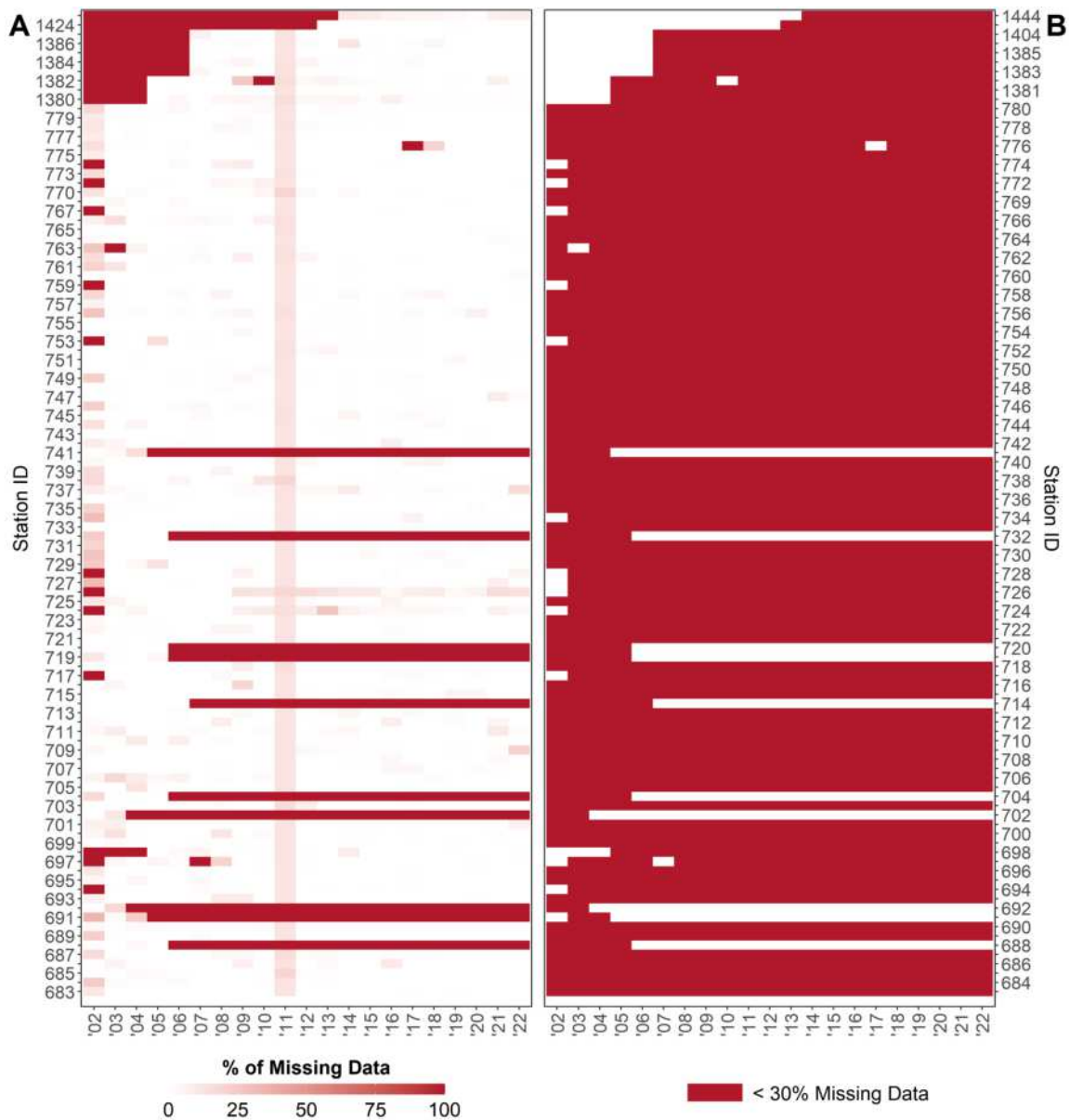


Figure 2.4: Completeness of the SIAS rain gauge network. Panel A shows the % of missing data in each station (rows) for each year (column). In panel B the red cells represent all those years for each station where the % of missing values is lower than 30%

The spatial distribution of the number of valid years is shown in Figure 2.5, while Figure 2.6 displays the spatial distribution of the MAP computed from this network. The MAP values are consistent with those previously reported above. Indeed the northeastern area is the one characterized by the higher MAP, while it decreases moving to the southwest. It is also worth noting that the regional MAP (715.7 mm) exactly matches that historically recognized for Sicily.

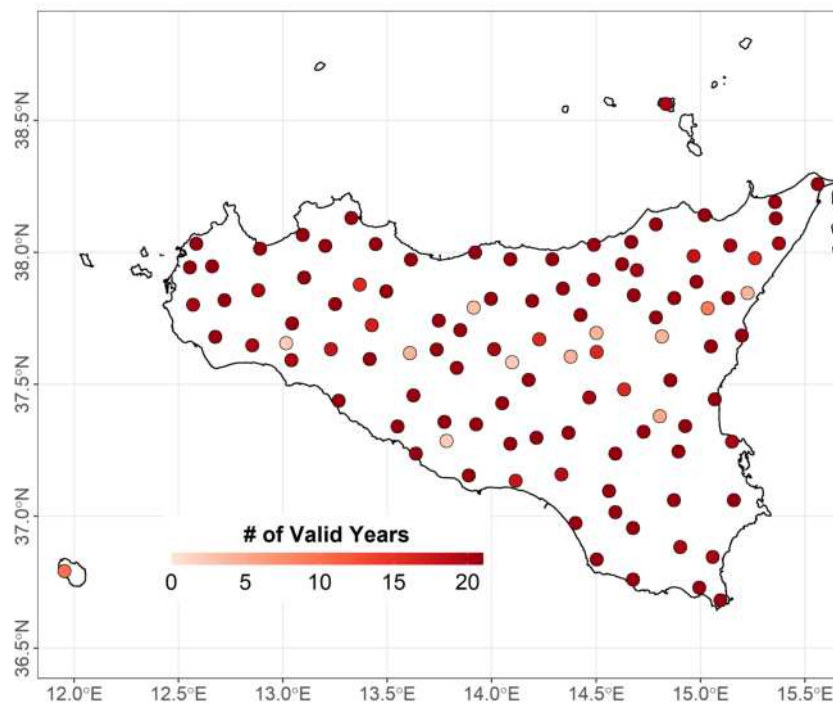


Figure 2.5: Spatial distribution of the number of valid years for the SIAS rain gauges

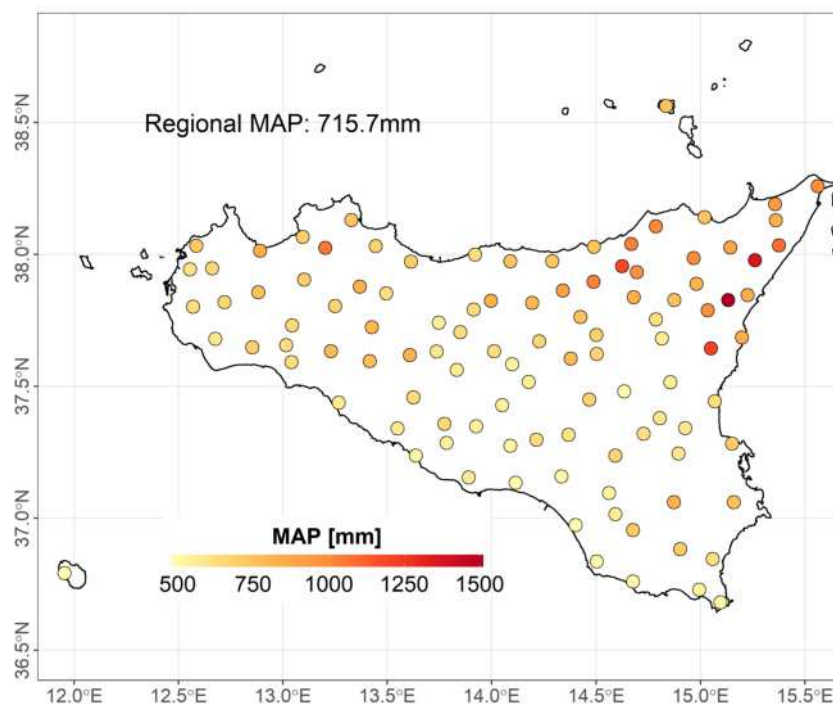


Figure 2.6: Spatial distribution of the mean annual precipitation values computed from the SIAS network

2.2.2. Asymmetric changes in the rainfall extremes magnitude with duration

There is no doubt that to study the changes in rainfall characteristics it is necessary to perform a robust statistical analysis of historical data. Over the years, one of the most used methods to detect trends in precipitation has been the non-parametric Mann-Kendall (hereinafter referred to as MK) test. It has largely been used also in trend detection for extreme events, often coupled with different methods used for extracting extremes (i.e., see section 1.2).

However, it is possible to use other tests which, unlike the MK test, do not require preliminary extraction of the extreme precipitation values. As an example, the quantile regression (hereinafter referred to as QR) analysis (Koenker and Bassett Jr, 1978; Koenker, 2005) allows one to perform a linear regression on the whole data time-series, taking into account those values greater than a selected quantile. This means that, if very high (low) quantiles are considered, QR allows exploring the upper (lower) tail of the probability distribution function of the data, allowing to check for potential asymmetries in their behavior. QR method has been applied in the past to study trends at different temporal and spatial scales for rainfall (Villarini et al., 2011b; Bartolini et al., 2014; Lausier and Jain, 2018) and other climatic variables, such as temperature (Barbosa et al., 2011). Lausier and Jain (2018) applied the QR method to the annual total precipitation at a global scale, comparing results with those provided by a linear regression model. The authors, who found different precipitation trends related to the mean (linear regression model) and the median (QR model at 0.5 quantile) of time-series, asserted that a wrong trend interpretation, deriving by using an easier method as simple linear regression, could have implications for some environmental systems. Hence, they suggested to use a more robust method, such as the QR. Lastly, by detecting trends for the lower and upper tails of precipitation probability density function, they classified the whole planet into three risk classes, with the aim to identify some strategies to deal with them. Bartolini et al. (2014) started from two hourly rainfall datasets to look for trends in precipitation amount, frequency, and intensity in two locations of Tuscany (Italy) by means of a QR method. Results showed a tendency to a decrease of total rainfall and wet hours, occurring in winter and spring, and to an increase of hourly average precipitation during wet hours. With reference to rainfall at sub-daily timescale, some studies used the QR with the aim to understand changes of sub-daily precipitation with temperature. For instance,

Adapted from: Treppiedi, D., Cipolla, G., Francipane, A. and Noto, L.V. (2021), ‘Detecting precipitation trend using a multiscale approach based on quantile regression over a Mediterranean area’, *International Journal of Climatology* 41(13), 5938–5955.

Van de Vyver et al. (2019) detected the scaling rates of sub-daily precipitation with dew point temperature at various quantiles, highlighting a general increase of rainfall extremes depicted by quantiles higher than 0.9, with dew point temperature in various cities of Europe.

Starting from the above-mentioned conjecture of Arnone et al. (2013) but using the QR methodology, in this section it has been investigated the possibility to identify statistically significant trends for Sicily at the sub-hourly durations; moreover, it was also checked whether hourly and daily precipitation are characterized by the same behavior, both in terms of trend direction and significance, thus verifying any asymmetry in precipitation characteristics. Finally, the presence of any spatial patterns of trends in magnitude is globally and locally verified through a spatial autocorrelation analysis based on the Global Moran's I Index (Moran, 1950) and the Local Moran (Anselin, 1995), respectively. Despite the observation period here investigated is not enough long to infer properly about climate change effects, the results may still be a further potential signal that something is probably changing in Sicilian and, more in general, in Mediterranean climate, as several studies have already pointed out over the years (Giorgi, 2006; Giorgi and Lionello, 2008; Arnone et al., 2013; Forestieri et al., 2018).

2.2.2.1. Quantile regression vs. Mann-Kendall trend test

QR method, as introduced by Koenker and Bassett Jr (1978), can be considered as a natural extension of the standard linear regression models, due to the possibility to perform a regression on quantiles rather than just on the mean. The capability to investigate, at any quantile level, the linear relationship between two or more variables provides a more complete view of the statistical properties of a sample, also inspecting the tails of its distribution. Furthermore, standard regression models are strongly influenced by the presence of outliers, aspect that could be quite annoying especially in detecting trends along time. The main difference between a simple linear regression and the QR method is on the evaluation of coefficients. While in a classical bi-dimensional simple linear regression the intercept and the slope of the regression line are evaluated through the least square minimization problem, the QR model is based on a minimization of the sum of the weighted absolute value of a difference between the i^{th} observation (y_i) and the τ^{th} quantile line $\beta_0(\tau) + \beta_1(\tau)x_i$ at x_i :

$$\min_{\beta_0(\tau), \beta_1(\tau)} \left(\sum_{y_i \geq \beta_0(\tau) + \beta_1(\tau)x_i} \tau \left| y_i - (\beta_0(\tau) + \beta_1(\tau)x_i) \right| + \sum_{y_i < \beta_0(\tau) + \beta_1(\tau)x_i} (1 - \tau) \left| y_i - (\beta_0(\tau) + \beta_1(\tau)x_i) \right| \right) \quad (2.2)$$

From equation 2.2 it is possible to evince the dependency of the intercept, β_0 , and the slope, β_1 , of the regression line on the quantile level τ , for any $0 < \tau < 1$. The role of τ and $(1 - \tau)$ is to weight the vertical distances, that depend on the position of the observations with respect to the τ^{th} quantile line. In particular, points above the quantile line are weighted by τ , while those below the quantile line are weighted by $(1 - \tau)$, thus meaning that the greater the considered quantile, the more relevant are points above the quantile line in the evaluation of the slope and intercept of the regression line. To evaluate the trends significance, the Student's t -test has been applied to the QR results. The test is here used to reject the null hypothesis, with a significance level of 0.05 and 0.1, that the slope of the quantile line is equal to zero. In order to have a measure of the accuracy in estimating the slope and the intercept of the QR line, the standard error is also computed with a sparsity method, known as "*nid*" ("*not independently and identically distributed error*") (Koenker, 2004). This method, as considered by Koenker and Machado (1999), allows one to estimate the sparsity function for data that are not independently and identically distributed, assuming local linearity of the conditional quantile function $Q(\tau|x)$ in x , where $Q(\cdot)$ indicates the conditional probability of the quantile τ given the observed variable x . The "*nid*" method is sensitive to the presence of many equal values in the analyzed dataset; indeed, such a condition could generate a singular matrix, from which the algorithm cannot compute the standard error and, consequently, the confidence interval. For further details on the QR method the reader is referred to Koenker (2005) and Hao and Naiman (2007).

Unlike the QR method, the MK test is usually not applied to raw precipitation data (i.e., time series of rainfall depth originally recorded by the gauges), but it is generally used with specific datasets, such as annual maxima (Bonaccorso et al., 2005; Arnone et al., 2013). The null hypothesis in the test indicates that the population from which the sample is extracted has no trend, while the alternative hypothesis is that a trend exists. To accept or decline the null hypothesis at a fixed significance level (i.e., α_{sig}) a comparison between α_{sig} and a local significance level (i.e., p -value) is required. This last term is obtained as follows:

$$p - value = 2[1 - \Phi(|Z_S|)] \quad (2.3)$$

where $\Phi(\cdot)$ is the CDF (Cumulative Distribution Function) of a standard normal variate. The standardized test statistic, Z_S , follows a standard normal distribution and can be computed as reported below:

$$Z_S = \begin{cases} \frac{S-1}{\sigma} & \text{if } S > 0 \\ 0 & \text{if } S = 0 \\ \frac{S+1}{\sigma} & \text{if } S < 0 \end{cases} \quad (2.4)$$

In equation 2.4, σ is the variance of the standardized normal distribution function followed by the Kendall's S statistic, under the null hypothesis. The S statistic is computed as the sign function of the difference between two consecutive observations, namely x_i and x_j :

$$S = \sum_{i=1}^{n-1} \sum_{j=i+1}^n \text{sign}(x_j - x_i) \quad (2.5)$$

In the case of an auto-correlated series, the MK test could detect a trend even if it is not real, as demonstrated by Von Storch (1999). For this reason, a pre-whitening procedure is usually suggested, especially when the observed dataset is shorter than 50 elements (Yue and Wang, 2002). It consists in removing from each observation, x_i , a component given by the product of the previous one and the lag 1 serial correlation coefficient. In literature, MK is quite often coupled with the Sen's slope method (Almeida et al., 2017; Güçlü, 2018), as an estimator of the trend magnitude. This latter assumes that the slope of the regression line (i.e., β) is estimated as the median of the ensemble of slopes derived by linking the pairs of consecutive observed data (Sen, 1968):

$$\beta = \text{Median}\left(\frac{x_j - x_l}{j - l}\right) \quad \forall l < j \quad (2.6)$$

where x_l is the l^{th} observation antecedent the j^{th} observation x_j .

2.2.2.2. Pre-processing of the SIAS data

In order to avoid any misinterpretation in calculating trends, the original dataset from SIAS was preprocessed by removing all those gauges with at least one year of missing data in the period 2002 - 2019. While this condition may seem excessively strict, on the other hand, it has been deemed necessary given the limited temporal coverage of the dataset

compared to the three-decade period suggested by the WMO. This operation has led to take into account only 72 stations whose name and ID are reported in Table A.2 (3rd column) in the Appendix A.

Before proceeding with the QR analysis, it was necessary to carry out a further two more operations. Firstly, in order to prevent a great number of null values from being weighted in equation 2.2, all the zero precipitation values were removed from the dataset. Moreover, to guarantee the correct sequence of rainfall in time, each record has been previously associated to a “timestamp” that fixes its position in the timeline. Secondly, since the “*nid*” method is sensitive to the presence of many equal values, as stated in paragraph 2.2.2.1, a Gaussian white noise (i.e., zero mean with a negligible standard deviation, here fixed equal to 10^{-5} mm) was added to the original time-series. Indeed, the raw 10-minute dataset includes plenty of values equal to the rain gauge resolution (i.e., 0.2 mm) and its multiples that invalidate such a method.

Starting from the modified dataset, data have been aggregated to coarser time resolutions (20, 30, 40 minutes and 1, 3, 6, 12 e 24 hours), for the further trend analysis detection with the QR. In order to leave unchanged the total precipitation amount at the different durations, a moving window with the size of the chosen duration and that moves with a time step equal to its size has been considered; at each step, all the data within the window have been summed up to return the value of the aggregated precipitation (Figure 2.7). The use of the above-mentioned “timestamp” to fix the position of the 10-minute record in the timeline, guarantees the correct sequence of rainfall in time also for the coarser time resolutions. Moreover, in order to compare results with those obtained with the MK analysis, the rainfall annual maxima for the previous nine durations have been extracted as well (by using the rolling window method in this case).

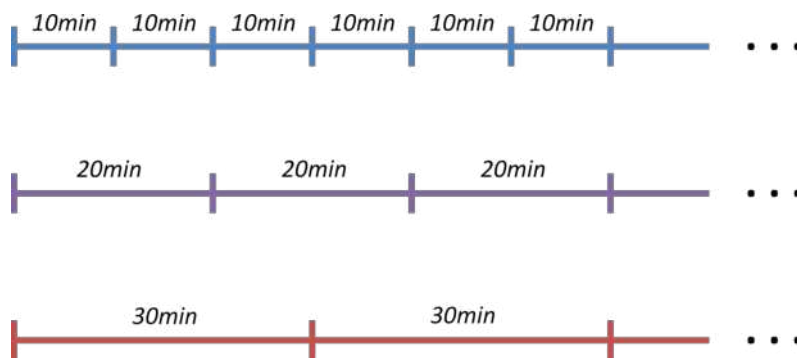


Figure 2.7: Example of the aggregation procedure for 20 and 30-minute duration

2.2.2.3. Precipitation trends through the QR method at the gauge level

In order to obtain the slope (i.e., the trend magnitude) and the intercept for a various range of quantiles, the R-package `quantreg` (Koenker, 2004) was used to apply the QR method to the rainfall time-series generated as in paragraph 2.2.2.1. Although the QR analysis was carried out for all the gauges displayed in Table A.2, for the sake of length, only the results related to the station of “Palermo” are reported and discussed in this paragraph. The significance of trends has been assessed by means of the Student’s t -test with reference to all the stations under study. The results of such an analysis are reported in paragraphs 2.2.2.4 and 2.2.2.5, where the procedure to identify the presence of spatial patterns has been carried out as well.

In order to provide a full view of the rainfall behavior at different timescales aggregations, Figure 2.8a, b, and c shows the results only for the shortest (10 minutes), intermediate (1 hour), and longest (24 hours) durations, respectively. Gray points represent the hourly rainfall intensities, i_h , obtained from aggregated rainfall depths, while QR lines (colored-solid lines) for the quantile levels 0.25, 0.5, 0.9, 0.95, and 0.99 are shown contextually to the ordinary least square (hereafter OLS) method line (black-dashed line).

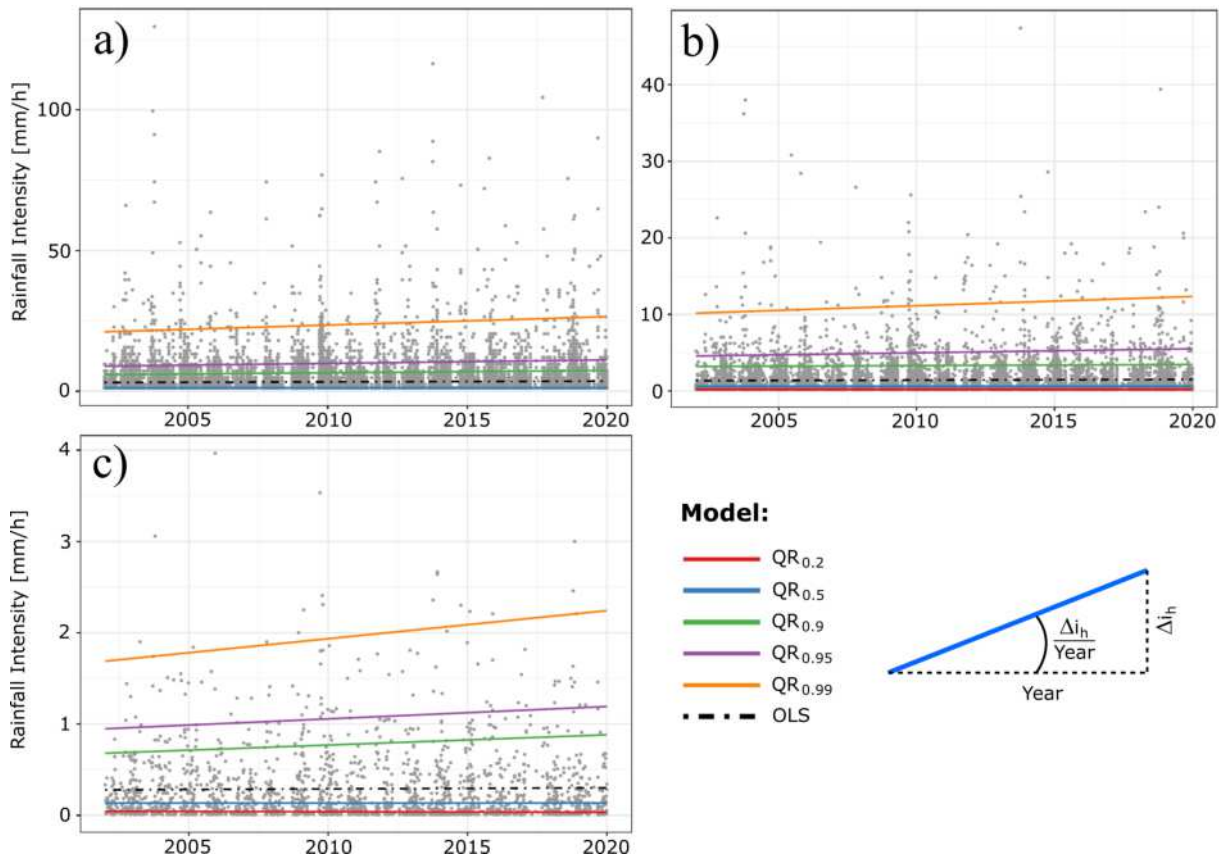


Figure 2.8: Graphic representation of QR lines (coloured-solid) and OLS line (black-dashed) for the station of ‘Palermo’ at (a) 10-min, (b) 1-hr, and (c) 24-hr durations. In the lower right panel, it is reported an exemplification of the annual increment of hourly intensity to compare slopes of rainfall intensity at different durations

Results confirmed that, as the considered quantile level grows, the intercept value grows as well. Indeed, for the highest quantiles, the highest rainfall intensity values have more weight than other values in the QR procedure, as expressed by equation 2.2. This behavior is not always valid for the slope since, depending on the data, there could be a trend inversion at any quantile level.

From Figure 2.8, it is noteworthy to highlight that the OLS regression line is not suitable to describe the behavior of extreme events, both in terms of high and low intensity precipitation, since the sample includes a great number of ordinary low rainfall events that affect the intercept of the regression line, thus pushing the regression line towards low values of intensity.

By observing the slope of the regression lines, it is possible to make some inferences about the trend magnitudes for the durations considered. In addition, to make possible the comparison of the trend magnitudes provided by the slopes of the regression lines at different durations, it was decided to refer the slope units to the annual increment of hourly intensity ($\Delta i_h/year$). A graphical representation of this transformation can be

observed in the lower right panel of Figure 2.8.

With this regard, Figure 2.9 represents the variation of slope with quantiles for the same durations shown in Figure 2.8. Black points are representative of the slope of the regression lines for different quantile levels, while the gray bands delimit the 90% confidence interval for the estimated slopes. The QR has been applied to 0.02 equal step quantiles ranging from 0.02 to 0.98, together with the quantiles 0.95 and 0.99 in order to extensively explore the relationship between slope and quantile. The slope of the OLS regression line, which is constant at a fixed duration, is indicated using a red-solid line whereas the related confidence intervals are displayed by means of some red-dashed lines.

In general, if one observes the results of QR analysis, an increasing (decreasing) trend at the higher quantiles corresponds to the probability (with a certain level of significance) to have more (less) severe events. With this in mind, from the three panels of Figure 2.9, it is possible to notice that for the lower quantiles the slope is always close to zero, while it tends to generally increase for the higher quantiles. Such a behavior is mainly due to the high number of low-intensity rainfall events which, for the lower quantiles, have more weight than the higher intensities. Moreover, with reference to the slope of the ordinary least square method (red – solid line in Figure 2.9), this is characterized by a slope significantly different from those relative to the highest quantiles. Such a behavior is not observable for the lower quantiles, which have points mostly within the confidence interval of the mean (red – dashed lines). This certifies the fact that the ordinary least square method is only representative of the average behavior of the sample and is not effective to characterize any trend at higher quantiles, which correspond to heavy and very heavy rainfall.

From the analysis of the confidence interval (gray bands in Figure 2.9), for each duration and rain gauge analyzed, it can be observed that the standard error grows with the quantile; this is mainly due to the reduced extent of the sample used in the QR procedure for the higher quantiles.

For completeness, it is noteworthy to highlight the presence of some peaks in the slope at the 10-minute duration for the higher quantiles (Figure 2.9a). This aspect can be explained by comparing the shape of the empirical PDF of rainfall intensity data at 10-minute, 1-hour and 24-hour durations, as shown in Figure A.1 in the Appendix A. In the case of the 10-minute duration (Figure A.1a), the PDF shows the highest peak in correspondence of the gauge resolution (i.e., 0.2 mm) and several other peaks for the multiples of the gauge resolution that become smaller and smaller as the multiple of the gauge resolution increases. This reflects in weighting data in the QR procedure, thus generating the spikes shown in Figure 2.9a. This aspect is lost at the higher durations (i.e., 1-hour and 24-hour durations in A.1b and c, respectively) since data are aggregated

and the empirical PDF of rainfall intensity assumes a smoother shape.

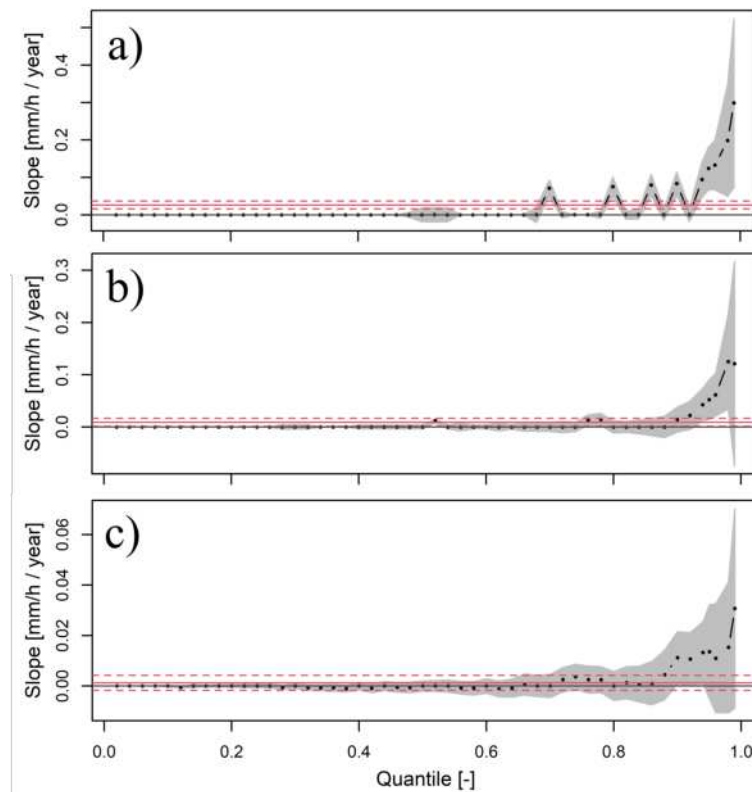


Figure 2.9: Slope of the regression lines versus quantile level for the station of ‘Palermo’ at (a) 10-min, (b) 1-hr, (c) 24-hr durations. Black points are representative of the slopes for various quantiles, while the grey bands stand for the 90% confidence intervals. The figure also displays the slope of the OLS regression line (red-solid line) and the related confidence intervals (red-dashed lines) at the three considered durations

2.2.2.4. Effects of duration and quantile on precipitation trends

Following the conjecture provided by Arnone et al. (2013) about the existence of trends in sub-hourly precipitation, a particular attention has been paid to identify eventual positive trends for the events at the sub-hourly durations and for the higher quantiles. Moreover, a further and most crucial aspect is linked to the fact that eventual positive trends for these events would correspond to an increase in rainfall events with a short-duration and high-intensity that, in certain cases (e.g., small catchments with low times of concentration), could cause flash flood events and, as a consequence, higher risks of economic damages and fatalities.

Figure 2.10 summarizes the QR results for all the considered rain gauges. It provides the percentage of gauges showing a significant positive (red), negative (green), or non-significant (gray) trend for the whole ensemble of considered durations and 0.2, 0.5, 0.9, 0.95, and 0.99 quantiles. Although not related to extremes, the 0.2 and 0.5 quantiles have

been considered to provide a comprehensive view of the changes in the whole precipitation distribution. The two columns of Figure 2.10 are representative of two different levels of significance (i.e., $\alpha_{sig} = 0.05$ and $\alpha_{sig} = 0.1$, respectively).

Focusing on the lowest and intermediate quantiles, namely 0.2 and 0.5, respectively, it is possible to notice that a high percentage of rain gauges show a non-significant trend for all the considered durations for both the levels of significance. However, it is noteworthy that a noticeable percentage of stations has a positive trend at the sub-hourly durations, reaching the maximum value at the 10-minute duration (i.e., 26.4% and 33.3% for $\alpha_{sig} = 0.05$ and $\alpha_{sig} = 0.1$, respectively). As the duration increases, there is an increase of the percentage of stations showing a negative trend and, at the same time, a corresponding decrease of the percentage of gauges manifesting a positive trend. This is more evident for the $\alpha_{sig} = 0.1$. When the percentages related to the shortest (10 minutes) and longest (24 hours) duration (Figure 2.10, top right panel) are taken into account, for instance, one can observe that the first bin (10 minutes) provides about 33% of gauges characterized by a significant positive trend and about 6% of gauges with a significant negative trend, while, on the other hand, the last bin of the panel (24 hours) displays an opposite behavior (about 4% with a significant positive trend and about 20% with a significant negative trend). Furthermore, it seems that as the duration increases there is a reduction of the very ordinary (i.e., 0.2 quantile) and ordinary (i.e., 0.5 quantile) long-duration events. If these negative trends for the lower quantiles (e.g., 0.2) will persist especially at the longer durations, they could result in an increased risk of dry conditions (Lausier and Jain, 2018) with a reduction of available water resources, impacting, for instance, the agricultural sector (Field, 2012), hence causing noticeable economic damages.

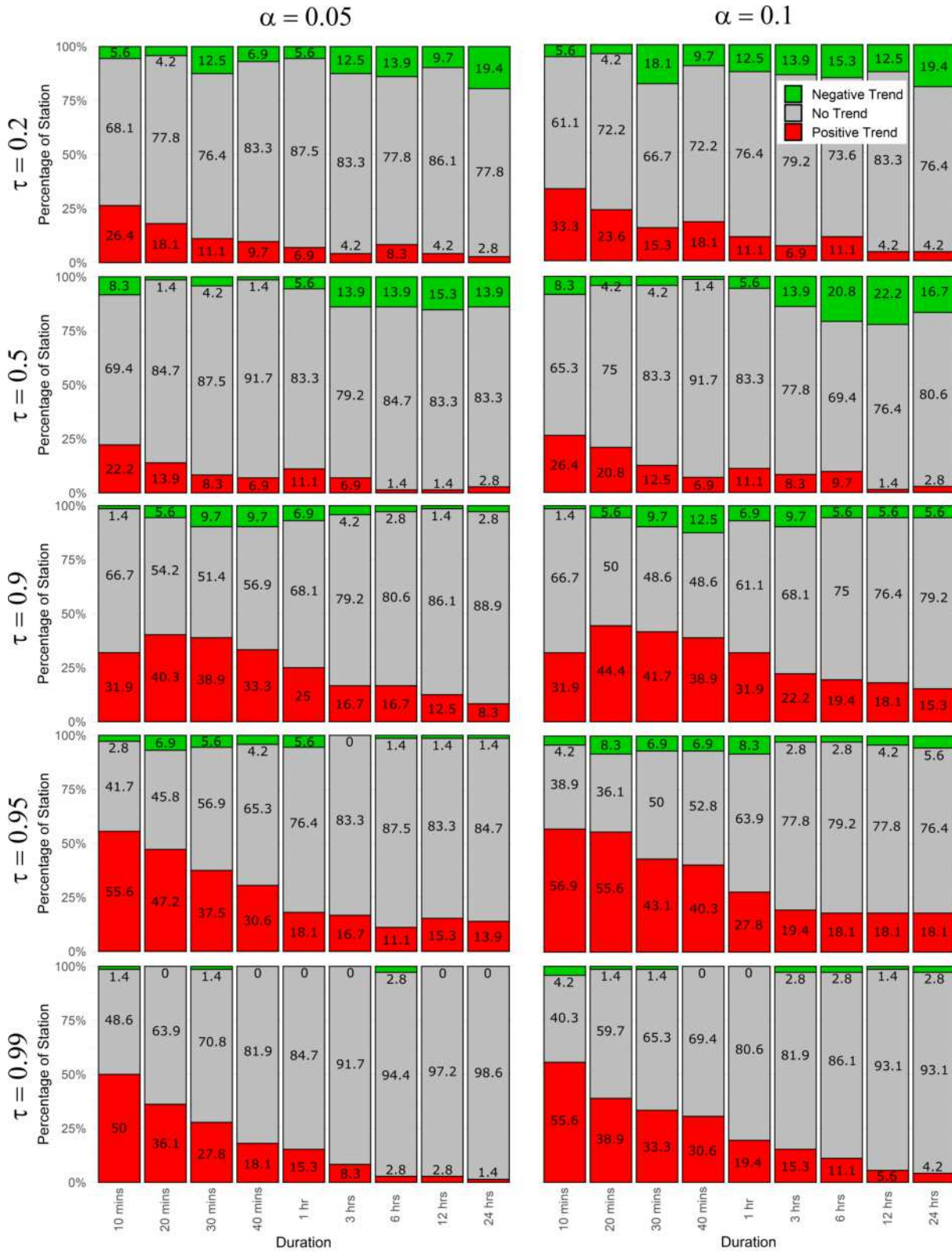


Figure 2.10: Percentage of rain gauges characterized by a positive (red), negative (green), and non-significant (grey) trend coming out from QR procedure at 0.2, 0.5, 0.9, 0.95, and 0.99 quantiles at all durations

Regarding the higher quantiles (i.e., 0.9, 0.95, 0.99), as quickly as the duration decreases, it is possible to observe a clear increasing pattern of the percentage of rain gauges with a positive trend. In particular, for the two highest quantiles (i.e., 0.95 and 0.99, respectively) and both the significance levels (i.e., 26.4% and 33.3% for $\alpha_{sig} = 0.05$ and $\alpha_{sig} = 0.1$, respectively), at least the 50% of the stations shows an increasing trend at the 10-minute duration. Regarding the quantile level of 0.9, unless for the 10-minute duration, which shows a percentage slightly lower than the other sub-hourly durations, the increasing pattern of positive trends with the decreasing of durations is still maintained. On the opposite, for the 24-hour duration, the stations with no-trend strongly prevail, especially for 0.99 quantile level, where about 98% of stations reveal a non-significant trend at $\alpha_{sig} = 0.05$. All of the previous considerations suggest an increase in rainfall intensity provided by sub-hourly extreme events in Sicily, thus confirming what Arnone et al. (2013) had already guessed for Sicily region and other studies had found for other parts of the world (De Toffol et al., 2009; Adamowski et al., 2010). As already said at the beginning of this section, such a condition could lead to an increase of flash floods, with all of its consequences, but also to other consequences such as an increase in the soil loss, due to its erosion, and a consequent decreasing in production of these soils as found by Wei et al. (2009) in the North-West of China.

Differently from the case of the lower quantiles, in the last cases (i.e., 0.90, 0.95, and 0.99) less than the 10% of stations show a negative trend at all the durations under study; this percentage becomes smaller and smaller as quickly as the quantile increases. Moreover, differently than for the positive trend, it is not possible to recognize any pattern with duration. Furthermore, for the 0.99 quantile and $\alpha_{sig} = 0.05$, almost no station reveals a significant negative trend at all durations.

In order to describe the variation of trend magnitudes with quantiles and durations, Figure 2.11 reports, the empirical cumulative distribution function (ECDF) of the trend magnitude for the gauges showing a statistically significant (positive and negative) trend for $\alpha_{sig} = 0.1$ and the durations of 10, 30-minute and 1, 6 and 24-hour and the 0.2, 0.95 and 0.99 quantiles.

Firstly, it is worth to focus on the entity of the trend magnitude, which considerably varies with quantiles. Indeed, at the 0.2 quantile (Figure 2.11a), it is possible to notice that, for all the durations, the trend magnitude values are close to zero, so that hourly and sub-hourly ECDFs, apart from those at 6 and 24-hour durations, cannot be distinguished. An opposite behavior is illustrated in Figure 2.11b and c, related to the 0.95 and 0.99 quantiles, respectively. In particular, as the duration increases, the sample size becomes even smaller, due to a general loss of statistical significance (see also Figure 2.9) and, at the same time, the trend magnitude grows. Furthermore, as the quantile increases,

the trend magnitude increases as well. As an example, focusing on the quantile 0.99 and sub-hourly durations, it is possible to notice that the 75% of stations present a trend magnitude greater than about 0.3 mm/h/year, which is approximately the maximum magnitude value which characterizes the analyses carried out for 0.95 quantile.

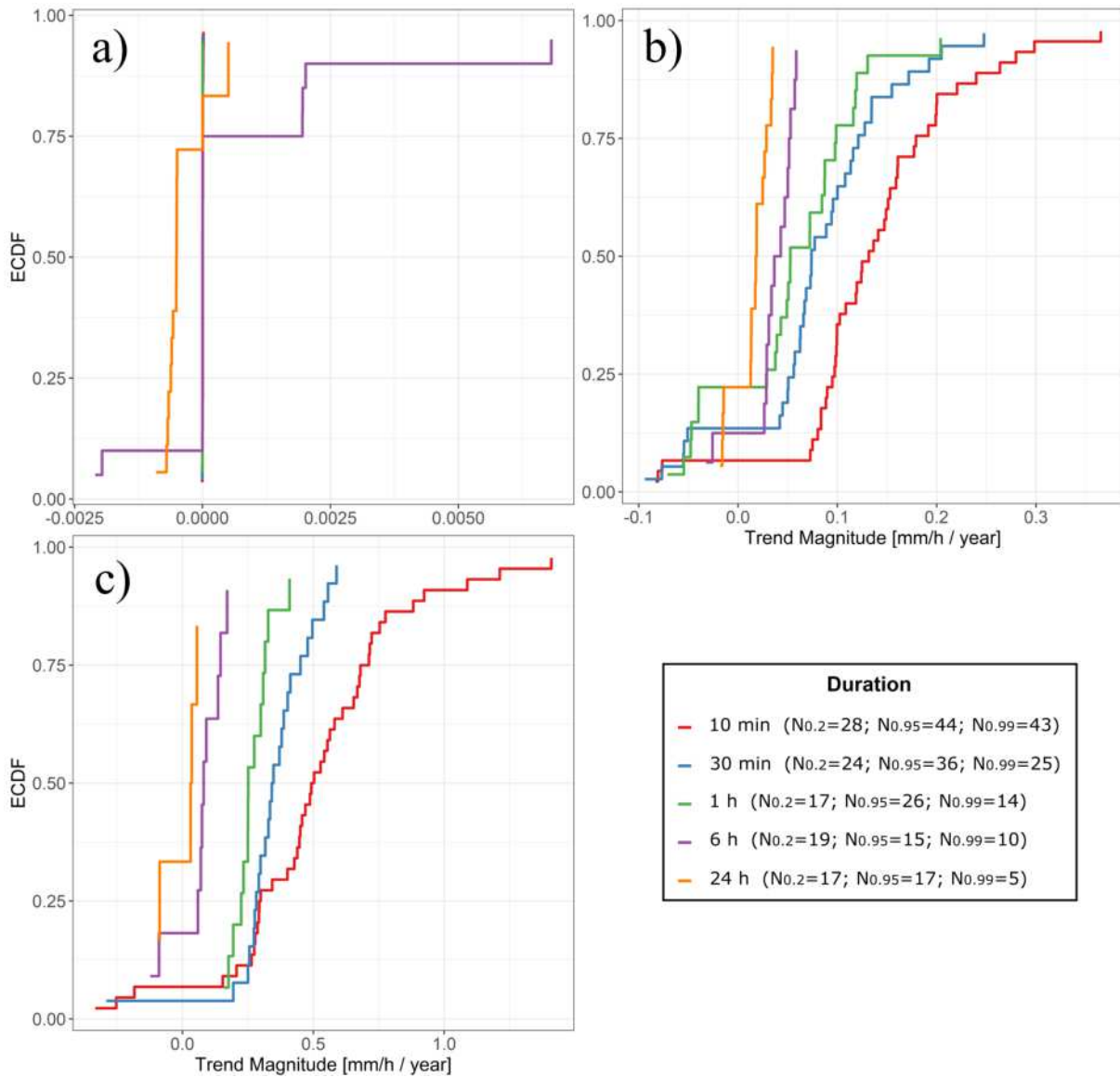


Figure 2.11: ECDF of the trend magnitude for 10, 30min and 1, 6, and 24hr at (a) 0.2, (b) 0.95 and (c) 0.99 quantile. ECDFs are representative of the positive and negative trend magnitude with a significance level of .1. The sample size for any quantile-duration combination is reported in the legend

These findings confirm that the short-duration and high-intensity rainfall events are occurring more frequently in Sicily, at least with reference to the considered period, thus confirming that in the last years we are experiencing an increase in short-duration high intensity rainfall events that could be probably a consequence of climate change, as affirmed

by Field (2012).

The remaining ECDFs, related to all the durations and quantiles considered, are reported in Figure A.2 in the Appendix A.

2.2.2.5. Spatial analysis of precipitation trends

In order to assess an eventual spatial distribution of the trends in Sicily, for each rain gauge station, Figure 2.12 represents the magnitude, direction, and significance of the trends detected with the QR approach. For the sake of clarity, the trend magnitude, which is expressed as the annual increment of hourly intensity, is symbolized by a graduated color, the trend direction is represented by the symbol orientation (i.e., positive or negative), while the dimension of the triangle is related to three different classes of significance level (i.e., ≤ 0.05 ; $0.05 \div 0.1$; > 0.1). The panels A, B, C, D, and E in Figure 2.12 represent the spatial distribution of detected trends for the quantiles 0.2, 0.5, 0.9, 0.95, 0.99, respectively, while the columns 1, 2, and 3 are relative to the durations of 10-minute, 1-hour, and 24-hour, respectively. For the sake of the length of this section, the plots related to all the other durations considered for the previous analyses are reported in are reported in Figures A.3 and A.4 in the Appendix A. By observing this figure, it is possible to notice that the number of stations showing a significant trend (positive or negative) increases with the quantile level and decreases as the duration increases, thus confirming what has been already shown in Figure 2.10. Moreover, it is possible to observe that the trend magnitude values decrease moving from the higher to the lower quantile for each duration. The low trend magnitudes, which have been obtained at the lower quantile levels, are strictly connected to the high number of similar low rainfall intensity values weighted in the QR process. For this reason, these trends are expected to be low but, at the same time, not negligible, since they refer to very ordinary rather than extreme events. Indeed, even small changes in events that frequently occur throughout the year could lead to an important alteration of the local hydrological cycle.

In order to objectively identify the potential spatial clustered situations in the trend magnitude, the spatial autocorrelation (hereafter SAC) analysis was carried out on those rain gauges showing a significant trend with $\alpha_{sig} = 0.1$ (i.e., all the medium and large colorful triangles in Figure 2.12) using the GeoDa software (Anselin et al., 2009).

Two different indicators, namely the Global Moran's I and the Local Moran have been used to perform a spatial autocorrelation (hereafter SAC) analysis in order to verify the presence of specific patterns in the spatial distributions of the trend magnitude.

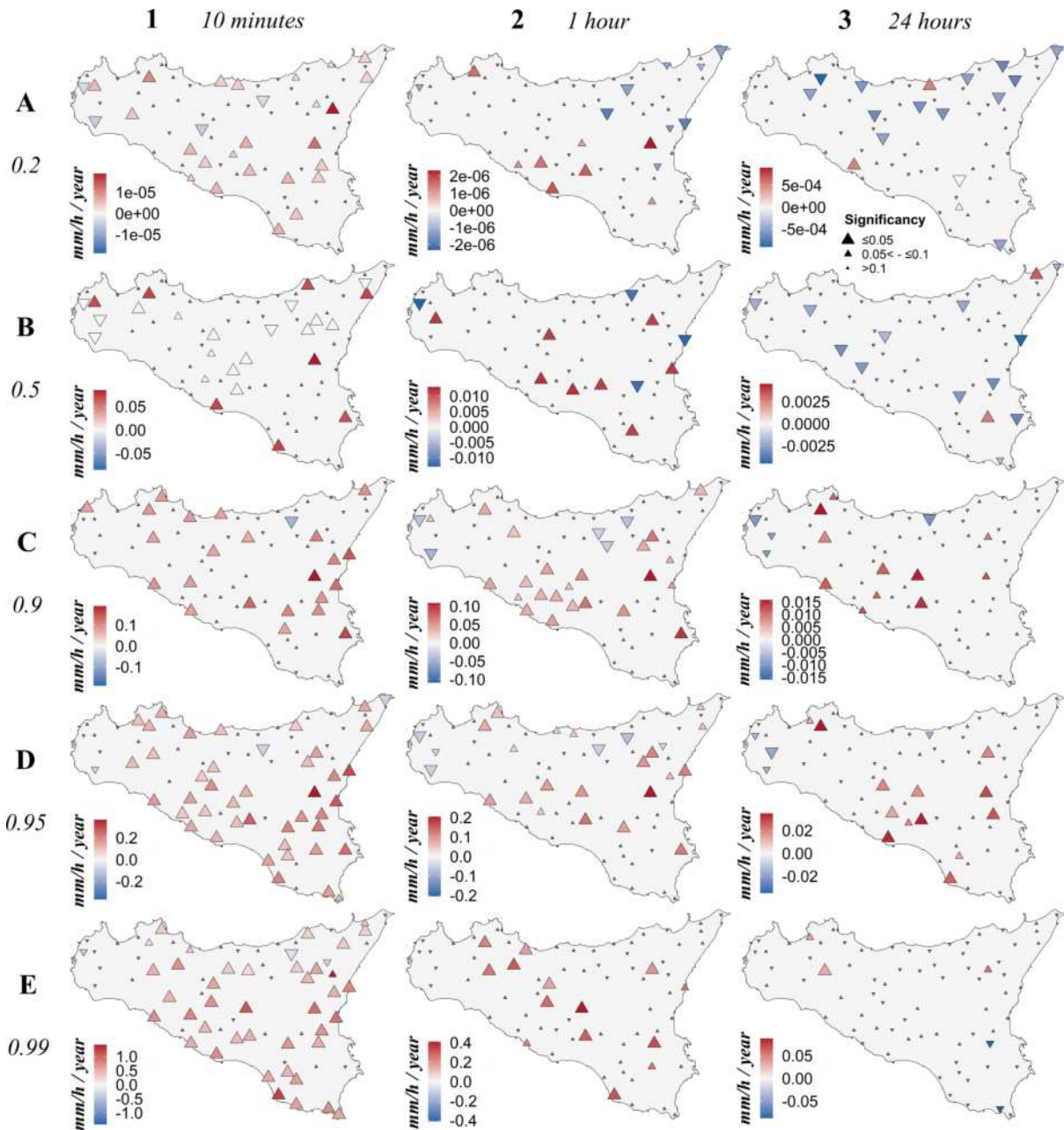


Figure 2.12: Spatial distribution of the gauges under study and magnitude (colour), expressed in $mm \cdot h^{-1} \cdot year^{-1}$, direction (triangles orientation) and significance (triangle size, large for $\alpha_{sig} \leq 0.05$, medium for $0.05 < \alpha_{sig} \leq 0.1$ and small for $\alpha_{sig} > 0.1$) from QR at 0.2, 0.5, 0.9, 0.95, 0.99 quantiles for 10-min, 1- and 24-hr durations. The bold letters, A-E, stand for the quantiles, while the bold numbers 1–3, denote the durations

The Global Moran's I statistic (Moran, 1950) can be interpreted as an extension of the autocorrelation coefficient, by means of a symmetric spatial weights' matrix filled by the inverse of the geographic distance between the pairs of points, where data are recorded. The value of Moran's I ranges from -1 to 1 (same as the autocorrelation). In order to establish whether data are randomly distributed or not, the Moran's I must be compared

to its expected value, $E[I]$. In general, if I is less than $E[I]$ data are dispersed, while I values greater than $E[I]$ indicate a clustered pattern. When I is close to its expected value, instead, data tend to be randomly distributed across the points. However, since SAC analysis is an inferential statistic, results must be interpreted on the base of null hypothesis, stating that data are randomly distributed across points. Therefore, the p -value and the Z -score of the analysis must be assessed. The null hypothesis cannot be rejected if the p -value is not statistically significant, thus meaning that data are randomly distributed across the points. On the other hand, for those cases in which the p -value is statistically significant, i.e., the spatial distribution of the processed variable is not the result of a random spatial process, a positive sign of the Z -score statistic reveals the presence of a clustered pattern of the analyzed feature, while a negative one means that the spatial pattern is dispersed.

The Global Moran's I statistic is useful to conclude if the spatial distribution of a given variable is globally clustered or not, but a local statistical analysis is necessary to derive the geographical position of a cluster. To this regard (Anselin, 1995) introduced a class of local indicators of spatial association, known as LISA. Among all the possible LISA, in this study the Local Moran has been applied. The link between the two global and local indicators is that the global I can be seen as an average value (up to a factor of proportionality) of local I_i , where the subscript i stands for the location of the measurement. It is worth to mention that, even if the Local Moran reflects the presence of significant local clusters, it does not mean that the global spatial distribution of the feature needs to be necessarily clustered. The local clusters are identified by means of the Moran scatterplot, in which points have $(x; y)$ coordinates given by the original and the spatially lagged variable, respectively. This scatterplot is divided into four quadrants, in which the axes intersect in the centroid of the point cloud. The upper-right and the lower-left quadrants refer to a positive spatial autocorrelation, representative of similar values at geographically near location. On the opposite, the other two quadrants represent a negative spatial autocorrelation, meaning that there are dissimilar values at neighboring locations. Combining the information provided by the Moran scatterplot with an indication of significance, it is possible to make a classification into four classes. In particular, significant clusters, identified in the upper-right and the lower-left quadrants, are denoted as High-High (HH) and Low-Low (LL), while significant outliers, identified in the lower-right and the upper-left quadrants, are denoted as High-Low (HL) and Low-High (LH), respectively.

Table 2.1 shows the SAC analysis results in terms of Global Moran's I estimated value, Z -score, p -value and sample size, related to all the possible combinations between durations and quantiles shown in Figure 2.12. It is important to remark that this analysis

aims to determine whether the trend magnitude is globally clustered or not over the island. In such a kind of analysis the sample size plays a very relevant role; Legendre and Fortin (1989) suggest to apply the SAC analysis to samples composed of about 30 values, in order to have a sufficient amount of data to reliably identify potential spatial patterns. Nevertheless, this threshold is not a strict limit and, in fact, Griffith (2010) suggest a minimum sample size of 25 elements.

The results of such an analysis are reported in Table 2.1, where the cases with a p -value lower than 0.1 but a sample size smaller than 25 are indicated with an italic font, while the cases with a p -value lower than 0.1 and a sample size greater than 25 data are reported with a bold-italic font. Normal font face, instead, is related to the quantile-duration combinations in which the p -value is higher than 0.1 and, consequentially, in which the spatial distribution of the magnitude can be considered as the result of a random spatial process.

Focusing on the lower (i.e., 0.2 and 0.5) and highest quantiles (i.e., 0.99), the results of Table 2.1 indicate that no spatial patterns of the trend magnitude can be found at any duration, given the resulting p -value and Z -score statistics. Indeed, regarding the 0.99 quantile and 10-minute duration, the p -value of the SAC analysis is higher than 0.1, probably due to a great variability of the trend magnitude. Therefore, it is not possible to assume that, globally, the distribution of the trend magnitude is significantly clustered. On the contrary, when one observes the quantile 0.9 it is possible to highlight that for the 1-hour and 24-hour durations, the p -value is less than 0.1 and, contemporary, the Z -score is positive. This means that the spatial distribution of the trend magnitude is clustered, even though the result related to the 1-hour duration may be considered more reliable than the 24-hour one due to the greater sample size.

Regarding the 0.95 quantile, while all the durations exhibit a p -value lower than $\alpha_{sig} = 0.1$ only the 10-minute and 1-hour durations are characterized by a sample size greater than 25. Furthermore, the Z -score is always positive, indicating that the trend magnitude is clustered.

The results of the SAC analysis for the remaining quantiles and durations are reported in Table A.3 in the Appendix A. With reference to all the durations under study, the Global Moran's I generally resulted in a spatially clustered distribution of the trend magnitude especially for the higher quantiles. This behavior is particularly enhanced at the 0.95 quantile for the whole ensemble of sub-hourly durations (i.e., 10, 20, 30, and 40 minutes), which are characterized by the greater sample sizes. Furthermore, for the 0.9 quantile, the same considerations are valid for the sub-hourly durations of 30 and 40 minutes.

In order to identify the clusters' position, a Local Moran analysis (Anselin, 1995) has

	0.2 quantile			0.5 quantile		
	10 min	1 h	24 h	10 min	1 h	24 h
Moran's I Index	0.0442	0.2722	0.0202	-0.0939	-0.5349	-0.2730
Z-score	0.5108	1.6065	0.4338	-0.4451	-1.4191	-0.9623
p-value	0.6095	0.1082	0.6645	0.6562	0.1559	0.3359
Sample Size	28	17	17	25	12	14

	0.9 quantile			0.95 quantile		
	10 min	1 h	24 h	10 min	1 h	24 h
Moran's I Index	0.0854	<i>0.1494</i>	<i>0.6666</i>	<i>0.2766</i>	<i>0.1744</i>	<i>0.4674</i>
Z-score	1.3501	<i>2.1511</i>	<i>3.5955</i>	<i>2.9122</i>	<i>1.7659</i>	<i>2.8604</i>
p-value	0.1770	<i>0.0315</i>	<i>0.0003</i>	<i>0.0036</i>	<i>0.0774</i>	<i>0.0042</i>
Sample Size	24	<i>28</i>	<i>15</i>	<i>44</i>	<i>26</i>	<i>17</i>

	0.99 quantile		
	10 min	1 h	24 h
Moran's I Index	0.0501	-0.1462	0.3266
Z-score	1.0981	-0.3092	0.8874
p-value	0.2722	0.7571	0.3749
Sample Size	43	14	5

Table 2.1: Global Moran's I estimated value, Z -score, p -value, and sample size for 0.2, 0.5, 0.9, 0.95, and 0.95 quantiles and 10-min, 1- and 24-hr durations. All cases in which the p -value is less than 0.1 but the sample size is less than 25 are indicated with an italic font, while those cases in which the p -value is less than 0.1 and the sample size is greater than 25 are written in bold-italic font. Normal font face is related instead to those cases in which the spatial distribution of the trend magnitude is the result of a random spatial process (p -value greater than 0.1)

been applied at the same samples and for the same duration-quantile combinations used in 2.12. In particular, panels a to c in Figure 2.13 show the results for 95th percentile at 10-minute, 1-hour, and 24-hour duration, respectively. This quantile has been chosen as representative mainly because the sample size criterion is satisfied both for 10-minute and 1-hour duration (i.e., 44 and 26 locations), while the sample size is the largest among those relative to the 24-hour duration (i.e., 17 points), even if it is smaller than 25 elements.

However, for the sake of completeness, Figure A.5 in the Appendix A shows the results relative to 0.2, 0.5, 0.90, and 0.99 quantiles at 10-minute, 1-hour, and 24-hour duration.

In Figure 2.13, red and blue circles are relative to HH and LL clustering cases, respectively, and characterized by a p -value lower than 0.1. The significant outliers, instead, are marked with the diamond shape and filled with pink (HL) or light blue (LH) colors. Therefore, the crosses represent those locations in which the significance level exceeds 0.1.

It is worth to mention that for all the panels in Figure 2.13 it is possible to distinguish two significant clusters. In particular, in the south-east there is a HH cluster, while the northern-west part is characterized by a LL cluster. Looking at the dimension of these two clusters, it is possible to observe as their extension changes with the duration. At the 10-minute duration (Figure 2.13a), for instance, a relevant number of stations composes both the clusters (i.e., 8 and 12 sites for the LL and HH, respectively). Moreover, by comparing this panel with the correspondent one in Figure 2.12 (i.e., panel D1) it is possible to notice that the HH cluster includes those stations characterized by the highest values of trend magnitude. Therefore, the LL cluster is composed by a group of gauges where the trend magnitude is moderately positive. Starting from this consideration, it is worth to highlight that the acronyms HH and LL do not necessarily refer to a cluster of gauges in which an increasing or a decreasing trend is observed.

Focusing on the 1-hour and 24-hour durations (i.e., Figure 2.13b and c, respectively), both the clusters reduce their dimension. Furthermore, the LL cluster seems to be more confined in the north-west side of the island. Looking at the trend magnitude of the gauges forming the LL cluster (panels D2 and D3 in Figure 2.12, respectively), it is also possible to observe that, in this case, they match with a decreasing trend magnitude cluster (i.e., except for the upper-left point in LL cluster of Figure 2.13c).

Looking at the Figure A.5 in the Appendix A, it is worth to focus that, when the HH and LL clusters are visible, their location is, more or less, the same of that highlighted in Figure 2.13. This consideration is not valid for 0.2 quantile at 1-hour duration, where different clusters can be detected.

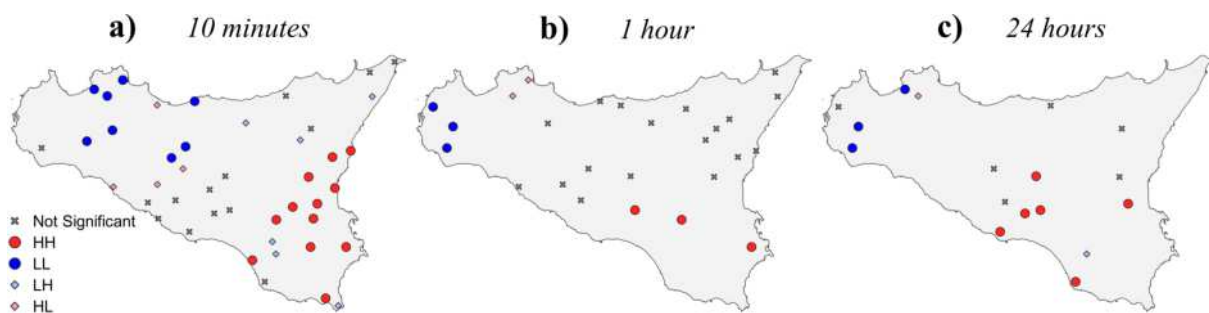


Figure 2.13: Local Moran analysis for the 0.95 quantile at (a) 10-min, (b) 1-hr, and (c) 24-hr duration. The LISA is applied to both the positive and negative trend magnitudes with a significance level of 0.1. Red and blue circles are relative to high-high (HH) and low-low (LL) clustering cases, respectively, and characterized by a p -value lower than 0.1. The significant outliers are marked with light blue and pink diamonds for low-high (LH) and high-low (HL) clustering cases, respectively. The crosses represent those locations in which the significance exceed the level of 0.1

2.2.2.6. Mann–Kendall test for rainfall annual maxima trends

This section shows the results of the MK method, applied to the pre-whitened annual maxima extracted by the SIAS dataset, as well as a qualitative comparison with the QR method results, with the aim to explore the advantages and drawbacks of both methodologies in trends detection.

As an example, the results of such an analysis for the rain gauge of Palermo are shown in Figure 2.14, where the subplot a) shows the annual maxima extracted for the durations of 10 minutes, 1 hour, and 24 hours, while the remaining plots show the results regarding the trend-duration dependency (Figure 2.14b) and the spatial variability of trends magnitude, direction, and significance (Figure 2.14c). The magnitude, in this case, is obtained through the Sen’s slope method and represents the variation of rainfall annual maxima per year (mm/year).

Focusing on canonical durations, it is possible to observe two different behaviors between positive and negative trends with duration. Indeed, as the duration increases, the percentage of stations characterized by a negative trend becomes greater, while the one featured with positive trend decreases. In particular, at the 24-hour duration, these percentages reach 18% and 0% for negative and positive trend, respectively. Regarding the sub-hourly durations, instead, no patterns with duration are noticeable. In any case, it is worth to observe that the majority of the rain gauges is characterized by a non-significant trend.

Although it is not possible to make a direct comparison between the results obtained with the QR and MK methods because of the different information they work with, it may be useful to highlight some differences, strengths and weaknesses of the two methods. First of all, focusing on the data, since the MK test works with the annual maxima (i.e., only a value of rainfall per year), it might be unsuitable to work with short datasets (i.e., few years of observed data) since it would return results statistically not significant. Moreover, working with annual maxima implies that all the rainfall depths slightly lower than the annual maxima, despite the fact that could be even higher than the annual maxima of other years, are discarded from the analysis.

In the QR method, instead, all data are processed to extract information about trends, even if only those exceeding the threshold related to the examined quantile are weighted in a more significant way. Nevertheless, by looking at the ECDFs of the aggregated time-series, related to 10-minute, 1-hour and 24-hour duration, for “Palermo” rain gauge, it is possible to observe that about 1,200, 470, and 100 values are above the 95th percentile, respectively. Moving to the 99th percentile, the number of observations above this percentile drops to about 240, 90 and 20, respectively, but, in any case, higher than

those used in the MK procedure that are 18 values (i.e., the annual maxima) for each of the considered durations. This could be the main reason why the QR approach is able to detect a consistent number of stations featured by a positive trend for the 0.95 and 0.99 quantile (i.e., about 57% and 56% at $\alpha_{sig} = 0.1$, respectively), while this information is not captured by the MK procedure.

With reference to the spatial patterns (Figure 2.14b), most of the stations shows a non-significant trend at all durations. Since the maximum number of rain gauges showing a significant trend is equal to seven (at 1-hour duration), the SAC analysis has not been carried out to avoid inconsistent and/or unreliable results. For all of these reasons, the QR could be a valid alternative to the MK procedure to detect trend in extreme rainfall, especially when the period under study is short. It is further worth to highlight that, also in the QR procedure, the loss of significance recorded especially at the longest duration could be attributable to a too small sample size.

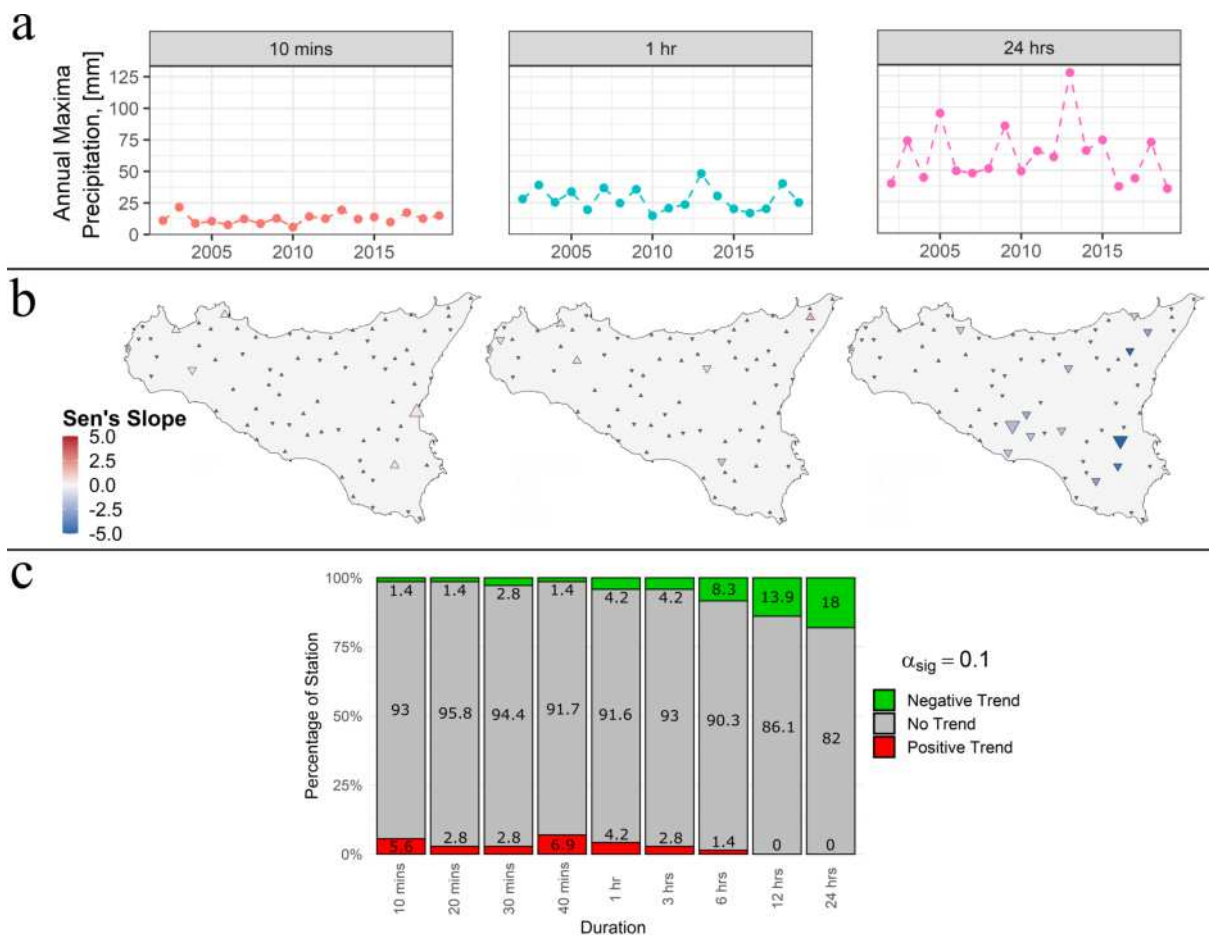


Figure 2.14: Annual maxima for the rain gauge of ‘Palermo’ of the SIAS data set at 10-min, 1-hr, 24-hr duration (a), spatial distribution of magnitude, direction and significance of trends (b), and percentage of stations having a negative (green), positive (red), or non-significant (grey) trend obtained through the MK test (c)

2.2.3. Larger and more frequent extremes affect the reliability of design rainfall

As shown in section 2.2.2, it is evident that the last two decades have been characterized by an increase in rainfall intensity in Sicily, particularly concerning the higher quantiles and shorter durations. The consequences associated with these increasingly intense phenomena can be various, affecting both the social and the economic sphere. For instance, the pluvial floods triggered by extreme rainfall events in the eastern of the region caused more than 13 fatalities in November 2018; the urban pluvial flood in July 2020 brought Palermo to its knees, fortunately with no fatalities (Francipane et al., 2021). Also agriculture is often plagued by these intense phenomena: during winter 2023 the damages to agricultural production were estimated at over € 1.8 M, while damages to the farm structures amounted to € 2.2 M in an area of 239 hectares in the center of Sicily, as stated by the Sicilian Regional Agency. From an engineering perspective it is fundamental to question whether the growing occurrence and severity of such events is exposing the susceptibility of the existing infrastructures towards a state of “physiological insufficiency” (Debortoli et al., 2017; Kumar et al., 2021). This implies that what was designed decades ago may no longer be safe today, since the stress induced by climate change has turned what was once considered "extreme" into more frequent. The other side of the coin is even more dramatic: persisting in using the same methodologies for hydraulic structure design could potentially lead to an increasing risk of failure in the future, consequently exposing the population to greater risks. In terms of hydrological risk, the rise in the frequency of the most intense phenomena implies considering the non-stationarity of their occurrence and, in turn, of the classical frequency distribution parameters with which these events are modelled (Cheng and AghaKouchak, 2014). This means that the concept of the return period should be revised to something that can no longer be considered a fixed entity but instead must vary over time.

Rainfall Depth–Duration–Frequency (DDF) curves are the instruments that are widely used in hydrology to estimate the design storm for urban drainage systems, water resources management, and flood risk assessment (Yu et al., 2017; Andimuthu et al., 2019). These curves provide precipitation quantiles for specific durations and return periods, and are typically expressed as a power-law:

Adapted from: Treppiedi, D., Cipolla, G., Francipane, A., Cannarozzo, M. and Noto, L. V. (2023), ‘Investigating the reliability of stationary design rainfall in a mediterranean region under a changing climate’, *Water* 15(12), 2245

$$h(d, T) = a(T) \cdot d^{n(T)} \quad (2.7)$$

which describes the variation of the critical rainfall depth $h(d, T)$ as the duration of the event d changes and once the return period T is assigned, meaning that the parameters $a(T)$ and $n(T)$ are known. These curves are obtained by carrying out a statistical analysis of historical rainfall data (e.g., annual maxima or precipitation exceeding a fixed threshold) to identify the relationship between the depth (or intensity), duration, and frequency (or exceedance probability) of rainfall events. These analyses estimate statistical parameters for a time series of a hydrological variable by assuming that the recorded series is stationary, which means that its statistical properties do not exhibit any trends, shifts, or periodicity (Scala et al., 2022). Moreover, the more extensive is the observed dataset, the more accurate and reliable are the DDF curves. Indeed, the probability distribution functions commonly used to rely on high-order sample statistic parameters can be estimated with confidence only if the available sample series has a significant length and the data source is reliable.

Recent studies have shown that the traditional approach of using stationary DDF curves may not be adequate for the design of hydraulic works or assessing hydrological risk in the context of possible climate change signals (Cook et al., 2020; Kourtis and Tsihrintzis, 2021, 2022). Changes in climate are altering weather circulation patterns, which are connected to precipitation fields (Cipolla et al., 2020) and may potentially lead to an increase in the frequency of occurrence and intensity of extreme rainfall events (Nissen and Ulbrich, 2017; Myhre et al., 2019).

The main objective of this section is to verify if quantiles (or DDFs) obtained through a stationary regional approach, which will be described in the next paragraph, can be suitable to describe the precipitation regime of the last two decades in the Sicily region. In particular, it has been conducted a comparative analysis for different durations and return periods between the rainfall quantiles calculated with the regional approach by Forestieri et al. (2018) and those estimated with an at-site analysis conducted on the SIAS dataset. The analyses provide a useful benchmark to verify the influence of the last two decades on the rainfall regime of this area.

2.2.3.1. Regional Depth Duration Frequency curves for Sicily

Constructing reliable DDF curves is impossible without a sufficiently extensive rainfall dataset. However, it can be difficult to find time series long enough to ensure a robust estimation of the distribution parameters. Furthermore, DDF curves are typically derived from measurements taken at a specific location (e.g., a rain gauge) and so they may not be

applicable to other sites without rainfall data. To address these issues, a regional analysis approach is often employed (Borga et al., 2005; Forestieri et al., 2018), which divides the study area into different levels of regionalization based on geographic and hydrological homogeneity. This hierarchical procedure is designed to capture the spatial variability of various parameter statistics and is calibrated using available data from the entire study region, even for ungauged areas or those sites that do not have long enough records.

For Sicily, the most up-to-date and valid regionalization analysis of heavy rainfall available is the one developed by Forestieri et al. (2018). This study used data recorded in the period 1928–2010 by the rain gauge network of the *Autorità di Bacino (AdB) del Distretto Idrografico della Sicilia* (i.e., *Basin Authority of the Sicilian River Basin District*), consisting of about 300 rain gauges uniformly distributed throughout the island. Specifically, the study started from a sub-division of the region into homogeneous zones through the selection of some supporting variables, such as meteo-climatic variables and site characteristics, followed by the identification of the probability distribution that best describes the precipitation quantiles for fixed duration, the analysis and modeling of the spatial variability of regional parameters, and, lastly, the creation of quantile maps for fixed return period and duration. In particular, the quantile expression is:

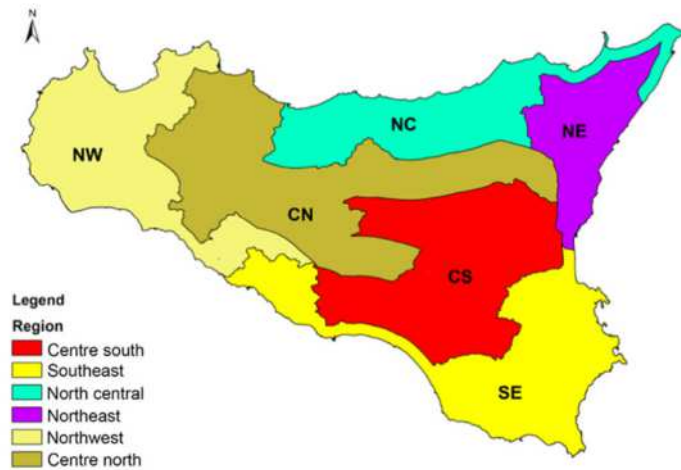
$$H_{i,r}(d, T) = \mu_i(d) \cdot h_r(d, T) \quad (2.8)$$

where $H_{i,r}(d, T)$ represents the precipitation quantile for a certain duration and return period related to the i^{th} location belonging to a homogeneous region r . Hereafter, this will be referred to as h_{reg} for the sake of simplicity. The term $\mu_i(d)$ in 2.8 represents a scale factor identified for fixed duration at each location of the region, and $h_r(d, T)$ indicates the regional growth curve, evaluated as a function of the return period and depending on the homogeneous zone where the area of interest falls. In Forestieri et al. (2018), Sicily is divided into six homogeneous regions (Figure 2.15a), which were obtained by means of a cluster analysis aiming to group areas characterized by similar precipitation features (e.g., the average annual maxima rainfall depth with duration d , or the mean annual number of dry days) together. To derive the growth curve, for each homogeneous region, different statistical distributions were fitted to the annual maxima, such as the three-parameter log-normal distribution (LN3), the generalized extreme value (GEV) distribution, and the two-component extreme value (TCEV) distribution. Among them, the TCEV provided higher accuracies. The scale factor, $\mu_i(d)$ was instead evaluated through a power-law, as follows:

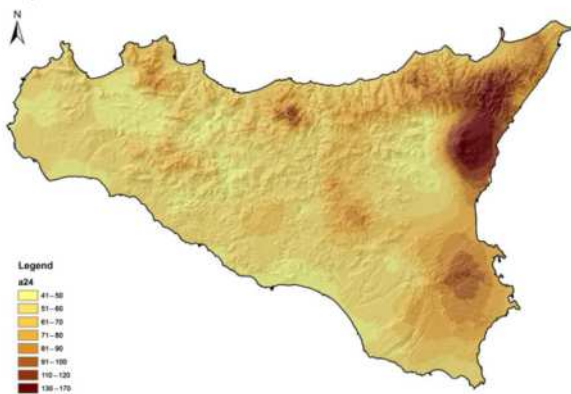
$$\mu_i(d) = a_{24} \cdot \left(\frac{d}{24}\right)^n \quad (2.9)$$

in which a_{24} and n are two parameters obtained by means of a linear regression between MAP and the median value of 24h extreme rainfall depth and n , respectively. The study provided a spatial distribution of these two parameters for the whole Sicily region (Figure 2.15b and c).

a)



b)



c)

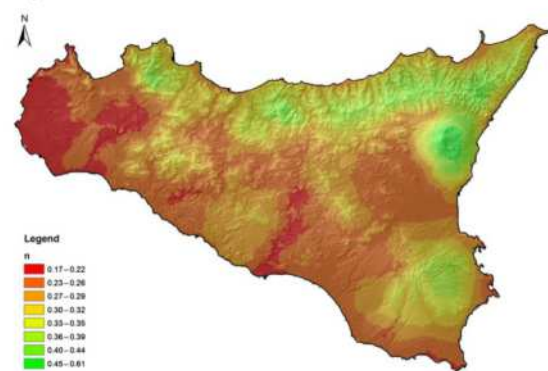


Figure 2.15: Homogeneous regions (a) and spatial distribution of values of the parameter a_{24} (b) and n (c) from Forestieri et al. (2018)

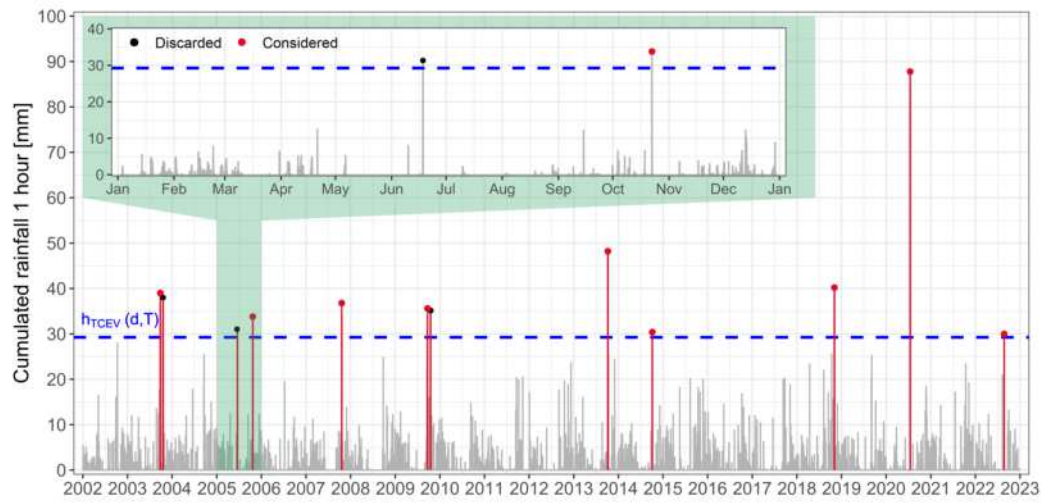
2.2.3.2. Regional Quantile Exceedance Detection

Original 10 min SIAS time series were initially aggregated by means of a rolling window, which moves in a 10 min step, with an amplitude equal to different reference durations (i.e., 1, 3, 6, 12, and 24 h), thus generating what from now on will be referred as aggregated data series. The station names and IDs are reported in Table A.2 (4th

column) in the Appendix A. After that, at the points where the SIAS gauges are located, regional rainfall quantiles (h_{reg}) were calculated according to the methodology developed by Forestieri et al. (2018). In particular, the TCEV distribution parameters have been used for the assessment of the regional growth curve, while the spatial distributions of a_{24} and n (Figure 2.15b and c) for the evaluation of the scale factor. The h_{reg} have been derived for the reference durations and the return periods of 5, 10, and 20 years. It was decided to consider a maximum return period of 20 years since SIAS data length is equal to 21 years, spanning the period from 2002 to 2022, which is not sufficient to apply a reliable probabilistic model for a return period greater than that.

Once the SIAS aggregated data series and the h_{reg} samples were available, it was possible to assess how many times the former exceeded the corresponding h_{reg} for each reference duration and return period. In order not to consider exceedances resulting from statistically dependent events of the aggregated data series, a selection criterion has been defined. In particular, two events of the aggregated data series are statistically independent if their interarrival time is at least 24 h. It is here noteworthy to highlight that such a condition might be too conservative for 1 h duration events. Many papers, indeed, agree on the fact that short-duration and high-intensity rainfall events can be associated with convective precipitation (Westra et al., 2014; Feloni et al., 2019; Treppiedi et al., 2023), which dissipates very quickly. Therefore, it is likely that more convective cells may develop in the surroundings of the rain gauge within 24 h, forming independent events. For this reason, considering interarrival times less than 24 h, it may be possible to achieve even more enhanced results (in terms of the number of exceedances of h_{reg}) at short durations. Another aspect that has been investigated is whether to consider more exceedances in the same year or to consider only the maximum exceedance. Since h_{reg} have been obtained from a set of annual maxima, thus from a sample composed of one single value per year, for a homogeneous comparison it has been imposed the condition that if more exceedances of h_{reg} occur in the same year, only the maximum value is considered. This basically corresponds to considering the exceedance of the SIAS annual maxima with respect to h_{reg} . This at-site comparison has been carried out for all the SIAS rain gauges to obtain a spatial representation of the number of h_{reg} exceedances.

The results of this procedure are depicted in Figure 2.16. The upper panel of this figure shows the at-site comparison between the aggregated data series of the SIAS rain gauge named “Palermo” and the h_{reg} relative to a 5-year return period and 1 h duration. Looking at the figure, it is possible to highlight that the h_{reg} (i.e., dashed blue line in the figure) was exceeded nine times. Within a 20-year time window and with reference to a 5-year return period, this value is more than double the expected exceedances relative to stationary conditions, which is equal to 4.



Exc. + 0 ● 1-2 ● 3-5 ● 6-8 ● 9-11 ● 12-14

Figure 2.16: At-site comparison between the hreg for the 1 h duration and the 5-year return period and the aggregated data series of the SIAS rain gauge named “Palermo” (upper panel) and spatial distribution of the number of exceedances for different durations (rows) and return periods (columns) over the entire region (lower panel)

Particularly, the focus on the events that occurred during 2005 in the upper panel shows that if two or more exceedances occur in the same year, only the greatest one, as compared to the h_{reg} , is considered. In the lower panel of Figure 2.16, the spatial distribution of the number of exceedances of the SIAS aggregated data series with respect to h_{reg} for different durations (rows) and return periods (columns) is shown. To different degrees, the outcomes described for the station of “Palermo” are also marked all over the region. With reference to the return period of 5 years (first column), almost all the gauges present an exceedance largely higher than that expected in 20 years, even reaching more than 12 in eastern Sicily. Although this result is remarkable for all the reference durations, it is evident how the number of exceedances is on average higher throughout the lowest durations (e.g., 1 and 3 h). For the 10-year return period, similar conclusions, although in a less evident way, can be drawn, keeping in mind that this time an average of two exceedances of the quantile is expected in the considered 20-year time window. Looking instead at the results related to the 20-year return period, fewer gauges show a few exceedances of h_{reg} higher than the expected, although this aspect is most likely due to the limited length of the SIAS annual maxima time series (i.e., 21 years from 2002 to 2022), as already stressed in the beginning of this section.

Once the number of h_{reg} exceedances is known, it was possible to compare it with the expected number of exceedances that is likely to occur under a stationary occurrence of the extremes. In other words, if Y is a random variable denoting the number of exceedances of a fixed rainfall depth in a n -year period, its Probability Density Function (PDF) is given by a binomial distribution as in the following:

$$P(Y = y) = \binom{n}{y} p^y (1 - p)^{n-y} \quad (2.10)$$

where p is the exceedance probability, which is equal to the inverse of return period $p = T^{-1}$. The PDF of the binomial distribution, which is valid only if the probability of more than one occurrence per year is null, provides the probability that y T-year events occur exactly in n successive years. Assuming $T = 5$, the mode value is 4 in a period of 20 years. The comparison between the PDFs of the binomial statistical distribution (i.e., histogram in blue) and of the number of h_{reg} 's exceedances (i.e., histogram in red) is shown in Figure 2.17, for the reference durations (rows) and return periods (columns). In each plot small panel representing the cumulative distribution functions for the binomial and the empirical distributions is also added, in order to make the comparison easier in terms of probabilities.

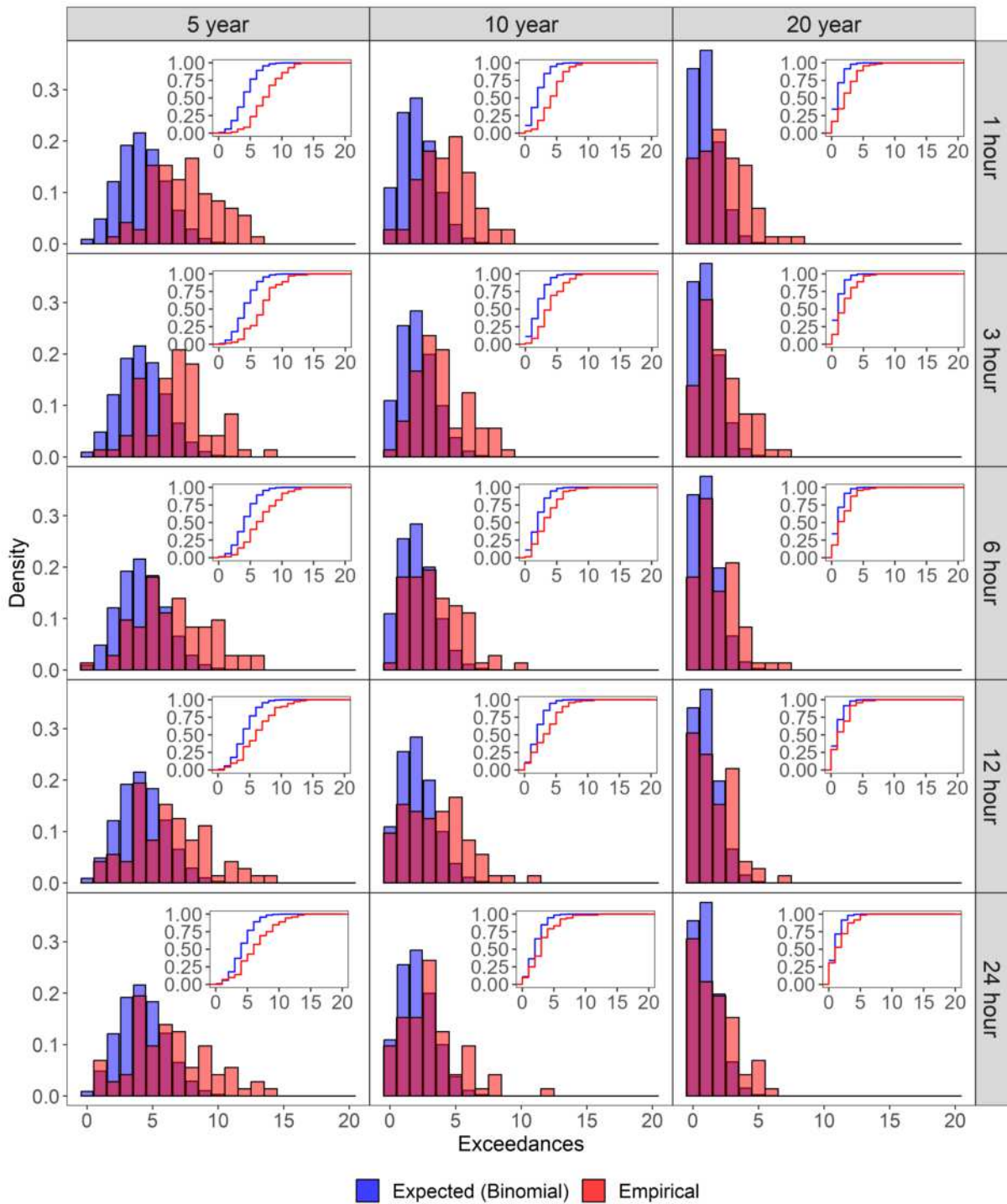


Figure 2.17: Probability density functions of the binomial statistical distribution, in blue, and of the number of h_{reg} exceedances, in red, for the reference durations (rows) and return periods (columns). The small panels represent the respective cumulative distribution function

From the comparison of the two PDFs, it can be observed that, especially at the lower durations and return periods, the peak (e.g., mode values) of the empirical distribution of the h_{reg} 's exceedances is shifted towards higher values of exceedances with respect to

the mode of the binomial distribution, while for longer durations these differences are less emphasized. To be clearer, considering a 5-year return period within a 20-year time window and under stationary conditions, the mode of the binomial distribution would correspond to 4 exceedances. However, at 1 and 3 h durations, for instance, the peaks of the empirical distribution are, respectively, 6 and 7 exceedances. This means that, over the whole region, for these durations and return period, the SIAS aggregated data series tend to exceed more than expected the corresponding h_{reg} .

2.2.3.3. Revision of the return periods defined with the regional approach

Given that the previous analysis resulted in a number of exceedances of the h_{reg} remarkably higher than the expected value, especially at the lower durations and return periods, a spontaneous question arises: how can these results be translated in terms of changes in the return period of extreme events?

To do this, rainfall annual maxima for the reference durations in the period 2002–2022 have been extracted from the SIAS aggregated data series. Then, for each rain gauge, the Gumbel (Extreme value type I—EV1) distribution (Gumbel, 1941) has been fitted to the annual maxima sample. The Cumulative Distribution Function (CDF) of the EV1 has the following formulation:

$$F(h) = \exp\left(-\exp\left(-\frac{h_T - \nu}{\alpha}\right)\right) \quad (2.11)$$

where α and ν are the location and scale parameters, respectively. The EV1, which is a statistical distribution function simpler than those used by Forestieri et al. (2018), has been applied here due to the limited sample size (i.e., 21 values).

The goodness of fitting for the EV1 to the SIAS annual maxima has been verified by means of the Kolmogorov–Smirnov (K–S) test (Massey Jr, 1951), using the one sample version. The null hypothesis affirms that the sample data is drawn from the specified distribution. The test identifies the maximum difference between the empirical and the theoretical CDFs and rejects the null hypothesis if this is greater than a critical value, which depends on the significance level (typically 0.05) and the number of data points of the empirical CDF. Alternatively, it calculates a p -value as a function of the maximum vertical difference between the empirical and the theoretical CDFs and compares it with the chosen significance level. The null hypothesis is rejected if the p -value is less than the significance level, and in this situation the sample data is not drawn from the specified distribution. If the p -value is greater than the significance level, the null hypothesis cannot

be rejected; thus the sample data is drawn from the selected distribution. Figure 2.18 shows, for the reference durations, the spatial distribution of the p -value resulting from the application of the K–S test with a significance level of 0.05. As it is possible to note, this resulted in an overall good fitting of the distribution function to the annual maxima. In particular, it can be inferred that for most of the stations it is not possible to reject, with a sufficient degree of significance, the null hypothesis, according to which the data sample belongs to the theoretical distribution used. The high p -values achieved all over the region made it possible to use the Gumbel distribution to estimate theoretical rainfall quantiles from the SIAS annual maxima.

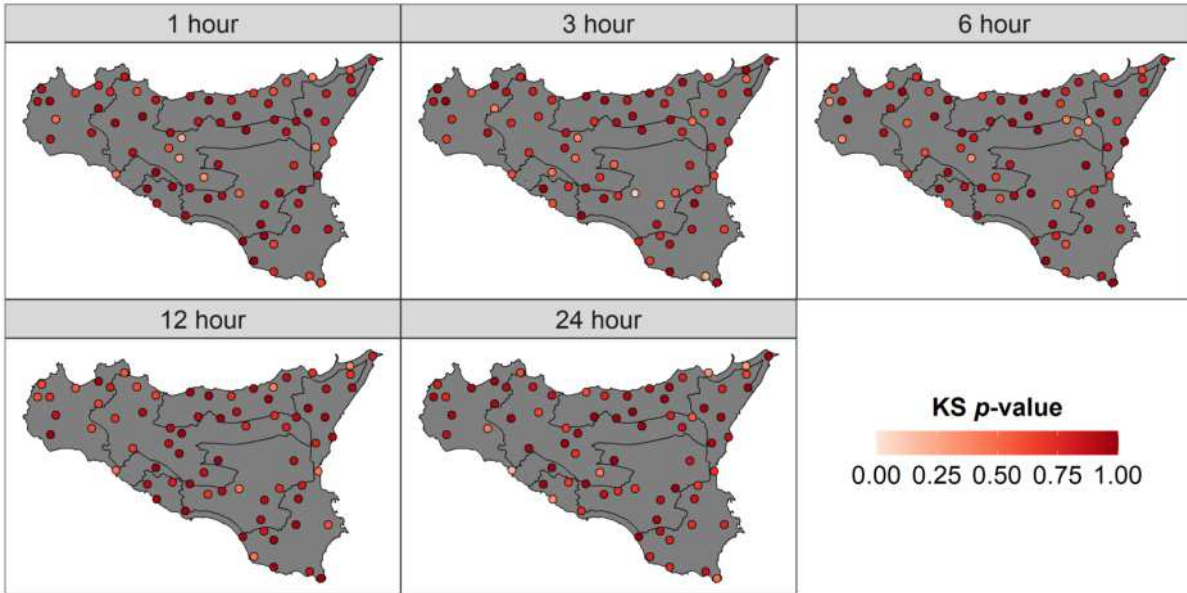


Figure 2.18: Spatial distribution of p -value for the K–S test for the reference durations. High p -values indicate greater significance in not rejecting the null hypothesis that the sample belongs to the theoretical EV1 distribution

Given the generally positive outcome from the K–S test, we could fit the Gumbel distribution to the SIAS annual maxima. Rainfall quantiles have been extracted for reference durations and the return periods of 5, 10, and 20 years as:

$$h(d, T) = b(d) - a(d) \cdot \ln \left(\ln \left(\frac{T}{T-1} \right) \right) \quad (2.12)$$

where $a(d)$ and $b(d)$ represent the parameters of the statistical distribution function estimated by means of the Maximum Likelihood Estimation (MLE) at each considered duration and T represents the return period. Since the fitting of the EV1 distribution has been carried out separately for each rain gauge, 72 values of the $a(d)$ and $b(d)$ parameters for each reference duration have been computed, which allowed to obtain the precipitation

quantiles for the three selected return periods and the reference durations. For the sake of simplicity, hereafter $h(d, T)$ computed from the SIAS annual maxima are indicated as h_{SIAS} .

Hence, a comparison between the two sets of return periods associated to the regional and the SIAS quantiles (i.e., h_{reg} and h_{SIAS} , respectively) has been carried out. In other words, the return period of h_{reg} (i.e., the imposed 5, 10, or 20 years for which h_{reg} is derived), which can be called T_{reg} , has been compared with the return period, derived by inverting equation 2.12 and imposing $h(d, T)=h_{reg}$, here referred to as T_{SIAS} . Given that the parameters of the EV1 distribution (i.e., $a(d)$ and $b(d)$) are calculated with the SIAS annual maxima, which refer just to the last two decades (i.e., from 2002 to 2022), such a comparison makes it possible to highlight if rainfall events characterized by a certain T_{reg} , expressed with reference to data mainly recorded in the last century (i.e., from 1928 to 2010), have been occurring more (or less) frequently in the last twenty years.

Pooling the T_{SIAS} achieved for all the 72 gauges, we derived the corresponding empirical distribution functions for all the reference durations and the three T_{reg} values. Considering that under the stationary condition of extremes occurrence, the mode of the empirical distribution functions of T_{SIAS} should match the corresponding T_{reg} , any difference between them can be considered as the result of a different frequency of occurrence of events. In other words, if precipitation extremes have become more frequent in recent decades in the Mediterranean area, as many studies affirm (Varouchakis et al., 2018; Noto et al., 2023a), potentially as a climate change effect, it is to be expected that their return period (i.e., the mode of T_{SIAS} statistical distribution) is lower than T_{reg} . Figure 2.19 shows the empirical distribution functions of the T_{SIAS} . The results highlight that, especially for the shortest durations and lower return periods, the peaks of these distributions are sharply shifted toward lower return periods than those expected with the regional approach by Forestieri et al. (2018). With reference to the last century, in the last 20 years the greatest proportion of events characterized by a T_{reg} of 5 years occurred more frequently and, consequently, are characterized by a lower return period (i.e., the greatest part of the empirical density distribution falls before the 5-year return period). This result is less evident as the return period increases, since it is most likely affected by the limited length of the SIAS annual maxima series (i.e., 21 years from 2002 to 2022).

Figure 2.20 shows a spatial representation of what is reported in Figure 2.19. For all the reference durations and return periods, the new return periods of the h_{reg} calculated with the Gumbel distribution fitted to the SIAS annual maxima (i.e., T_{SIAS}) are shown in correspondence with each of the SIAS rain gauges. Looking at Figure 2.20, it is possible to note that, especially at low durations and for the 5-year return period, almost all the gauges show a return period lower than the expected value of 5 years, which is indicated

with the red color on the map.

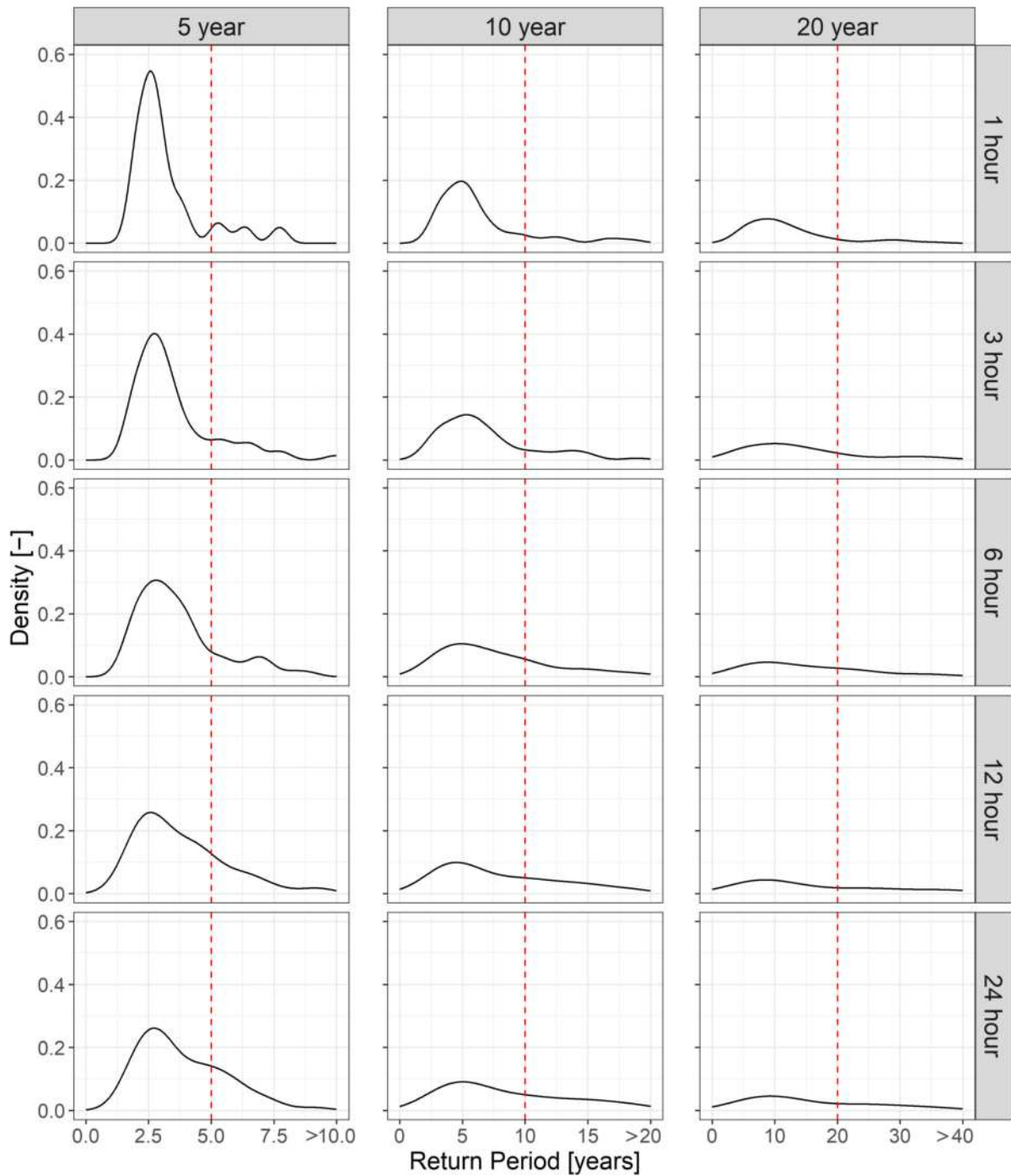


Figure 2.19: Empirical density distribution of the T_{SIAS} of all 72 considered SIAS rain gauges, compared to the corresponding T_{reg} (red dashed line). Results are expressed for all the reference durations (rows) and the return periods of 5, 10, and 20 years (columns)

This aspect is increasingly being missed as the duration increases. When the return period increases, a similar behavior is less noticeable, although this aspect, as previously

specified, most likely depends on the limited length of the SIAS annual maxima series.



Figure 2.20: Spatial representations of the T_{SIAS} for the 72 considered SIAS rain gauges. Results are expressed for all reference durations (rows) and the T_{reg} of 5, 10, and 20 years (columns)

Looking at the spatial distribution of these values, the return periods lower than the expected one (i.e., $T_{SIAS} < T_{reg}$) are almost everywhere for the shorter durations and the

lower return periods, while they tend to be more localized along the coasts and especially in the southeastern part of the region as the duration and the return period gradually increase. These results agree with those of several recent studies on the intensification of extreme precipitation in the Mediterranean area, especially for the short durations, i.e., hourly and sub-hourly (Arnone et al., 2013; Treppiedi et al., 2021). This could be potentially linked to global warming, as the increase in surface and atmospheric temperature, as well as the frequency of heatwaves, may cause a change in the Clausius–Clapeyron relationship (Pumo et al., 2019). Indeed, increased temperature enables the air to retain a greater amount of water vapor, consequently leading to the atmosphere becoming more unstable, favoring increasingly frequent intense and short-lived convective phenomena.

What has been obtained should raise awareness of the need to consider the non-stationarity of the return period in the design of hydraulic works or other purposes related to the hydrological and geological risk. Future research in this area will be crucial for improving the performance of water management and hydro-logical risk detection in a climate change context, especially considering the not reassuring predictions about the occurrence of extremes in the future.

2.2.4. Convective or stratiform? A partitioning algorithm to separate the rainfall regimes

Up to now, this chapter mainly focus on changes in the characteristics of the rainfall regime in Sicily. Sections 2.2.2 and 2.2.3 have revealed a clear increase in intense precipitation associated with higher quantiles and shorter durations. However, it is appropriate to inquire about the physical mechanism underlying these intense - short-duration phenomena and whether, as hydrologists, we can recognize and study it.

As expressed in section 1.2, the Clausius-Clapeyron relationship is the key equation that allows to correlate the amount of water vapor holds by the atmosphere with temperature. In other words, the water-holding capacity of the atmosphere increases by approximately 6–7% for every 1°C rise in temperature, meaning that, the higher the air temperature, the higher the probability of having a water content sufficient to generate a more or less significant precipitation event. Despite other mechanisms contribute to the generation of extreme precipitation events, it has also been show as intense hourly and sub-hourly rainfall can be characterized by higher rate of the apparent CC scaling (Lenderink et al., 2017; Fowler et al., 2021). In this context, since event duration and intensity are strictly related to the mechanisms that generate the precipitation, a topic that has often been a source of interest is the one related to the classification of precipitation into stratiform and convective components (Tremblay, 2005; Ruiz-Leo et al., 2013; Feloni et al., 2019; Cipolla et al., 2020) and, consequently, to the identification of convective events (Tremblay, 2005; Feloni et al., 2019; Sottile et al., 2022) and the detection of any trend in their characteristics (Rulfová et al., 2014; Llasat et al., 2021). At the spatial scale starting from the radar echoes, Houze Jr (1997) defines the convective regime as the precipitation associated with young and active atmospheric convection. In this condition, the strong updraft that condenses a large amount of water in the air generates cumulus and cumulonimbus clouds and the related precipitation is generally characterized by short-duration and high-intensity (Llasat, 2001; Berg et al., 2013; Westra et al., 2014). On the other hand, stratiform precipitation occurs in a different atmospheric condition, namely when the convection is weak and the air motions are lower, thus producing precipitation events with opposite characteristics to the previous. Although the physical mechanisms that generate convective and stratiform precipitation have been widely discussed in the past, separating the two regimes is not trivial. Indeed, the convective and stratiform

Adapted from: Treppiedi, D., Cipolla, G., and Noto, L. V. (2023), ‘Convective precipitation over a mediterranean area: From identification to trend analysis starting from high-resolution rain gauges data’, *International Journal of Climatology* 41(13), 5938–5955

precipitation could occur separately or as a part of the same complex of clouds, not allowing a net distinction between the regimes (Houze Jr, 1997; Tremblay, 2005; Rulfová and Kyselý, 2013; Kyselý et al., 2016).

Nevertheless, over the years the issue of a correct distinction between precipitation in convective and stratiform components has been carried out from different points of view. The first attempts to deal with such a separation were mostly concerned with the spatial aspect of the problem, i.e., to distinguish between convective and stratiform regions using weather radar imagery or remote sensing techniques (Steiner et al., 1995; Reudenbach et al., 2001; Rigo and Llasat, 2004; Sandford et al., 2017).

Concerning the distinction of precipitation regimes on the base of ground observations, Tremblay (2005) analyzed precipitation data of about 3500 rain gauges collected by the World Meteorological Organization (WMO) at the global scale, setting up an algorithm for the classification of convective and stratiform precipitation components. The study revealed that the relationship between cumulative precipitation and its intensity can be described by a negative exponential law, independently from the period under study and the time step used to cumulate the raw rainfall data. Starting from this finding, Tremblay (2005) based the classification of the total precipitation into convective and stratiform components by assuming that the exponential curve corresponds with the stratiform component, while the difference between the total precipitation and exponential curves provides the convective component; moreover, the author define a rainfall intensity threshold to classify, at the gauge scale, as convective (stratiform) all the events with an intensity higher (lower) than that threshold. Ruiz-Leo et al. (2013) applied a similar algorithm to the 6-hour rainfall data recorded from 1998 to 2008 by twelve rain gauges located on the north-eastern Mediterranean coast of Spain. The authors confirmed the above-mentioned assumption of Tremblay (2005), namely that an exponential distribution is observed when the total rainfall depth is represented versus the rainfall intensity. Considering both the annual and the seasonal convective precipitation, the application of a trend analysis reveals a significant increase in such a variable in the autumn. Feloni et al. (2019) applied the same approach presented in Tremblay (2005) to 6-hour rainfall time series of thirty-two rain gauges in the Attica region (Greece), obtained by aggregating the original 10-minute rainfall time series in the period 2005-2015. The authors identified the critical intensity thresholds for each year under study, to detect the convective events and evaluate the annual fraction of convective rainfall. Moreover, results were validated using some indices representative mainly of the convective component, such as the lightning activity, which is very common in presence of cumulonimbus clouds that generate convective events. The validation procedure highlights how the separation algorithm is characterized by high performance in classifying the correct type of precipitation, thus

providing a useful tool to identify convective rainfall in gauged sites. Starting from the rainfall annual maxima at fixed durations (1, 3, 6, 12, and 24 hours) for Sicily (Italy), Cipolla et al. (2020) developed a criterion to classify annual maxima between convective and stratiform, also taking into account a third class containing mixed/unresolved events, by means of two reanalysis indexes, namely the Convective Available Potential Energy (CAPE) and the Vertical Integral of Divergence of Moisture Flux (VIDMF) retrieved by the ERA-Interim archive. The authors found that, in general, at 1-hour duration, the percentage of convective events predominates in the other classes of events mainly in the summer season, while the percentage of stratiform tends to increase at 24-hour duration during the winter period. The significant percentage of mixed/unresolved annual maxima, which is recognized at all durations, highlights the presence of many rainfall events which could be classified as both convective and stratiform events or do not show a sufficiently clear distinction between the two classes. In this section, starting from the SIAS (Servizio Informativo Agrometeorologico Siciliano) database for Sicily in the period 2002-2020 (see 5th column of Table A.2 in the Appendix A), 20-minute precipitation time series have been created from the original rainfall time series and then used to (i) separate the convective and the stratiform precipitation at a 5-day scale according to the framework proposed by Tremblay (2005), (ii) determine a critical threshold able to identify the predominant convective events at at-site scale in the whole period under study and, (iii) investigate the spatial pattern relative to the occurrence and the percentage of convective events and their possible trend.

2.2.4.1. The partitioning framework

The framework used to separate the stratiform and the convective component of precipitation on a monthly scale, proposed by Tremblay (2005), involves different steps. The first one consists of defining an empirical total precipitation distribution, $P_T(I)$, considering a specific average time interval $\Delta\tau$. Then, a negative exponential curve is fitted to model the stratiform precipitation component, $P_S(I)$. The convective component, $P_C(I)$ is therefore defined by the difference between the total precipitation and the stratiform components. A detailed explanation of this procedure can be found in the following paragraphs.

The total precipitation distribution. Starting from the data manipulation, the original 10-minute rainfall time-series have been aggregated to the 20-minute resolution by dividing the whole period into not overlapping 20-minute intervals and cumulating the rainfall depth within them; in this way, the amount of rainfall that occurred in

20 minutes, namely an average intensity of precipitation (e.g., $\text{mm}\cdot 20\text{min}^{-1}$) has been derived. Compared to the original 10-minute resolution, the choice of 20-minute time resolution increases the probability that single-cell thunderstorms peaks are included in a single interval since individual cell life cycle is generally between 30 and 60 minutes (<https://www.nssl.noaa.gov/education/svrwx101/thunderstorms/types/>). At the same time, the high resolution of the available dataset is maintained, being a novelty compared to the previous studies (Tremblay, 2005; Ruiz-Leo et al., 2013; Feloni et al., 2019), in which time-series have been used with a frequency of 6 hours. Indeed, while considering 6-hour intervals could be a good compromise when convective and stratiform contributions are analyzed at a global scale, such as in Tremblay (2005), it is necessary to use finer resolution when the studied area is limited, such as in the case of Sicily. There is also evidence that convective precipitation can develop in time intervals significantly shorter than six hours (Llasat, 2001; Hardwick Jones et al., 2010; Berg et al., 2013).

As mentioned before, obtaining the empirical total precipitation distribution is essential to distinguish the stratiform component and, consequently, also the convective one. To derive the monthly $P_T(I)$, a pre-processing procedure is required.

The first step aims to remove the dependency of the data on the location of the rain gauges, the separation between the two regimes takes place on a spatial scale defined by the available ground observations. For example, Tremblay (2005) applied the algorithm on a global scale, while the goal of this study is to work at a higher spatial resolution, defined over Sicily. Nevertheless, our study area is larger than the one used by Ruiz-Leo et al. (2013) (i.e., a part of the Spanish Mediterranean coast and the Balearic Island) and Feloni et al. (2019) (i.e., the Attica peninsula). To move from an at-site to a regional scale, the data recorded by all the gauges in the same 20-minute interval (i.e., corresponding with Δt) needs to be gathered on the base of their rainfall intensity. With this purpose, an intensity bin size, namely ΔI , is used to define a certain number of intensity classes, obtained by dividing the intensity range of variability by ΔI . Hence, the empirical total precipitation distribution $P_T(I)$ for the considered time interval Δt is obtained by grouping and cumulating the rainfall data according to the intensity class to which they belong. More specifically, the latter $P_T(I)$ describes how the total rainfall depth is distributed with the intensity, in a specific Δt . It is important to specify that such a distribution is derived for the region under study as a whole as previously stated (e.g., no spatial information is included in the empirical total precipitation distribution $P_T(I)$).

Before applying the partitioning algorithm, it is necessary to choose an average time interval, $\Delta \tau$, to which the analysis is referred. The first way may consist in considering a $\Delta \tau$ equal to the time-series resolution Δt , such as in Tremblay (2005), thus providing

four empirical distributions per day for further partitioning ($\Delta t = \Delta \tau = 6$ hours). On the other hand, it is possible to choose $\Delta \tau > \Delta t$, such as the year (Ruiz-Leo et al., 2013; Feloni et al., 2019), or a 5-day scale here proposed. More specifically, 30-day months are divided into 6 identical intervals, while the last one contains i) one day more in the case of 31-day months or ii) two days less in the case of February (or one day less for the leap years). This kind of subdivision has been preferred to a constant 5-day window so that each interval falls within a specific month, and therefore it allows for analyzing the monthly behavior of the considered variables. To obtain the 5-day empirical $P_T(I)$, it is necessary to select all the 20-minute distributions within the considered $\Delta \tau$ (i.e., 5 days in our case) and aggregate them at the same intensity classes. Through this aggregation procedure, the number of distributions per year is reduced from 26,280 (e.g., 72 distributions per day for a total of 365 days) to 72 (e.g., six per month).

The partitioning algorithm. According to Tremblay (2005), an exponential structure can be always detected by looking at total precipitation distributions, regardless of the $\Delta \tau$. Indeed, the total precipitation depth tends to decrease exponentially as the rainfall intensity class increases. From a statistical point of view, this is mainly connected to the relationship between the probability of occurrence of the rainfall events and their related severity. Indeed, the total volume of rain associated with events that occur frequently with lower intensities is probably higher compared to the one connected to a single very intense event. As explained by Tremblay (2005), this is a consequence of the fact that the rainfall intensity strictly depends on the residence time of particles in the clouds and, in turn, the probability of observing a certain residence time can be modelled with an inverse exponential distribution. Moreover, Tremblay (2005) has shown that this exponential structure mainly prevails in correspondence of classes with lower intensity, while the total precipitation distribution generally exhibits an irregular behavior for the higher intensities, as if some local peaks are superimposed to an exponential curve. Since it is realistic to assume that in these anomalies the convective component is significant, especially when the intensity of rainfall is relevant, it is possible to associate the exponential structure to the stratiform component and the anomalies with the convective one.

Starting from the previous considerations, for a certain $\Delta \tau$, the convective component of the precipitation can be obtained by subtracting a pure exponential curve from the total precipitation one:

$$P_C(I) = P_T(I) - P_S(I) = P_T(I) - a \cdot e^{-bI} \quad (2.13)$$

where $P_T(I)$ is the total precipitation distribution, $P_C(I)$ and $P_S(I)$ are the convective and the stratiform component, respectively, while a and b are the parameters needed to

model the latter. Since the above-mentioned distributions have been defined as time scale dependent, it is worth highlighting that each term in equation 2.13 is a function of the $\Delta\tau$ fixed. For the 5-day scale approach, 72 couple of parameters (namely a and b) must be derived per year.

Since mathematical modeling cannot be separated from the physical phenomenon, these parameters need to be estimated after defining a series of constraints. Indeed, a stratiform component greater than the total precipitation would result in a negative convective component, which has no physical meaning. For this reason, the curve should pass through the relative minima of $P_T(I)$ or, when it is not possible, it must be fixed equal to $P_T(I)$, meaning that there is no convective contribution in the considered intensity class.

Model dependencies. Before delving into the results, it is useful to focus the attention on some dependencies of the partitioning algorithm. The ability of the model to differentiate between the stratiform and the convective component of the precipitation depends not only on the ΔI , as highlighted by Ruiz-Leo et al. (2013) and Feloni et al. (2019), as well as the sample size and the $\Delta\tau$ as originally pointed out by Tremblay (2005).

Since ΔI represents the resolution required to describe the total precipitation distribution, a greater intensity bin size may result in an excessively smooth curve, thus reducing the accuracy of the algorithm in identifying convective rainfall. On the contrary, even if one may think that the smaller this value, the greater the capability of the algorithm to separate the two regimes, and since the exponential curve is forced to pass through the minima of $P_T(I)$, an excessive number of local peaks or anomalies following Tremblay (2005) could lead to an overestimation of the convective component. To overcome this issue, Ruiz-Leo et al. (2013) proposed a criterion useful to choose ΔI according to a parameter, derived from the standard deviation of precipitation intensity and the number of no-null precipitation data for all the gauges considered. Nevertheless, this empirical method for choosing ΔI has been probably calibrated for the annual $\Delta\tau$, leading to unrealistic results in the case of lower $\Delta\tau$. This is especially true for the driest months, in which the standard deviation is high and the resulting ΔI is excessively wide to separate the regimes. Since in this work a high-resolution dataset is used, four different values of ΔI have been tested. In particular, it has been fixed equal to 0.6, 1, 1.4, and 1.8 mm·20min⁻¹ and then applied to discretize the total precipitation distribution $P_T(I)$ for each 5-day interval.

Another parameter that influences the algorithm is the $\Delta\tau$. In particular, Tremblay (2005) proved that, for fixed sample numerosity, the greater the $\Delta\tau$ (e.g., 6 hours, 1 day, 1 month, 1 year), the smoother the total precipitation distribution $P_T(I)$, tending

to a perfect exponential distribution. From a statistical point of view, this evidence is explained by the fact that a higher $\Delta\tau$ value implies that a greater number of events are aggregated in each intensity class and, at the same time, that it is likely that low-intensity events occur more frequently than high-intensity ones.

The opposite effect could be reached by considering, for a fixed $\Delta\tau$, a lower sample size. This could occur if data are aggregated using a higher time window (e.g., using the 1-hour or 6-hour time resolution to obtain the hourly or the hexa-hourly rainfall time-series, instead of the 20-minute resolution) or even if a decreasing number of stations is available. As an example, Ruiz-Leo et al. (2013) and Feloni et al. (2019) were forced to choose the annual $\Delta\tau$ because of the small number of rain gauges involved (i.e., 12 and 11 on average, respectively) even if the authors do not explicitly mention this aspect in their works, while, on the opposite Tremblay (2005) was able to apply the algorithm for a 6-hour $\Delta\tau$ because of availability of a global rain gauges network. For this reason, the 5-day $\Delta\tau$ can be considered as a good trade-off between sample size and average time interval in the case of this work, as indicated from the analysis over different time averaged periods conducted by Tremblay (2005). Indeed, the use of a higher $\Delta\tau$ (e.g., the month) could result in excessive smooth empirical total precipitation distribution $P_T(I)$, while choosing a lower $\Delta\tau$ (e.g., the day) could lead to an opposite behavior and to a higher probability of not having rainfall depth within the fixed $\Delta\tau$, particularly during the driest months.

Detection of convective events. As previously mentioned, the spatial information of the precipitation is lost during the derivation of the empirical total precipitation distribution, $P_T(I)$, and the consequent partitioning technique. Indeed, since the separation between the convective and the stratiform regimes is carried out at the regional scale, it does not allow to identify for each rain gauge those events characterized by the predominance of the convective component. To overcome this limit and pass from a regional to an at-site classification of the two components, Tremblay (2005) introduced a critical intensity threshold (hereinafter I_{cr}), representing the value of intensity from which the convective component begins prevailing on the stratiform one. In other words, starting from the results of the separation for the fixed $\Delta\tau$ the I_{cr} threshold splits the intensity domain into two parts: a first part where the stratiform prevails on the convective component for $I < I_{cr}$, and a second one where the convective is predominant for $I > I_{cr}$. Consequently, I_{cr} is defined as the first intensity value that ensures:

$$P_C(I_{cr}) > P_S(I_{cr}) \quad (2.14)$$

As pointed out by Ruiz-Leo et al. (2013), this criterion could lead to an important

underestimation of the threshold, mainly because $P_C(I)$ could be locally greater than $P_S(I)$ for lower values of intensity, due to the exponential fitting. Therefore, this criterion has been subsequently modified by Ruiz-Leo et al. (2013) and Feloni et al. (2019). In particular, Ruiz-Leo et al. (2013) suggested that this threshold should be fixed when the convective component represents 60% of the total cumulative precipitation since Houze Jr (2014) found that this percentage can be considered a characteristic of the convective rainfall in a Mesoscale Convective System (MCS). Nevertheless, it has been noticed that in Europe these organized complexes of cumulonimbus are characterized by different features (e.g., size and duration) compared to other parts of the world (Rigo and Llasat, 2007; Kolios and Feidas, 2010; Michaelides et al., 2018) and are mainly continental (Morel and Senesi, 2002; Kolios and Feidas, 2010), suggesting that also other types of a thunderstorm (e.g., single- and multi-cell storms) need to be considered in deriving I_{cr} for Sicily. Feloni et al. (2019), instead, shifted the previous threshold from 60% to 50% of the total cumulative precipitation.

Nevertheless, considering cumulative convective precipitation among the intensity classes may misrepresent the results of the separation algorithm, since the convective and the stratiform amount of rainfall strictly depends on the intensity class to which they belong, as shown in equation 2.13. Moreover, the convective rainfall corresponding to higher intensity is certainly associated with a different atmospheric mechanism than the one related to lower intensity values. For such reasons, a different method for obtaining I_{cr} is proposed in this paper. In particular, it has been noticed that the median value of the percentage of convective rainfall for a certain month and intensity increases as the intensity values increase, as a result of the partitioning procedure. Therefore, it is possible to set the monthly I_{cr} as the first intensity from which the median percentage of convective exceeds a certain value, which would mark it out as predominant on the stratiform regime (e.g., 50% or 75% whose effects are assessed in the next section).

2.2.4.2. Data pre-processing and total precipitation distribution

The pre-processing of data, as described in the previous section, is fundamental to derive the empirical total precipitation distribution $P_T(I)$. In particular, the 20-minute rainfall intensity time series of all the gauges have been combined and gathered in rainfall intensity classes, whose width ΔI has been fixed in 0.6, 1, 1.4, and 1.8 mm·20min⁻¹. As an example, Figure 2.21 shows a comparison between the cumulative precipitation heatmap (i.e., a 2-D matrix where the magnitude of the variable of interest in each cell is represented through a color scale) for a) February and b) September of the year 2006, considering 1) $\Delta I=0.6$ mm·20min⁻¹ and 3) $\Delta I=1.8$ mm·20min⁻¹, which are the upper and

lower bounds of the interval analyzed. Considering a generic 20-minute time interval (on the x-axis), for each intensity class (on the y-axis), the colors from red to blue represent the total precipitation recorded by all the rain gauges within that class. The black color, instead, is used to mark those time intervals in which no events in the intensity class have been recorded. The sub-panels inside each heatmap provide a zoom of a specific day (i.e., 23rd February 2006 and 15th September 2006) for 2) $\Delta I=0.6 \text{ mm}\cdot 20\text{min}^{-1}$ and 4) $\Delta I=1.8 \text{ mm}\cdot 20\text{min}^{-1}$. Panel c) and d), instead, show the 20-minute total precipitation distribution for two dates (i.e., black color for 15:00 of the 15th of September 2006 and red color for 17:00 of the 23rd of February 2006) related to $\Delta I=0.6 \text{ mm}\cdot 20\text{min}^{-1}$ and $\Delta I=1.8 \text{ mm}\cdot 20\text{min}^{-1}$, respectively, while the gray dashed line is the perfect agreement line. In other words, the black and red curves are representative of two columns of the above heatmaps, and the single rainfall events lying on the perfect agreement line are characterized by the same value of intensity and cumulative precipitation. For both months and especially at the lower ΔI (panels a1 and b1), three different regions can be identified as a function of intensity; indeed, focusing on the lower intensity, it is possible to notice that the blue prevails on the other colors and even on the black, meaning that the total precipitation is generally low but, at the same time, it is more frequent across the month. As a result of the heatmap definition procedure, these total precipitation values consider a high number of very low intensity events that are recorded in the entire region during the month. As the intensity increases, the total precipitation assumes greater values but with a lower occurrence frequency, thus defining an intermediate region where the yellow color is noticeable, especially in some spikes, representing those temporal intervals in which the whole region was interested in more severe rainfall events. Finally, in the zone characterized by the higher values of intensity, the rainfall events are particularly rare, and black becomes the main color (i.e., no-occurrence). Moreover, these events are generally due to single high-intensity precipitation, as it is visible also in panel c) and d), and they are probably dominated by a convective component. It is also important to highlight that these kind of spikes in the heatmaps are more frequent in September rather than in February, as featured by the daily enlargements. From a physical point of view, this is probably caused by the different climatic conditions in these two months, which implies that a seasonality in the occurrence of convective/stratiform events needs to be analyzed.

The effect of the selection of a wider ΔI is evident moving from panel 1) to panel 3) for both months. Indeed, with a higher ΔI , the resolution of the heatmap worsen, even if the global appearance is maintained. Moreover, as a result of a wider intensity class, the maximum total precipitation is likely not to be found in the higher intensity classes, as it is possible to notice in the daily zooms and, contemporary, in panels c)

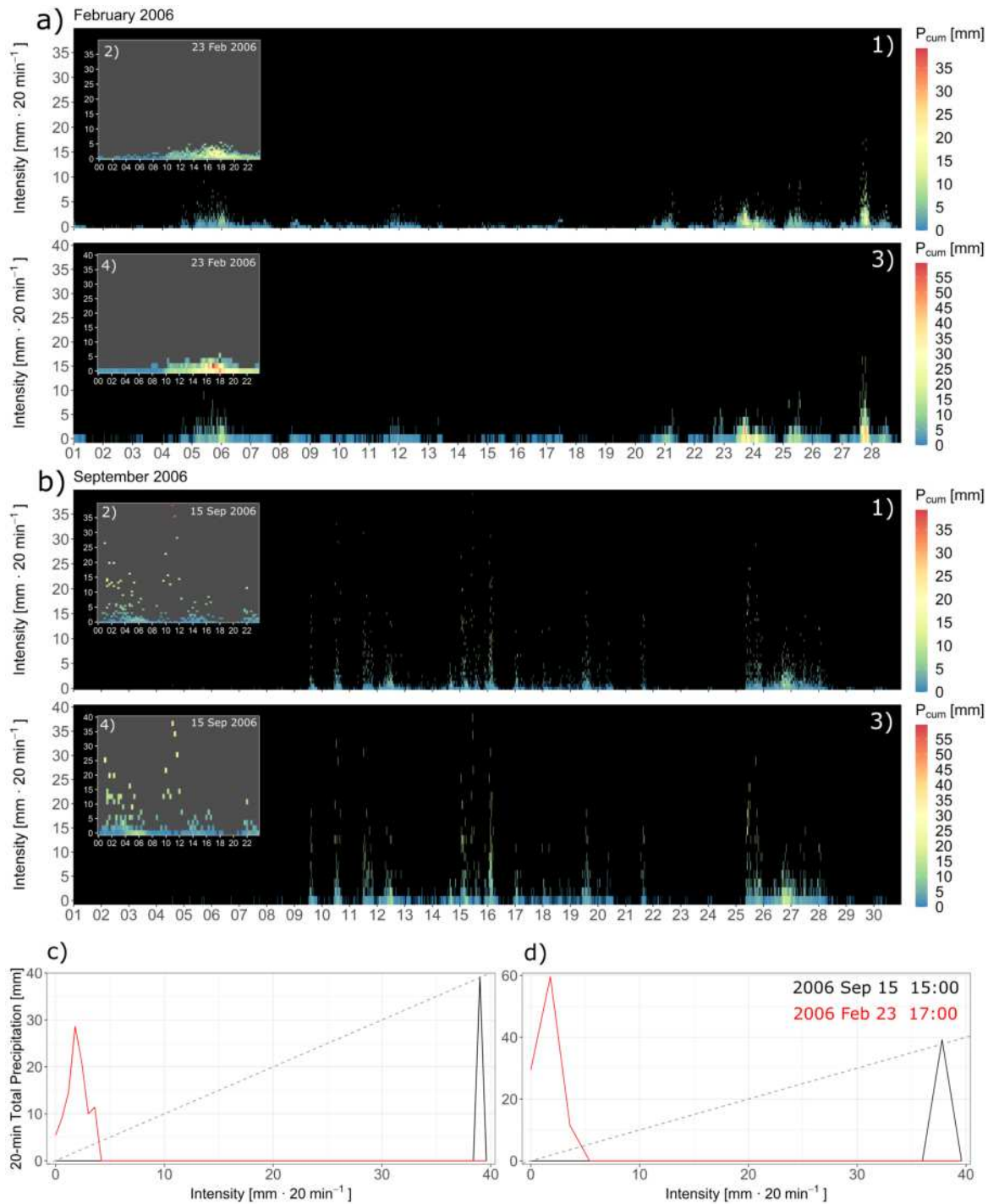


Figure 2.21: Precipitation intensity heatmap for a) February and b) September of the year 2006 at 1) $\Delta I = 0.6 \text{ mm} \cdot 20 \text{min}^{-1}$ and 3) $\Delta I = 1.8 \text{ mm} \cdot 20 \text{min}^{-1}$. The colorbar indicates the total precipitation values, while black color indicates no rainfall records. The sub-panels inside each heatmap provide a zoom for 23rd Feb. 2006 and 15th Sep. 2006 for 2) $\Delta I = 0.6 \text{ mm} \cdot 20 \text{min}^{-1}$ and 4) $\Delta I = 1.8 \text{ mm} \cdot 20 \text{min}^{-1}$. The 20-minute precipitation distribution related to the 15:00 of the 15th Sep. 2006 (black curve) and to the 17:00 of the 23rd Feb. 2006 (red curve) are depicted for c) $\Delta I = 0.6 \text{ mm} \cdot 20 \text{min}^{-1}$ and d) $\Delta I = 1.8 \text{ mm} \cdot 20 \text{min}^{-1}$

and d). Indeed, while for $\Delta I=0.6 \text{ mm}\cdot 20\text{min}^{-1}$ the maximum value (i.e., about 40 mm) occurs in mid-September with an intensity equal to $40 \text{ mm}\cdot 20\text{min}^{-1}$, the highest total precipitation for $\Delta I=1.8 \text{ mm}\cdot 20\text{min}^{-1}$ (i.e., about 60 mm) occurs the 23rd of February with an intensity value of $3.6 \text{ mm}\cdot 20\text{min}^{-1}$. As depicted in panels c) and d), this aspect is strictly connected to the ΔI width: considering the smaller ΔI (panel c), the single high-intensity event (about $40 \text{ mm}\cdot 20\text{min}^{-1}$) recorded on the 15th of September 2006 (the black curve) corresponds to the maximum value of the total precipitation; by enlarging the ΔI to $1.8 \text{ mm}\cdot 20\text{min}^{-1}$ (panel d), the events recorded on the 23rd of February 2006 (the red curve) and characterized of intensity around $3.6 \text{ mm}\cdot 20\text{min}^{-1}$ fall into the same class, so that a total precipitation value greater than 40 mm is achieved. Furthermore, focusing on panels c) and d) it is possible to notice that the 20-minute total precipitation distributions are excessively discrete and do not always follow a negative exponential curve for both $\Delta I=0.6 \text{ mm}\cdot 20\text{min}^{-1}$ and $\Delta I=1.8 \text{ mm}\cdot 20\text{min}^{-1}$, not allowing the partitioning procedure as stated in Tremblay (2005).

For this reason, the heatmaps shown in Figure 2.21 can be considered a practical instrument to understand whether it is possible to use the partitioning algorithm directly, or it is first necessary to set a higher $\Delta\tau$. In the case of this work, after fixing $\Delta\tau$ equal to the 5-day scale, the total precipitation within each 5-day window has been aggregated for each intensity class (i.e., across the rows of the heatmap).

The results of such a procedure are shown in Figure 2.22, where the 5-day total precipitation heatmaps related to the year 2006 are presented, in a similar manner to Figure 2.21, for a) $\Delta I=0.6 \text{ mm}\cdot 20\text{min}^{-1}$ and c) $\Delta I=1.8 \text{ mm}\cdot 20\text{min}^{-1}$. The same figure shows the 5-day $P_T(I)$ related to the periods 1) 21-25 January, 2) 11-15 June, 3) 26-31 August, and 4) 21-25 November and for three different ΔI : a) $0.6 \text{ mm}\cdot 20\text{min}^{-1}$, b) $1 \text{ mm}\cdot 20\text{min}^{-1}$ and, c) $1.8 \text{ mm}\cdot 20\text{min}^{-1}$.

As it is possible to observe from the heatmaps a) and c), the aggregation procedure generates a monthly total precipitation distribution generally decreasing with the intensity, in clear contrast with the 20-minute $P_T(I)$ shown in panels c) and d) of Figure 2.21. It is worth to observe that this behavior is more evident for the 5-day intervals related to the winter months (i.e., from December to March), where a high $P_T(I)$ at the lower intensities is due to a high number of low-intensity events, which typically occur in such a period. On the contrary, the ones within the months from May to August are generally drier and, for this reason, the 5-day $P_T(I)$ in the lower intensity classes assumes smaller values if compared to those in the winter months. However, a pattern decreasing with the intensity is maintained.

These aspects are enhanced by looking at the distributions for the four 5-day intervals shown in panels a1-a4, b1-b4, and c1-c4. As an example, passing from January to June

and August, it is possible to notice an important reduction in the integral of the curves which represents the total rainfall recorded in the considered time interval, despite some spikes in correspondence of higher intensities are present. In other words, even if the amount of low-intensity precipitation clearly decreases in June, and August, this does not happen with the high-intensity events. This can be considered a consequence of the fact that these months are generally drier but, at the same time, they are proportionally more characterized by high-intensity events. Finally, concerning the 5-day interval related to November, the general behavior of the total precipitation distribution is more similar to the one in January, even if some high-intensity spikes can be identified between 5 and 15 $\text{mm}\cdot 20\text{min}^{-1}$. Passing from the first to the third column of Figure 2.22, the main consequence of a wider ΔI is that the total precipitation distribution becomes smoother and smoother. Furthermore, by observing the $P_T(I)$ curves related to 21-25 November (i.e., panels a4 – c4), it is noteworthy that the maximum value of $P_T(I)$ is not always reached in the first intensity class. This aspect, in general, tends to become less important or disappear as ΔI increases.

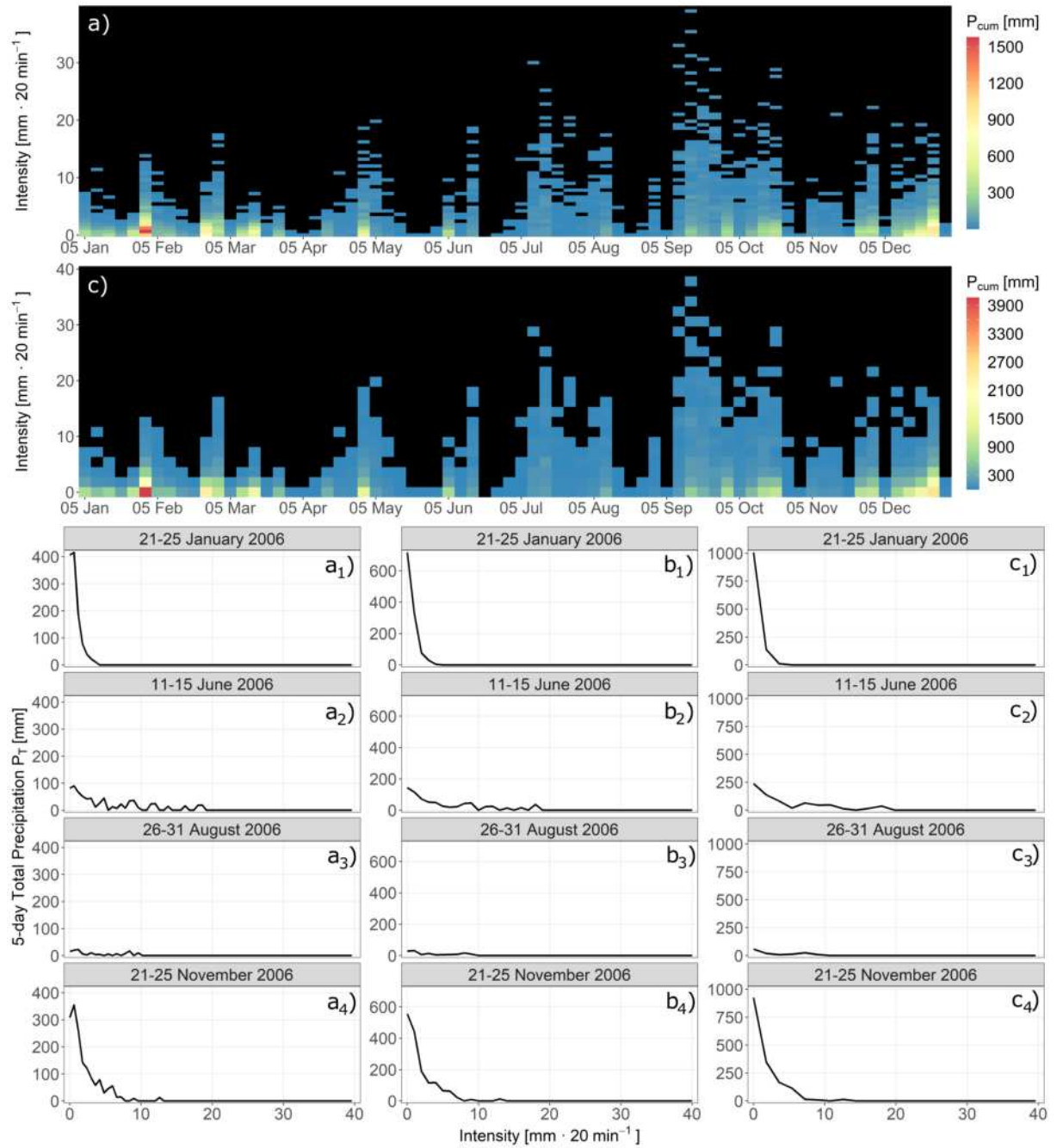


Figure 2.22: Precipitation intensity heatmap for the year 2006 at the 5-day scale a) $\Delta I = 0.6$ mm·20min⁻¹ and c) $\Delta I = 1.8$ mm·20min⁻¹. The colorbar indicates the total precipitation values, while black color indicates no rainfall records. The remaining panels show the $P_T(I)$ for 1) 21-25 January, 2) 11-15 June, 3) 26-31 August, and 4) 21-25 November combined with a) $\Delta I = 0.6$ mm·20min⁻¹, b) $\Delta I = 1$ mm·20min⁻¹, and c) $\Delta I = 1.8$ mm·20min⁻¹

2.2.4.3. Partitioning procedure

The application of the partitioning algorithm to the 5-day precipitation distribution allows classifying the percentage of convective and stratiform components considering all the intervals in the period 2002 – 2020. Figure 2.23 shows the results of the algorithm described in Section 2.2.4.1 when applied to the same cases of Figure 2.22, namely 1) 21-25 January, 2) 11-15 June, 3) 26-31 August, and 4) 21-25 November of the year 2006, for a) $\Delta I=0.6 \text{ mm}\cdot 20\text{min}^{-1}$, b) $\Delta I=1 \text{ mm}\cdot 20\text{min}^{-1}$, and c) $\Delta I=1.8 \text{ mm}\cdot 20\text{min}^{-1}$. The black and the red solid lines represent the total precipitation distribution and its stratiform component represented by the negative exponential curve, respectively, while the convective amount of rainfall for each class of intensity is depicted with the gray bars.

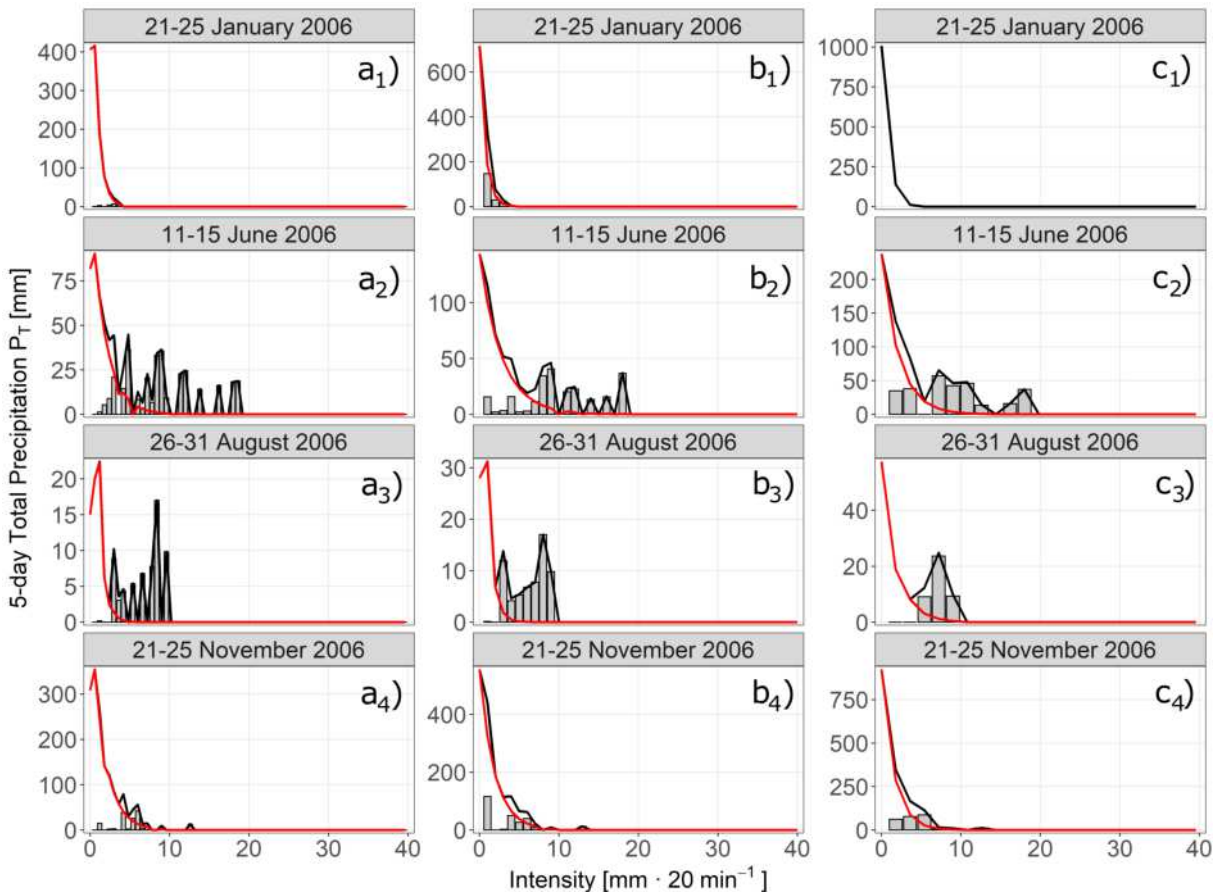


Figure 2.23: Results from the application of the partitioning procedure for the same combinations between 5-day interval and ΔI depicted in Figure 2.22. The black lines represent the 5-day total precipitation distribution, while the red lines stand for the stratiform component (i.e., the negative exponential curve). The gray bars, instead, quantify the convective amount of rainfall for each class of intensity

The negative exponential curve has been fitted through a nonlinear weighted pro-

cedure. In particular, the curve is constrained to the absolute maximum and the first absolute minimum (i.e., the first value equal to zero in the majority of cases) of the total precipitation distribution. Then, a decreasing weight is assigned to the relative minima between the two points previously defined.

At a first sight, the results seem to confirm that the algorithm is not significantly affected by the ΔI considered. Indeed, by observing the convective bars for the whole panels, it is possible to notice that these are mainly located in the right part of the total precipitation distribution, namely that there is a predominant convective rainfall at high rainfall intensity classes. This aspect confirms what Tremblay (2005) affirmed about the characteristics of convective precipitation, such that for a certain duration (i.e., 20 minutes in the case of this study) it is likely that the convective precipitation is generally characterized by higher intensity values. Moreover, this aspect is enhanced for the 5-day windows in the driest months (i.e., June and August), confirming what other authors have found about a greater occurrence of convective events during the summer months. As an example, Sottile et al. (2022) found a seasonality in the percentage of convective events in Sicily, with the highest ones from May to October, despite the authors used a different framework and pre-processing of data. Concerning other regions in the Mediterranean Muñoz-Díaz and Rodrigo (2006) indicate the important role of local and convective processes in the summer and autumn seasons for Spain, as well as Nastos et al. (2014) suggest that these seasons are more interested in convective events due to the high lightning activity.

Nevertheless, it is also possible to affirm that a lower ΔI would be excessively close to the resolution of the gauges used (i.e., $0.2 \text{ mm}\cdot 20\text{min}^{-1}$ for the SIAS network) and, during the aggregation procedure, an excessively jagged pattern of the total precipitation distribution would be generated, resulting in a difficult fitting of a negative exponential curve. This aspect would determine, in turn, an overestimation of the convective component especially for the lower intensities, since a great number of local peaks result in overfitting of the negative exponential law, as highlighted by Ruiz-Leo et al. (2013). Indeed, too much low ΔI lead to a greater variability of $P_T(I)$ even for low intensity values, thus resulting in an increased probability that no values are present in that classes. This aspect tends to excessively raise the b parameter of the negative exponential curve, and, in turn, to generate a high convective amount at all intensities, misrepresenting the outcome of the algorithm. On the other side of the spectrum, the wider the ΔI , the greater the probability that the $P_T(I)$ is over-discretized. Evidence of this aspect can be noticed considering the 21-25 January interval for all the considered ΔI (i.e., panels a1, b1, and c1). Indeed, considering panel a1 (e.g., $0.6 \text{ mm}\cdot 20\text{min}^{-1}$), there is an almost perfect overlap between $P_T(I)$ and the negative exponential curve, while moving to c1 (e.g., 1.8

mm·20min⁻¹) the fitting has been avoided, since forcing the curve for less than 4 points would have probably led to unrealistic results. Focusing on panel b1, instead, it is possible to observe that the differences between $P_T(I)$ and the negative exponential curve are caused by the mathematical framework of the algorithm and result in an overestimation of the convective amount of rainfall in the first class of intensity, as suggested by Ruiz-Leo et al. (2013). For this reason, a consequence of the choice of a wider ΔI is the decreasing capacity of the algorithm to separate the regimes at the lower intensity class. Ruiz-Leo et al. (2013) and Feloni et al. (2019) suggested calculating the percentage of convective rainfall as the integral of the area between the total and the stratiform curve. Here a different procedure is suggested, taking into account the differences between various intensity classes or, in other words, giving importance to the atmospheric processes that support the formation of convective rainfall. In particular, considering a generic 5-day distribution, the percentage of convective rainfall can be derived as the ratio between convective and total precipitation for each intensity class considered. Once this process has been repeated for all the 5-day distributions in the period 2002 – 2020, it is possible to have a sample of convective rainfall percentages for all the intensity classes taken into account. Figure 2.24 shows the median value of the percentage of convective rainfall as a function of the intensity class, for fixed the month (e.g., the panels) and the ΔI (e.g., the colors); one can observe that the median value tends to increase moving from low to higher intensities, and this occurs regardless of the month. There is a clear correlation between the highest intensities reached and the months analyzed; in particular, from June to November, months have been interested in events characterized by higher intensities (i.e., even more than 30 mm·20min⁻¹), that are generally classified as convective according to the algorithm here proposed, since the corresponding median percentage of convective rainfall is about 100%. On the contrary, the maximum intensities that characterize the months from December to May are definitely lower, with exception of a few isolated situations. About the differences among the various ΔI , it is worth noticing that they are significant from June to November while becoming negligible from January to May and in December. The greater variability in the summer/autumn months could be due to the presence of a smaller number of rainfall data recorded, which may reduce the sensitivity of the algorithm in separating the two regimes, especially when high values of ΔI are considered, as stated in Section 2.2.4.1 where the model dependencies have been analyzed.

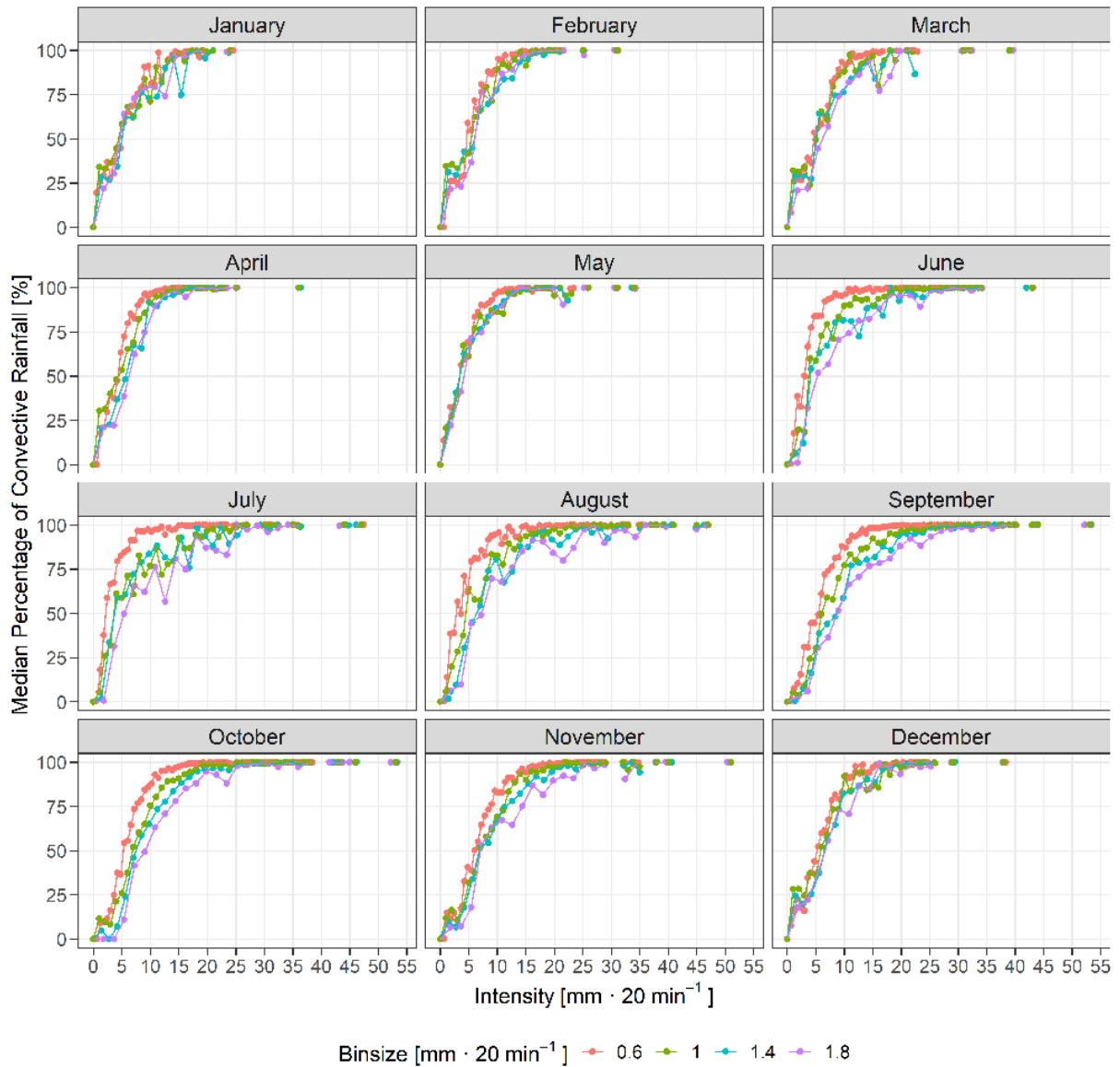


Figure 2.24: Median percentage of convective rainfall with respect to the intensity class, as a function of the month (e.g., the panels) and the ΔI (e.g., the colors). In particular, red, green, blue and purple curve stands for 0.6, 1, 1.4 and, 1.8 $\text{mm} \cdot 20\text{min}^{-1}$, respectively

2.2.4.4. Detection of convective events

Once the median values of the percentage of convective rainfall have been identified for each class of intensity, it is possible to derive a median value of the critical intensity threshold I_{cr} for each month and for each ΔI considered. As introduced in Section 2.2.4.1, the monthly I_{cr} has been derived as the first intensity value which ensures that the median values of the percentage of convective rainfall exceeds a certain limit (hereinafter λ). In particular, two λ have been tested, namely the 50% and 75%. In other words, the monthly

I_{cr} can be considered a simple method that allows detecting, at the site scale, those events in which the convective component is predominant at the 50% and 75% on the median behavior. The use of these two thresholds, instead of 50% only, has been preferred to consider the uncertainty caused by a binary classification of rainfall regimes. Figure 2.25, which reports the monthly I_{cr} values for a) $\lambda=50\%$ and b) $\lambda=75\%$ and 1) $\Delta I=0.6 \text{ mm}\cdot 20\text{min}^{-1}$, 2) $\Delta I=1 \text{ mm}\cdot 20\text{min}^{-1}$, 3) $\Delta I=1.4 \text{ mm}\cdot 20\text{min}^{-1}$ and, 4) $\Delta I=1.8 \text{ mm}\cdot 20\text{min}^{-1}$, highlights that the monthly I_{cr} increases as the λ increases, since an event is likely to be classified as convective with more confidence at the higher intensities. Focusing on $\Delta I=0.6 \text{ mm}\cdot 20\text{min}^{-1}$, a seasonality in the I_{cr} can be observed regardless of the λ considered. As an example, focusing on panel a1, it is worth to notice that the I_{cr} is lower in July (i.e., about $2.5 \text{ mm}\cdot 20\text{min}^{-1}$), while it doubles in January (i.e., about $5 \text{ mm}\cdot 20\text{min}^{-1}$). Indeed, it is likely that the convective component is predominant even for lower intensity values during the summer period when it is favored by higher air temperature and relative humidity. This behavior is identifiable also in panel b1, but with higher intensity values, as previously mentioned. I_{cr} decreases from January to July, where it reaches the minimum for all the λ and then it increases towards the winter months. As opposed to the pattern shown for $0.6 \text{ mm}\cdot 20\text{min}^{-1}$, the seasonal behavior disappears moving to the higher ΔI s and λ . In particular, if on the one hand, it is possible to recognize a similar pattern for $\lambda=50\%$ and the others ΔI s (i.e., panels a2, a3, and a4), the inter-seasonal variability of I_{cr} appears excessively high considering $\lambda=75\%$. As previously introduced, this behavior is due to a loss of sensitivity of the algorithm in identifying convective rainfall as the ΔI parameter increases, which could lead to a mis-classification of convective events (i.e., classifying as convective events that may be mainly stratiform or vice versa).

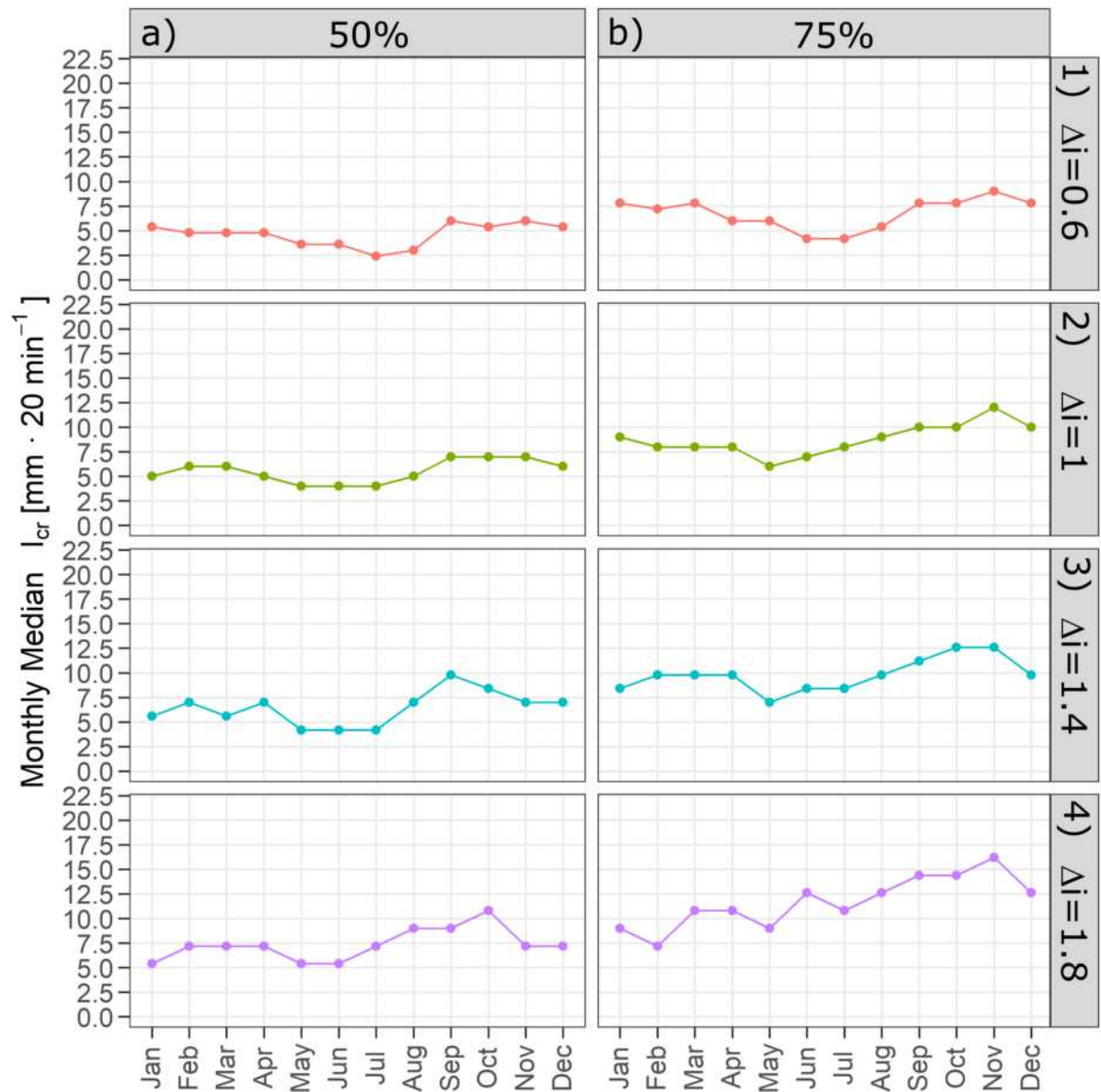


Figure 2.25: Monthly median critical intensity threshold I_{cr} values for a) $\lambda=50\%$ and b) $\lambda=75\%$ considering 1) $\Delta I=0.6$ mm·20min⁻¹, 2) $\Delta I=1$ mm·20min⁻¹, 3) $\Delta I=1.4$ mm·20min⁻¹ and, 4) $\Delta I=1.8$ mm·20min⁻¹

Considering the results shown in Figures 2.24 and 2.25, therefore, the monthly median I_{cr} values for $\Delta I=0.6$ mm·20min⁻¹ have been chosen for the at-site classification and so used to identify the convective events in the 20-minute time-series for all the gauges considered. In particular, all the events characterized by rainfall depth greater than the corresponding monthly median I_{cr} values are considered as convective, while the others are supposed to be mainly stratiform. Nevertheless, a further consideration when defining convective events needs to be carried out. Differently from the previous works where the time series are characterized by a 6-hour time resolution, the data here used have a higher

temporal frequency (i.e., 20-minute), implying that continuous exceedances of I_{cr} may refer to the same convective event. To preserve the condition of independence for the identified events, it has been imposed that the two consecutive convective events must be separated by a minimum duration of 1 hour to be considered independent (Sottile et al., 2022). Once this aggregation procedure is applied, for each convective event is possible to derive i) the peak of the event (i.e., as the maximum value recorded) and ii) the total convective precipitation (i.e., the sum of all the values that exceed I_{cr}).

Figure 2.26 summarizes the results obtained through this detecting procedure. In particular, panel a displays an example of the aggregation procedure for the Catania rain gauge. As it is possible to observe, considering the I_{cr} value for $\lambda=50\%$, $\Delta I=0.6$ mm·20min⁻¹ and the related month, two different convective events can be identified on the 16th of November 2018. With this in mind, by considering the ensemble of the ground stations that have worked continuously since 2006, panels b1 and b2 show the at-site annual average number of events classified as convective considering $\lambda=50\%$ and $\lambda=75\%$, respectively; panels c1 and c2, instead, show the at-site annual average percentage of convective rainfall for the same λ . Both latter variables have been obtained by averaging the annual values for each station and, for sake of completeness, their spatial distribution in each year considered is reported in Figure A.6 - A.9 in the Appendix A.

On the base of the average occurrence of convective events (i.e., panels a1 and a2), Sicily could be divided into two zones: the west and central part of the island, generally interested by few convective events in a year (i.e., from five to about ten on average for $\lambda=50\%$, but this number decreases considering panel a2), and the east side, where most of these kinds of events are concentrated. In particular, by looking at the eastern and the north-eastern zone it is worth to notice that an important number of stations is characterized by more than 10 convective events per year on average.

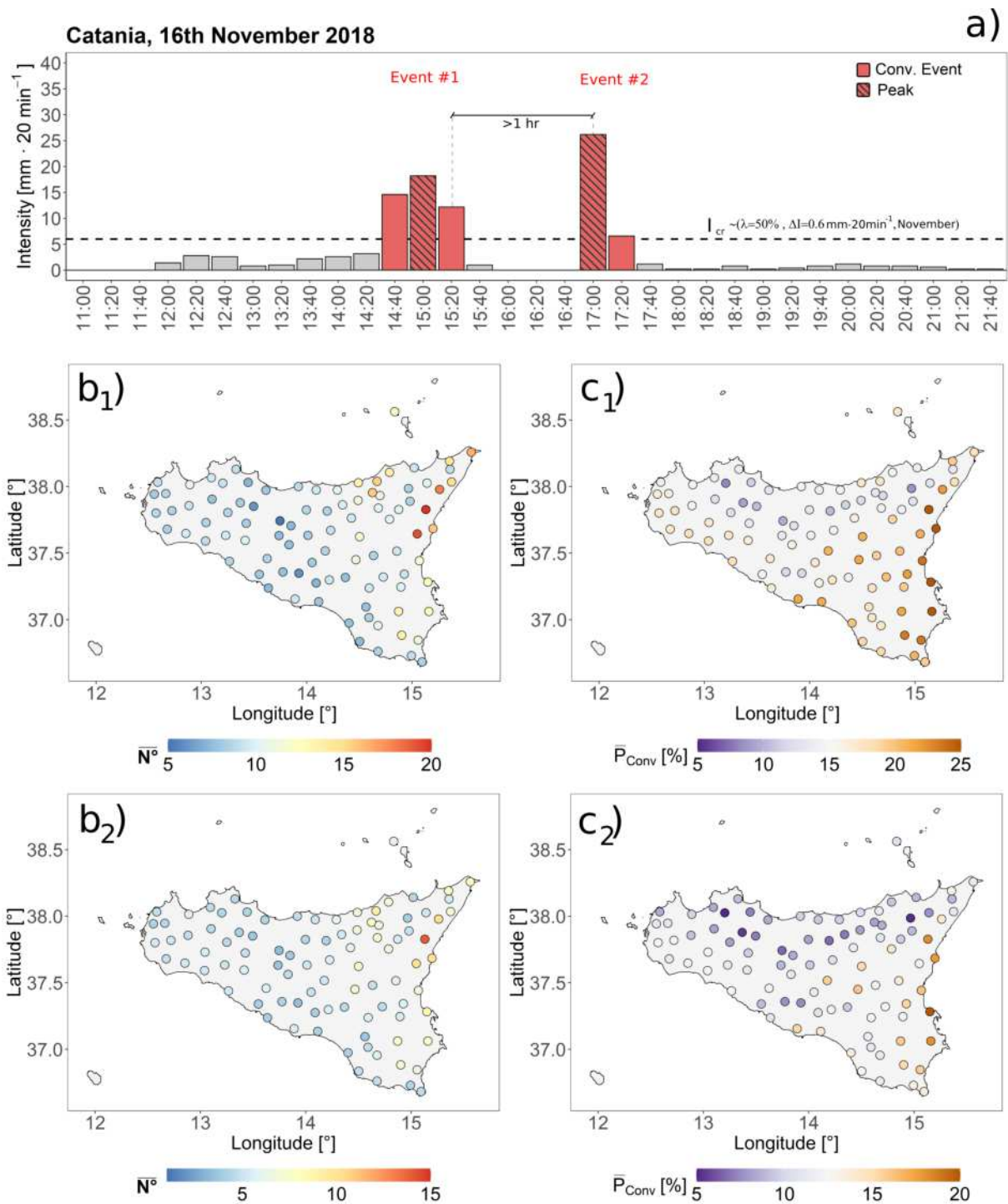


Figure 2.26: Example of the aggregation procedure (panel a) related to 16th of November 2018 for Catania rain gauge considering the I_{cr} value for $\lambda=50\%$, $\Delta I=0.6 \text{ mm} \cdot 20 \text{ min}^{-1}$ and November. The other panels show the spatial distribution of b) the average annual occurrence of convective events and c) the average annual percentage of convective rainfall for 1) $\lambda=50\%$ and 2) $\lambda=75\%$, obtained by considering the monthly median I_{cr} related to $0.6 \text{ mm} \cdot 20 \text{ min}^{-1}$

Moving to the spatial distribution of the average annual percentage of convective rainfall (panels b1 and b2), a similar pattern can be observed. Even in this case, most of

the gauges with the highest average annual percentage of convective rainfall for each λ are in the eastern part of the island. This outcome was partially expected due to the presence of the Etna volcano and the Peloritani and Nebrodi mountains in this area; indeed, the warm and humid air coming from the south, especially during the summer, runs into this orographic barrier and cools rapidly as it lifts, thus generating convective heavy rainfall (Caccamo et al., 2017), as depicted in Figure. Nevertheless, this result is alarming since the catchments in the Peloritani mountains have morphological characteristics that make convective events even more dangerous, increasing the risk of flash floods or debris flows (Aronica et al., 2012; Arnone et al., 2016).

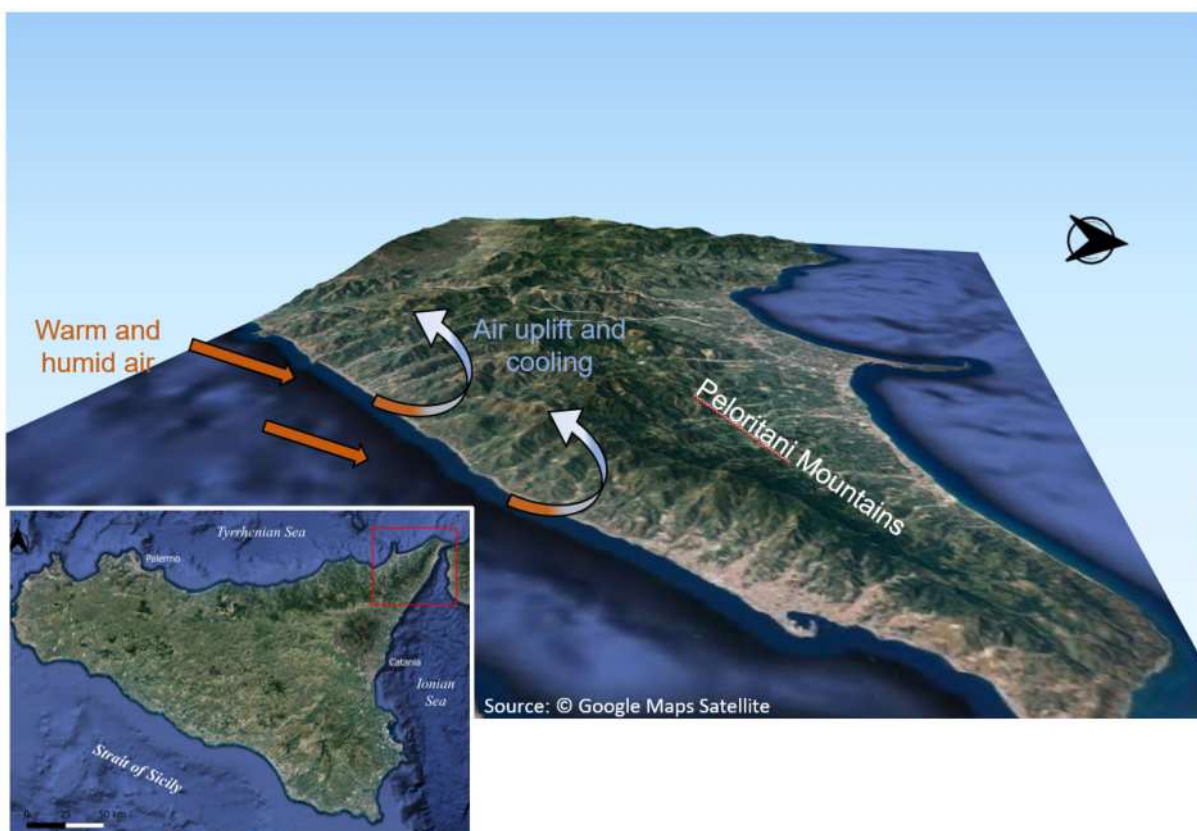


Figure 2.27: Representation of the orographic effect that generates convective rainfall in the northeastern area of Sicily

The results' consistency has been verified by comparing them with Sottile et al. (2022) outcomes. It is worth to specify that Sottile et al. (2022) used classification of the rainfall regimes into four classes (i.e., 'definitely convective', 'possible convective', 'slightly convective', and 'stratiform') and, for this reason, it has been first necessary to relate these categories to a binary classification. In particular, the 'definitely convective' and 'possible convective' events are here considered as belonging to the convective regime, while the other to the stratiform one. To ensure a coherent comparison, the only rain gauges

common to both works (i.e., 40 stations) have been selected over the same operating period (i.e., 2002-2018). Figure 2.28 provides a comparison between a) the monthly absolute number of convective events and b) the monthly percentage of convective precipitation using $\lambda=50\%$ and $\lambda=75\%$ depicted by the red and green curves, respectively, and the outcomes obtained from Sottile et al. (2022) identified by the blue curve.

As it is possible to observe from both the panels, the seasonal behavior of the two variables is caught and maintained from the proposed approach. More specifically, for both the classifications, panel a shows that the highest values in the occurrence of convective events occur in September/October (i.e., from about 700 to 1200 convective events per month affect Sicily in the period 2002-2018). Moving to panel b, instead, the highest percentages of convective rainfall affect the summer season (i.e., from 50% to 60%). The apparent contrast between the position of the peaks in the latter panels is justified by the fact that the greater number of convective events generally recorded in the autumn is balanced by a greater amount of stratiform precipitation; summer months, instead, are generally drier, but the limited number of events that characterize these seasons are probably predominantly convective. Another aspect that deserves to be considered is that the curves related to Sottile et al. (2022) lie between $\lambda=50\%$ and $\lambda=75\%$ for almost every month. In particular only one point is outside the shaded area in panel a (i.e., the one related to June), even if the local pattern, i.e., the presence of a peak in June, is captured by the proposed method.

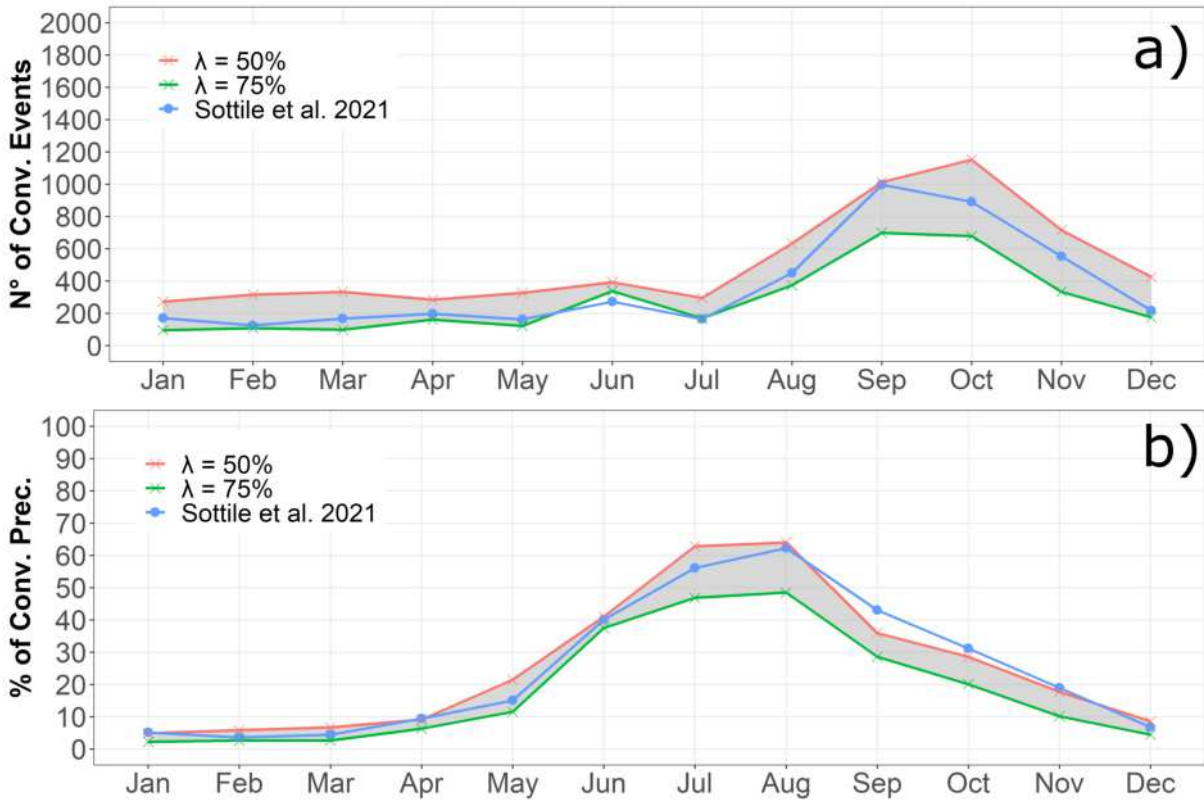


Figure 2.28: Comparison between a) the monthly absolute number of convective events and b) the monthly percentage of convective precipitation using $\lambda=50\%$ and $\lambda=75\%$ (i.e., the red and green curve, respectively) and the outcomes obtained from Sottile et al. (2022) (i.e., the blue curve). The gray shaded area represents the differences between the two λ

2.2.4.5. At-site and regional trend analysis

Once the regimes are separated, a trend analysis on the peaks of convective events and on the total convective precipitation has been applied in order to verify if significant changes in these proxies occurred in the last twenty years. To do this, the Mann-Kendall trend test (see Section 2.2.2.1) has been applied at-site. The evaluation of trends have been also conducted at the regional scale through the Regional Kendall Test (Douglas et al., 2000; Cannarozzo et al., 2006; Helsel and Frans, 2006). The Kendall's S statistic is evaluated through equation 2.5 at each location and then the average, S_m , is computed. The p -value is finally derived from equation 2.3 after that the regional standardized test statistic, Z_R , is obtained as follow:

$$Z_R = \begin{cases} \frac{S_m - 1}{\sigma_{S_r}} & \text{if } S > 0 \\ 0 & \text{if } S = 0 \\ \frac{S_m + 1}{\sigma_{S_r}} & \text{if } S < 0 \end{cases} \quad (2.15)$$

where σ_{S_r} takes into account the sample numerosity at each gauge through n_l :

$$\sigma_{S_r} = \sqrt{\sum_{l=1}^m \frac{n_l(n_l - 1)(2n_l + 5)}{18}} \quad (2.16)$$

Figure 2.29 shows the Mann-Kendall trend analysis results, carried out using a level of significance equal to 0.1, for the peak of convective events (i.e., panels a1 and a2) and the total convective precipitation (i.e., panels b1 and b2), considering $\lambda=50\%$ and $\lambda=75\%$. In all the panels, the cross symbol points out the gauges where no significant trend has been detected, while the colored triangles pointing up (pointing down) represent the gauges interested by a significant increasing (decreasing) trend. Observing the findings of the trend analysis, it is possible to notice that about 90% of the gauges are characterized by the absence of any trend for both the variables considered. Nevertheless, when detected, the general behavior of the significant trend is related to an increase in the considered variable, as evidenced in Section 2.2.2 and in previous works Arnone et al. (2013) albeit with different methods and datasets. Moreover, considering panels a1 and b1, two possible clusters of sites showing increasing trends are maintained for both the variables: the largest one connects the north-west to the south-east corner, while the second one is related to the Peloritani area (i.e., the north-east zone). The Regional Kendall test has been applied to check if a general behavior in the trend direction can be identified through the whole region. It has been obtained that the null hypothesis (i.e., no trend detected) has been rejected for the peak of convective events considering $\lambda=50\%$ and $\lambda=75\%$, considering a level of significance equal to 0.05 and 0.1, respectively. Hence, there is evidence for a significant concordance in the trend signs considering the whole region. Indeed, the most of stations shows a positive sign, even if for the at-site Mann-Kendall test it is significant only for only a limited number of them. In the case of the total convective precipitation, instead, it has been found that a positive trend can be identified for $\lambda=50\%$ (i.e., level of significance equal to 0.05), while it is not significant for $\lambda=75\%$. The associated p -values are reported in the bottom-left corner of each panel in Figure 2.29.

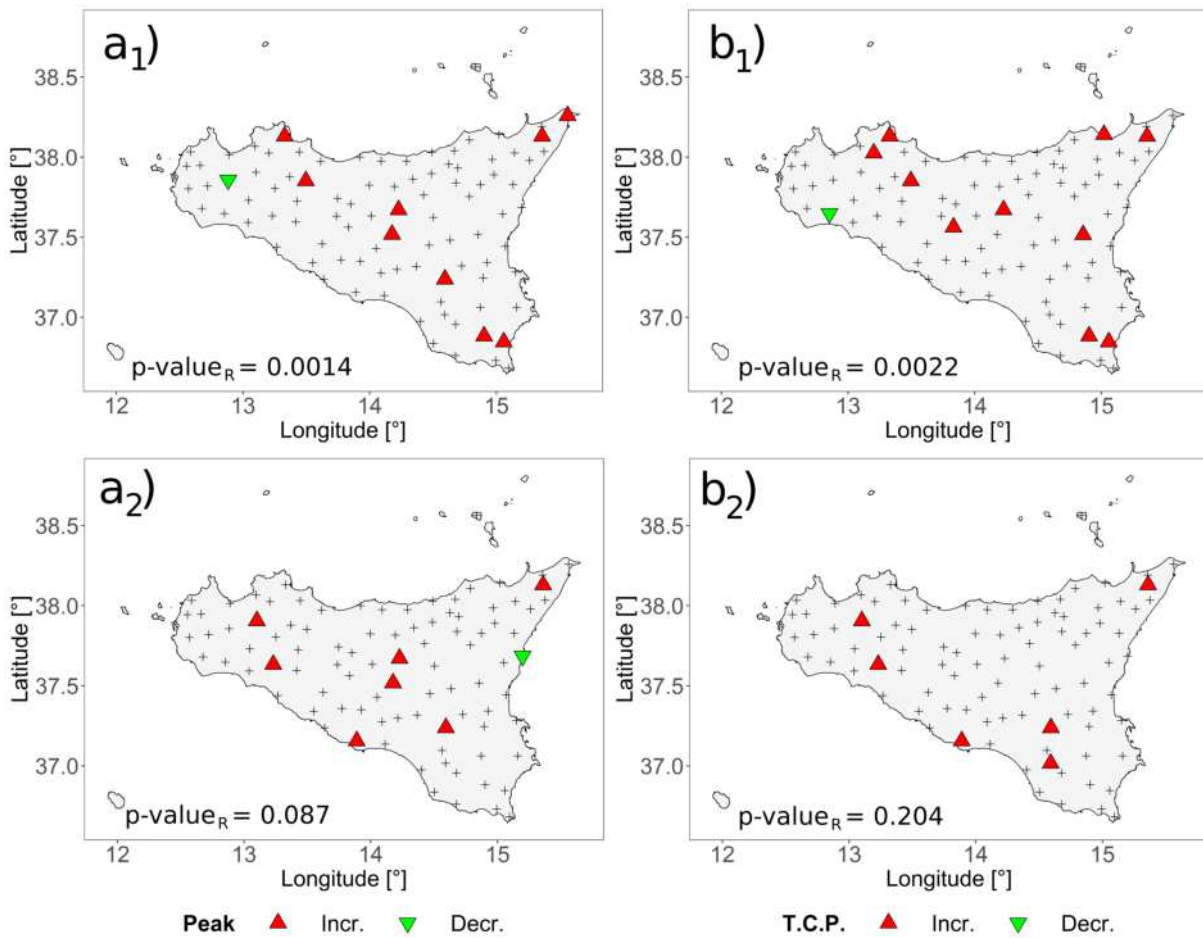


Figure 2.29: Trend analysis results for a) the peak of convective events and b) the total convective precipitation for 1) $\lambda=50\%$ and 2) $\lambda=75\%$. The cross symbol stands for the gauges where no significant trend has been detected, while the colored triangles pointing up (pointing down) represents the gauges interested by a significant increasing (decreasing) trend. The p-value from the Regional Kendall test is shown in the bottom-left corner of each panel

3 | Chapter three

3.1. A global perspective on past and future changes in rainfall characteristics

As previously mentioned, heavy precipitation events are becoming more intense and frequent (Pörtner et al., 2022), exacerbating known impacts and emphasizing new ones. Severe storms can directly affect agriculture, triggering a cascade of events that can induce crop failure, worsen poverty, starvation, and conflicts across the globe (Rosenzweig et al., 2002; Raleigh and Kniveton, 2012; Abiodun et al., 2017; W.H.O., 2018). They also pose a significant threat for public health, increasing the possibility of waterborne disease (Checkley et al., 2000; Curriero et al., 2001; Thomas et al., 2006; Khan et al., 2015). All these impacts are enhanced when extreme rainfall events are the driver for flooding. As an example, the flood induced by the extraordinary rainfall during the 2022 monsoon season stroke Pakistan with brutal violence, killing more than 1,700 people and exceeding USD 30 billion of damages and economic losses. These effects are felt in terms of the global economy, especially for the high-income countries (Kotz et al., 2022).

Therefore, it is no surprising that changes in the characteristics of extreme precipitation events have been extensively investigated across different spatial and temporal scales (Westra et al., 2014; Donat et al., 2016; Fowler et al., 2021). Among these characteristics, intensity is probably the one that have found their most widespread use in the work of the scientific community, while fewer studies are present for seasonality, as already mentioned in section 1.2. However, these features have always been treated separately, examining changes in one or the other and ruling out the possibility that they may be two sides of the same coin.

3.1.1. Magnitude or seasonality: why choose one?

In the analysis of a precipitation time series (e.g., the one shown in Figure 3.1a), the study of extreme events is typically carried out by selecting all the exceedances above a specific percentile. By choosing, for instance, the 99th percentile and representing the POT (red points), different conclusions can be drawn depending on what is being examined.

If the intensity of the events is considered and represented over time (Figure 3.1b), trend tests can be performed, as in Section 2.2.2. The magnitude is also the variable used in the Extreme Value Theory (EVT) for modeling the right tail of the distributions and deriving, for example, the DDF (or IDF) curves (as in section 2.2.3). However, by examining Figure 3.1b, it is not possible to draw conclusions about the seasonality of extreme events. If, at this point, the intensity of events is neglected and the day of the year when they occur is considered (Figure 3.1c), it is possible to provide additional information about the timing of these events. A clustering of points between April and November is evident from the last figure, showing a marked seasonality of rainfall extremes for the considered time series.

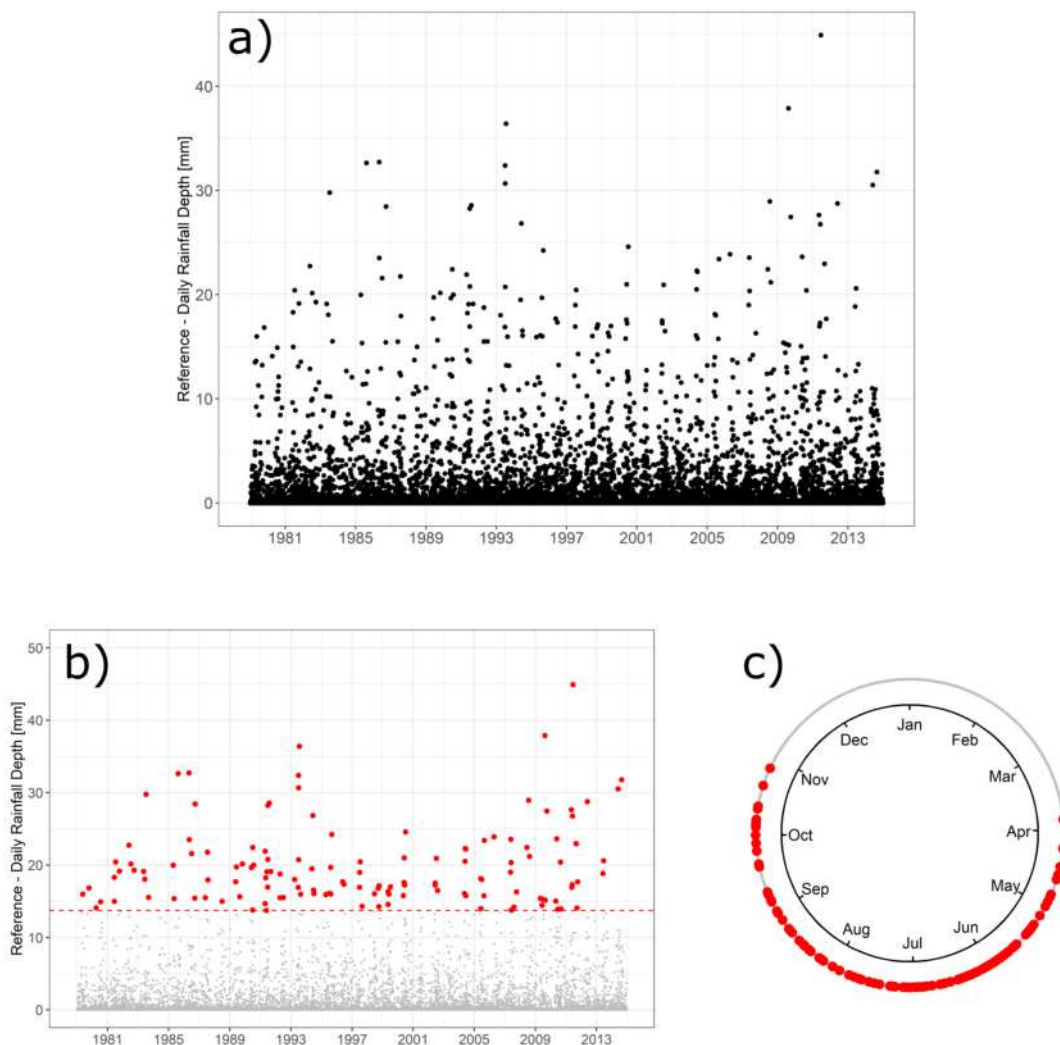


Figure 3.1: Example of time series for daily rainfall precipitation (a). Exceedances of the 99th percentile (red points) represented as function of time (b) and as day of occurrence of the events(c)

Up to now, there is an implicit assumption of stationarity in the process. The seasonality of precipitation extremes is generally not projected to change when the main focus is on the magnitude and vice versa. The understanding of the projected changes in these events is predicated on the assumption that they will continue to occur in the same season (or with the same intensity), and, consequently, also the management of the water resources and response to their impacts is based on this supposition. What if extreme precipitation at a given location tends to be generally associated with, say, extratropical cyclones that occur during the cold months, but in the future tropical cyclones during the warm months become more intense and dominant? Are these two characteristics independent of each other, or are they actually two sides of the same coin? If so, the approaches typically used may overlook a fundamental part of the problem. Indeed, a different perspective of the problem arises when the two quantities in Figure 3.1 are represented together, as in Figure 3.2. The latter combines the occurrence of the events (i.e., the position on the circle) with their severity (i.e., the position along the radius).

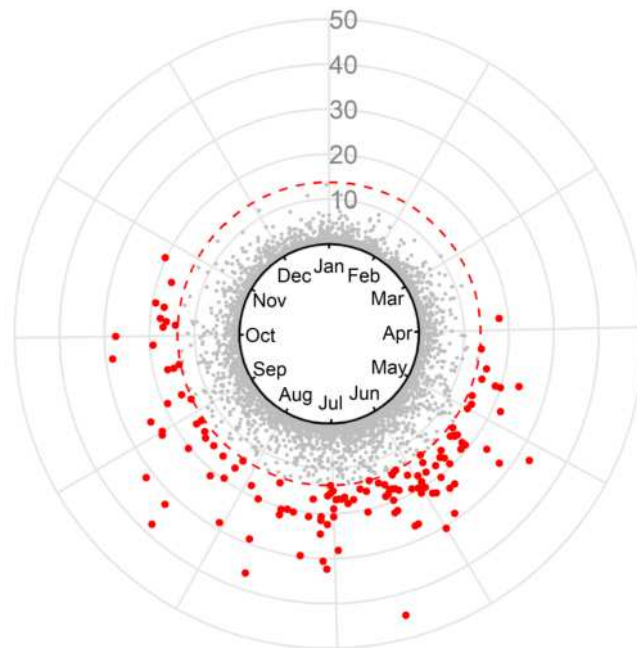


Figure 3.2: Bivariate representation of the magnitude (i.e., position along the radius) and the seasonality (i.e., position on the circle) for the precipitation POT in Figure 3.1

From this representation, it is possible to observe that most of the exceedances are concentrated between May and July, albeit with lower values for the magnitude. On the opposite, the months between July and September are characterized by a smaller number of events but associated with higher intensity. Therefore, the bivariate study of these two

variables can provide a "third perspective", helping not to overlook the information that can be gleaned from their combined picture.

3.2. A joint projected change in magnitude and seasonality of extreme precipitation events

Despite the importance of this topic and its potential implications in terms of water resources management and ecosystem health, there is no study that examines these two extreme precipitation characteristics jointly despite their potential dependence. A first attempt to test whether this dependence exists or not is to examine the correlation between the intensity of the extreme precipitation and the month in which the events occur.

To achieve this goal, the Multi-Source Weighted-Ensemble Precipitation version 2 (MSWEP V2) (Beck et al., 2019) has been used as reference dataset for the period 1979 – 2014. This is a global gridded product with a 0.1-degree spatial and daily time resolution, derived by merging quality-controlled gauges, satellites, and reanalysis precipitation estimates. For each pixel, the 99th percentile of the precipitation distribution has been selected as the threshold to detect extreme precipitation events.

Figure 3.3 highlights the monthly percentages of extreme precipitation events (i.e., the number of extreme events in a certain month referred to the total) together with their magnitude (i.e., the median value of the events exceeding the 99th percentile), highlighting how the extreme events are distributed or concentrated during the year. The white-to-purple scale represents the percentage of events in the month, while the white-to-green characterizes the magnitude of the median of the events exceeding the threshold. Hence, the greener (more purple) the color, the greater (lower) the magnitude of the precipitation event in a given month, and at the same time, the lower (higher) the number of extreme events that characterize it. Dark colors represent high percentages and high magnitudes of these events, while totally white pixels indicate that no events occurred during the study period (i.e., 1979-2014).

By starting to analyze the patterns from a univariate perspective, it is easy to recognize areas where there is not a dominant season, with large precipitation extremes that can occur throughout the year. This is the case, for instance, for the southeastern United States, where large precipitation events can occur during almost any month due to extra-tropical cyclones, tropical cyclones, and mesoscale convective systems. This is also the case for South America, especially across the Amazon Forest and equatorial and tropical regions, because of the seasonal migration of the Intertropical Convergence Zone (ITCZ) driven by the combined interaction between the South Pacific Ocean Dipole (SPOD) and

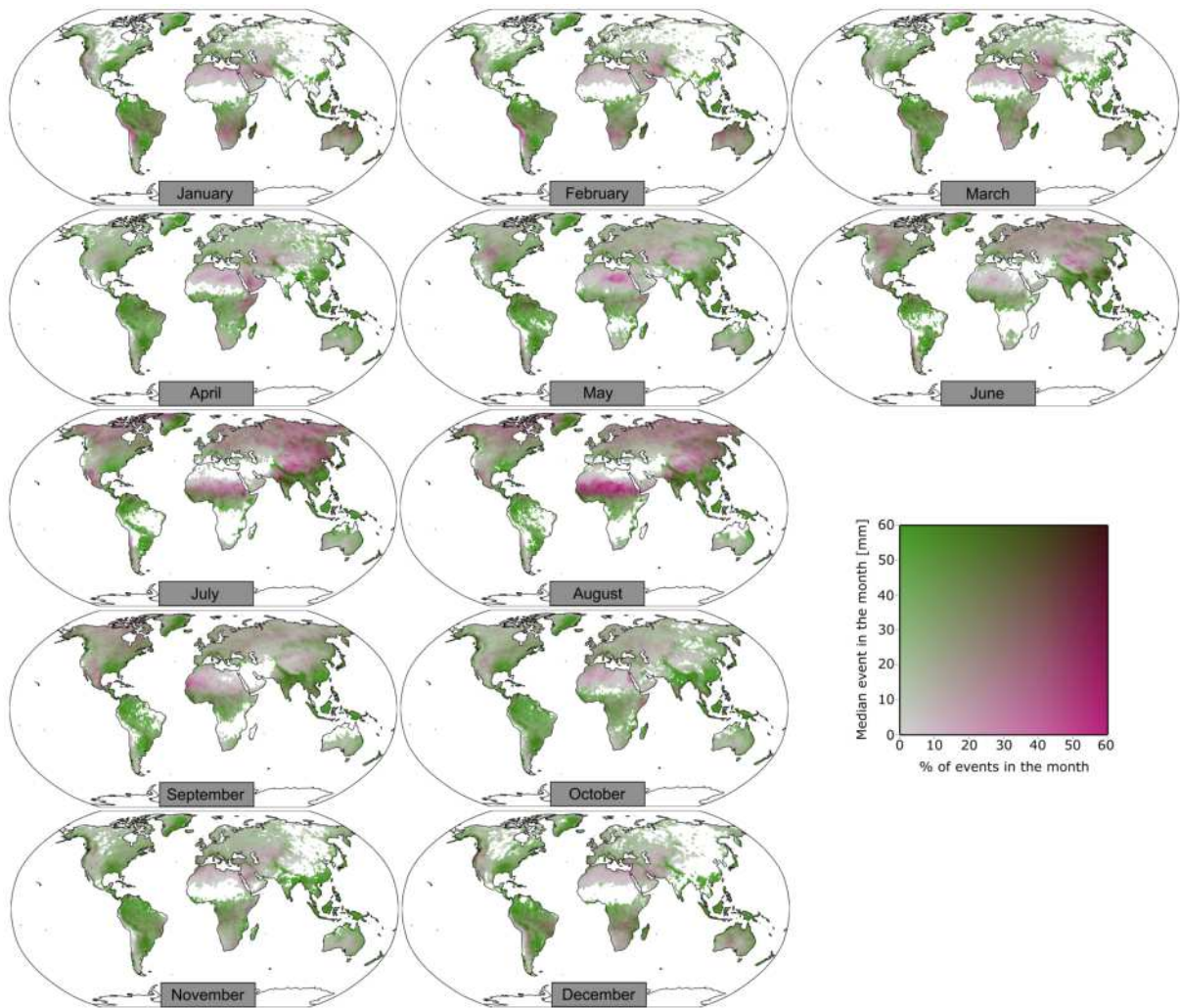


Figure 3.3: Bivariate representation of the monthly correlation between the percentages of events that exceed the 99th percentile of the at-site distribution and their median value at a global scale over the 1979-2014 period. The white-to-purple scale represents the percentage of events in the month, while the white-to-green characterizes the magnitude of the median of the events exceeding the threshold. Hence, the greener (more purple) the color, the greater (lower) the magnitude of the precipitation event in a given month, and at the same time, the lower (higher) the number of extreme events that characterize it. Dark colors represent high percentages and high magnitudes of these events, while totally white pixels indicate that no events occurred during the study period

the El Niño Southern Oscillation (ENSO) (Guan et al., 2023). Similar to South America, equatorial Africa is characterized by the presence of extreme precipitation throughout the year due to the ITCZ that determine the two rainy seasons in the region (Nicholson, 2018). Finally, the Mediterranean area and Central Europe exhibit a similar behavior: in addition to the extreme precipitation that can occur during the wet season from October to March, intense precipitation events can also occur during the boreal summer due to convective phenomena (Llasat et al., 2021) favored by high values of convective available potential energy that time of the year (Riemann-Campe et al., 2009).

On the other side of the spectrum, some regions are characterized by a strong synchronism between the frequency and the magnitude of extremes, such as Russia or continental China, where the highest values are concentrated between July and August, despite the magnitude of the precipitation extremes in these regions is lower than other areas. This is also the case for Saharan Africa, where most events occur between May and August, but with an intensity close to zero. Areas with a strong precipitation seasonality are also located in India, the Indochinese Peninsula and the Chinese coast, with events concentrated between June and September due to the monsoon. For these areas, as well as for southern Africa and northern Australia in the austral summer, there is a high frequency of occurrence of extreme events coupled with large intensities; there are other regions, such as central America, central and western United States, Canada and central and southern Australia, where the dependence of these two precipitation characteristics is not strong, highlighting the need of a joint analysis.

3.2.1. How to model the bivariate dependence

Based on the results in Figure 3.3, the seasonality and magnitude of extreme precipitation events exhibit regional variability; however, these two variables are also clearly connected, requiring them to be analyzed together rather than independently to get the full picture of how this hazard is projected to change.

In achieving this goal, two considerations must be addressed. The first one is related to the nature of these two different variables: while the rainfall depth can be studied through the linear statistic principles (being the variable potentially defined between 0 and ∞), the occurrence (i.e., referred as the day of the year when the event occurs) needs a circular approach to be properly defined (Fisher, 1995). Thus, a complexity arises from this first consideration: how is it possible to model these two quantities in a bivariate statistical space? Indeed, the statistical instruments generally used in hydrology or climatology to model the dependence between two (or more) variables, namely *copulae*, have been widely employed for features that are not characterized by periodicity, such as

temperature and precipitation (Piani and Haerter, 2012; Lazoglou and Anagnostopoulou, 2019), precipitation and floods (Xie and Wang, 2013), and so on. However, a peculiar branch of copulae (i.e., circular-linear copulae) have been recently developed in ecology, representing a useful tool for application in other disciplines. Therefore, the next two sub-paragraphs will be devoted to provide more information on circular statistic, which is a cornerstone in this research, and insights about the methodology behind the circular-linear copulae.

3.2.1.1. Circular statistics for periodic variables

Circular statistics (Fisher, 1995; Pewsey et al., 2013), often referred to as 'directional statistics', is a particular branch within the field of statistics. It has been designed for the analysis of data that can be quantified in angles, directions, or any other form of periodic time measurements. Unlike classical statistics, where variables are arranged on a linear support, the one for circular data is the unit circle. Hence, after defining the origin and the direction of rotation (e.g., clockwise or counterclockwise) circular data are usually expressed in radians or degrees. When dealing with wind direction, for instance, circular statistics takes into account that an angle of 0° and 359° are only 1° apart, while attempting to analyze this in a linear manner would suggest a significant separation of 359° .

Pewsey et al. (2013)'s popular example on the flight of homing pigeons clarifies what risks are faced in not using it. Assuming that the angles measured when four homing pigeons take flight are 10° , 20° , 340° , and 350° respect to the geographic north, it would be reasonable to conclude that the preferred direction for these animals to take flight is approximately north. However, without using circular statistics, this simple conclusion could be misleading. Indeed, the arithmetic mean of these angles is 180° , resulting in the completely opposite direction.

From what has just been shown, it is not possible to apply the arithmetic mean to a sample of circular data, but it is necessary to use an alternative that takes into account the periodicity of the data. Considering a sample of n circular observation $(\theta_1, \theta_2, \dots, \theta_n)$ and working in the unit circle ranging between 0 and 2π (but keeping in mind that any angle θ corresponds to $\theta + 2\pi \cdot p$, where $p = \pm 1, \pm 2, \dots$), it is possible to define a mean resultant vector, having length \bar{R} and direction $\bar{\theta}$, defined as follows:

$$\bar{R} = (a^2 + b^2)^{\frac{1}{2}} \in [0, 1] \quad (3.1)$$

$$\bar{\theta} = \text{atan2}(b, a) \quad (3.2)$$

where

$$a = \frac{1}{n} \sum_{i=1}^n \cos\theta_i, \quad b = \frac{1}{n} \sum_{i=1}^n \sin\theta_i \quad (3.3)$$

$$\text{atan2}(b, a) = \begin{cases} \arctan(b/a) & \text{if } a > 0 \\ \arctan(b/a) + \pi & \text{if } b \geq 0, a < 0 \\ \arctan(b/a) & \text{if } b < 0, a < 0 \\ \arctan(\pi/2) & \text{if } b > 0, a = 0 \\ \arctan(-\pi/2) & \text{if } b < 0, a = 0 \\ \text{undefined} & \text{if } b = 0, a = 0 \end{cases} \quad (3.4)$$

Hence, for circular data the sample mean direction, $\bar{\theta}$, and length, \bar{R} , are the most commonly used measure of location and concentration, respectively (Pewsey et al., 2013).

However, such as in linear statistics, the median is a robust alternative to the mean when the sample is skewed. In the case of the circular statistics, the sample median direction, $\tilde{\theta}$, is defined as any angle ψ for which half of the data points lie in the arc $[\psi, \psi + \pi)$ and the majority of the points are nearer to ψ than to $\psi + \pi$. This definition implies that \bar{R} remains the same as the one defined for the circular mean, but also that the median direction depends on whether the length of the sample is even or odd. In particular, this direction will correspond to one of the data points if the sample size is odd; when it is even, it is taken to be the mean of those data points immediately to its left and right (Pewsey et al., 2013). In general, the sample median direction is obtained by minimizing the dispersion measure:

$$d(\psi) = \frac{1}{n} \sum_{i=1}^n \{\pi - |\pi - |\theta_i - \psi||\} \quad (3.5)$$

As an example, in Figure 3.4 the two metrics are computed for a sample of wind directions (Agostinelli and Lund, 2023) and represented on a circular plot.

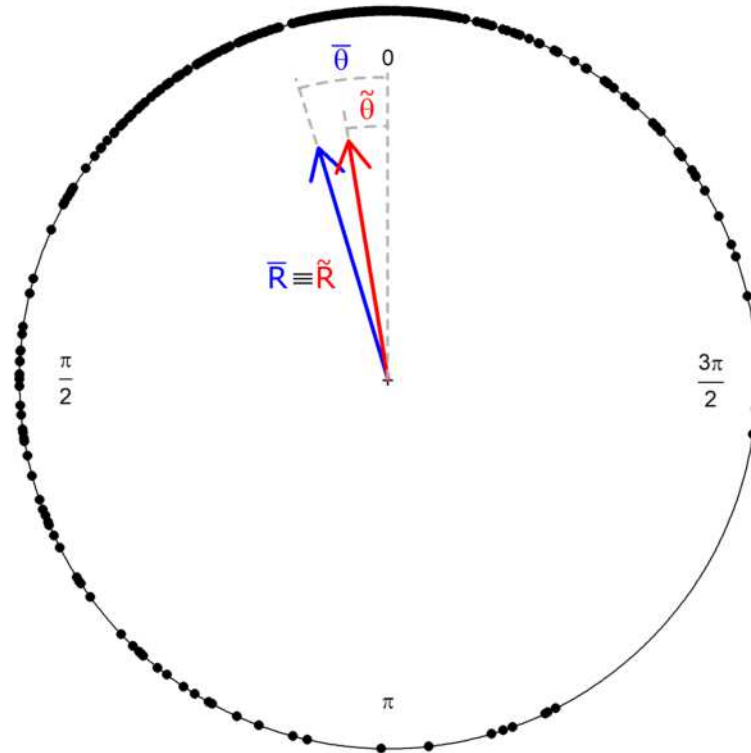


Figure 3.4: Example of circularized data with the length and the direction of the sample mean (blue) and sample median (red) vectors. The wind dataset is available in the `circular` package (Agostinelli and Lund, 2023) in R

Slightly complicating the homing pigeons example, what would be the consequences of using the wrong approach in modeling the variable distribution? For instance, Figure 3.5 shows the histogram of the wind directions shown in Figure 3.4 (although this can be extended to any other directional variable) ranging from 0 to 2π . The variable has been considered once linear and once circular, and for both cases it was computed an empirical probability density function with a smoothing kernel. As it is possible to observe, when the wind directions are treated using the linear statistic (i.e., red line), two different peaks are identified. However, according to the circular approach (i.e., blue line), there is actually only one peak, since the values close to 2π represent the left shoulder of the total distribution.

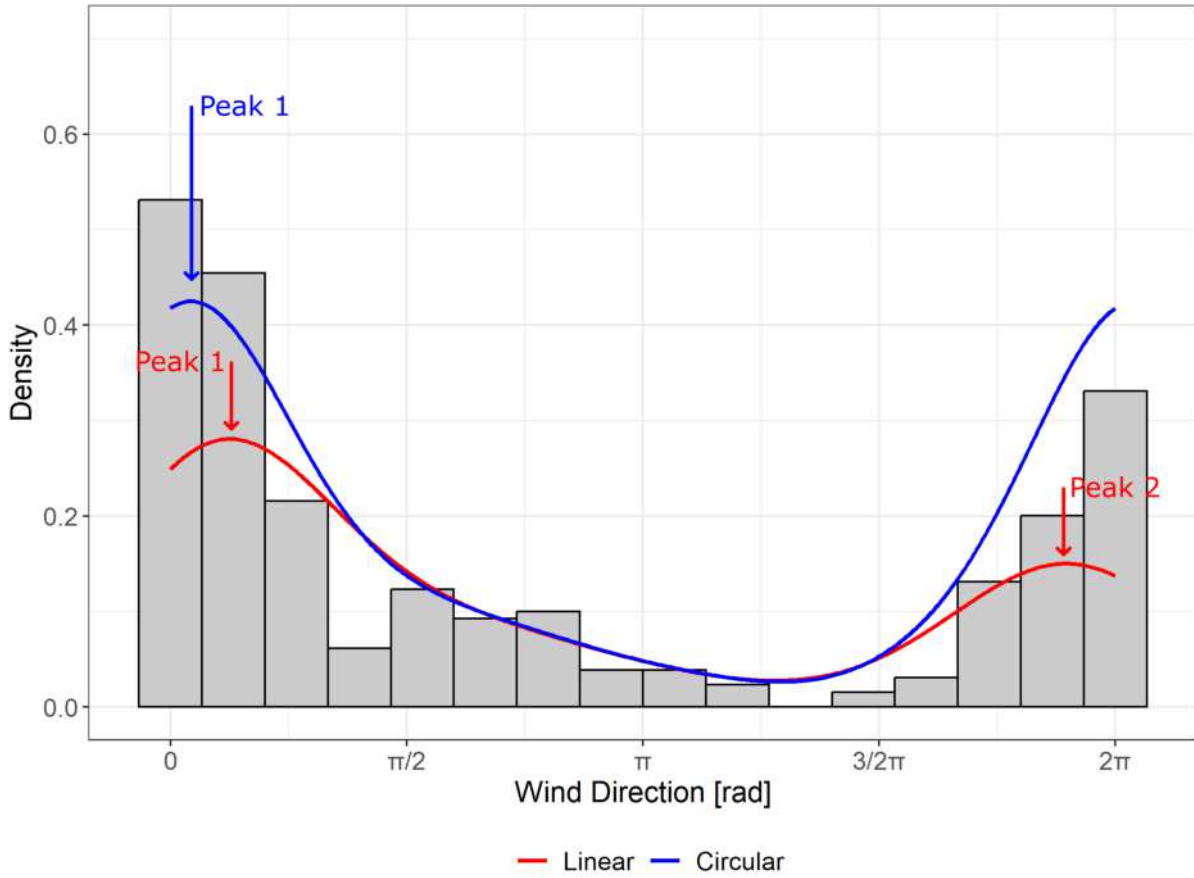


Figure 3.5: Example of empirical probability density function for wind directions treated as a linear (red line) and circular (blue line) variable. The wind dataset is available in the `circular` package (Agostinelli and Lund, 2023) in R

As well as for sample moments, the theoretical distributions must also be suitable for modeling the circular nature of the variables. In particular, their periodicity determines two main implications (Pewsey et al., 2013): the first one is that the definition of a circular distribution function strictly depends on the definition of initial direction, orientation and units of measurement used; the second one regards the fact that the distribution needs to be periodic, since an angle θ corresponds to $\theta + 2\pi \cdot p$, where $p = \pm 1, \pm 2, \dots$. Hence, a circular distribution function, $F(\cdot)$, can be specified as the function given by:

$$F(\theta) = P(0 < \Theta \leq \theta), \quad 0 \leq \theta \leq 2\pi \quad (3.6)$$

$$F(\theta + 2\pi) - F(\theta) = 1, \quad -\infty < \theta < \infty \quad (3.7)$$

In equation 3.6 it is easy to recognize the usual definition of a distribution function for a random variable in the linear statistic, while equation 3.7 is the condition that

guarantees the periodicity of the circular distribution.

Among all circular unimodal distributions, one of the most widely used is the von Mises-Fischer (vMF) distribution (Fisher, 1995). The vMF distribution, which can be defined on the $(p - 1)$ -sphere in \mathbb{R}^p , has the following probability density function:

$$f(\mathbf{x}|\mu, \kappa) = c_p(\kappa)e^{\kappa\mu^T\mathbf{x}} \quad (3.8)$$

where \mathbf{x} is a p -dimensional random vector, μ is the mean direction vector and κ is the concentration parameter ($\kappa \geq 0$), which describes the degree of concentration of the unit vectors around the mean direction μ . The normalizing constant $c_p(\kappa)$ is given by:

$$c_p(\kappa) = \frac{\kappa^{p/2-1}}{(2\pi)^{p/2}I_{p/2-1}(\kappa)} \quad (3.9)$$

where $I_p(\cdot)$ is the modified Bessel function of the first kind and order p . When $p = 2$, the vMF distribution degenerates in the von Mises (vM) distribution (von Mises, 1918), which represents its bi-dimensional case and can be considered a circular analogue of the normal distribution.

$$f(\theta|\mu, \kappa) = \frac{1}{2\pi I_0(\kappa)}e^{\kappa \cos(\theta-\mu)} \quad (3.10)$$

One of the major limits in using the vMF of the vM distribution is their unimodality. This apparent restriction, however, can be solved by using a finite number of mixtures of these distributions (Mardia, 1975; Banerjee et al., 2005). Remaining in the bi-dimensional case and considering a mixture of N vM distributions, the resulting distribution is characterized by the following probability density function:

$$f(\theta|\{\alpha_j, \mu_j, \kappa_j\}_{j=1}^N) = \sum_{j=1}^N \alpha_j f(\theta|\mu_j, \kappa_j) \quad (3.11)$$

where each $f(\theta|\mu_j, \kappa_j)$ is a vMF density function defined by its directional mean (μ_j) and concentration parameter (κ_j) and scaled according to a mixture proportion (α_j). It is obvious that ($\alpha_j \geq 0$) and $\sum_{j=1}^N \alpha_j = 1$. Since no analytical solution exists for equation 3.11, the parameters $\{\alpha_j, \mu_j, \kappa_j\}_{j=1}^N$ are computed via maximum likelihood estimates under the expectation maximization framework (Banerjee et al., 2005; Veatch and Villarini, 2020).

Equation 3.11 can be applied while considering a potentially high number of mixtures. However, the "optimal" number is not known a priori, and an excessively high value may increase the risk of overfitting. To ensure improvements in the model performance while reducing this risk, the Bayesian Information Criterion (BIC) (Schwarz, 1978) can be

employed:

$$BIC = k \ln(n) - 2 \ln(\hat{L}) \quad (3.12)$$

where k is the number of parameters estimated by the model, n is the sample size and \hat{L} is the maximized value of the likelihood function of the model. In particular, the optimal number of mixtures is the one that results in the lowest BIC (Veatch and Villarini, 2020).

3.2.1.2. Circular-linear copulae

As introduced before, copulae are "*functions that join or couple multivariate distribution functions to their one-dimensional marginal distribution functions*" (Nelsen, 2006). In other words, they represent an useful instrument to describe the inter-relation between two or more random variables (Schmidt, 2007).

From the mathematical point of view, being X and Y two random variables, a bi-dimensional (or bivariate) copula, $C(x, y)$, is a cumulative distribution function (CDF) with uniform marginals. Since it is a 2-dimensional CDF, its domain will vary between $[0, 1]^2$, namely $[0, 1]$. Sklar's theorem (Sklar, 1959) provide an essential property for describing the joint distribution of X and Y using their specified marginal distributions together with a copula. Indeed, for any multivariate distribution $F_{X,Y}(x, y)$, there exists a copula that fully characterizes the dependence structure between its marginal distributions, $F_X(x) = P(X \leq x) = u$, and $F_Y(y) = P(Y \leq y) = v$:

$$F_{X,Y}(x, y) = C(F_X(x), F_Y(y)) = C(u, v) \quad (3.13)$$

Sklar's theorem is not only valid for CDF, but also the probability density function (PDF) of a joint distribution can be obtained through the copula:

$$f_{X,Y}(x, y) = c(u, v) f_X(x) f_Y(y) \quad (3.14)$$

where $f_X(x)$ and $f_Y(y)$ indicate the marginal PDFs of X and Y , respectively, and $c(u, v)$ is the copula density, defined as:

$$c(u, v) = \frac{\partial^2 C(u, v)}{\partial u \partial v} \quad (3.15)$$

Among all the classes of copulae, the Archimedean are the most widely used, especially for their simplicity in being constructed and the wide range of families of copulae which belong to this class (Nelsen, 2006). In particular, the following equations represent the mathematical structure of the Gumbel (Émile and Gumbel, 1960), Clayton (Clayton,

1978) and Frank (Frank, 1979) copula, which are those considered in this Chapter and, therefore, need to be introduced.

$$\text{Gumbel:} \quad C_{\theta}(u, v) = \exp\left(-\left[(-\ln u)^{\theta} + (-\ln v)^{\theta}\right]^{1/\theta}\right) \quad (3.16)$$

$$\text{Clayton:} \quad C_{\theta}(u, v) = \left(\max\{u^{-\theta} + v^{-\theta} - 1, 0\}\right)^{-1/\theta} \quad (3.17)$$

$$\text{Frank:} \quad C_{\theta}(u, v) = -\frac{1}{\theta} \ln\left(1 + \frac{(e^{-\theta u} - 1)(e^{-\theta v} - 1)}{e^{-\theta} - 1}\right) \quad (3.18)$$

As it is possible to observe, the copulae listed above are all monoparametric (i.e., θ). In Figure 3.6, an example of the three copulae generated with random parameter is shown.

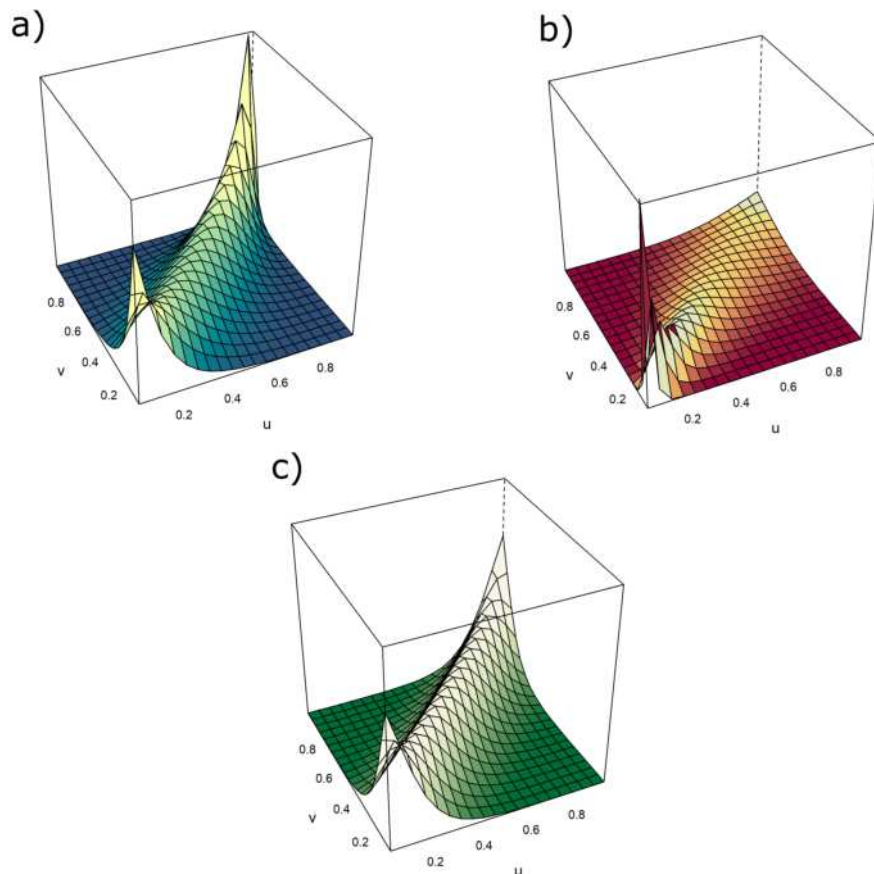


Figure 3.6: Example of Gumbel (a), Clayton (b) and Frank (c) copula generated with random parameter

More detailed information on these families of copulas, as well as on their generators,

the range of the parameter, and some special and limiting cases can be found in (Nelsen, 2006).

Up to now the two variables X and Y have been implicitly assumed to be linear, without any periodicity in their values or distributions. What would happen if one of them were instead a circular variable? Suppose X remains a linear variable, while the variable Y is replaced with Θ , defined on the unit circle between 0 and 2π . According to what explained in paragraph 3.2.1.1, the PDF of this variable needs to be 2π -periodic. This means that, while the domain of a linear-linear copula is the unit square (i.e., $[0, 1]^2$), the one related to a circular-linear copula is the surface of a cylinder, characterize by unit height (i.e., the support for the linear variable) and unit circle (i.e., the support for the circular variable). Hence, according to *Theorem 5* in Johnson and Wehrly (1978), the probability density function in equation 3.14 for a circular-linear copula can be written as follows:

$$f_{\Theta, X}(\theta, x) = 2\pi g(2\pi(F_{\Theta}(\theta) - F_X(x)))f_{\Theta}(\theta)f_X(x) \quad (3.19)$$

where $f_X(x)$ and $f_{\Theta}(\theta)$ are the marginal density on the line and on the circle, respectively, $F_X(x)$ and $F_{\Theta}(\theta)$ their cumulative distribution distribution functions and $g(\cdot)$ a 2π periodic density function on the circle.

Equation 3.19 represents one of the possible way to generate circular-linear copulae. However, Hodel and Fieberg (2021, 2022) develop a second approach that allows to obtain copulae with densities not only periodic, but also symmetric respect to the circular variable. This approach is based on combining two (or more) linear-linear copulae, considering the properties introduced in Nelsen (2006). In particular any convex linear combination of copulae is a copula and the orthogonal reflections of a copula density with respect to the lines $u = 0.5$ or $v = 0.5$ are also the density of the copula. Hence, the authors introduced two new types of copulae:

- **Rotated copulae (RC)**: obtained from the arithmetic mean between any linear-linear copula $C(u, v)$ and its othogonal reflection along the line $u = 0.5$ (i.e., assuming that u refers to the circular variable):

$$\text{CDF:} \quad C_{RC}(u, v) = 0.5[C(u, v) + v - C(1 - u, v)] \quad (3.20)$$

$$\text{PDF:} \quad c_{RC}(u, v) = 0.5[c(u, v) + c(1 - u, v)] \quad (3.21)$$

Figure 3.7 depicts a schematic representation on how these copulae are built. Moreover, the PDF of the rotated Clayton and Gumbel copula are shown.

- **Rectangular patchwork of copulae (RPC):** in this case the domain of the copula is divided into rectangular regions, R_i . The situation treated by Hodel and Fieberg (2021) is the case of two rectangles that are symmetric about $u = 0.5$:

$$\begin{aligned} R_1 &= [u_1, u_2] \times [0, 1] \\ R_2 &= [1 - u_2, 1 - u_1] \times [0, 1] \end{aligned} \quad (3.22)$$

with $0 \leq u_1 < u_2 \leq 0.5$. Hence, the patchwork-copula is periodic and symmetric in u if C_2 is the orthogonal reflection of C_1 with respect to $u = 0.5$ and if the two rectangles (i.e., R_1 and R_2) cover the entire unit square. In this case, the CDF and the PDF of a patchwork copula can be written as:

$$\text{CDF: } C_{RPC}(u, v) = \begin{cases} 0.5C_1(2u, v) & \text{if } u, v \in R_1 \\ 0.5(v - C_1(2u - 1, v)) + 0.5v & \text{if } u, v \in R_2 \end{cases} \quad (3.23)$$

$$\text{PDF: } c_{RPC}(u, v) = \begin{cases} 0.5c_1(2u, v) & \text{if } u, v \in R_1 \\ 0.5c_1(2 - 2u, v) & \text{if } u, v \in R_2 \end{cases} \quad (3.24)$$

As for Figure 3.7, Figure 3.8 shows a schematic representation on how rectangular patchwork of copulae are created. The PDF of the rotated Clayton and Gumbel copula are also represented.

Rotated Circular-Linear Copulae

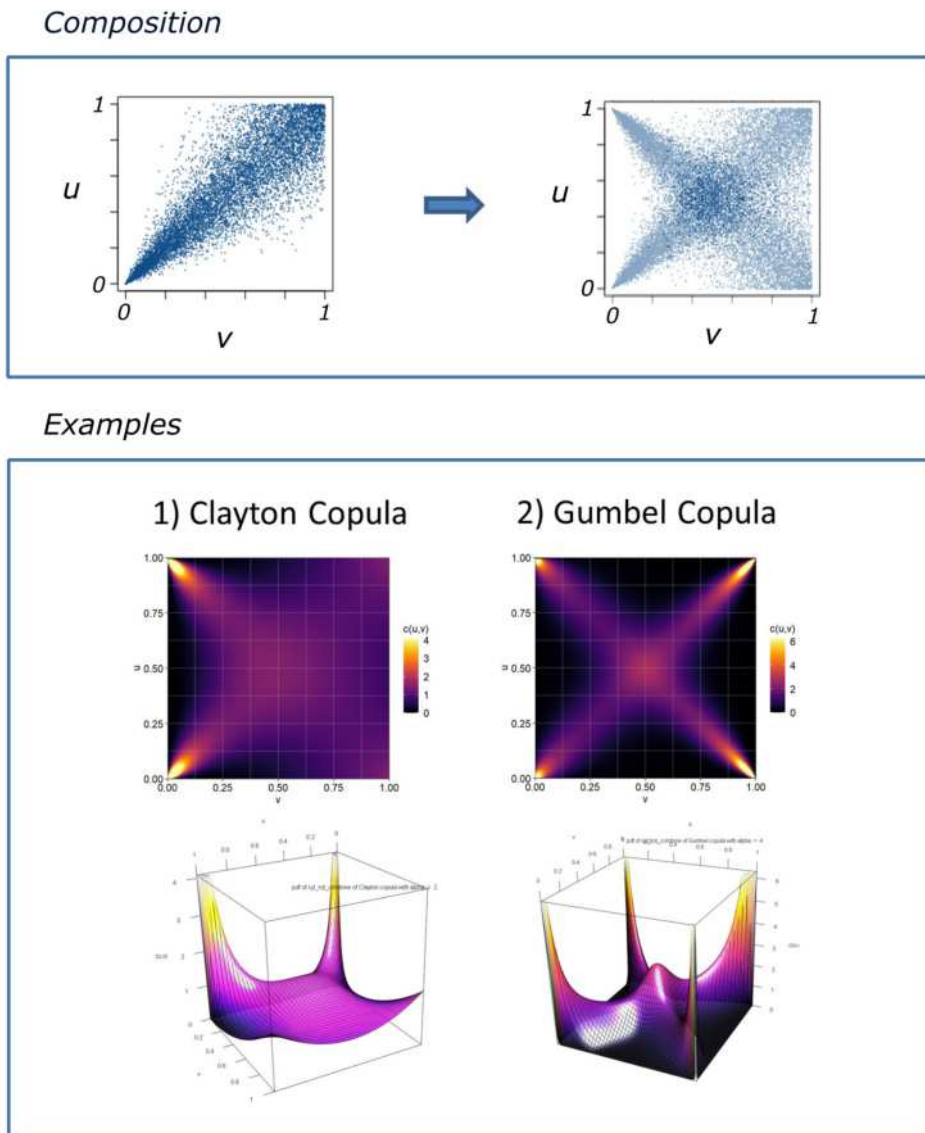
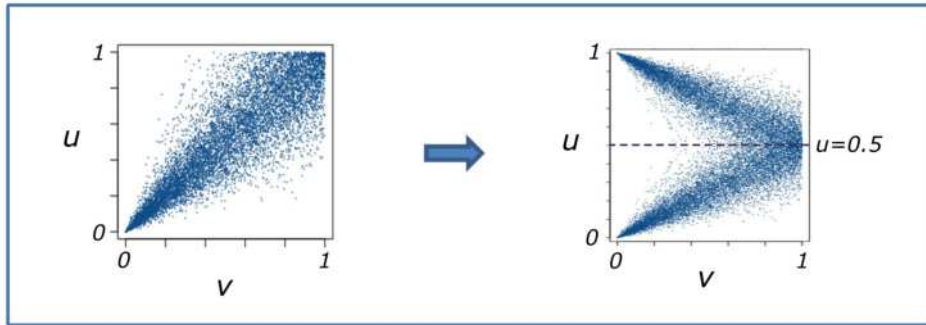


Figure 3.7: Example of rotated circular-linear copulae. The PDFs of the rotated Clayton and Gumbel copula is shown in a 2-D and 3-D visualization

Rectangular patchwork Circular-Linear Copulae

Composition



Examples

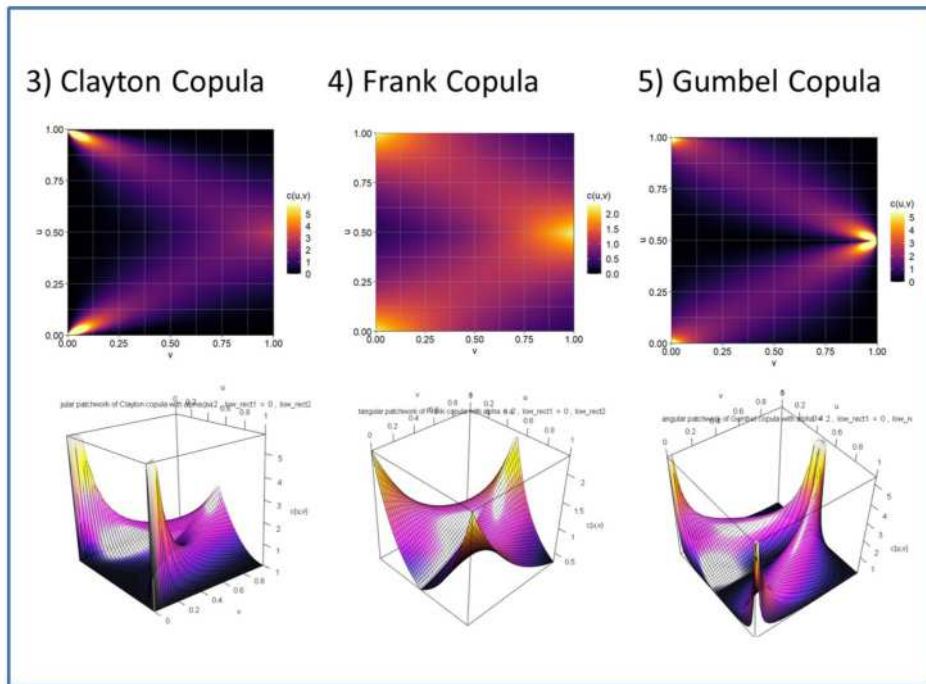


Figure 3.8: Example of rectangular patchwork of copulae. The PDFs of the rotated Clayton, Frank and Gumbel copula is shown in a 2-D and 3-D visualization

For further details on the mathematical and statistical framework of copulas, see Hodel and Fieberg (2022) and the `cylcop` package (Hodel and Fieberg, 2021) in R.

3.2.2. Precipitation datasets and data pre-processing

While the MSWEP-V2 has been used as reference dataset (see the beginning of this section), the Global Circulation Models (GCMs) projections provided by the Coupled Model Intercomparison Projects Phase 6 (CMIP6) (Eyring et al., 2016) are used to assess the future changes in the precipitation characteristic. All the models whose nominal resolution is ~ 100 km ($\sim 1^\circ$) and that have the historical and the future scenario (i.e., SSP1-2.6, SSP2-4.5, SSP3-7.0 and, SSP5-8.5) experiments available for precipitation have been selected. In particular, nine models (i.e., CESM2-WACCM, CMCC-CM2-SR5, CMCC-ESM2, EC-Earth3, EC-Earth3-Veg, GFDL-ESM4, MPI-ESM1-2-HR, MRI-ESM2, and TaiESM1) meet these conditions and the ‘r1i1p1f1’ variant (see section 1.1.4 for further details) has been chosen for each of these. The period for the historical experiment matches the one used for the reference (i.e., 1979-2014), while last 36 years of the 21st century (i.e., 2065 – 2100) have been considered for the future scenarios. Moreover, since the reference data and GCM outputs have different spatial resolutions, the MSWEP-V2 has been upscaled to the GCMs resolution by means of bilinear interpolation.

For each pixel, the 99th percentile of the precipitation distribution has been considered as the threshold to detect extreme precipitation events. Since the focus on extreme precipitation, it has been examined whether it was necessary to consider all landmasses or limit the study area to those zones characterized by more intense precipitation. To do this, the Köppen – Geiger climate classification map has been considered. In the Köppen – Geiger climate classification, climates are divided into five main group; each of these main groups is further subdivided into subgroups based on seasonal rainfall and temperature. The resulting zones are marked by an alphabetical code, in which the first letter represents the main group (i.e., tropical - A, arid - B, temperate - C, continental - D, and polar - E), while the others are related to the subgroups. As an example, *Af* refers to a tropical climate (A) characteristic of the rainforests (f), while *Dwa* refers to a continental climate (D) characterized by dry winter (w) and hot summer (a). Figure 3.9 shows a recent improvement of the Köppen – Geiger climate classification map presented in Beck et al. (2018).

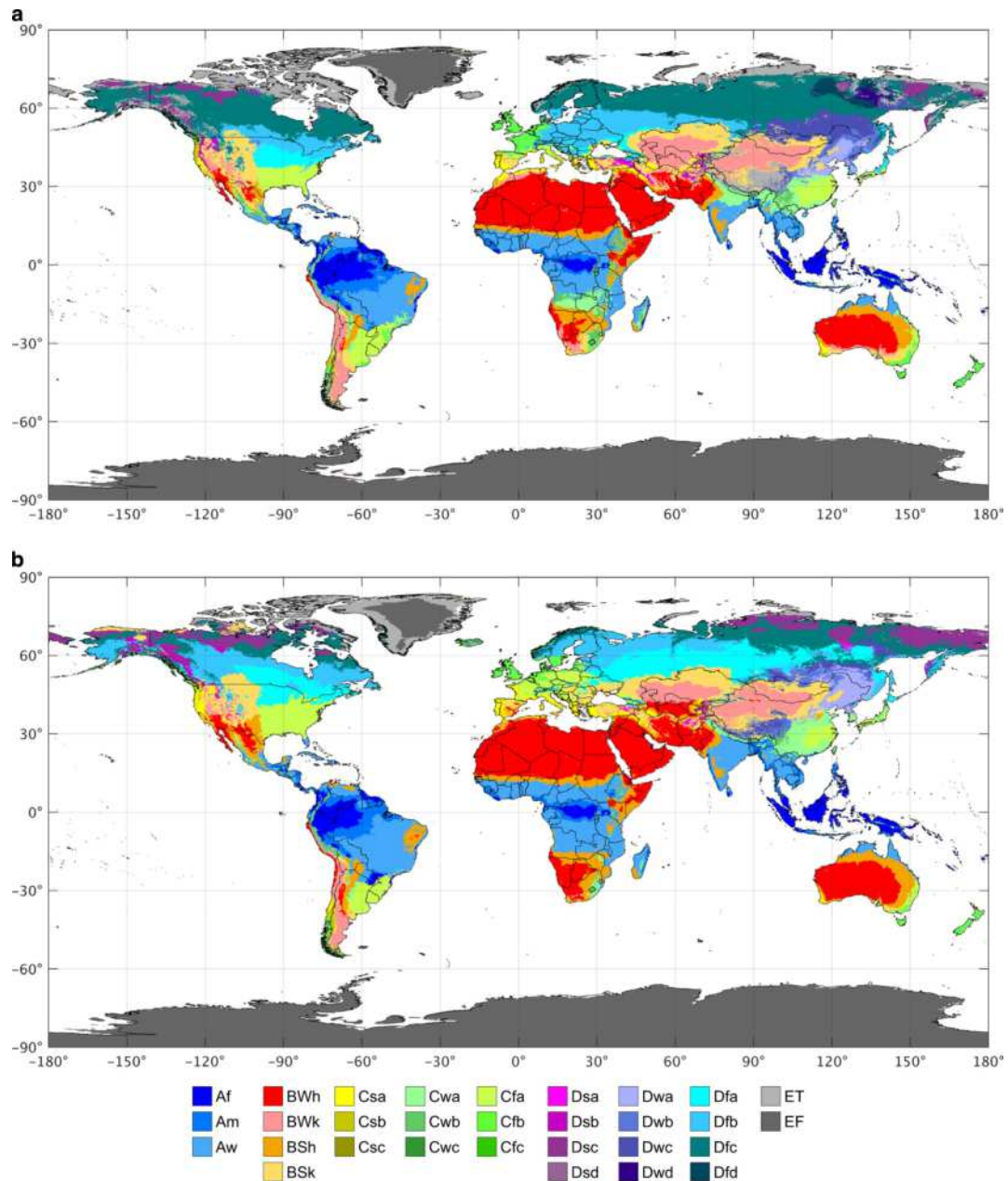


Figure 3.9: From Beck et al. (2018): Present-day (1980–2016) (a) and future (2071–2100) (b) Köppen-Geiger climate classification maps. The acronyms stand for: Tropical rainforest (Af), monsoon (Am), savannah (Aw); Arid desert - hot (Bwh), desert-cold (BWk), steppe-hot (BSh), steppe-cold (BSk); Temperate dry summer - hot summer (Csa), dry summer - warm summer (Csb), dry summer - cold summer (Csc), dry winter - hot summer (Cwa), dry winter - warm summer (Cwb), dry winter - cold summer (Cwc), no dry season - hot summer (Cfa), no dry season - warm summer (Cfb), no dry season - cold summer (Cfc); Cold dry summer - hot summer (Dsa), dry summer - warm summer (Dsb), dry summer - cold summer (Dsc), dry summer - very cold winter (Dsd), dry winter - hot summer (Dwa), dry winter - warm summer (Dwb), dry winter - cold summer (Dwc), dry winter - very cold winter (Dwd), no dry season - hot summer (Dfa), no dry season - warm summer (Dfb), no dry season - cold summer (Dfc) no dry season - very cold winter (Dfd); Polar tundra (ET), Polar frost (EF)

This map has been derived by using an ensemble of four high-resolution, topographically-

corrected climatic maps and it has been downscaled up to $\sim 1\text{km}$ spatial resolution. The advantage of using this product is that it also provides future conditions (2071 – 2100) derived from an ensemble of 32 climate model projections under the RCP8.5 scenario, allowing to evaluate the future changes the considered variables in light of the different climate zones.

Hence, the box plots of the extreme precipitation events for the reference dataset has been computed for each climate type and the outcomes are shown in Figure 3.10. In this figure, rows are representative of the five main climate groups, while the sub-climate spatial distributions are depicted on the left together with the box plots of the corresponding threshold values in the right column. Each box ranges from the 25th to the 75th percentile and the median is depicted with the black solid line; the whiskers show the 5th and the 95th percentile as the minimum and the maximum value, respectively. As it is possible to observe, the box plot median values are relevant especially for the Tropical and the Temperate climatic zones, while they slightly decrease Cold and Polar areas. However, focusing on the the Arid climate, it is possible to observe that the 50% of the extreme precipitation events are below 5 mm while the 3rd quartile is below 10 mm in the “Arid, desert, hot” (*Bwh*) and the “Arid, desert, cold” (*Bwk*). Hence, these areas have been removed in order to avoid unrealistic results, since the connotation of "extreme" is lost for precipitation events.

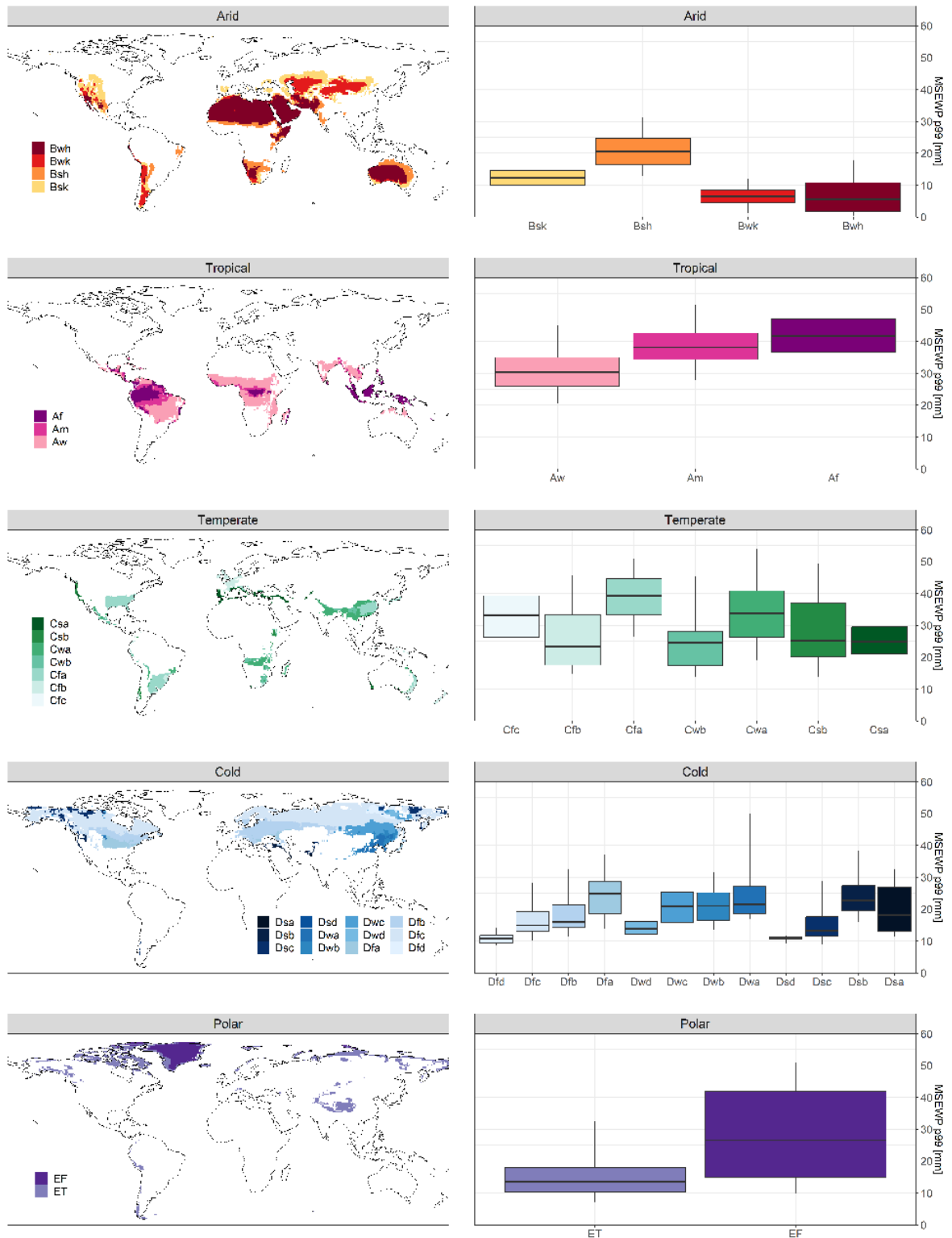


Figure 3.10: Value of the 99th percentile of the precipitation distribution for different climates according to a future Köppen – Geiger climate classification map (Beck et al., 2018). Rows are representative of Arid, Tropical, Temperate, Cold, and Polar classification, while the sub-climate spatial distributions are depicted on the left together with the box plots of the corresponding threshold values in the right column

3.2.3. GCMs validation and statistical framework

Based on what reported in paragraphs 3.2.1.1 and 3.2.1.2, here for the first time circular-linear copulae are used to model the bivariate dependence between the intensity and time of occurrence of precipitation extremes, as well as to derive future changes in these joint characteristics.

The rainfall depth, h (mm), has been analyzed through standard linear statistics (i.e., being a variable with support from 0 and ∞), while the day within a year in which a given event occur, d (day), has been shaped through circular statistics because of its periodic nature. First, the seasonal variable has been circularized, as explained in paragraph 3.2.1.1 by converting the days of the year into angles. At this point, it has been possible to compute the empirical (u,v) probabilities for both features. Then, five different circular-linear copulae, derived from a linear combination and a rectangular patchwork of Archimedean copulae (i.e., Gumbel, Clayton and Frank copulae), has been used to model their bivariate dependence. This analysis has been performed on a pixel-by-pixel basis for the reference dataset and the Akaike Information Criterion (AIC) has been used as performance metric to select the best copula. In particular, since this parsimony provides an estimate of the discrepancy to the “true model”, the copula with the smallest value has been selected. Figure 3.11 shows a schematic representation of the statistical framework. In this case, a rotated Clayton copula has been chosen as the best circular-linear copula to shape the bivariate dependence between the magnitude and the seasonality of the extremes.

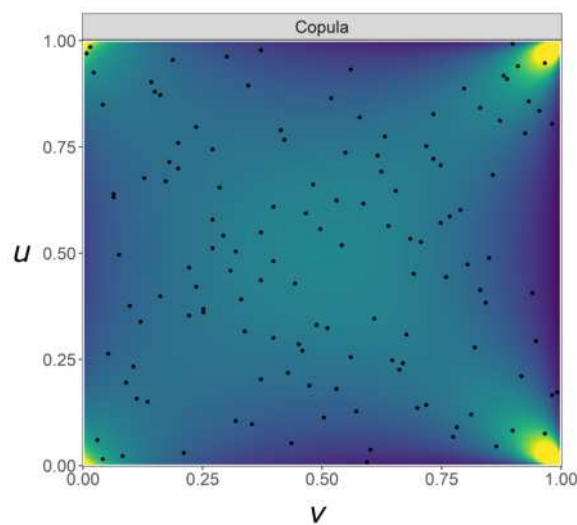


Figure 3.11: Empirical (u,v) points overlaid to the best selected copula according to the Akaike Information Criterion. u refers to the circular variable, while v to the linear one. The viridis colors represent the copula density. In particular the density decreases as the colors change from yellow to purple

To verify if the GCM historical experiments can capture the statistical dependence between the two variables, a bootstrap approach based on the AIC has been developed. Indeed, the AIC is an estimator of relative quality (i.e., test different models for a given set of data) and it cannot be directly used in an "absolute" sense. Hence, the procedure applied to each pixel is explained in the following and outlined in Figure 3.12:

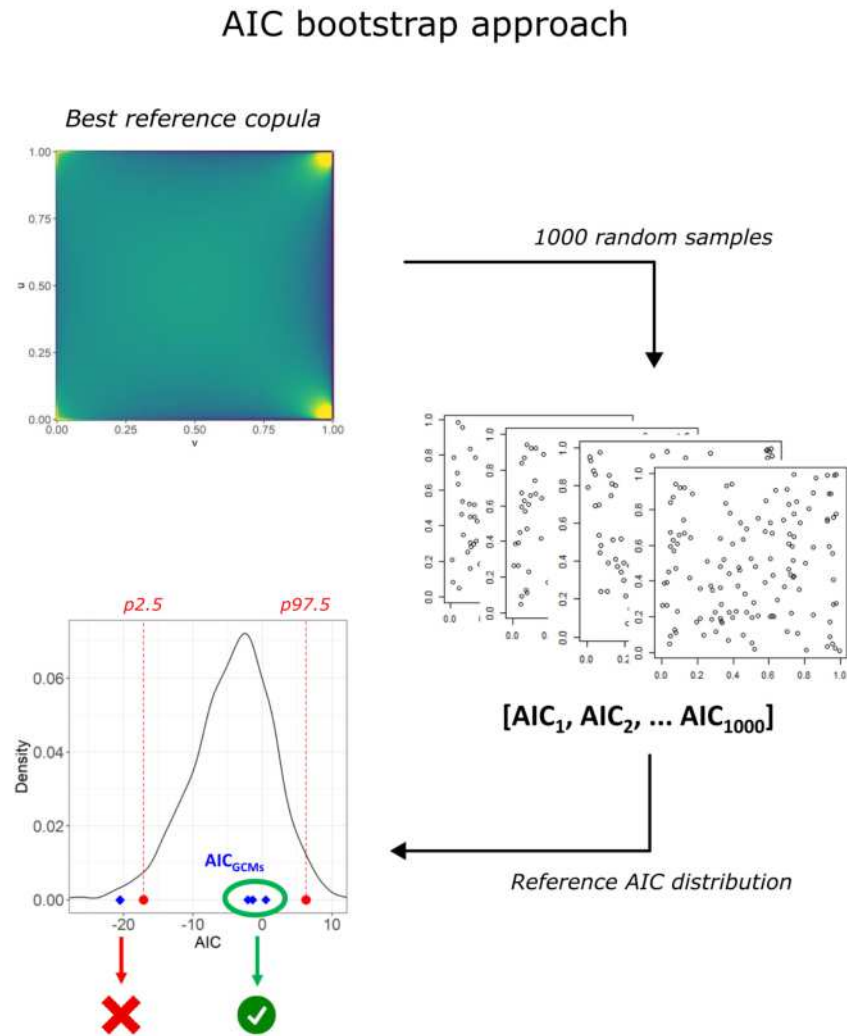


Figure 3.12: Outline of the AIC bootstrap approach

1. one thousand random samples is generated from the best copula selected for the reference data;
2. for each sample, which has the same size as the original one, the AIC is recomputed, allowing to derive a reference AIC distribution for each pixel of the dataset;
3. the reference best copula is then fitted to the extremes extracted from the historical experiment of the nine GCMs and the corresponding AIC are computed;

4. if these AIC values are between the 2.5 and the 97.5 percentiles of the reference AIC distribution, then there is not enough evidence to reject the null hypothesis that the GCM data are extracted from the same copula as the reference data. Hence, it is possible to consider this as a case in which the GCM can reproduce the statistical dependence in the reference data. Although a two-sided test for the AIC may seem counterintuitive, it has been used in this case as the sole objective is to validate the historical experiment of the GCMs.

The results of this procedure are shown in Figure 3.13, where the panels indicate the IPCC reference regions (Stocker et al., 2014) (see Figure B.1 in the Appendix C for more details), while the bars refer to the nine GCMs analyzed. The red color indicates the percentage of pixels where there is not enough evidence to reject the null hypothesis that the GCM outputs can be extracted from the same copula as the reference data. As it is possible to notice from this figure, the possibility to not reject the null hypothesis of the test is always higher than 75% for all IPCC zones, reaching more than 90% in most of the cases. For this reason, it is possible to conclude that globally the GCMs can capture the precipitation characteristics in the reference data and can be used to assess the projected changes in the magnitude and seasonality of precipitation extremes.



Figure 3.13: Results of the AIC bootstrap approach for the validation of the GCMs. The panels indicate the IPCC zones, while the bars refer to the nine GCMs analyzed. The red color indicates the percentage of pixels where there is not enough evidence to reject the null hypothesis that the GCM outputs can be extracted from the same copula as the reference data

Once the reference best copula has been used for the validation procedure between reference dataset and historical experiment, the copula fitting procedure has been reapplied for each GCM and experiment. Indeed, even if it is not possible to reject the hypothesis that the precipitation extremes from the GCMs are extracted from the reference best copula, there may be one that better fits the data according to the AIC.

After this step, the marginal distributions of the two variables have been fitted. More specifically, the Generalized Pareto Distribution (GPD) has been considered as the marginal distribution for the rainfall depth, while a mixture of N von Mises distributions (vMD) has been chosen to model the marginal distribution of the circular variable. The choice of these two distributions is motivated by the fact that the GPD is often used in the case of POT values, whereas mixtures of vMD allow for greater flexibility in modeling more than one peak, where present, in the seasonality of the extremes. However, the goodness-of-fit of the GPD distribution has been evaluated through the application of the Anderson-Darling test where the significance of the test is computed by means of a Monte Carlo approach (Choulakian and Stephens, 2001).

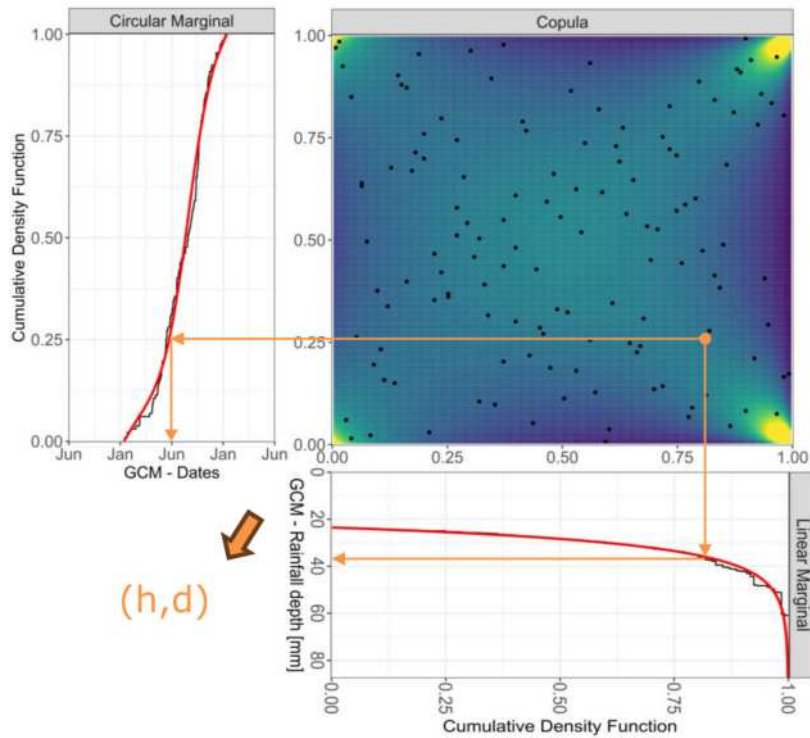


Figure 3.14: Example of the procedure followed to derive the bivariate dependence between magnitude and occurrence of precipitation extremes. In the top right panel, the empirical (u,v) points are overlaid to a circular-linear copula. The other panels show the linear (bottom-right) and the circular (top-left) marginal distribution. The empirical CDF is depicted in black, while the theoretical GPD and vMD with red color

Regarding the circular variable, since it is not possible to know a-priori the optimal number of mixtures for the vMD, this number has been tested ranging from one to four, and at the end the model with the lowest Bayesian Information Criterion (BIC) has been chosen (Veatch and Villarini, 2020, 2022). Figure 3.14 shows a representation of the described procedure. From this figure it is possible to observe that the marginal distributions can capture well the shape of the empirical CDF.

3.2.4. Future changes in the bivariate dependence

Once the bivariate dependence and the marginal distributions are known, it is possible to quantify the variation in the characteristics of the extremes. Indeed, the combination between copula and its marginal distributions can be used as "stochastic extreme precipitation generator". Hence, for each experiment and GCM, one million random (u,v) pairs have been generated from the selected copula of every single pixel.

Transforming these values to the original units through the marginal distributions, (h,d) , it is possible to obtain a sample of rainfall depth, h , per each day, d , of the year.

These extreme daily data samples have been used to compute the empirical cumulative distribution function conditioned to the date (ECDF($h|d$)), providing for each day of the year the exceedance probability of the precipitation extremes.

Given the need to find a way to condense this large amount of information, the median value of the daily ECDF($h|d$), $h_{50}(d)$, has been used as a proxy for the extreme value that might occur in that day. An example is shown in Figure 3.15, in which the red line indicates the $h_{50}(d)$ and is superimposed onto the 2-D density of the generated rainfall depth.

Therefore, the maximum of the daily median values has been considered as the reference rainfall depth (H_{50}) that may happen on a specific day ($D(H_{50})$) of the year according to the bivariate statistical structure derived from the data.

Once these values are defined for each pixel (i) in each GCM (m) and experiment (*hist* and *SSP*), we can quantify the future changes in the magnitude ($\Delta\bar{R}_{i,SSP}$) and seasonality ($\Delta\bar{S}_{i,SSP}$) of precipitation extremes, compared to the historical experiments, by computing the following quantities:

$$\Delta\bar{R}_{i,SSP} = 100 \cdot \frac{\bar{H}_{50i,SSP} - \bar{H}_{50i,hist}}{\bar{H}_{50i,hist}} \quad (\%) \quad (3.25)$$

$$\Delta\bar{S}_{i,SSP} = \frac{\bar{D}(H_{50})_{i,hist} - \bar{D}(H_{50})_{i,SSP}}{30} \quad (month) \quad (3.26)$$

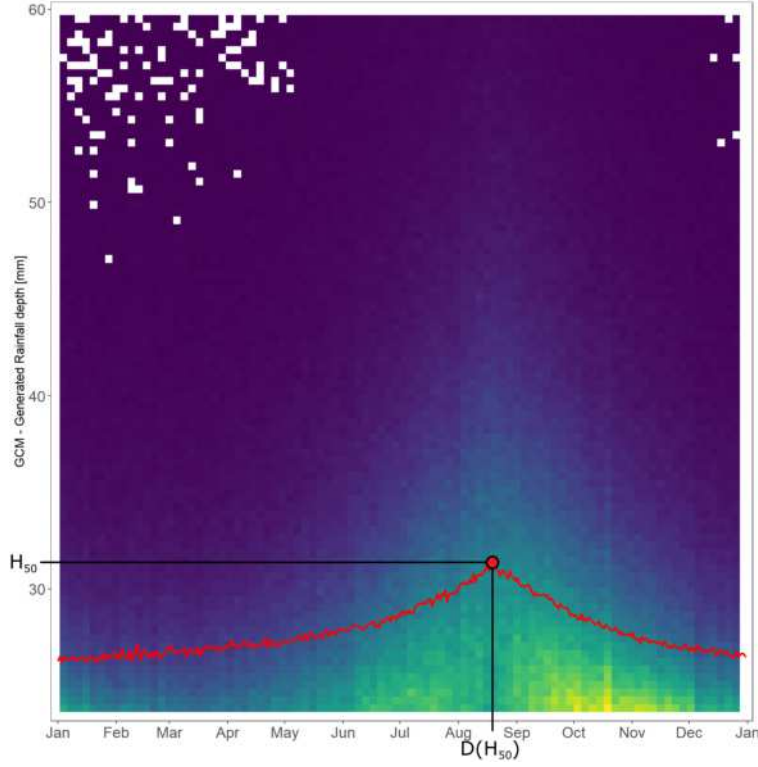


Figure 3.15: Example of exceedances of the 2-D density generated from the selected copula and marginal distributions. As for Figure 3.11, the density decreases as the colors change from yellow to purple. The red line indicates the median daily extreme precipitation depth $h_{50}(d)$. The red dot corresponds to the maximum of the $h_{50}(d)$ and represents the reference precipitation depth (H_{50}) that is projected to occur on a specific day ($D(H_{50})$) of the year according to the developed bivariate model

where:

- $\bar{H}_{50i,SSP}$ and $\bar{H}_{50i,hist}$ represent the average of the H_{50} among the nine GCMs (m):

$$\bar{H}_{50i,SSP} = \frac{1}{N} \sum_{m=1}^N H_{50i,SSP_m} \quad (3.27)$$

$$\bar{H}_{50i,hist} = \frac{1}{N} \sum_{m=1}^N H_{50i,hist_m} \quad (3.28)$$

- $\bar{D}(H_{50})_{i,SSP}$ and $\bar{D}(H_{50})_{i,hist}$ represent the the circular mean of the $D(H_{50})$ among the nine GCMs (m):

$$\bar{D}(H_{50})_{i,SSP} = circular.mean(D(H_{50})_{i,SSP_m}) \quad (3.29)$$

$$\bar{D}(H_{50})_{i,hist} = circular.mean(D(H_{50})_{i,hist_m}) \quad (3.30)$$

It is worth emphasizing that the change in seasonality is considered by taking into account the dominant mode, as expressed by equation 3.5. For both the quantities the average value among the GCMs has been computed to reduce the uncertainty associated with any individual model. Moreover, it is worth noting that, while in the case of $\overline{H}_{50,i,SSP}$ and $\overline{H}_{50,i,hist}$ it is possible to use the linear way to compute the average among the models, for $\overline{D}(H_{50})_{i,SSP}$ and $\overline{D}(H_{50})_{i,hist}$ it is important to compute the circular mean. In Figure 3.16 we show a schematic representation of the meaning of $\Delta\overline{R}_{i,SSP}$ and $\Delta\overline{S}_{i,SSP}$ on the circular-linear plane.

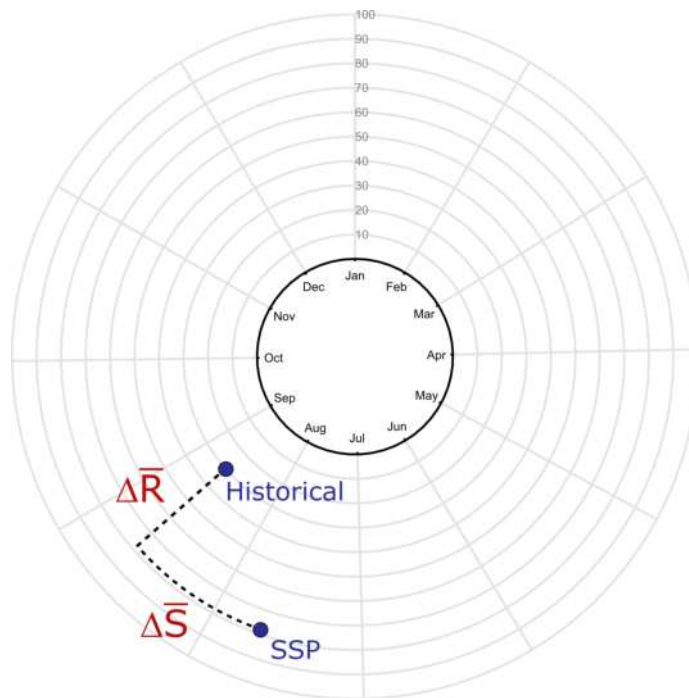


Figure 3.16: Example of how $\Delta\overline{R}_{i,SSP}$ and $\Delta\overline{S}_{i,SSP}$ are derived, starting from the historical and SSP average values (blue dots)

Figure 3.17 shows the projected changes in the characteristics of the extreme precipitation for the 2065–2100 period with respect to the historical baseline (1979–2014) across the four different SSPs. To display the results in a concise and visible way, a bivariate circular palette has been developed to display the changes in seasonality $\Delta\overline{S}$ (i.e., change in color) and the changes in magnitude $\Delta\overline{R}$ (i.e., change in brightness). Positive (negative) percentages for $\Delta\overline{R}$ indicate an increase (decrease) in the intensity of the future extreme events compared to the past, while positive (negative) values for the $\Delta\overline{S}$ indicate a backward (forward) shift in seasonality.

Globally, the results suggest that climate change is expected to make precipitation extremes more intense compared to the past. However, the changes in the magnitude are particularly tied with the emission scenario, moving from an increment that ranges from

0 to 50% in the case of the SSP1-2.6, to values up to 100% for highest emission scenario. The areas that are expected to experience the largest changes are mainly located in India and in the Bay of Bengal, pointing to a strengthening of monsoon in the future (Menon et al., 2013; Katzenberger et al., 2021).

Similar large changes in magnitude are projected for the equatorial Africa, consistent with other published results (Diem et al., 2019; Jiang et al., 2021). These increases are large, and are expected to lead to even larger impacts considering that they are projected to occur in the upper tail of the precipitation distribution, jeopardizing the reliability of the infrastructures designed in the past (Nissen and Ulbrich, 2017) and posing a serious threat to human life and global economy.

The results so far are just one side of the coin. Indeed, the potential changes in the time of the year in which these events occur represent the other side of the coin. There are large areas of the world exhibiting large temporal shift in the \overline{H}_{50} , such as South America, Southern and Eastern United States, Central Africa, Central Europe, India, China, Indochinese Peninsula and Indonesia. These findings are generally consistent regardless of the SSPs considered, even though there are asymmetries moving from SSP1 and SSP2 (i.e., the scatterplots that are relatively symmetric around the no-change value) to SSP3 and SSP5 (i.e., there is a shift towards negative values). From a physical point of view, this forward shift (i.e., extreme events occurring later in the season) might be the result of a longer duration of the rainfall season driven by global warming, thus increasing the risk of extreme precipitation events to last for longer periods (Pfleiderer et al., 2019). Indeed, a global increase in air temperature might lead to higher evaporation rates from the oceans, enhancing their contribution in the global hydrological cycle (Findell et al., 2019); moreover, rising temperatures play a fundamental role in the latent heat flux that is responsible for storm intensification (Pendergrass, 2018). The changes in seasonality are particularly evident across the Amazon Forest and the southeastern part of South America, where there are shifts ranging from 15 days up to 3 months later in the season, larger than what shown in Marelle et al. (2018) (possibly because of different methodologies and model resolution); one possible explanation for our results is the potential impact of climate change in the seasonal precipitation related to ENSO (Grimm, 2011). Indonesia is another region exhibiting a particularly strong forward shift in the occurrence of precipitation extremes; this is in agreement with what (Supari et al., 2017) observed in the historical data regarding an increasing trend for some precipitation indicators (i.e., monthly maximum 1-day precipitation and annual total precipitation divided by the number of wet days in the year) during the months that follow the recognized wet season. While the general tendency is towards precipitation extremes to occur later in the year, there are locations like Thailand, the Bay of Bengal, Philippines, and the eastern

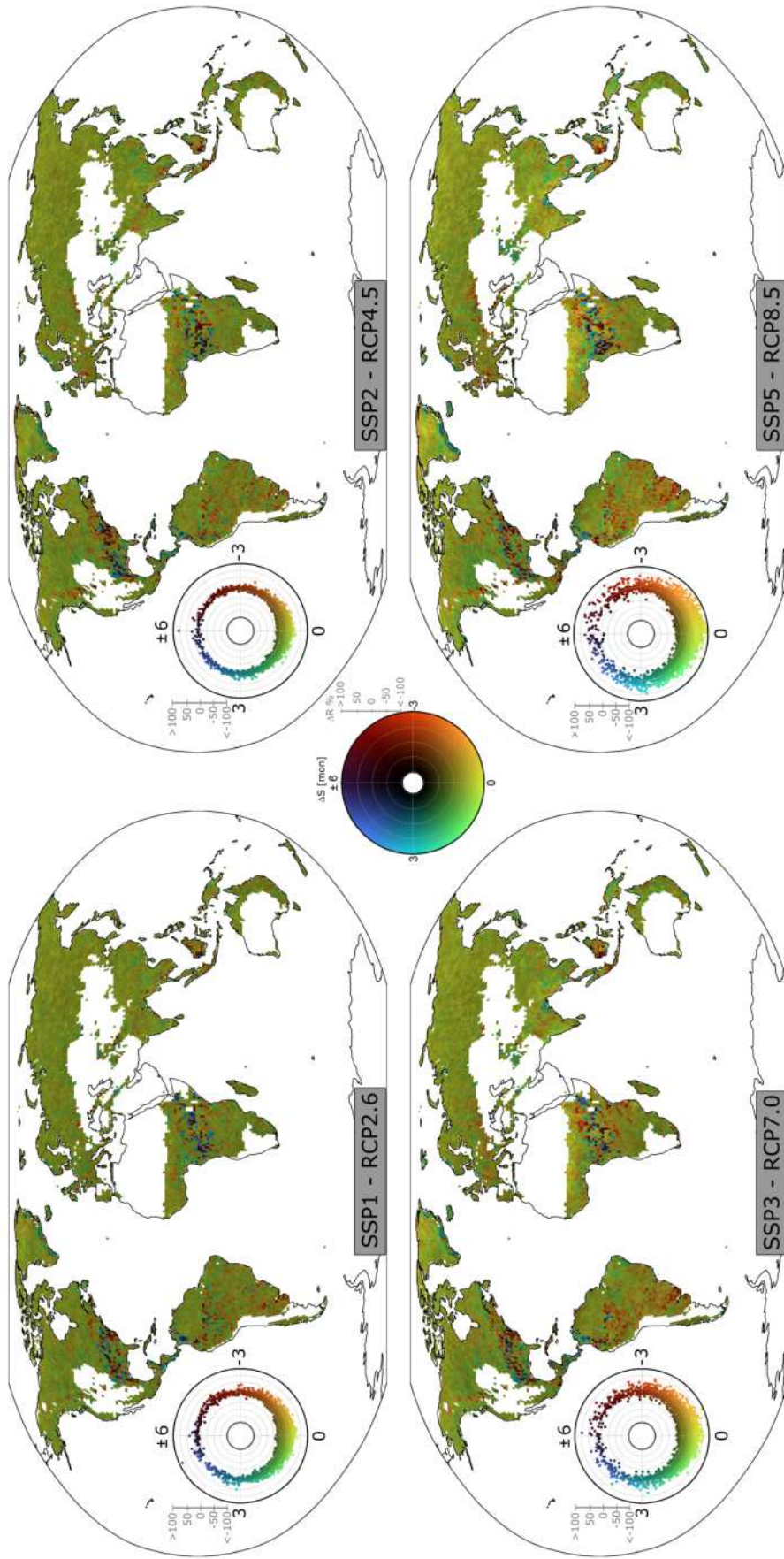


Figure 3.17: Average projected changes in the characteristics of the extreme precipitation for the 2065- 2100 period with respect to the historical baseline (1979 – 2014) under four difference scenarios (SSP1-RCP2.6, SSP2-RCP4.5, SSP3-RCP7.0, and SSP5-RCP8.5). The bivariate circular palette is here used to concurrently display the shift in the seasonality (i.e., $\Delta\bar{S}$ change in color) and the changes in the magnitude (i.e., $\Delta\bar{R}$ change in brightness). Positive (negative) percentages for the $\Delta\bar{R}$ indicate an increase (decrease) in the intensity of the future extreme events compared to the past, while positive (negative) values for the $\Delta\bar{S}$ indicate a backward (forward) potential shift in the seasonality. The scatterplot inside each panel shows where the pixel values are located within the bivariate circular plane

coast of Greenland, where these events are expected to occur earlier in the year (Marelle et al., 2018).

The southeastern United States and central Africa exhibit large shifts in the seasonality of the precipitation extremes, with the seasonality of extreme precipitation that exhibits both positive and negative shifts within these regions. Looking back to Figure 3.3, these areas have already been recognized as not having a clear dependence of the extremes with the season. Hence, is it possible that these large changes in seasonality (i.e., on the order of months) belong to areas where it would be too reductive to consider a single mode in the seasonality of heavy precipitation? In other word, is it possible that these important shifts are due to changes from one dominant physical mechanism to another? To answer this question, the results of the analyses have been stratified by the number of von Mises distributions mixtures selected. Indeed, requiring more than one mixture in modeling the seasonal component implicitly means assuming that the extremes are not seasonally clustered, but that multiple modes (i.e., physical processes that generate intense precipitation) can be identified in their annual distribution. Figure 3.18 shows the percentage of pixels characterized by a given number of mixture components and the corresponding values of $\Delta\bar{S}$ for the different SSPs.

For small changes in seasonality (i.e., $\Delta\bar{S}$ around 0), the greatest part of pixels are characterized by a single mode (i.e., season) or two. However, the picture changes as the $\Delta\bar{S}$ values increase, with a transition towards a larger contribution by 2- and 3-component distributions compared to the single mode. While the number of pixels with large changes in seasonality increases moving from SSP1–RCP2.6 to SSP5–RCP8.5, the picture does not change across the different scenarios, suggesting that this is a behavior that is not dependent on SSP considered. Hence, these results point to large changes in seasonality that are not so much tied to an extension of a given season or to a complete reversal of the seasonal characteristic of extreme precipitation, but rather to the shifts in extreme precipitation across different generating mechanisms. This is particularly true for locations (e.g., southeastern United States, central Africa) that are characterized by different weather systems responsible for extreme precipitation events (i.e., mesoscale convective systems, tropical cyclones, oscillation of the ITCZ).

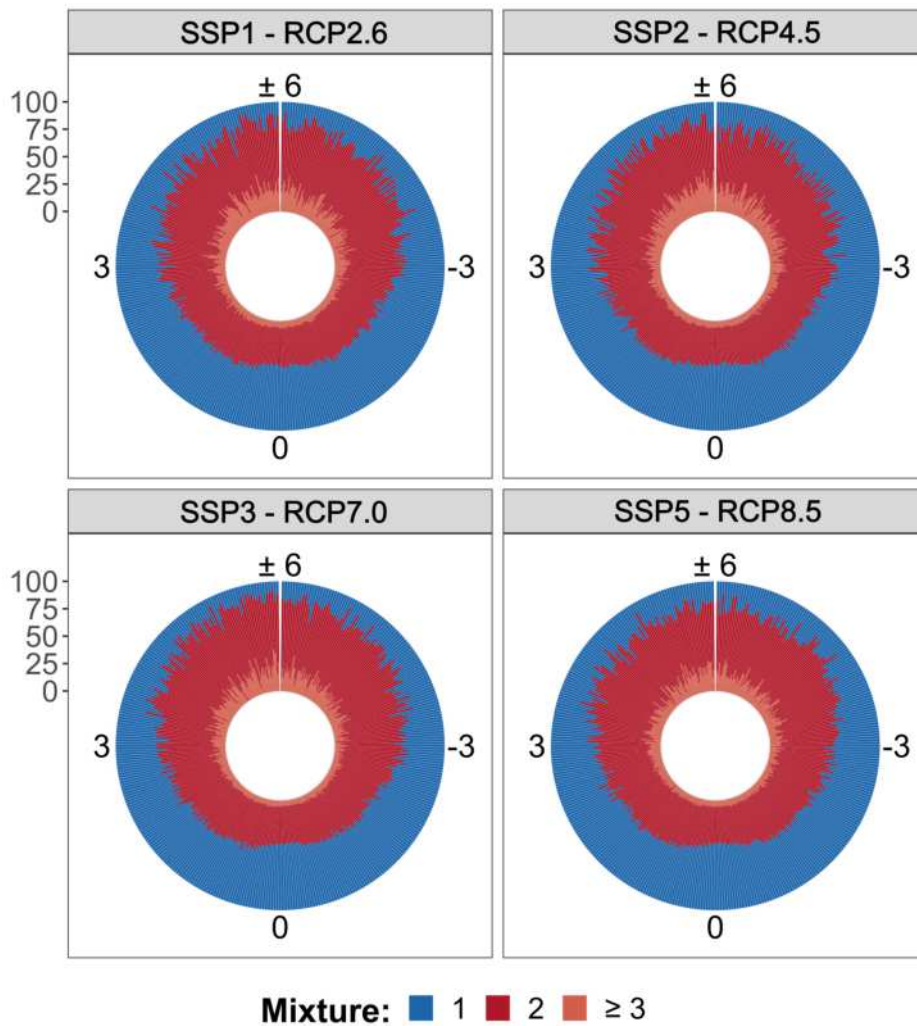


Figure 3.18: Projected changes in seasonality as a function of seasonal components. Percentage of pixels characterized by one, two or more than three von Mises distributions per discrete values of $\Delta \bar{S}$ (in months) for SSP1-RCP2.6, SSP2-RCP4.5, SSP3-RCP7.0, and SSP5-RCP8.5 scenario.

3.2.5. Final considerations on the changes in the characteristics of precipitation extremes

In this chapter, two primary precipitation characteristics, namely intensity and seasonality, have been jointly analyzed for the first time. What has been found points not only to an increase in the magnitude of the extreme precipitation events, but also to changes in their seasonality, leading to potentially serious impacts across different sectors and spheres of our lives, from human health to economy and ecology. The bivariate circular-linear model appears to be the proper way to highlight that there are potentially large changes regarding the expected occurrence of extreme precipitation events,

especially for high emission scenarios. These findings highlight to the need to develop mitigation and adaptation strategies and water resources planning that are flexible to account for the occurrence of extremes for periods out of the expected season. Indeed, these findings may raise different questions. How should the management of hydraulic infrastructures (e.g., dams, detention basins, etc.) change in this scenario? Are the climate change adaptation and resilience strategies implemented so far reliable in this case? What could be the consequences for the agricultural and industrial sectors? Moreover, based on the SSP scenarios, the intensity of the precipitation extremes is expected to be exacerbated globally from SSP1 (i.e., “sustainability”) to SSP5 (i.e., “fossil fueled development”), emphasizing the importance that actual policies and behaviors could have in addressing future climate change issues. Finally, these results point to the need to consider the characteristics of extreme precipitation events in a more holistic way, accounting for the potential interdependencies among them.

4 | Chapter four

4.1. Compound events for an improved risk assessment

The Earth's climate and hydrology systems are intricate, interconnected, and highly dynamic. Climate change, driven by various natural and anthropogenic factors, is causing shifts in weather patterns, precipitation regimes, and temperature extremes across the globe (Masson-Delmotte et al., 2021). At the same time, the study of the impacts and consequences of climate change on hydro-meteorological variables represents a challenge for the scientific community, given the growing awareness of the global public opinion about the climate crisis and the increasing availability of data and computational resources. While the emphasis is generally focused on a single hazard (e.g., heat stress, extreme precipitation, floods, droughts), their compounding effects under climate change have been the subject of a growing number of studies (Wahl et al., 2015; Zscheischler et al., 2018, 2020; Ridder et al., 2020), leading to a better understanding and an improved assessment of the risk associated with the occurrence of these extremes (Leonard et al., 2014; Zscheischler and Seneviratne, 2017; Bevacqua et al., 2019). As an example, Figure 4.1 shows the the number of publications on the topic of *compound events* since 1992. The curve, which considers only publications in the field of *Earth Sciences*, *Environmental Sciences*, *Atmospheric Sciences*, and *Engineering*, exhibits a clear exponential trend, indicative of the growing interest and attention to this topic.

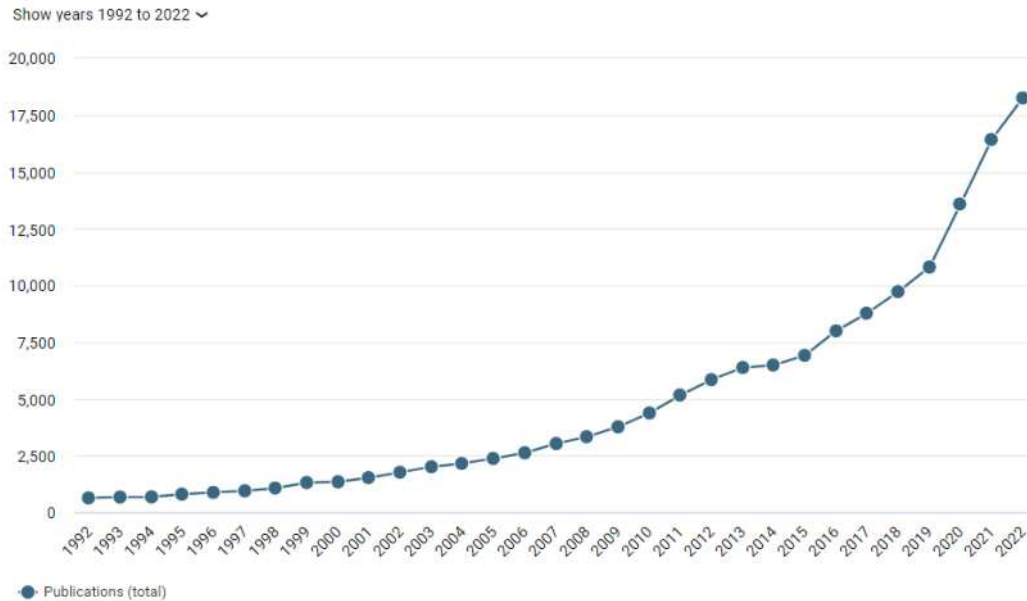


Figure 4.1: From app.dimensions.ai: Number of publications per year on the topic of compound events. The number of publications was filtered considering only those in the following macro areas: *Earth Sciences*, *Environmental Sciences*, *Atmospheric Sciences*, *Engineering*

Compound events refer to the simultaneous or sequential combination of multiple climatic or hydrological drivers and/or hazards, that can lead to more significant societal or environmental risk (Zscheischler et al., 2018, 2020; Masson-Delmotte et al., 2021). In other words, it has been realized that the complexity of the climatic and atmospheric system, as well as the interactions between intense phenomena and surface impacts, can hardly be totally explained by considering a single driver. On the contrary, by combining multiple phenomena and/or hazards it is easier to provide a clearer and more comprehensive picture of the resulting impacts and risks. The contributing events can have similar characteristics (clustered multiple events) or can grasp to different types (Seneviratne et al., 2012; Zscheischler et al., 2020). This aspect has been emphasized across a wide spectrum of hazards, including droughts (Vogel et al., 2021), heatwaves (Geirinhas et al., 2021), wildfires (Moftakhari and AghaKouchak, 2019), coastal extremes (Wahl et al., 2015), and floods (Zhang and Villarini, 2020).

A schematic representation of a compound event is provided by Zscheischler et al. (2020) and shown in Figure 4.2. From this figure it can be seen that there are four key elements that constitute such an event: modulator, driver, hazard and impact. The *modulator* represents the large-scale climatological system that regulate the mechanisms of compound events. In compound events, therefore, knowledge of climatology is crucial because it is precisely the modulators that determine the frequency and location of the drivers. In turn, the *drivers* represent the physical phenomena that result from them,

such as storms, tropical cyclones, cold fronts, and so on. If this first part of the scheme related to compound events defines the "physical" aspect, the second part is inherently connected to the "probabilistic" one. In fact, the study of climatic drivers is fundamental when there is a real *hazard*, namely that they have the potential to trigger one or more *impacts* (e.g., economic, social, or in terms of human lives).

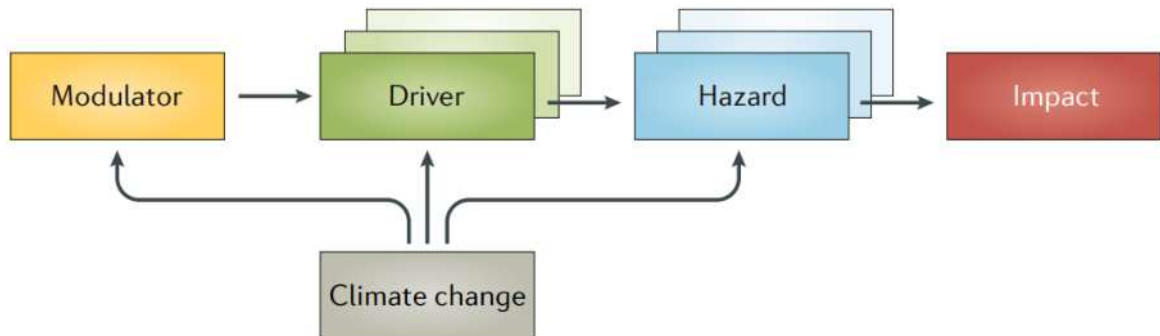


Figure 4.2: From Zscheischler et al. (2020): Overview of elements in the climate and weather domain that make up a compound event

Anthropogenic climate change is able to affect all elements that constitute compound events, directly conditioning climatology (and thus modulators) by amplifying the magnitude of drivers, increasing the hazard of events, and exposing society to more impacts. Hence, one aspect worth highlighting is how climate change alters the representation of the hydro-meteorological variables involved in the compounding. As depicted in Figures 1.3b and c, a potential effect of climate change is to create alterations in the mean and variance of the variable's distribution, thereby resulting in an increase (or decrease) in the frequency and magnitude of the events in the distribution's tails. However, what is shown in these figures refers to a single variable, namely to a univariate space. Since compound events refer to a combination between multiple phenomena, it is necessary to consider the bivariate (or multivariate) distributions to correctly estimate the response in the total risks. Figure 4.3 (Zscheischler et al., 2020) helps to clarify this key point in the theory of compound event. In an equilibrium system with no external pressures, the probability distributions of two generic drivers/hazards could be the red for drivers/hazards 1 and the gray for drivers/hazards 2. The occurrence probability of the compound event of a certain intensity is necessarily represented in a two-dimensional space, specifically depicted by the gray contour lines at the center of each panel. If one now imagines altering this equilibrium state by modifying the statistics of only one of the two distributions (e.g., due to the future effects of climate change), the final picture might be dramatic. Indeed, a shift in the mean of the distributions of driver/hazard 2 (panel a) it would translate to

an increase (or decrease) in the probability of occurrence of more (or less) intense events, from a univariate perspective.

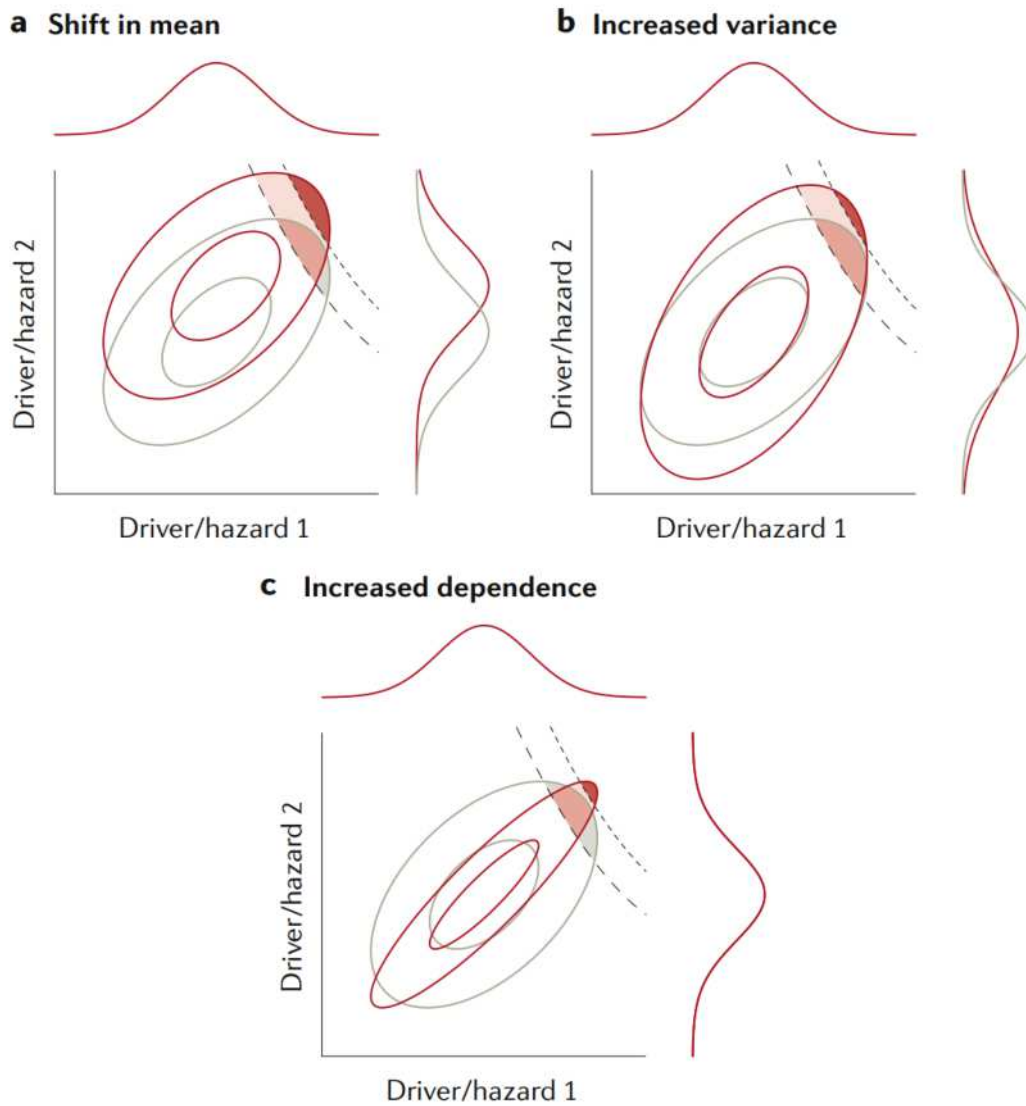


Figure 4.3: From Zscheischler et al. (2020): Hypothetical responses in the probability of compound events (shift of the bivariate distribution from grey to red) arising from a shift in the mean of driver or hazard 2 (panel a), an increase in the variability of driver or hazard 2 while holding correlation between the variables constant (panel b) and an increase in the strength of the dependence between driver or hazards 1 and 2 (panel c). The dashed line represents a moderate impact threshold, assumed constant for both present and future climates. The dotted line represents a threshold surpassed only under altered climate conditions. The colored areas indicate events with moderate (light shading) and substantial (darker shading) impacts

However, by combining this response with the one from the second driver/hazard, the joint distribution of the compound shifts, leading to a wider spectrum of consequences. First of all, even if the statistical properties of driver/hazard 1 have not changed, the

compound events might occur more frequently and cause higher impacts, as depicted by the colored area above the dashed line (i.e., representing the threshold of moderate impacts of the compound). Moreover, this strengthen in the compounding might lead to the rise of new compound events, which could result in impacts with unprecedented magnitude (i.e., the dark red area).

A changes in the variance of driver/hazard 2 (panel b), generates similar consequences. In this case the resulting bivariate distribution under the altered scenario is wider than the original one, mainly driver by the the fattening of the tails of the driver/hazard distribution. If the cases depicted up to now imply an alteration in the statistical properties of the driver/hazard distributions, a third scenario can arise when climate change strengthen the dependence between the variables (panel c). This might happened, for instance, in the case of a shift in the temporal occurrence of a driver/hazard: even if its resulting distribution does not change, the possibility of it occurring concurrently with another phenomenon exacerbates the overall risk of the compound event.

Another example from Zscheischler et al. (2018) helps to clarify how the risk perspective change when considering different hazards (Figure 4.4).

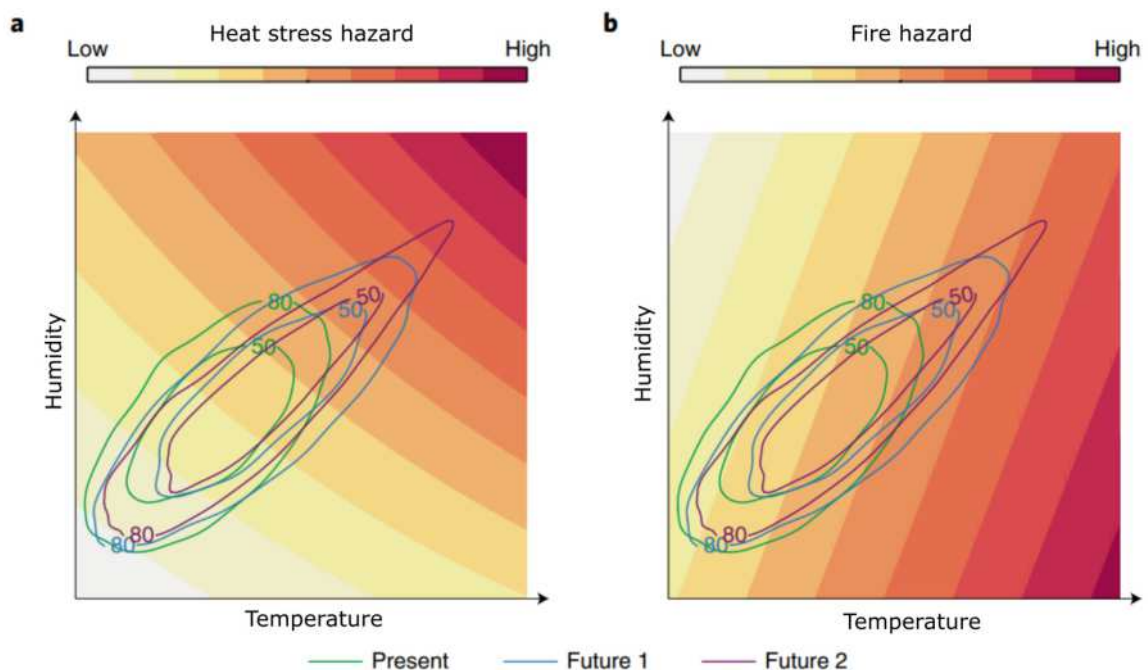


Figure 4.4: Modified from Zscheischler et al. (2018): The hypothetical distribution of temperature and humidity in the present climate (green), a future climate with a shift in mean, variability and correlation between the drivers (Future 1, blue) and a future climate with an increase in dependence in the upper tail of both drivers (Future 2, purple). The intensity of Hazard 1 increases towards the upper right of the climate space (a). The same climate distributions as in a for Hazard 2, which increases towards the lower right of the climate space (b)

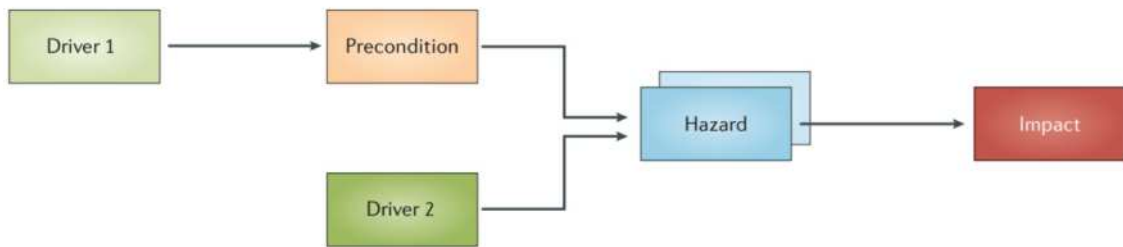
Temperature and humidity are the climatic drivers and the green lines in the panels represent the 50th and 80th percentiles of the bivariate distribution in an hypothetical present climate. If two different future scenarios are considered (i.e., it might be two different future projections with distinct climate forcing) and some changes in the mean, variance and dependence happen, the future distributions might evolve in those depicted by the blue and the purple lines. Up to now there is nothing new from what is shown in Figure 4.3. The different perspective emerges when linking the compound event to the hazards that may result and the direction in which its intensity varies: the same projected distribution increase both the heat stress (panel a) and fire (panel b) hazards. Indeed, the hypothetical future climate is characterized by hotter and more humid conditions, which are responsible for an increasing occurrence of heat stress events. Hence the heat-related hazard has to worsen moving towards the top-right corner of the climate space. At the same time, the future distributions seem to spread toward the bottom-right corner, where the fire hazard is higher since the occurrence of hot and dry conditions is increased.

Due to the complexity of the topic, Zscheischler et al. (2020) made an attempt to simplify the modeling framework by tracing compound events to four potential types: pre-conditioned event, multivariate event, temporal compounding event and, spatially compounding event.

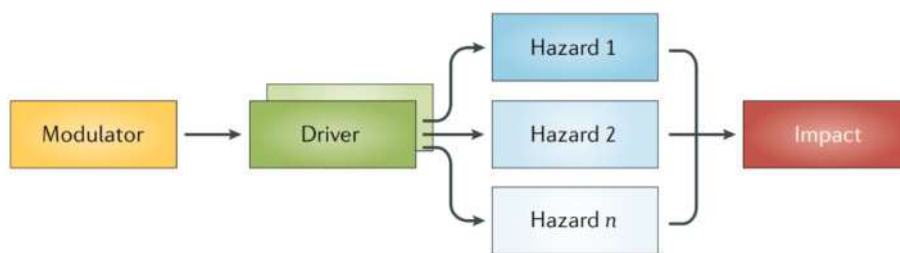
In a *preconditioned event* (Figure 4.5a), a pre-existing weather-driven or climate-driven condition exacerbates the impacts of a climatic impact-driver. An example might be the water storage deficit in Central Europe during the drought of 2019 (Boergens et al., 2020). In this case, the 2018 drought severely affected the soil moisture levels and the winter between these two events could not sufficiently recharge the deep storages, leading to higher water availability deficit in 2019.

The impacts from a *multivariate event* (Figure 4.5b), result from the interaction of multiple climate drivers and/or hazards in the same geographical region. A pragmatic example was the flood that hit Ravenna in 2015. This event was led by the co-occurrence of severe rainfall generated by a low-pressure system and a storm surge driven by southeasterly winds over the Adriatic sea (Bevacqua et al., 2017). A similar example can be what happened in New Orleans in 2005 (Dykstra and Dzwonkowski, 2021). Storm surges and river flooding caused by Hurricane Katrina's strong winds and exceptionally heavy rainfall led to more than 50 failures of the levees and flood walls that were supposed to protect the city, exacerbating the impact of the resulting floods.

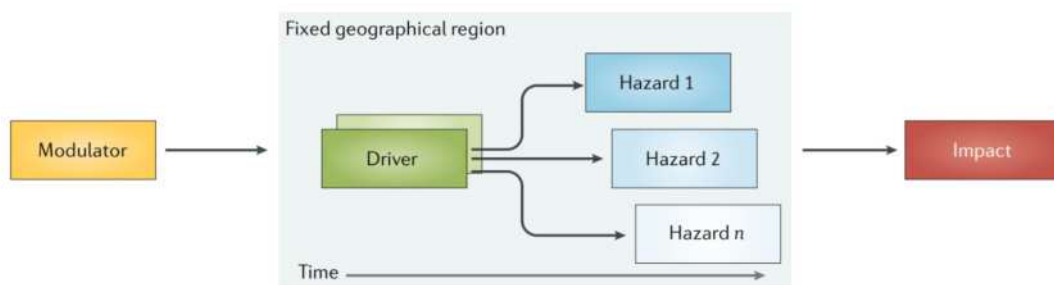
a) Preconditioned event



b) Multivariate event



c) Temporal compounding event



d) Spatially compounding event

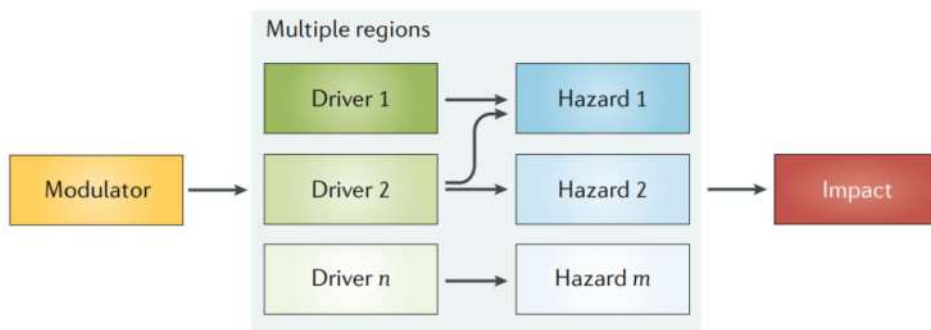


Figure 4.5: From Zscheischler et al. (2020): Typologies of compound events: a) preconditioned event, b) multivariate event, c) temporally compounding event, d) spatially compounding event

Temporally compounding events (Figure 4.5c), refer to a series of successive hazards affecting a specific geographical region, resulting in an impact that is either intensified when compared to a single hazard. This can be the case of the so called "hot and dry" and "hot and wet" events, in which one or more heatwaves set the stage for subsequent dry or wet conditions, such as droughts (Mazdiyasi and AghaKouchak, 2015) or intense rainfall (Sauter et al., 2023), respectively.

Finally, in the *spatially compounding events* (Figure 4.5d), events occurring in multiple interconnected locations combine their effects to produce a greater impact. As an example, simultaneous heatwaves and floods occurring in different area of the world may induce synchronous crop failure constituting a potential risk to global food security (Kornhuber et al., 2020; Mehrabi et al., 2022).

Among compound events, heat stress was recently found to be a precursor of summer flooding across the central United States (Zhang and Villarini, 2020) with these two hazards that were connected through atmospheric conditions leading to increased convective available potential energy (CAPE) and stormy weather. After an in-depth discussion on the elements of this compounding, the next section will explore whether their resulting risk is relevant in other regions of the globe. Moreover, by using the outcomes from several Global Circulation Models (GCMs) at different Shared Socioeconomic Pathways (SSPs) and Representative Concentration Pathways (RCPs), it will be examined whether the strength of this compounding is projected to increase or decrease in the future, considering the potential threats to society and the economy.

4.2. Climate change exacerbates the compounding of heat stress and flood

Heat stress and flood impacts have been studied extensively because of their significant societal and economic impacts. Both these two natural disaster have been responsible for million of fatalities during the last century, as shown in Figure 4.6. Moreover, it has been demonstrate that significant increasing trend in the number of death due to heat waves and floods occur in different area of the world (Mazdiyasnı et al., 2017; Franzke and Torelló i Sentelles, 2020), requiring substantial effort from populations to adapt and be resilient in a changing climate. (Pörtner et al., 2022)

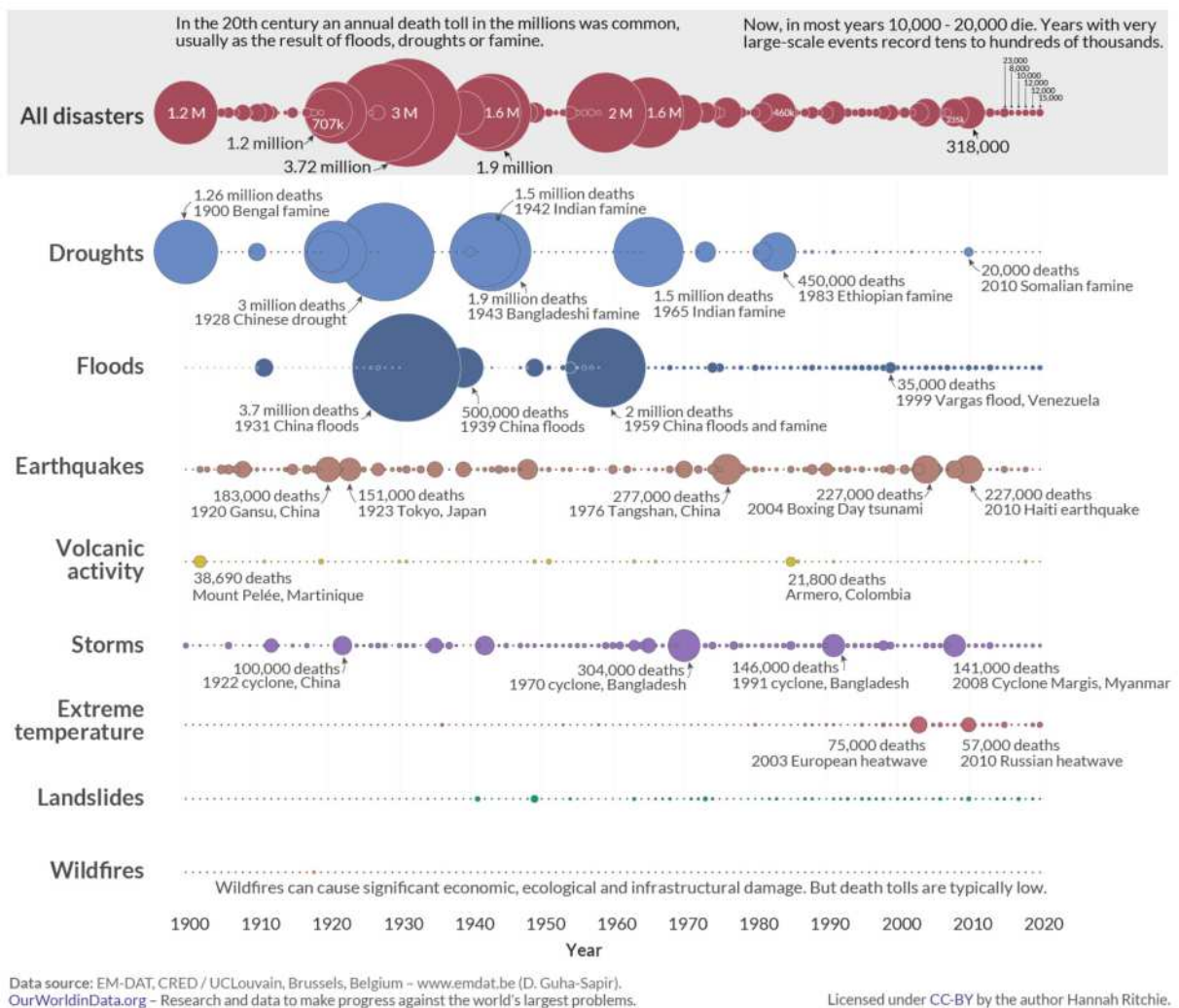


Figure 4.6: From Our World in Data: Global deaths from disasters over the period 1900 - 2020. The size of the bubble represents the estimated annual death toll

More than a climatic or atmospheric variable, heat stress is generally recognized as

an indicator of work-related physical discomfort (i.e., occupational heat stress). Indeed, it is a condition that occurs when the body's temperature-regulating system (i.e., primarily sweating) are overwhelmed by excessive heat and humidity, resulting in heat stroke, heat exhaustion and other negative impacts on human health (Kovats and Hajat, 2008; Zander et al., 2015; McGregor and Vanos, 2018). However, since the factors that contribute to heat stress are mainly high air temperatures and humidity, over the years its use has encouraged the contamination of medical studies with climate, environmental, and social research (Alahmad et al., 2022; Fan et al., 2022; Chapman et al., 2022). For instance, urban areas are recognized as particularly subjected to dangerous heat stress events (Oleson et al., 2015; Luo and Lau, 2018), due to several factors (e.g., weak air circulation, emissions from vehicle, presence of commercial and residential buildings, and so on) that contributes to the urban heat island effect (Stone Jr, 2012).

Heat stress itself is also responsible for major negative impacts on livestock production. The effects are evident on various aspects such as feed consumption, production efficiency (such as milk yield or weight gained), growth rate, egg production, and reproductive efficiency (Daramola et al., 2012). Not only livestock, but also the productivity of agricultural crops is drastically reduced when heat stress events occur during the reproductive period (Teixeira et al., 2013). The 2010 Euro-Russian heatwave and the following wildfires resulted in a 25% decrease of the annual crop production, leading to a total loss of more than \$15 billion to the local economy (Barriopedro et al., 2011; Katsafados et al., 2014) and an increasing of more than 50% in the cost of wheat on the international market (FAO, 2011). When referred to areas of the globe where population is expected to grow and where there might be an increasing demand for food availability, all these consequences might exacerbate poverty, food insecurity and starvation (Rahimi et al., 2021; Hasegawa et al., 2021). Finally, there is also evidence that heat stress may influence human behavior (e.g., migration) much more than other natural hazards (Mueller et al., 2014).

If these negative aspects alone were enough to explain how much impactful heat stress is, a wide spectrum of worst-case scenarios may arise when heat stress can be considered as a driver for summer flooding. For instance, agriculture can be highly undermined during a flood, leading to a reduction in yield or even a loss of the entire crop (Posthumus et al., 2009; Bremond et al., 2013). Livestock is also a vulnerable target because it can perish or experience indirect consequences (e.g., disease, lack of food), resulting in an increased risk of poverty (Deen, 2015). Moreover, flooded roadways can complicate the access to the medical infrastructure, leading to the inability to provide early medical care or interrupting patients' treatments during these events (Tomio et al., 2010; Yusoff et al., 2017).

The physical mechanism behind the compounding of heat stress and flood events is described in details in Zhang and Villarini (2020) and depicted in Figure 4.7. High humidity and temperatures in the lower troposphere generally provide the source of moisture and the dynamical forcing to increase atmospheric instability (i.e., CAPE). Indeed, as the temperature near the surface increases, the difference between the lower and the upper troposphere favours the vertical movement of the air masses, namely convection. If during this process the environmental lapse rate is greater than the dry-adiabatic lapse rate, the atmosphere is "absolutely unstable", generating the conditions favorable for the development of thunderstorms, severe weather, and convective cells. However, high temperatures alone do not guarantee atmospheric instability: humidity (but also relative wind conditions at different layers of the atmosphere) plays a crucial role, since it provides the amount of water that might turn into precipitable water. The resulting intense precipitation event led to an increasing risk of flooding, which could cause all the impact previously described.

According to the typologies shown in Figure 4.5, this kind of events can be traced back to both the "preconditioned" and the "temporally compounding" categories. Indeed, if on the one hand heat stress can be seen as a pre-existing climate condition that intensify the magnitude of intense precipitation and floods, on the other the whole process is characterized by a clear time evolution.

For the sake of knowledge, other studies that considered the link between the two hazards used only temperature, rather than heat stress, as the modulator for the compound. For instance, Chen et al. (2021) show that northwestern and southern China has been increasingly affected by sequential flood – heatwave (i.e., a flood event followed by a heatwave within a certain temporal interval) during the period 1960 – 2019, mainly driven by increases in temperature. Gu et al. (2022) reversed the order of the previous compounding, analyzing the projected changes in the compound of flooding and hot extremes at a global scale. However, the physical processes connecting high temperature with flooding are much less clear than what described in Zhang and Villarini (2020) due to the lack of focus on humidity as the link between these two hazards. As previously highlighted, high temperatures combined with high relative humidity are together the two key components for severe rainfall events and, in turn, for flooding. Therefore, there is a need to connect floods and heat stress beyond the central United States and to other areas of the globe, as well as to assess how their nexus may change because of climate change.

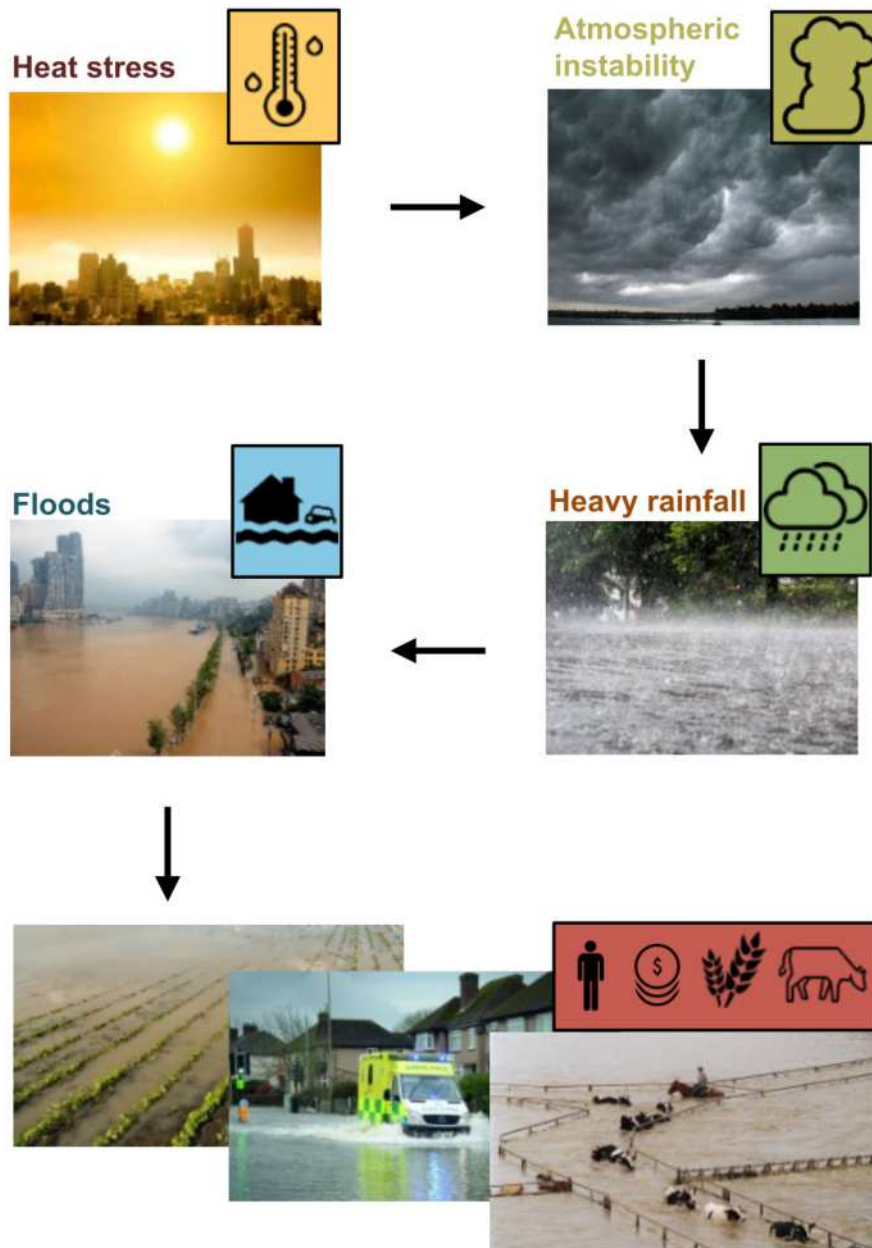


Figure 4.7: Physical mechanism behind the compounding of heat stress and flood

In a climate change context, there is a high probability that the impacts of these two hazards could worsen. In terms of heat stress, the projected increases in temperature are expected to lead to an increased capacity of the atmosphere to hold water vapor (Fowler et al., 2021), with negative impacts in terms of heat stress conditions (Mora et al., 2017; Coffel et al., 2017; Pörtner et al., 2022; Vargas Zeppetello et al., 2022). While there is a general agreement in terms of the projected changes in heat stress, much more uncertain are the projected changes in flooding (Arnell and Gosling, 2016; Kundzewicz et al., 2017),

with large regional variability (Hirabayashi et al., 2013; Blöschl et al., 2019). Despite these uncertainties, there is an overall consensus that the impact of disastrous river floods is projected to increase in the future (Merz et al., 2021).

Therefore, after a first paragraph where the data and the methodology are presented, the section will be divided into 3 main parts. In the first one, the areas of the globe which have experienced compounding between heat stress and flooding are identified. After this, the projected changes in these compound events are assessed using global climate models (GCMs) from the Coupled Model Intercomparison Project (CMIP6) (Eyring et al., 2016) and different Shares Socio-economic Pathways (SSPs). Finally, the outcomes are combined with a global dataset related to the projected future changes in the population of urban agglomerations (Kii, 2021) to quantify the projected changes in human exposure to the risk of the analyzed compound at the end of the 21st century.

4.2.1. How to compound heat stress and flooding: data, methods and remarks

The datasets used belong essentially to two categories: reference datasets and climate models. The use of a reference dataset is crucial when examining the outputs of GCMs, since these are numerical models that may have systematic errors (biases) (Oreskes et al., 1994). As already shown in paragraph 1.1.4, these biases are potentially caused by a wide range of factors, such as simplification in the thermodynamics and physics processes (Wehrli et al., 2018) or coarse spatial resolution where it is not possible to resolve small-scale phenomena (e.g., convective storms), especially in regions with complex topography (Rhoades et al., 2018). Therefore, before making inferences about future projections, it is essential to validate the GCMs considering an historical baseline.

In terms of reference data, which cover the 1979 – 2014 period, 2-m air temperature and relative humidity from Multi-Source Weather (MSWX) (Beck et al., 2022) have been used to compute the wet bulb temperature. This is a global gridded product with a 0.1-degree spatial and daily time resolution, derived by rescaling and bias correcting the ERA5 reanalysis (Hersbach et al., 2020) through high-resolution data, including station observations, satellite imagery and model output. For runoff, the 0.25-degree National Aeronautics and Space Administration’s Global Land Data Assimilation System Version 2 (GLDAS-2) (Rodell et al., 2004; Li et al., 2018) daily dataset has been used, in which the fluxes of the land surface are reproduced through satellite and ground-based observation. The total runoff has been obtain as the sum of the baseflow-groundwater and storm surface runoff. Since the products have different spatial resolutions, the MSWX products have been upscaled to the GLADS resolution by means of bilinear interpolation.

The GCMs have been chosen from the CMIP6 (Eyring et al., 2016). In particular, those with available data for the required variables (i.e., total runoff, near-surface air temperature and near-surface relative humidity) and whose nominal resolution is ~ 100 km ($\sim 1^\circ$). In particular, the historical and the future scenario (i.e., SSP1-2.6, SSP2-4.5, SSP3-7.0 and, SSP5-8.5) experiments have been considered for seven models (i.e., CMCC-CM2-SR5, CMCC-ESM2, EC-Earth3, INM-CM4-8, INM-CM5-0, MPI-ESM1-2-HR and, NorESM2-MM), and only the ‘r1i1p1f1’ member has been considered. The time period for the historical experiment matches the one used for the reference (i.e., 1979-2014), while the last 36 years of the 21st century (i.e., 2065 – 2100) have been selected for the future scenario experiments. A schematic summary of the characteristics of the datasets used is shown in the Figure 4.8.

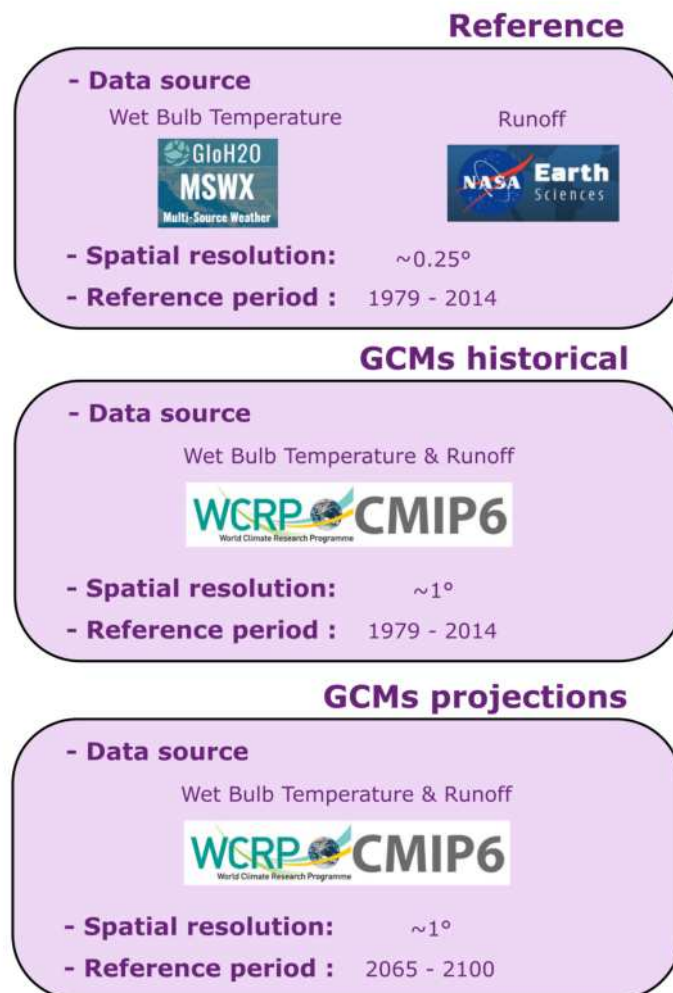


Figure 4.8: Characteristics (e.g., source, spatial resolution, and analysis period) for both reference dataset and GCMs

To derive both heat stress (HS) and extreme runoff (ER) events a pixel-by-pixel peak-over-threshold (POT) approach has been applied to the reference data and the GCM historical experiments. Figure 4.9 shows an example of the POT procedure. For the 1979 - 2014 period, heat stress events have been define as those days exceeding the 95th percentile of the at-site wet bulb temperature distribution (Zhang and Villarini, 2020) (Figure 4.9a). The wet bulb temperature (T_{wb} ; units: °C) has been computed by using the following empirical formulation (Stull, 2011; Karwat and Franzke, 2021):

$$\begin{aligned}
 T_{wb} = & T \cdot \arctan\left[0.151977 \cdot (RH + 8.313659)^{\frac{1}{2}}\right] + \arctan(T + RH) + \\
 & - \arctan(RH - 1.676331) + 0.00391838 \cdot RH^{\frac{3}{2}}. \\
 & \cdot \arctan(0.023101 \cdot RH) - 4.686035
 \end{aligned}
 \tag{4.1}$$

where T (°C) is the air temperature, and RH (%) the relative humidity. The use of wet bulb temperature to define heat stress events has another positive effect in addition to considering humidity in the compounding. Indeed, from the GCMs point of view it has been shown that the combination of these two variables produce less uncertain results than treating them in a separate form (Fischer and Knutti, 2013).

To identify POT runoff events (Figure 4.9b), the procedure was slightly different. Indeed, unlike heat stress events, runoff peaks exhibit high temporal correlation even at the daily scale. Therefore, using a percentile threshold derived from the empirical distribution would increase the likelihood of not having statistical independence among the identified events. Hence, for each pixel it has been fixed a threshold to have, on average, two events per year, with two peaks separated by at least 7 days (Lang et al., 1999).

Finally, the same thresholds computed for the historical period have been used to identify future heat stress/extreme runoff events. Of course, while the sample size remains the same for the historical baseline, the number of events for both variables might changes in the future, depending on the variability and trends characterizing different regions of the globe.

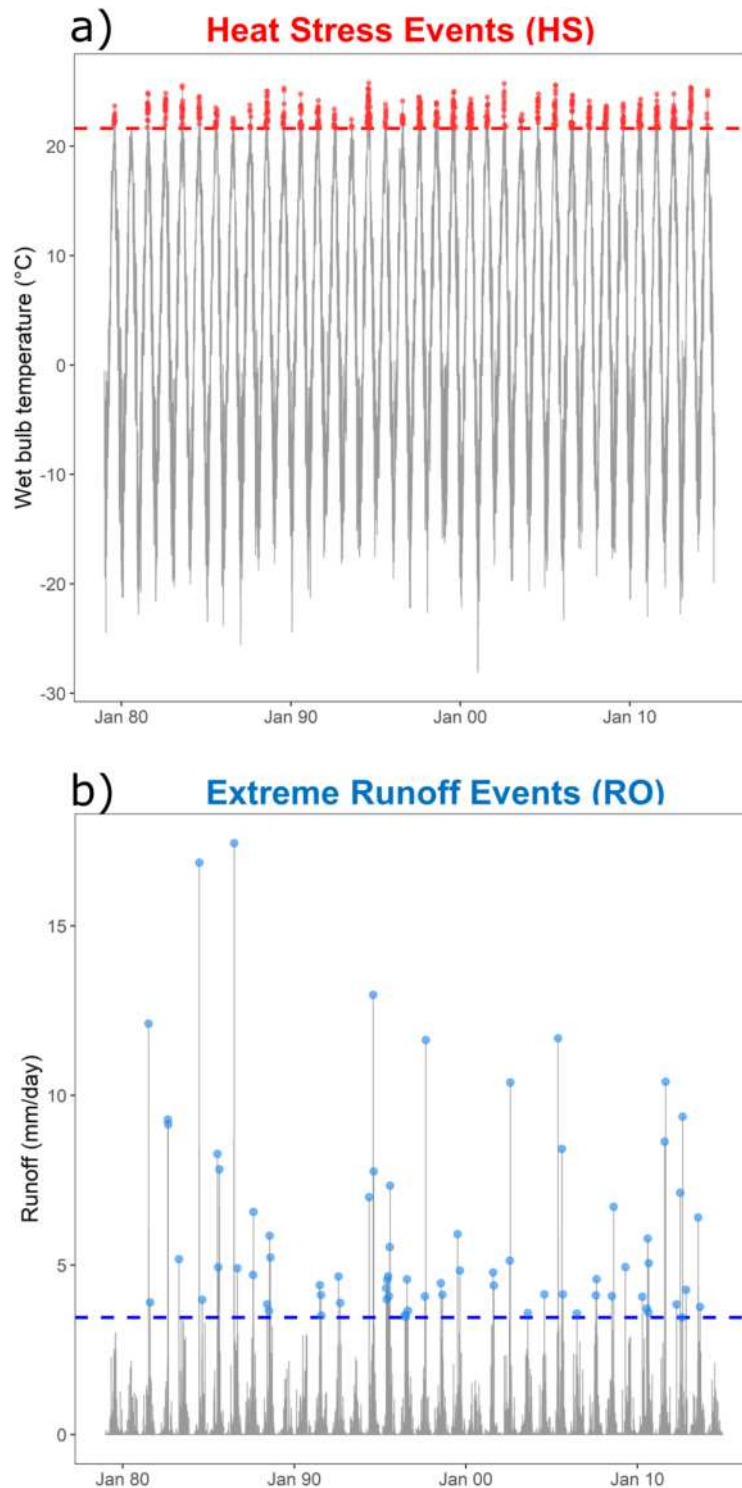


Figure 4.9: Example of peak-over-threshold to extract heat stress (a) and extreme runoff (b) events from the reference datasets and the historical experiments of GCMs

Before describing the procedure to compound the extremes, some considerations need to be made regarding the areas that could be more prone to these events. Indeed the use of

POT does not guarantee to focus on areas particularly susceptible to heat stress events or for which it makes sense to talk about runoff phenomena. For this reason, three conditions have been set to identify the areas where the compound heat stress - flooding may occur:

1. the 95th percentile of the T_{wb} threshold in the reference data is at least 20°C. This criterion allows to focus on areas where heat stress would have negative societal and economic impacts and where it is feasible to expect humidity to be the main physical driver for flooding;
2. the *Arid desert* or *Arid steppe* zones are masked using the already mentioned Köppen – Geiger climate classification map (Beck et al., 2018) because of our focus on humidity.
3. the analyses has been restricted to the “summer” months of June-July-August (JJA) for the northern hemisphere and December-January-February (DJF) for the southern hemisphere because this is the season that mostly experiences heat stress events.

The areas that meet these three conditions are depicted in Figure 4.10. As it is possible to observe from the figure, the eastern part of the United States, the majority of Europe, Russia and the continental China (i.e., the Tibetan Plateau) are not considered in the analysis because of the limit on the 95th percentile of the wet bulb temperature.

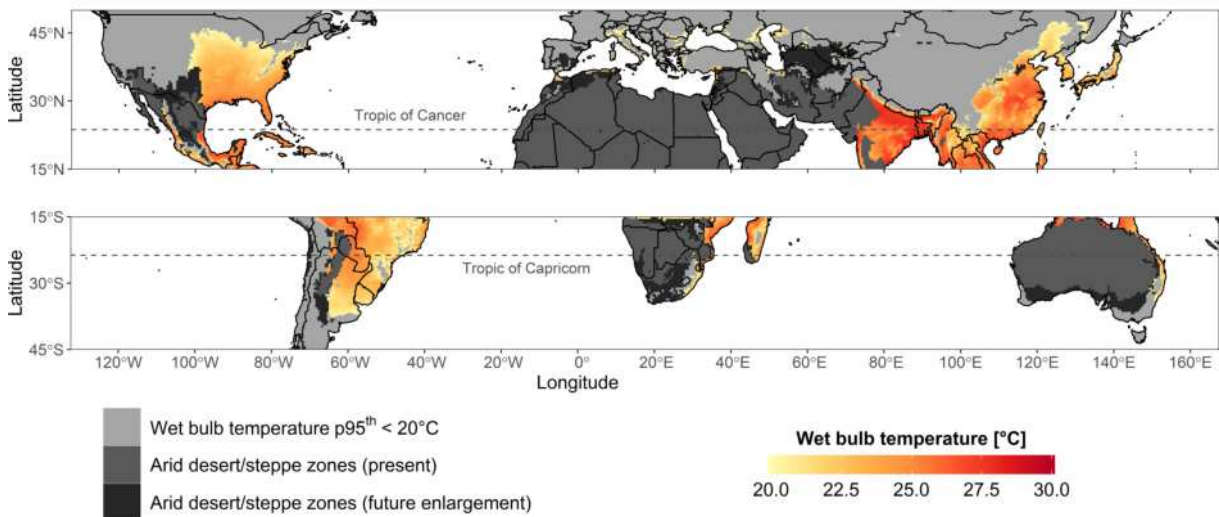


Figure 4.10: Spatial distribution for the 95th percentile of the wet bulb temperature. The colorbar is related to those area in which the 95th percentile is greater than 20°C, while the light grey area represents the pixels in which this threshold is not exceeded. The present and future Köppen - Geiger arid desert/steppe zones are shown in grey and dark grey, respectively

This does not mean that these areas could not be subjected to this kind of compound event, but that the occurrence might be so rare as to be related only to exceptional events. On the other side, the Saharan and large part of the southern Africa, the United Arab

Emirates, the central Australia and, the northern Mexico are not considered due to the second limitation. Although temperatures in these areas are frequently high and above the fixed threshold, the air tends to be dry and flood events are very rare, if not virtually impossible.

Among the remaining areas, India and eastern China, are characterized by the highest values of the 95th percentile of the wet bulb temperature distribution. Regarding India, it can be attributed to the anomalous inflow of marine air from the Arabian Sea into the Indus Valley, accompanied by large positive humidity anomalies and moderate warm temperature anomalies (Monteiro and Caballero, 2019). For China, the high air temperature and humidity condition that led to heat stress events are generally concomitant with anomalous high-pressure and notable water vapor flux convergence (Wang et al., 2019).

By looking at Figure 4.10, it is also possible to notice that the equatorial zone is missing (i.e., 15°S to 15°N). This happens as a consequence of the third condition. Indeed, the percentage of summer heat stress ($\%ofHS_{summer}$) is highly correlated with the latitude. This quantity has been defined as follows:

$$\%ofHS_{summer} = 100 \cdot \begin{cases} \frac{N_{HS(JJA)}}{N_{HS(TOT)}} & \text{if } Lat > 0^\circ \\ \frac{N_{HS(DJF)}}{N_{HS(TOT)}} & \text{if } Lat < 0^\circ \end{cases} \quad (4.2)$$

where $N_{HS(JJA)}$ and $N_{HS(DJF)}$ refers to the number of heat stress events occurring during summer, while $N_{HS(TOT)}$ is the total number of heat stress events. Looking at its spatial distribution Figure 4.11a, it is possible to notice that $\%ofHS_{summer}$ decreases moving from the tropics to the Equator, with almost 100% of these events occurring during June-July-August (JJA) in the United States east of the Rocky Mountains and eastern China. Indeed, by narrowing the analysis to the summer months, the frequency of heat stress events in the equatorial area is drastically reduced, since it is plausible that extreme heat and humidity exhibits there a shifted seasonality.

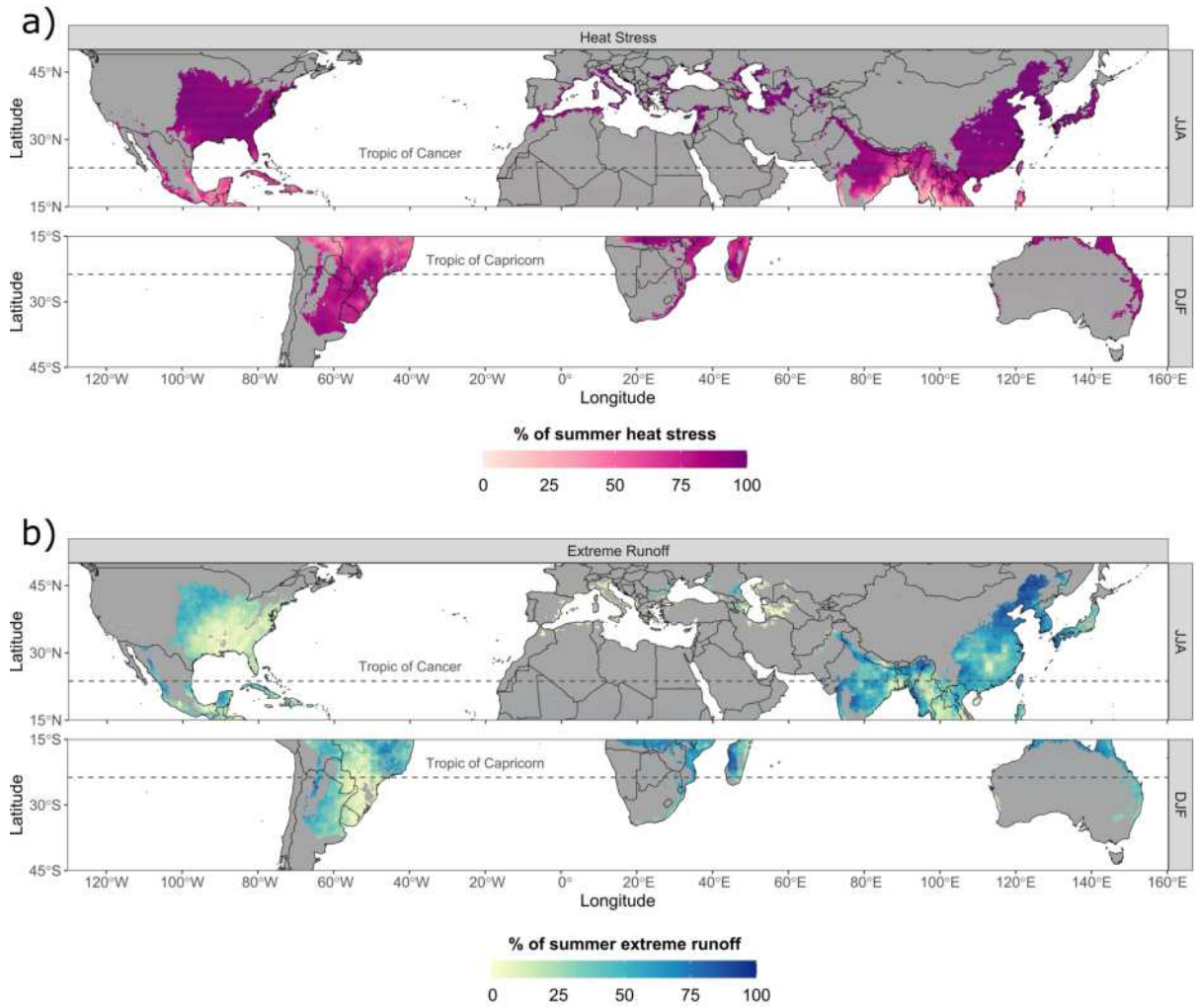


Figure 4.11: Spatial variability of the percentage of summer heat stress events (a) and extreme runoff (b). The summer period includes June, July, and August (December, January, and February) for the northern (southern) hemisphere. The percentage is computed as the ratio between the number of heat stress/extreme runoff events that occurred during the summer and the total number of events

This strong dependence on latitude is less apparent for the percentage of summer extreme runoff (Figure 4.11b), defined as:

$$\%of ER_{summer} = 100 \cdot \begin{cases} \frac{N_{ER(JJA)}}{N_{ER(TOT)}} & \text{if } Lat > 0^\circ \\ \frac{N_{ER(DJF)}}{N_{ER(TOT)}} & \text{if } Lat < 0^\circ \end{cases} \quad (4.3)$$

where $N_{ER(JJA)}$ and $N_{ER(DJF)}$ refers to the number of heat stress events occurring during the boreal and austral summer, respectively, while $N_{ER(TOT)}$ is the total number of heat stress events. Indeed, while the occurrence of heat stress is dominated by air temperature

and humidity and exhibits a clear seasonality, flood seasonality is more complex with a high spatial variability.

After extracting the POT events for both variables from the reference data and GCMs and for the historical and future periods, the compound heat stress – flooding events have been characterized. In particular, it is considered a compounding when a heat stress occurs within 3 days before the occurrence of the runoff peak (Zhang and Villarini, 2020). Since the GCMs' spatial resolution is $\sim 1^\circ$, for the reference data an heat stress event might occur in a centered 5×5 kernel to have similar spatial resolutions for both products. Figure 4.12 clarifies this difference for the reference (panel a) and GCMs experiments (panel b).

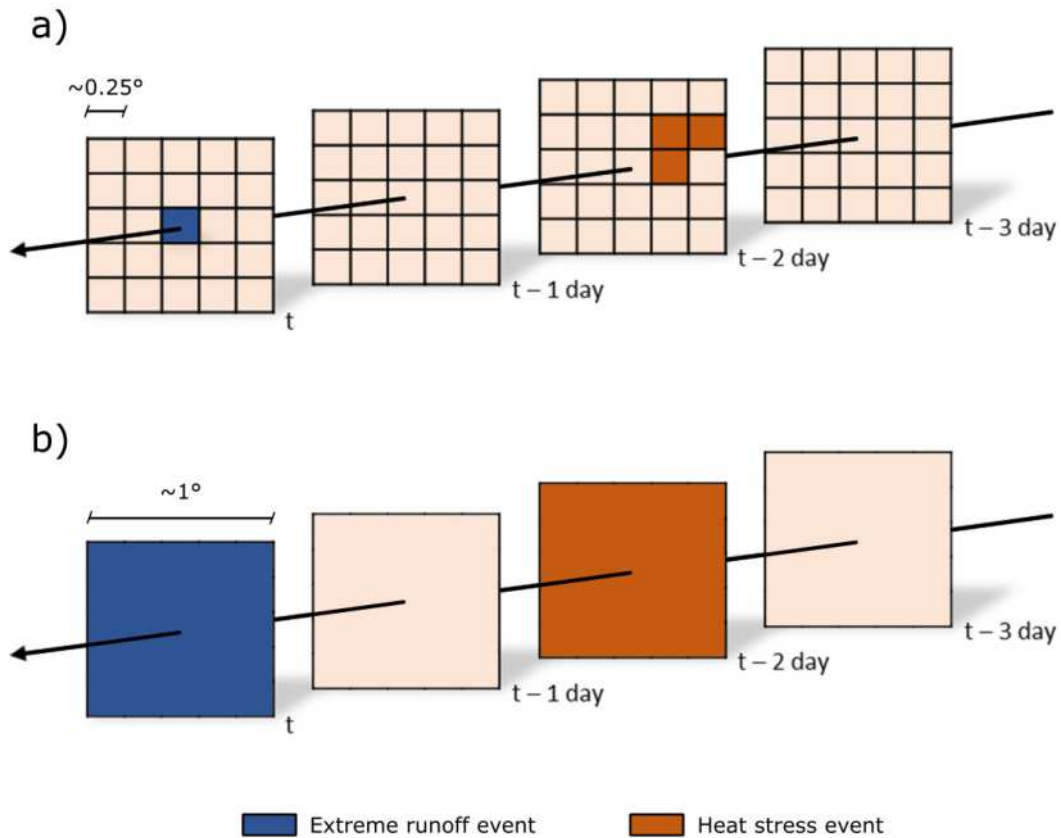


Figure 4.12: Representation of the criterion to compound heat stress and flooding events for the reference (a) and the GCMs experiments (b)

By counting the number of runoff peaks that are anticipated by an heat stress event, it is possible to compute the percentage of the compounding ($\%ofComp_{HS,ER}$) as follows:

$$\%ofComp_{HS,ER} = 100 \cdot \frac{N_{ER \leftarrow HS}}{N_{ER}} \quad (4.4)$$

where $N_{ER \leftarrow HS}$ is the number of extreme runoff preceded by an heat stress, while N_{ER} is the total number of extreme runoff detected.

4.2.2. Historical response and GCMs validation

As expressed in paragraph 4.2, the first step has been to verify the strength of the compounding in the reference dataset. Figure 4.13 shows the percentage of the of compound heat stress – runoff in the areas selected. Based on the reference data, the compounding between heat stress and floods is strong in the mid-latitudes, such as the central and eastern United States, the central-eastern part of the South America, and the area between India and eastern China. For instance, $\sim 50\text{-}75\%$ of the extreme runoff events in the central United States were preceded by a heat stress event, consistent with the extremely hot and humid weather conditions across the area during those decades (Raymond et al., 2017; Zhang and Villarini, 2020), with this percentage that decreases moving from the center to the south. This decreasing percentage in this area may also be the result of using pixel runoff instead of discharges. Indeed, when a heat stress event creates the atmospheric conditions for intense rainfall and then flood, the compounding must necessarily be upstream in the basin. When the runoff propagates downstream, the correlation with the heat stress is lost. In East Asia and South America, where high values of wet bulb temperatures are often present (Wang et al., 2019; Sun et al., 2019; Ning et al., 2022), heat stress tends to be a weather precursor for most of the summer flood events. Moreover, India and China are characterized by monsoons which periodically strike this region between June and July (Monteiro and Caballero, 2019). Hence, in the context of the compounding, high values of T_{wb} can intensify the rainfall induced by these phenomena, exacerbating the resulting floods.

The compounding between these two hazards also interests areas in southern Africa and along the east coast of Australia. Although these land portions are small in comparison to the masked area, they face a significant risk due to the substantial population residing there. Europe is not identified as an area where heat stress precedes floods because the 95th percentile of the heat stress distribution is generally below 20°C. Nevertheless, except for the southeast and the east coast of the United States and the central part of the south America, the percentage of summer runoff events in the other areas is higher than 30-40%, reaching about 100% in northeastern China.

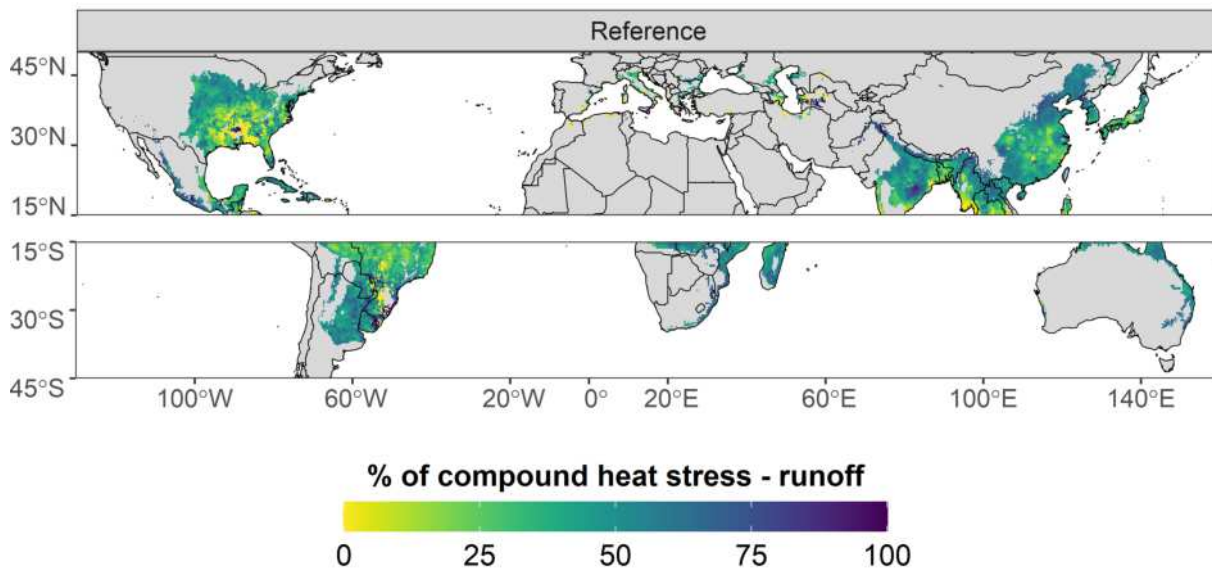


Figure 4.13: Spatial distribution of the percentage of compound heat stress – runoff based on the reference data. The study period is 1979-2014. The gray shaded areas represent “Arid desert” or “Arid steppe” zones (according to the global Köppen – Geiger classification) or the regions where the 95th percentile of the wet bulb temperature distribution does not exceed 20°C and, therefore, are excluded from the analyses

The results shown in Figure 4.13 highlight the regions where the compounding of heat stress and floods plays an important role in the historical record; such results can be also used to evaluate the GCMs’ performance. Figure 4.14 shows the outcomes for the seven models considered; the top-left panel refers to the reference dataset (i.e., the same of Figure 4.13) and it is shown with the aim to facilitate the comparison. First, the extension of the domain is similar for all the models and the reference data. With the exception of those areas classified as arid that are a-priori removed, this means that the 95th percentile of the wet bulb temperature distribution exceeds 20°C approximately in the same areas both for reference dataset and CMIP6 historical experiments. Overall, the models capture the observed results both in terms of regional extent and strength of the compounding. For the southern hemisphere, the models reproduce the spatial patterns occurring in the reference data well, with the exception of INM-CM4-8 and INM-CM5-0, exhibiting a tendency to overestimate the compounding in central Brazil and South Africa. In the northern hemisphere, the models perform well in East China, with a slight underestimation in eastern India. The performance in the United States is generally good, with a slight tendency towards underestimating the strength of the heat stress-flood compounding, especially for MPI-ESM1-2-HR.

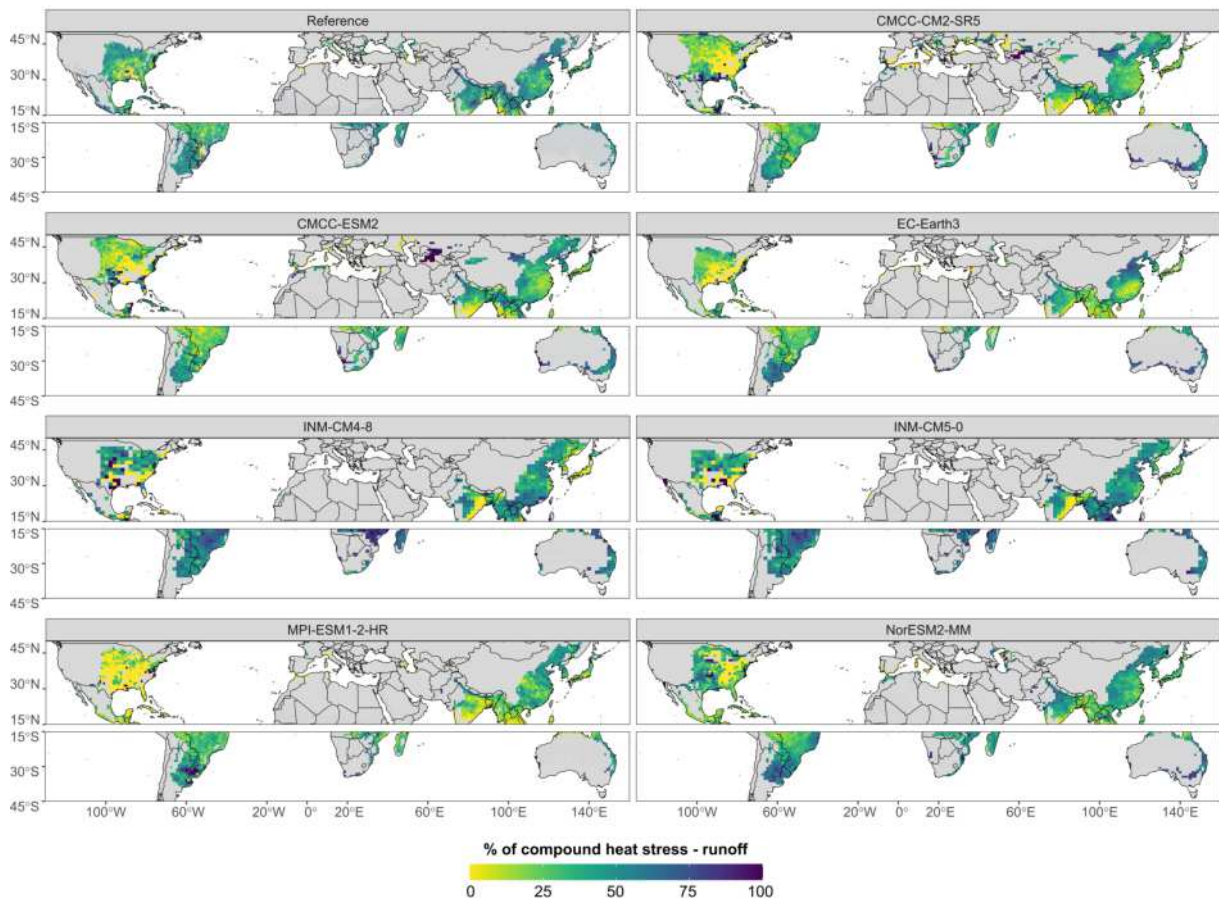


Figure 4.14: Spatial distribution of the percentage of compound heat stress – runoff. The results in the top-left panel are based on the reference data, while the remaining panels show the results for the historical runs of seven CMIP6 GCMs

As shown in the Figure 4.14, individual models exhibit biases that could be relevant. However, a completely different perspective arises when an ensemble of GCMs is created. Specifically, a pixel-by-pixel average of the composition percentage has been performed, and the results are displayed in the Figure 4.15. Based on the previous findings, the analysis has been limited to five subzones, each depicted in the figure’s panels. The two degrees of color transparency are used to distinguish regions where at least four GCMs agree on the presence of compounding (i.e., no transparency) from regions where the average response is more uncertain (i.e., transparency). By comparing this average with the reference, it is possible to notice the ensemble significantly reduces the intra-model uncertainties, both in the percentage and in the geographical extension of the compounding. The signal reduction in the southeastern United States as well as near the east coast of China are realistically captured by the ensemble. The bias remains particularly significant only along the east coast of India.

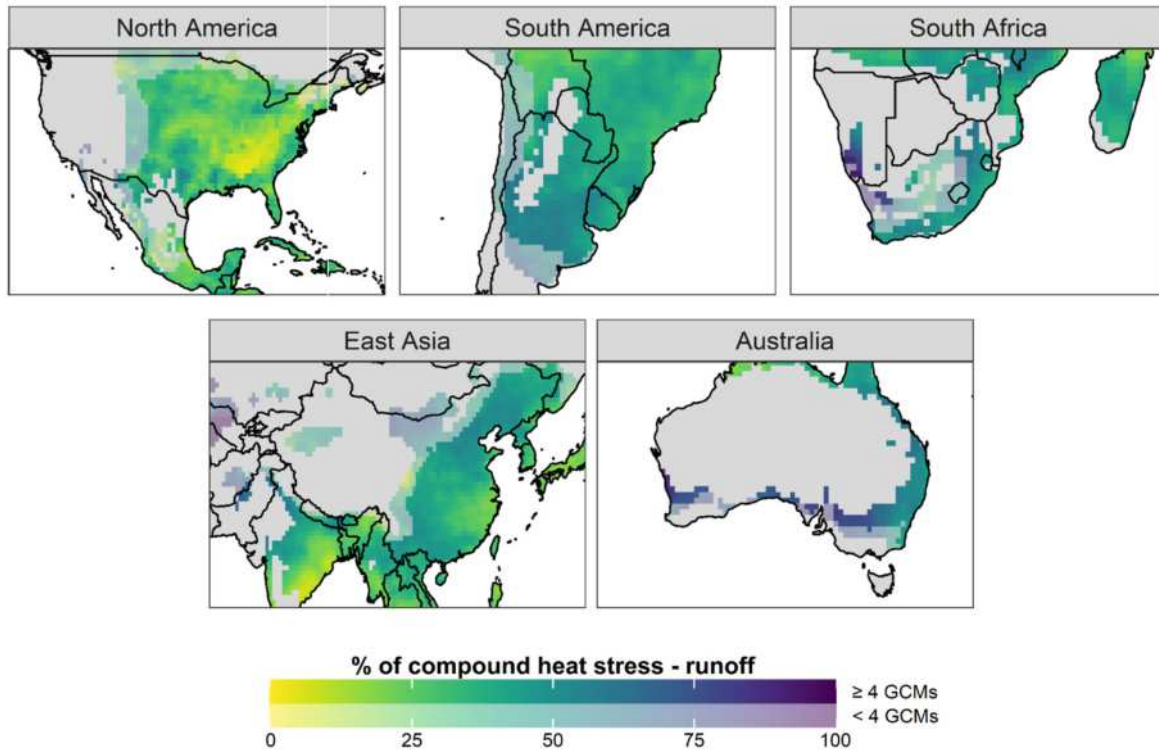


Figure 4.15: Averaged percentage of compound heat stress – runoff for the GCMs historical experiments. The color transparency is used to distinguish those areas in which at least four GCMs agree with the presence of compounding (i.e., no transparency) from those where the response of GCMs is more uncertain (i.e., transparency)

4.2.3. Future evolution of the compounding

Based on the results in Figure 4.15, it is possible to conclude that the GCM ensemble can reproduce the compounding between heat stress and floods in the reference data, and that they can be used for the assessment of future conditions (Figure 4.16). Compared to the historical simulations (top row in Figure 4.16), the compounding of heat stress and runoff is projected to increase for all the SSP scenarios. For all the identified subzones, most extreme runoff events are expected to be preceded by a heat stress event. Focusing on the United States, under the SSP1-2.6 the percentage increases in all pixels, with an almost constant value around 50%, with even higher values along the Gulf Coast. Moving from SSP1-2.6 to SSP5-8.5, the percentage of flood events preceded by a heat stress event increases further, approaching 75-100% across the United States for SSP5-8.5.

In South America, the stronger compounding is in the southern part of the continent, while it is projected to be exacerbated more in the northern part under the SSPs considered here. This pattern reversal is present in East Asia as well, where the projected

percentages of compounding decrease moving from the Indochinese Peninsula to north-eastern China. Also considering the east coast of India, where the percentage is lower with respect to the other areas up to SSP2-4.5, the compounding increases to values close to 100% under the worst-case scenario.

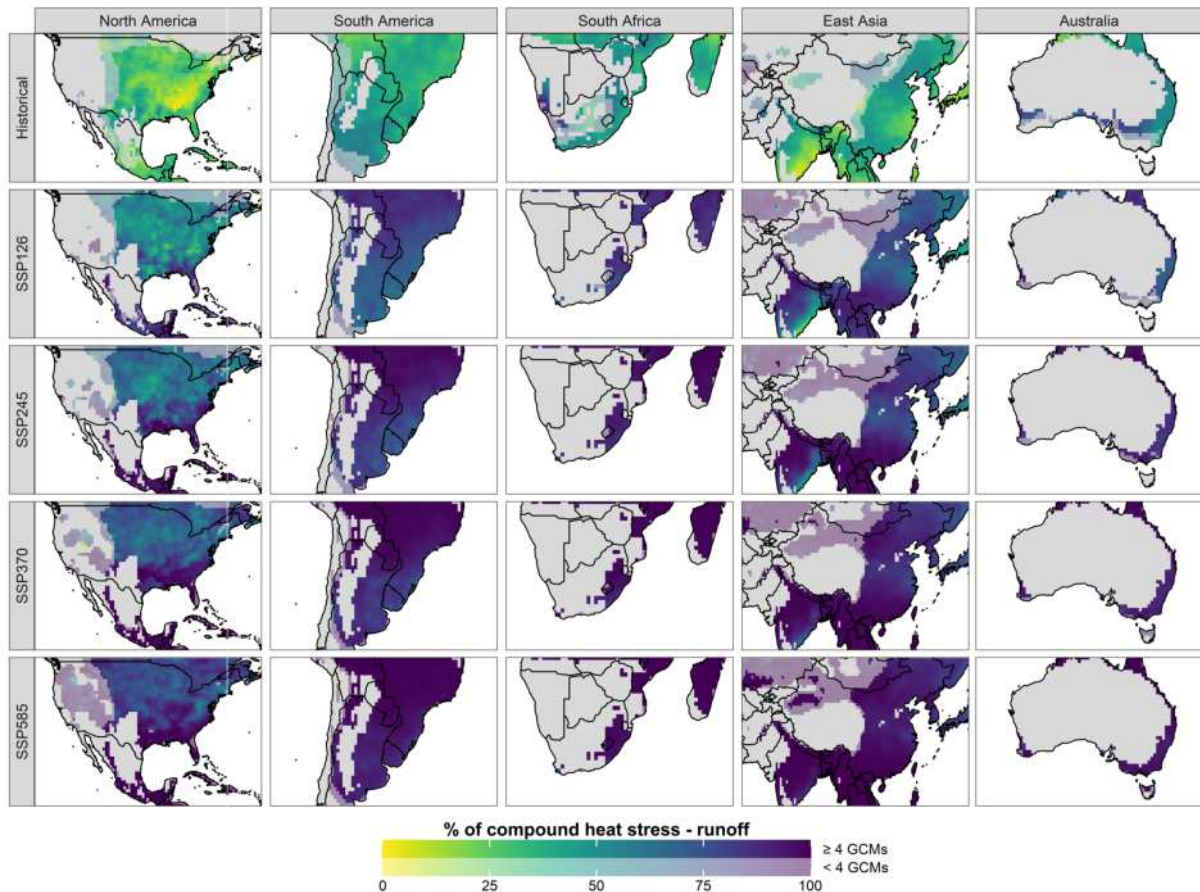


Figure 4.16: Averaged percentage of compound heat stress – runoff for the GCMs historical experiments and the SSPs. The rows show the results for the different experiments, while the columns for the different regions. The historical simulations (top row) focus on the 1979-2014 period, while the future conditions on the 2065-2100 period. The color transparency is used to distinguish those areas in which at least four GCMs agree with the presence of compounding (i.e., no transparency) from those where the response of GCMs is more uncertain (i.e., transparency). The shaded gray areas are excluded because of future arid conditions based on the Köppen – Geiger zones or because the threshold for the wet bulb temperature is lower than 20°C

In general, this increase is driven by the expected rise in heat stress, because of higher temperatures and relative humidity, which may trigger or facilitate extreme rainfall events (Hardwick Jones et al., 2010; Westra et al., 2014). Regardless of the region, the strength of the compounding always increases moving from SSP1-2.6 to SSP5-8.5. There is also an expansion of the regions where compounding will be important due to the increase in the 95th percentile of the wet bulb temperature distribution beyond 20°C. This is particularly

evident for the United States and East Asia. On the other hand, Australia and South Africa show a reduction in the interested areas due to the expansion of the arid zones under the future projections (Beck et al., 2018). Overall, the percentages drastically increase across much of the domains, confirming the global trend in exacerbating the expected compounding of heat stress and extreme runoff events.

The reason for this global strengthening in the compounding has been also investigated. For each experiment the ratio between the number of heat stress events preceding an extreme runoff event, $N_{ER \leftarrow HS}$, and the total number of heat stress events, N_{HS} has been computed; the changes moving from the historical simulations to the different SSPs have been quantified and shown in Figure 4.17.

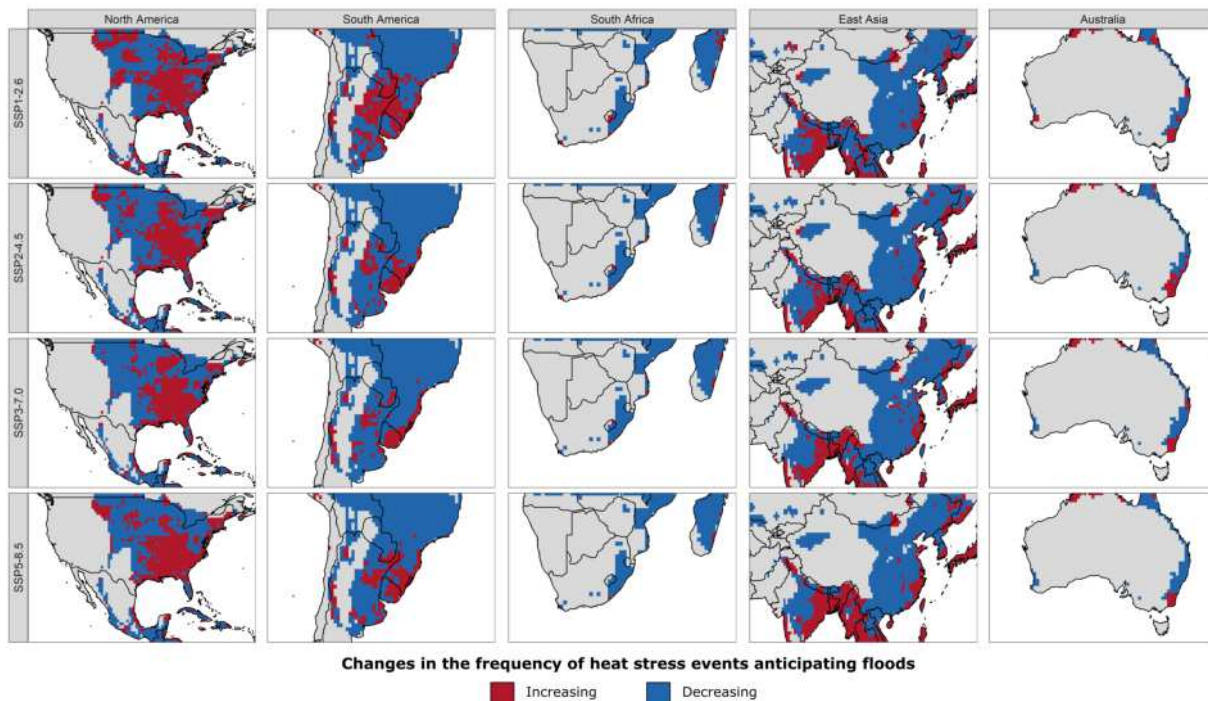


Figure 4.17: Averaged changes in the future frequency of heat stress events preceding floods compared with the historical experiments. The red color (i.e., increasing changes) indicates those areas where in the future there may be more heat stress events preceding floods, while the blue color (i.e., decreasing changes) represents a reduction in these changes. The rows show the results for all the SSPs considered, while the columns for the different regions

The major positive changes interest the central and the southeastern area of the United States, consistent with the findings by Zhang and Villarini (2020). Focusing on the East Asia, an increase in the frequency of heat stress events modulating floods is projected to occur in eastern India, Bangladesh, Japan, and part of the Indochinese peninsula. In general, the other zones characterized by a similar behavior are mainly located in the coastal areas of China, Australia, Brazil, and Uruguay. This outcome might also be more

dramatic when considering additional hazards that may impact these areas, such as the co-occurrence of storm surges and/or the effects of tropical cyclones (Wahl et al., 2015; Kim et al., 2023), which could further enhance the overall impacts of these events.

On the other side of the spectrum, the reason why there are large areas where there is a decrease in the frequency of heat stress events preceding extreme runoffs (i.e., the blue areas in Figure 4.17) has been also investigated. Since this result may seem counter to what found in Figure 4.16, namely a large increase in the compounding, the future changes in the frequency of the individual components, i.e., heat stress and extreme runoff events, for each SSP has been examined. For both variables the ratio between the number of events in the future scenarios and in the historical experiment has been computed. This means that values greater (lower) than one imply an increase (reduction) in the frequency of the events (i.e., heat stress and extreme runoff). Figure 4.18 confirms what has been already mentioned in the beginning of section 4.2, namely that there is an asymmetry in the projected increase of these two hazards.

Indeed, while there is a strong rise in the future number of heat stress events, the distribution of extreme runoff events changes but less sharply. For instance, the heat stress distributions for all the subzones shift toward higher values of the ratio as the greenhouse gas emissions increase. The shift in the mode (or in the modes in the case of Australia) of the distributions progressively increases by $0.5 \div 1$ moving from SSP1 to SSP5. Focusing on the extreme runoff, instead, this increase is more moderate. Even though the distributions are almost centered on the no-changes value (i.e., the dashed horizontal line equal to one) for the SSP1, it is possible to observe an overall shift moving to SSP5, especially for East Asia, South America, Australia and South Africa. In this case, what it is worth noticing is that these shifts are often coupled with a fattening of their right tail for all the subzones. So, even if there are some pixels where the number of extreme runoff events is projected to remain the same or decreases, in others this number is twice or some time three times as large. For what has been seen so far, this explains the apparent inconsistency between Figure 4.16 and 4.17. However, climate change affects not only the frequency but also the magnitude of the events. In a warming climate, extreme rainfall events are projected to become more intense (Fowler et al., 2021), and this may propagate to the flood impacts, despite with more uncertainties and regional differences (Do et al., 2020). Hence, all the areas found in Figure 4.16 are worth considering in the compounding of heat stress and flooding, since heat stress phenomena, even when not modulating floods directly, can still exacerbate flood impacts.

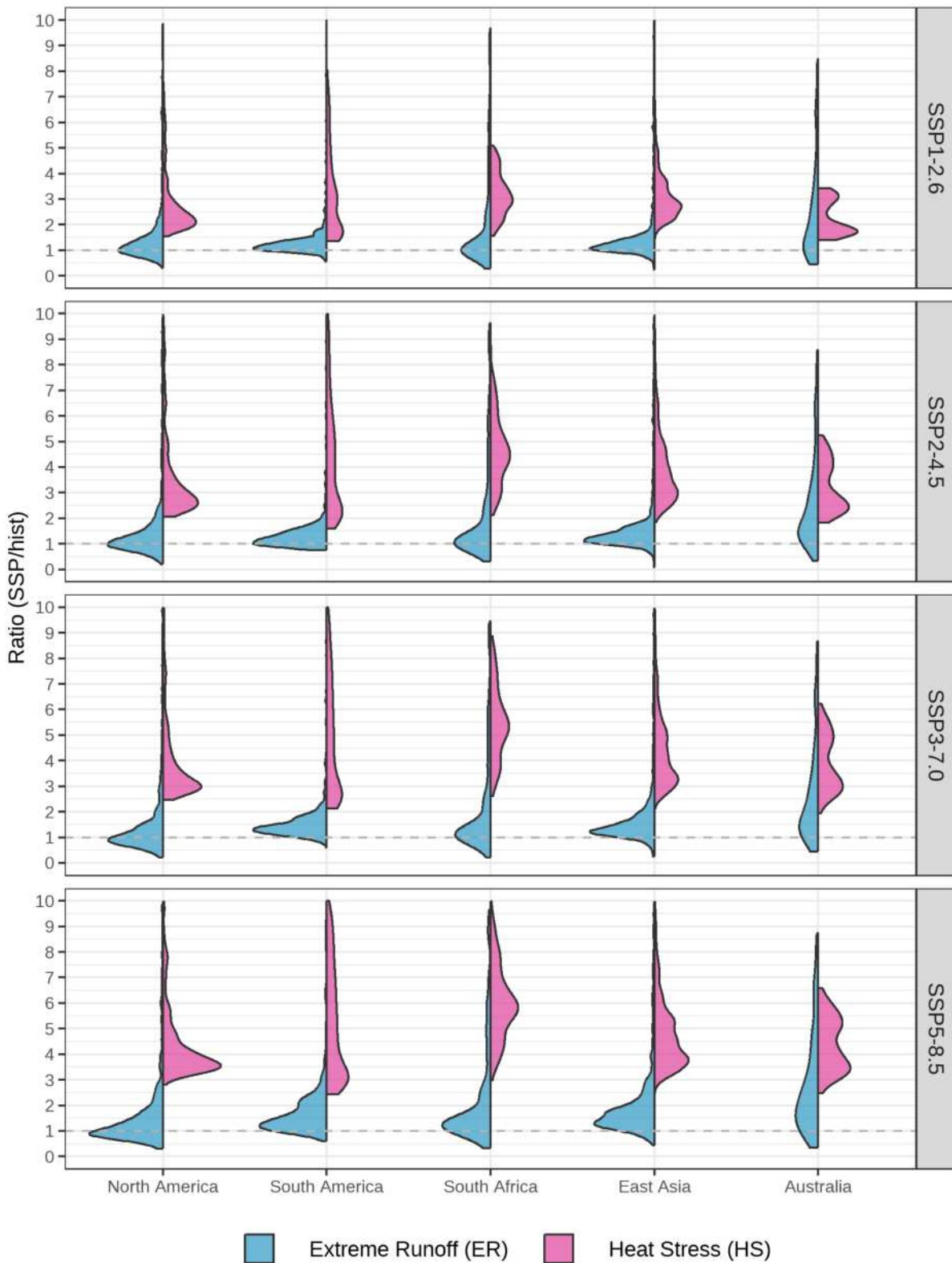


Figure 4.18: Distributions of the ratio between the number of events (heat stress in pink and extreme runoff in blue) in the future scenarios and in the historical experiment. The rows show the results for the different SSP scenarios

To quantify how the strength of the compounding between heat stress and floods varies under the different scenarios, the empirical cumulative distribution functions (ECDFs) for the different GCMs, regions and GCM experiments are shown in Figure 4.19. Moving from the historical run to SSP5-8.5, the ECDFs all shift towards higher compounding values, consistent with the results in Figure 4.16. In South America, South Africa, East Asia and Australia, the median of the distributions is twice as large in SSP1-2.6 compared to the historical run, reaching almost 100% for SSP5-8.5. Moreover, the differences between the curves for the four SSPs tend to be generally small compared to the historical simulations, which is troublesome considering how different these are in terms of climate policies. Furthermore, the ECDFs for most of the SSP5-8.5 are almost vertical and close to 100%, indicating that under that scenario, almost all flood events are projected to be preceded by a heat stress event. The results for North America are qualitatively similar to the other regions, even though there is a weaker gradient from the historical run to SSP5-8.5.

Due to a projected warmer and wetter climate, larger and new areas can be affected by more frequent and intense heat stress events. According to the future projection, Europe and parts of western Asia (i.e., Russia) could become a hot spot for this type of compounding (Figure 4.20). This expansion is due to an increase in the projected distribution of the wet bulb temperature, which implies higher values of the 95th percentile of the wet bulb temperature distribution and exposes these regions to high heat stress levels (Karwat and Franzke, 2021; Freychet et al., 2022). Although the INMs and MPI-ESM1-2-HR models do not show these areas as potentially affected the compounding because the 95th percentile of the wet bulb temperature distribution does not reach the 20°C-threshold, the other GCMs show that a high percentage of extreme runoff events may be preceded by heat stress. This is particularly true under SSP5-8.5, leading to higher risk of having human life and economic losses in the future for such areas.

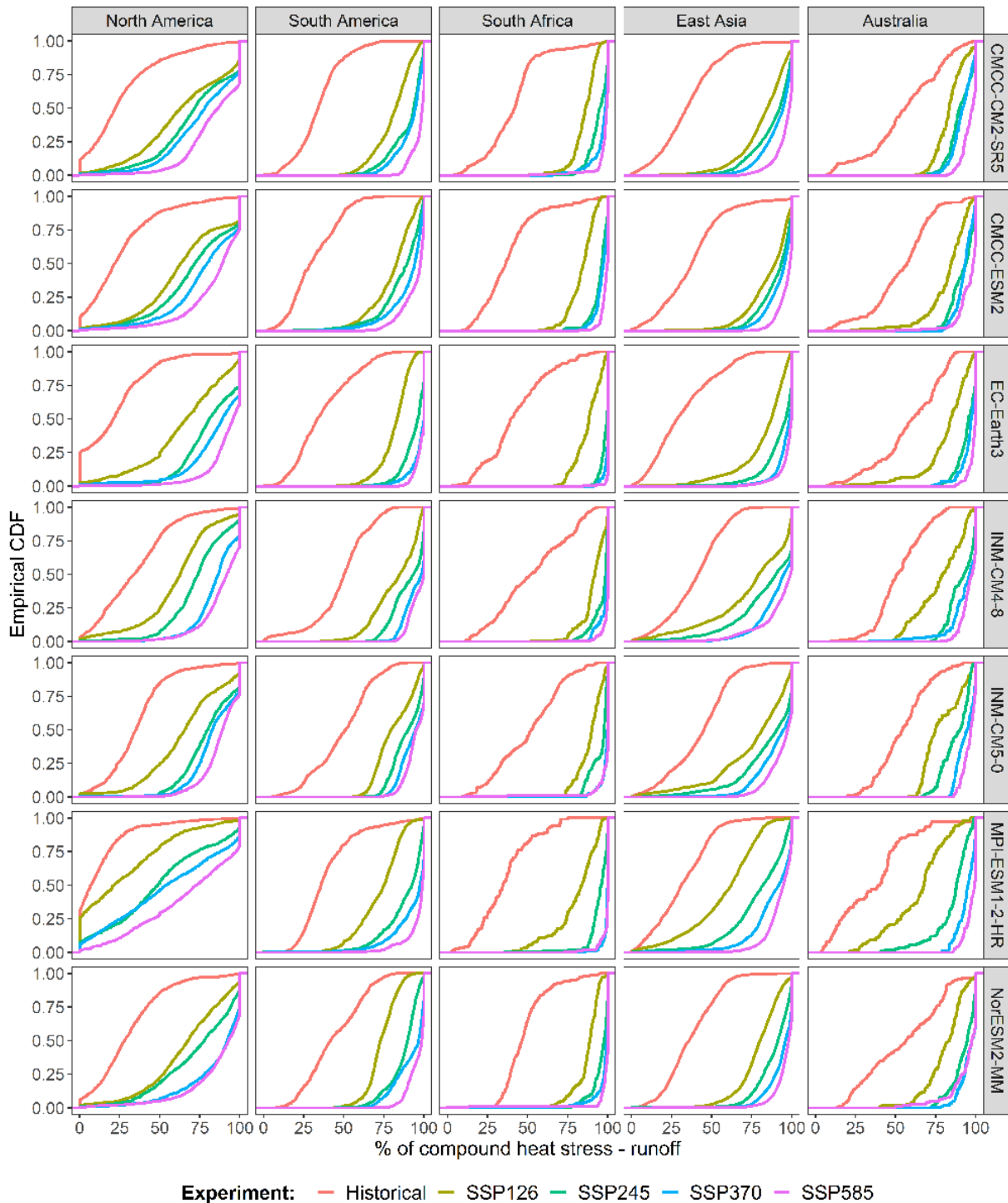


Figure 4.19: Empirical cumulative distribution functions for the percentage of compounding heat stress – runoff. The results for the GCMs are summarized on the rows, while the regions are on the columns. The red line represents the historical experiments (1979 – 2014), while the other colors are related to the SSP projection (2065 – 2100)

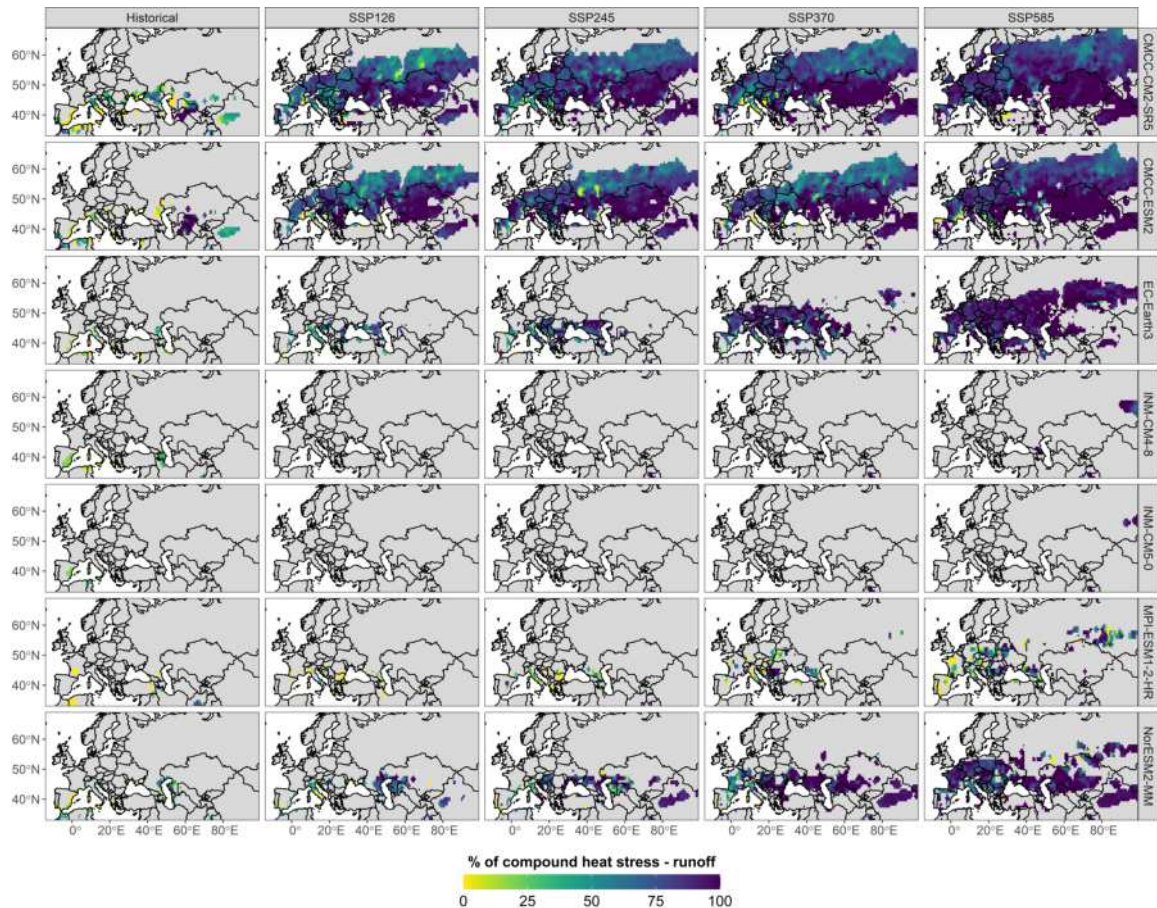


Figure 4.20: GCMs outcomes in the compounding of heat stress – runoff for Europe and western Asia. The first column represents the historical experiment for the seven GCMs (one per row), while the other columns correspond to the future expansion of the affected areas according to the different SSPs. The shaded gray area represents what is described in Figure 4.13

4.2.4. A growing risk to the future population

To provide a clearer insight related to the population that may be exposed to compound heat stress - runoff events in the future, the previous results have been intersected with the projected population of urban agglomerations. These results have been obtained by Kii (2021) by using an urban growth model in the context of the SSPs trajectory. For sake of completeness, Figure C.1 in the Appendix C shows the spatial distribution of urban agglomerations by the population scale different scenarios. The projection of the population for SSP1-2.6 for the year 2100 has been compared with the historical experiment outcomes, while the expected population at 2100 at the different SSPs has been used for the projected results in the compounding.

To intersect the results, only the cities within a radius of 100 km from the centroid of the pixels in which more than four GCMs agree with the presence of compounding have

been considered. Figure 4.21 shows the number of people (i.e., in million) who already live or might live in areas characterized by a certain percentage of the compounding according to the GCMs experiments. The majority of the population is currently concentrated within areas that are impacted by 20 – 35% of the compound and the distribution is positively skewed, ranging from 0 to 80%. According to the SSP scenarios, at the end of the 21st century an increasing number of people is projected to live in areas characterized by high values of the compound of heat stress and runoff. Moreover, the higher the emissions, the greater the shift of these distributions towards high percentages. Indeed, under the SSP2-4.5, SSP3-7.0 and SSP5-8.5, most of the population is expected to live in areas characterized by 100% of extreme runoff following heat stress. Furthermore, the overall impact can be higher since only non-rural areas have been considered, where heat stress events alone generally strike harder due to the urban environment (Zhao et al., 2014; Li et al., 2020).

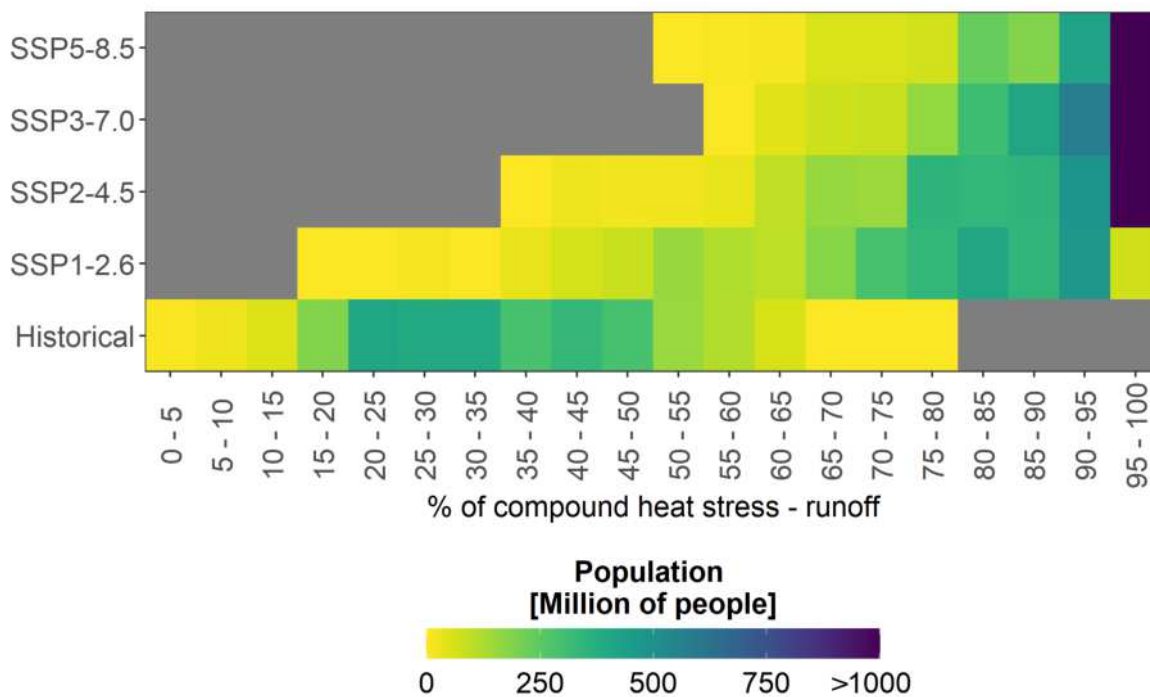


Figure 4.21: Population exposed to the compounding of heat stress – runoff for the GCMs historical experiment and SSP scenarios. Colors from yellow to purple represent the number of people that might be exposed to a certain percentage of compound heat stress – runoff events, while dark gray is representative of no data values

4.2.5. Final considerations on the heat stress - flooding compound events

In this chapter, the projected changes in the compounding of heat stress and flooding, which could represent a serious concern for human health, economy, and society, have been analyzed, identifying the areas of the globe where these two hazards are connected. The main findings can be summarized as follows:

- in the mid-latitudes, heat stress tends to precede most of the summer floods, representing a weather precursor for these events; large areas in the central and eastern United States, the central-eastern part of the South America, India, the eastern China and the east coast of Australia and South Africa are particularly involved in this type of compounding;
- the GCMs' ensemble from the CMIP6 reproduces the compound of heat stress and runoff over the period 1979–2014 reasonably well, especially when their average is considered;
- considering the wet bulb temperature instead of the dry bulb temperature and the relative humidity in a separate form reduces the uncertainty in the modulator of the compound; moreover, both the POT procedure to identify the extreme runoff and the use of the percentage as a proxy for the compounding are useful in reducing the systematic biases that can affect individual models;
- there is an asymmetry in the future growth of the number of heat stress and extreme runoff events, with the first featuring increases at a faster rate than the second one; this is mainly due to the fact that the forcings used to simulate the climate scenarios at different SSP-RCP directly affect temperature and relative humidity, while the runoff is also constrained by the land component;
- the SSP projections for the end of the 21st century show an increase in the percentage of the compounding in the different subzones considered, reaching up to 100% in large areas of United States, South America, India and China, and setting the stage for a growing risk in societal and economic related issues;
- the potential societal impacts of this compound hazard are projected to impact a large segment of the population living in urban areas.

Based on the SSP projections, the strengthening of the compounding is expected to exacerbate regardless of the scenario and to expand to areas where it did not play a major role in the past (e.g., Europe and Russia). This is alarming, given the large differences between SSP1 (i.e., “sustainability”) and the SSP5 scenarios (i.e., “fossil fueled development”) in terms of sustainable turnaround in policies and behavior; it can be also considered as a further proof of how difficult it is to counteract the inertia of climate

change. Even being able to curb the CO₂ emissions abruptly, several future generations would continue to experience the effects of global warming (Gillett et al., 2011; Frölicher et al., 2014). Therefore, these results highlight the importance of the need to immediately act to mitigate future climate impacts, and to adapt and increase our resilience against these events in response to climate change.

Conclusion

For about fifty years climate change has been, and still today is, one of the most relevant and debated topics for the scientific community. The signals, impacts, and effects of climate change appear to be obvious and we have been hearing more and more about matters such as global warming, rising of oceans and seas temperature, rising of global sea level, decreasing of arctic sea ice extent, melting of glaciers, increasing of extreme events (e.g., heavy rainfall events and/or droughts), and so on.

The research activity developed and presented in this doctoral thesis is framed within the context of studying the effects of climate change on the extreme precipitation regime. This topic is of central importance not only in the context of research, but also for a multitude of other purposes. From an engineering perspective, for example, knowing whether, how, and where extreme precipitation events are changing would allow to improve the state-of-the-art of the modeling frameworks and the design criteria that can increase the resilience of hydraulic infrastructure for years to come. A clear and comprehensive understanding of these phenomena could bridge the gap between the research community and civil society, aiding and supporting the latter in advancing rapidly toward the climate change adaptation phase. Moreover, governments could and should also benefit from this knowledge, so as to define clear objectives on climate policies to be pursued at national and international levels, establishing a synergy between society and stakeholders.

At the academic level, there is a large scientific literature on the effects of climate change on extreme rainfall events. Most of these papers have recently supported the findings of the "Sixth Assessment Report" (AR6) published in 2021 by the Intergovernmental Panel on Climate Change (IPCC). This report is lapidary in stating that the frequency and intensity of extreme precipitation events are likely to have increased on a global scale in most regions with a good network of observations, suggesting that, on a continental scale, especially North America, Europe, and Asia have been particularly prone to these changes. Indeed, the increase in the frequency and magnitude of extreme events is one of the consequences that is most attributed to climate change and, therefore, needs to be further investigated.

Given this premise, the study of changes in extreme precipitation characteristics was initially conducted focusing on Sicily. The island, being located in the center of

the Mediterranean area, can be considered an outpost for researching the signatures of climate change. In addition, it has an almost unique characteristic, namely the presence of the Sicilian Agrometeorological Information System (SIAS) precipitation database, which consists of about 100 rain gauge stations, homogeneously distributed throughout the regional territory, that have been recording data at 10-minute temporal resolution since 2002. This has made it possible to focus on intense precipitation events at the sub-hourly scale. In particular, by applying the quantile regression technique to the rainfall series aggregated at different time scales, it has been observed that especially extreme rainfall at short durations exhibit increasing and statistically significant trends for most of the island.

From these considerations a question arises: can the concept of stationarity (underlying the definition of return time) still be a cornerstone in hydrological modeling? To answer this question, the rainfall Depth-Duration-Frequency (DDF) curves derived from this new dataset were compared with those from the last regional frequency analysis carried out for the island. This last was conducted from data collected mainly in the past century. Again, there was a noticeable underestimation of the shortest return periods (5 and 10 years) at the lowest durations, which perfectly matches the apparent "physiological insufficiency" of the drainage systems that has been observed in recent years among Sicilian cities.

The intense short-lived phenomena that generally induce flash floods in urban environments are triggered by highly energetic convective processes that are exhausted in a very short time. Nevertheless, they are able to pour large volumes of rain on the ground. For this very reason, the last step in the local study of extreme rainfall involved the improvement and the application of a statistically based algorithm for separating convective and stratiform precipitation. In this case, it was observed that the highest amounts of convective rainfall characterized the areas of Catania and Messina, given the presence of the Peloritani and Etna mountains. Indeed, these orographic barriers enhance the uplift of warm and humid air masses coming from North Africa, which, cooling rapidly, spill large amounts of water in these areas.

However, local changes in the characteristics of extreme rainfall are often influenced by changes in the large-scale regime. In other words, it is appropriate to know what is happening on a global scale in order to have a complete picture of the phenomena being studied on a regional or local scale. Furthermore, in order for people to be prepared for the concepts of adaptation and resilience to climate change, it is necessary that the study be conducted in parallel on two different time fronts: the past and the future. While it is obvious that the evolution of the past climate can be reconstructed through observations, it is more complex to think about how one can assess the climate condi-

tion in the middle or, even, the end of the century. In this case, what can be used are the outputs of the global climate models (GCMs). The latter are physical-mathematical models that describe the interactions among the major components of the climate system (atmosphere, landmasses, oceans, etc...) through quantitative methods based on solving differential equations. These models are forced by combining scenarios that define specific greenhouse gas concentrations in the atmosphere (Representative Concentration Pathways, RCPs) and scenarios that represent different future socioeconomic pathways (Shared Socioeconomic Pathways, SSPs). The RCPs quantify GHG concentrations in terms of radiative forcing, i.e., the warming effect on the Earth caused by these concentrations, while SSPs are useful for understanding how human activities and socioeconomic policies might influence GHG emissions and, consequently, climate change. Their combination provides a more comprehensive view of how climate might respond in different socio-economic and emission situations.

Starting from these considerations and using the outputs of different GCMs, it has been analyzed how the characteristics of precipitation extremes might change at the end of the 21st century. The analysis has been conducted focusing not only on the intensity of events, but also considering the seasonality of the rainfall regime, which is crucial for water resource management. Representing two sides of the same coin, changes in the intensity and seasonal occurrence of heavy rainfall have been studied using a peculiar branch of copulae, namely bivariate statistical models capable of modeling the correlation between linear (the magnitude) and circular (the seasonality) variables. Globally, it has been observed that as the climate scenario worsens, extreme events may not only become more severe by the end of this century but that they may also occur with greater frequency later in the season. Moreover, for some areas, such as the southeastern United States and central Africa, this shift in the regime of extremes could be due to changes in the predominant weather systems that generate extreme precipitation events.

Among the main causes of the increase in the magnitude and frequency of extreme rainfall, it has been shown that global warming plays a key role. In fact, according to the Clausius-Clapeyron relationship, an increase in air temperature leads to an increased capacity of the air to hold water vapor and, at the same time, increases the possibility of convection in the atmosphere. These phenomena, therefore, could induce intense precipitation and, in turn, even more destructive flood events. In the context of research on compound events, i.e., events that include the combination of two or more meteorological or climatic phenomena occurring simultaneously or in close succession, the last part of this thesis is based on the compounding of heat stress and flood events. Specifically, it has been observed how heat stress preceded extreme runoff events in large areas of the United States, Asia, South America, and Australia between 1979 and 2014. Examining

the outputs of an ensemble of GCMs, this correlation is likely to be exacerbated in the future regardless of the RCP-SSP scenario, mainly due to future temperature increases. By intersecting these results with future projections for population growth in major urban centers, it has been possible to observe how a large segment of the global population could be subjected to increasing risk from these compound phenomena in the future.

A | Appendix: supplementary material for Chapter two

Table A.1: SIAS rain-gauges list with WGS84 coordinates and heights

Station Name	ID	Longitude	Latitude	Height
Agrigento Scibica	683	13.55	37.34	225
Agrigento Mandrascava	684	13.64	37.24	40
Aragona	685	13.62	37.46	305
Bivona	686	13.42	37.6	350
Cammarata	687	13.74	37.63	379
Monte Cammarata	688	13.61	37.62	1600
Canicattì	689	13.77	37.36	475
Licata	690	13.89	37.16	80
Sambuca di Sicilia	691	13.02	37.66	300
Naro	692	13.78	37.29	290
Ribera	693	13.27	37.44	30
Sciacca	694	13.04	37.59	90
Caltanissetta	695	14.05	37.43	350
Delia	696	13.93	37.35	360
Gela	697	14.33	37.16	70
Butera	698	14.11	37.14	54
Mazzarino	699	14.21	37.3	480
Mussomeli	700	13.83	37.56	375
Riesi	701	14.09	37.28	300
S. Caterina Villermosa	702	14.1	37.58	630
Sclafani Bagni	703	13.85	37.71	497
Adrano	704	14.82	37.68	400
Bronte	705	14.79	37.75	424
Catania	706	15.07	37.44	10

Continued on next page

Table A.1 – continued from previous page

Station Name	ID	Longitude	Latitude	Height
Riposto	707	15.2	37.69	50
Linguaglossa	708	15.13	37.83	590
Maletto	709	14.87	37.83	1040
Mazzarrone	710	14.56	37.1	300
Mineo	711	14.73	37.32	205
Paternò	712	14.85	37.52	100
Pedara	713	15.05	37.64	803
Ramacca Pollaci	714	14.81	37.38	50
Randazzo	715	14.98	37.89	680
Caltagirone	716	14.59	37.24	260
Aidone	717	14.47	37.45	350
Enna	718	14.18	37.52	350
Gagliano Castelferrato	719	14.5	37.7	580
Leonforte	720	14.38	37.61	340
Nicosia	721	14.42	37.76	700
Piazza Armerina	722	14.37	37.32	540
Caronia Buzza	723	14.49	38.03	50
Caronia Pomiere	724	14.49	37.9	1470
Cesarò Vignazza	725	14.68	37.84	820
Cesarò Monte Soro	726	14.69	37.93	1840
Fiumedinisi	727	15.38	38.04	440
Leni (Salina)	728	14.83	38.56	315
Messina	729	15.56	38.26	420
Militello Rosmarino	730	14.67	38.04	460
Mistretta	731	14.34	37.86	690
Taormina	732	15.23	37.85	60
Naso	733	14.79	38.11	468
Novara di Sicilia	734	15.14	38.03	750
Patti	735	15.02	38.14	88
Pettineo	736	14.29	37.97	210
San Fratello	737	14.62	37.96	1040
San Pier Niceto	738	15.36	38.13	460
Torregrotta	739	15.36	38.19	26
Alia	740	13.75	37.74	560

Continued on next page

Table A.1 – continued from previous page

Station Name	ID	Longitude	Latitude	Height
Caltavuturo	741	13.91	37.79	810
Camporeale	742	13.1	37.91	460
Castelbuono	743	14.09	37.97	430
Contessa Entellina	744	13.04	37.73	200
Corleone	745	13.25	37.8	450
Lascari	746	13.92	38	55
Mezzojuso	747	13.5	37.85	390
Misilmeri	748	13.44	38.03	160
Monreale Vigna Api	749	13.2	38.03	612
Palermo	750	13.33	38.13	50
Partinico	751	13.09	38.07	120
Gangi	752	14.19	37.82	833
Petralia Sottana	753	14.01	37.63	720
Polizzi Generosa	754	14	37.83	650
Termini Imerese	755	13.61	37.97	350
Ragusa	756	14.68	36.96	650
Comiso	757	14.59	37.02	220
Ispica	758	14.99	36.73	30
Modica	759	14.9	36.88	300
Santa Croce Camerina	760	14.5	36.84	55
Sciacca	761	14.68	36.76	51
Acate	762	14.4	36.98	60
Augusta	763	15.15	37.28	90
Siracusa	764	15.16	37.06	90
Francofonte	765	14.89	37.25	100
Lentini	766	14.93	37.34	50
Noto	767	15.06	36.85	30
Pachino	769	15.1	36.68	50
Palazzolo Acreide	770	14.87	37.06	640
Calatafimi	772	12.88	37.86	299
Castellammare del Golfo	773	12.89	38.01	90
Castelvetrano	774	12.85	37.65	120
Erice	775	12.59	38.03	590
Marsala	776	12.57	37.8	120

Continued on next page

Table A.1 – continued from previous page

Station Name	ID	Longitude	Latitude	Height
Mazara del Vallo	777	12.68	37.68	30
Salemi	778	12.72	37.82	280
Trapani Fontanasalsa	779	12.55	37.94	50
Trapani Fulgatore	780	12.66	37.95	180
Montalbano Elicona	1380	14.97	37.99	1250
Giuliana	1381	13.23	37.63	260
Prizzi	1382	13.43	37.72	990
Agira	1383	14.5	37.62	467
Antillo	1384	15.26	37.98	796
Calascibetta	1385	14.23	37.67	650
Monreale Bifarera	1386	13.37	37.88	730
Ramacca Giumarra	1404	14.63	37.48	263
Pantelleria	1424	11.95	36.79	161
Linguaglossa Etna Nord	1444	15.03	37.79	1875

Table A.2: SIAS rain-gauges used in Section 2.2.2, 2.2.3 and 2.2.4

Station Name	ID	Section 2.2.2	Section 2.2.3	Section 2.2.4
Agrigento Scibica	683	X	X	X
Agrigento Mandrascava	684	X	X	X
Aragona	685	X	X	X
Bivona	686	X	X	X
Cammarata	687	X	X	X
Monte Cammarata	688			X
Canicattì	689	X	X	X
Licata	690	X	X	X
Sambuca di Sicilia	691			X
Naro	692			X
Ribera	693	X	X	X
Sciacca	694			X
Caltanissetta	695	X	X	X
Delia	696	X	X	X
Gela	697			X

Continued on next page

Table A.2 – continued from previous page

Station Name	ID	Section 2.2.2	Section 2.2.3	Section 2.2.4
Butera	698			X
Mazzarino	699	X	X	X
Mussomeli	700	X	X	X
Riesi	701	X	X	X
S. Caterina Villermosa	702			X
Sclafani Bagni	703	X	X	X
Adrano	704			X
Bronte	705	X	X	X
Catania	706	X	X	X
Riposto	707	X	X	X
Linguaglossa	708	X	X	X
Maletto	709	X	X	X
Mazzarrone	710	X	X	X
Mineo	711	X	X	X
Paternò	712	X	X	X
Pedara	713	X	X	X
Ramacca Pollaci	714			X
Randazzo	715	X	X	X
Caltagirone	716	X	X	X
Aidone	717			X
Enna	718	X	X	X
Gagliano Castelferrato	719			X
Leonforte	720			X
Nicosia	721	X	X	X
Piazza Armerina	722	X	X	X
Caronia Buzza	723	X	X	X
Caronia Pomiere	724			X
Cesarò Vignazza	725	X	X	X
Cesarò Monte Soro	726			X
Fiumedinisi	727	X	X	X
Leni (Salina)	728			X
Messina	729	X	X	X
Militello Rosmarino	730	X	X	X
Mistretta	731	X	X	X

Continued on next page

Table A.2 – continued from previous page

Station Name	ID	Section 2.2.2	Section 2.2.3	Section 2.2.4
Taormina	732			X
Naso	733	X	X	X
Novara di Sicilia	734	X	X	X
Patti	735	X	X	X
Pettineo	736	X	X	X
San Fratello	737	X	X	X
San Pier Niceto	738	X	X	X
Torregrotta	739	X	X	X
Alia	740	X	X	X
Caltavuturo	741			X
Camporeale	742	X	X	X
Castelbuono	743	X	X	X
Contessa Entellina	744	X	X	X
Corleone	745	X	X	X
Lascari	746	X	X	X
Mezzojuso	747	X	X	X
Misilmeri	748	X	X	X
Monreale Vigna Api	749	X	X	X
Palermo	750	X	X	X
Partinico	751	X	X	X
Gangi	752	X	X	X
Petralia Sottana	753			X
Polizzi Generosa	754	X	X	X
Termini Imerese	755	X	X	X
Ragusa	756	X	X	X
Comiso	757	X	X	X
Ispica	758	X	X	X
Modica	759			X
Santa Croce Camerina	760	X	X	X
Scicli	761	X	X	X
Acate	762	X	X	X
Augusta	763			X
Siracusa	764	X	X	X
Francofonte	765	X	X	X

Continued on next page

Table A.2 – continued from previous page

Station Name	ID	Section 2.2.2	Section 2.2.3	Section 2.2.4
Lentini	766	X	X	X
Noto	767			X
Pachino	769	X	X	X
Palazzolo Acreide	770	X	X	X
Calatafimi	772			X
Castellammare del Golfo	773	X	X	X
Castelvetrano	774			X
Erice	775	X	X	X
Marsala	776			X
Mazara del Vallo	777	X	X	X
Salemi	778	X	X	X
Trapani Fontanasalsa	779	X	X	X
Trapani Fulgatore	780	X	X	X
Montalbano Elicona	1380			X
Giuliana	1381			X
Prizzi	1382			X
Agira	1383			X
Antillo	1384			X
Calascibetta	1385			X
Monreale Bifarera	1386			X
Ramacca Giumarra	1404			X
Pantelleria	1424			X
Linguaglossa Etna Nord	1444			X

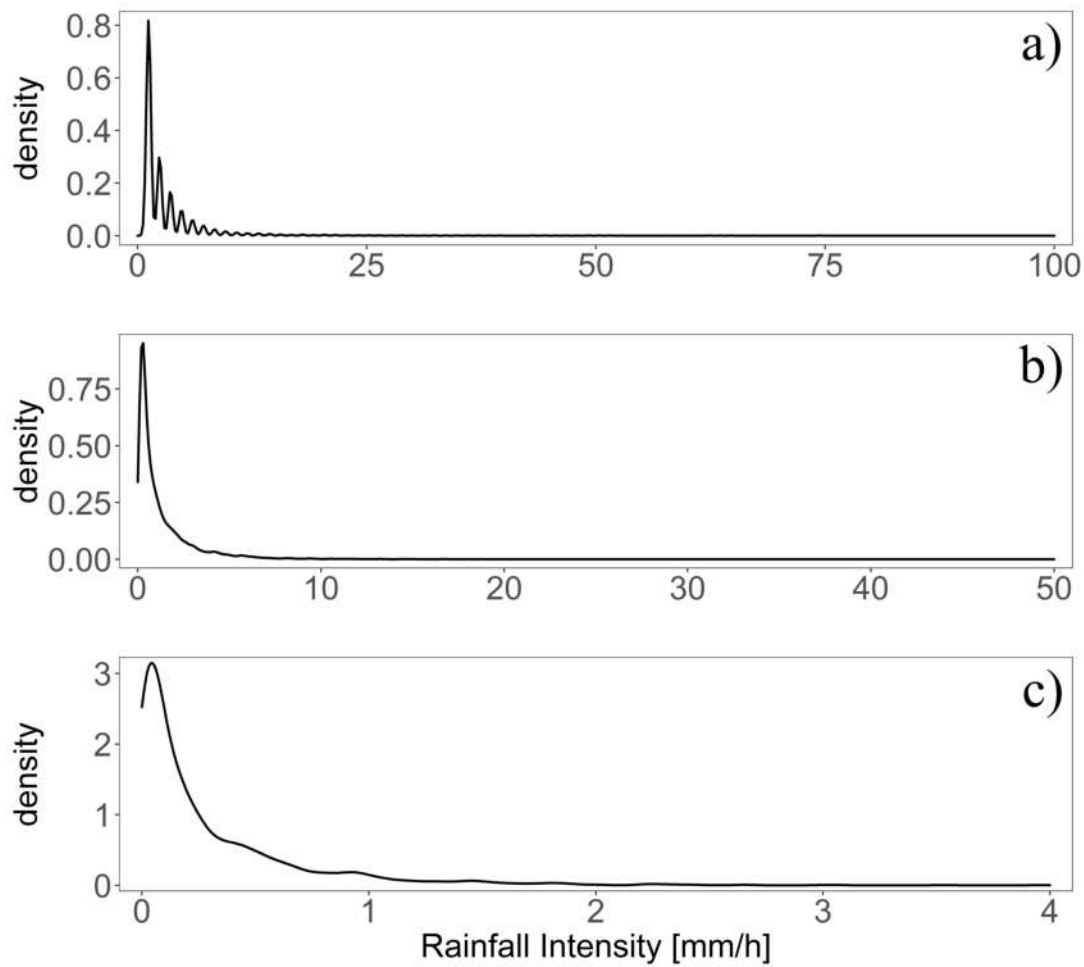


Figure A.1: Empirical PDFs of rainfall intensity data for Palermo's station at a) 10-minute, b) 1-hour and c) 24-hour durations

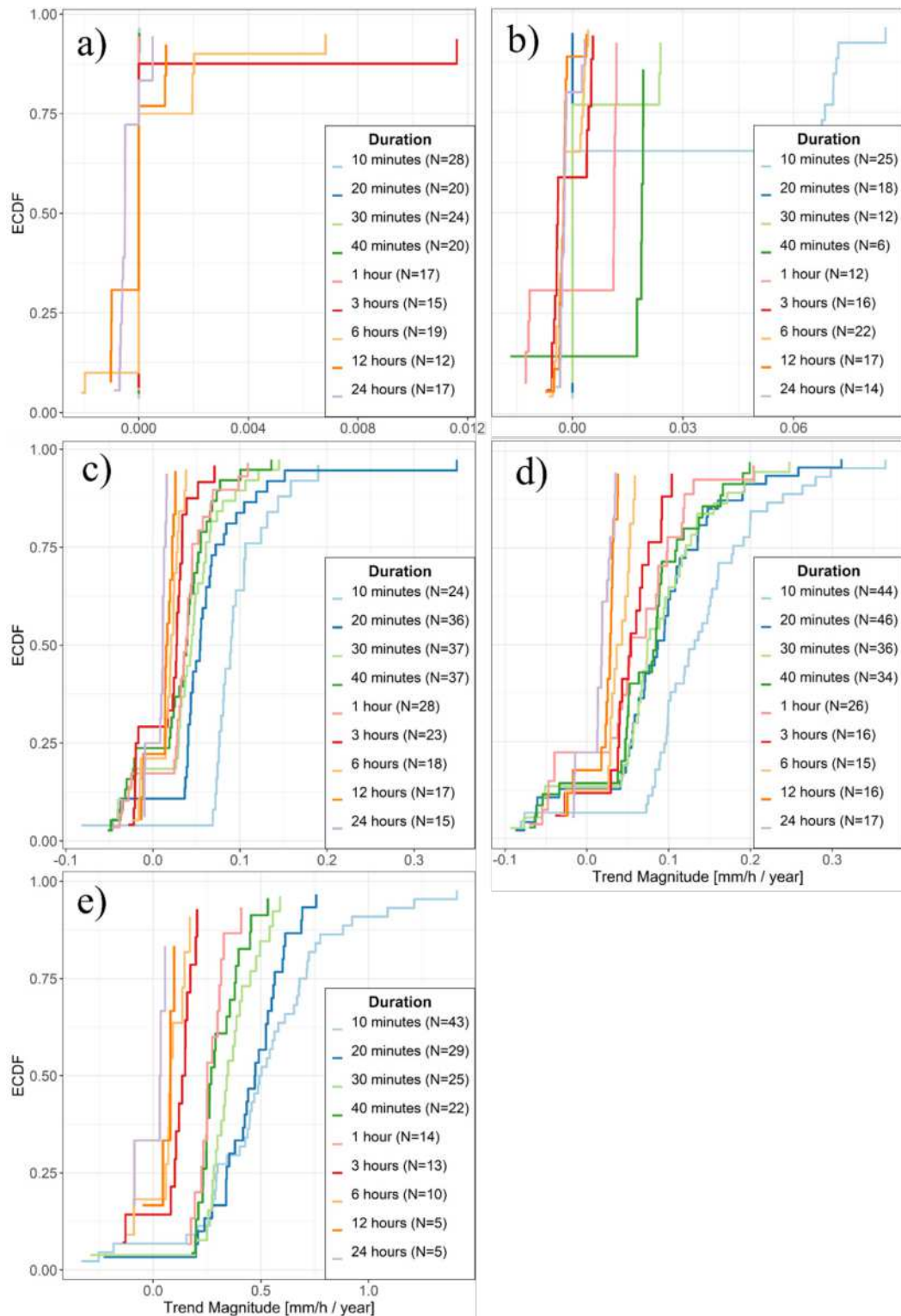


Figure A.2: Empirical CDFs of the trend magnitude for 10, 20, 30, 40 minutes and 1, 3, 6, 12 and 24 hours at a) 0.2, b) 0.5, c) 0.9, d) 0.95 and e) 0.99 quantile. ECDFs are representative of the positive and negative trend magnitude with a significance level of 0.1. The sample size for any quantile-duration combination is reported in the legend of each panel

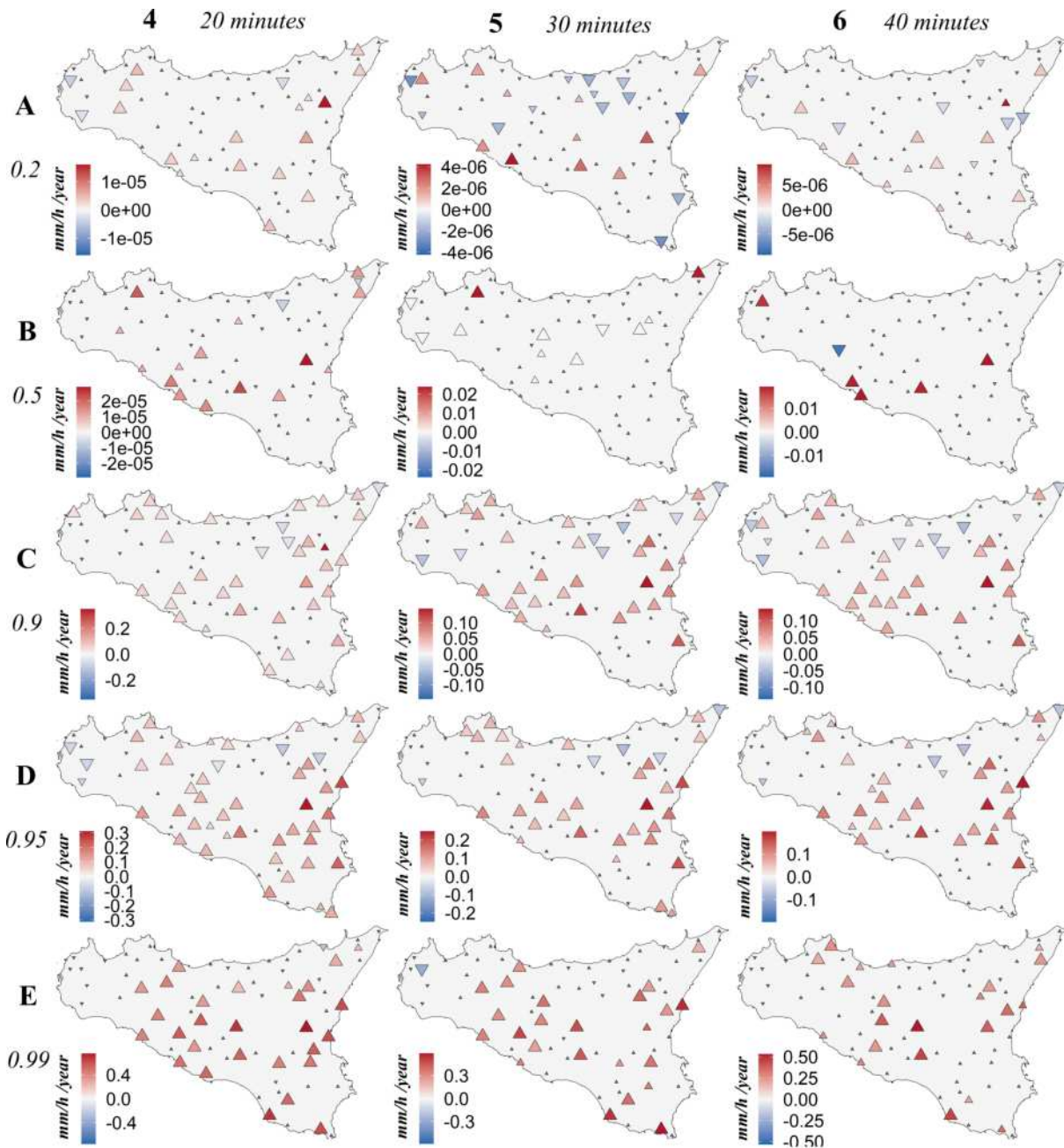


Figure A.3: Spatial distribution of the gauges under study and magnitude (color), expressed in mm/h/y, direction (triangles orientation) and significance (triangle size) from QR at 0.2, 0.5, 0.9, 0.95, 0.99 quantiles for 20-minute, 30-minute and 40-minute durations. The bold letters, A-E, stand for the quantiles, while the bold numbers 4-6, indicate the durations

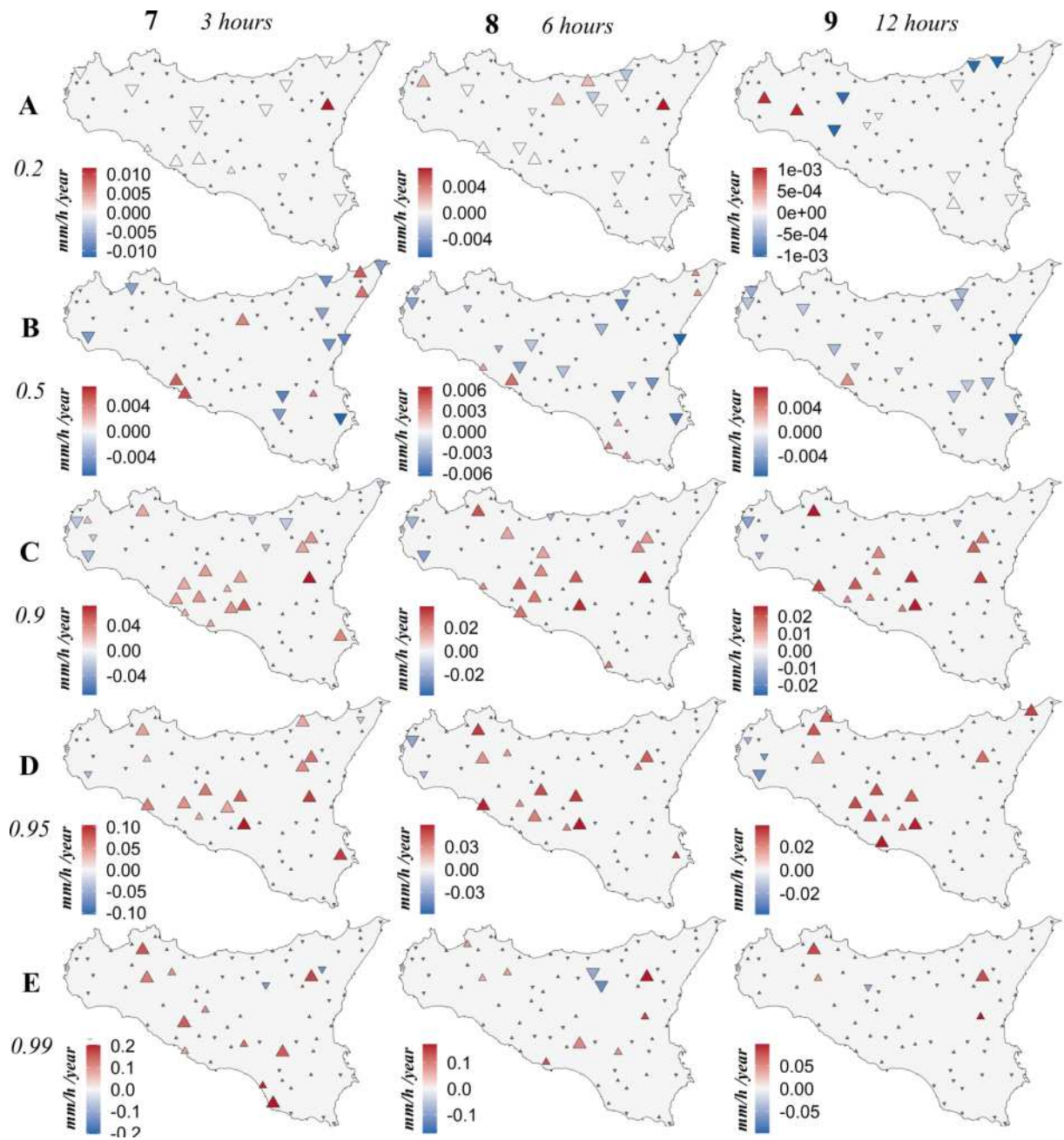


Figure A.4: Spatial distribution of the gauges under study and magnitude (color), expressed in mm/h/y, direction (triangles orientation) and significance (triangle size) from QR at 0.2, 0.5, 0.9, 0.95, 0.99 quantiles for 3-hour, 6-hour and 12-hour durations. The bold letters, A-E, stand for the quantiles, while the bold numbers 7-9, indicate the durations

Table A.3: Global Moran's Index estimated value, Z -score, p -value and sample size for 0.2, 0.5, 0.9, 0.95, and 0.99 quantiles and for the whole durations under study. All cases in which the p -value is less than 0.1 but the sample size is less than 25 are indicated with an italic font, while those cases in which the p -value is less than 0.1 and the sample size is greater than 25 are written in bold-italic font. Normal font face is related, instead, to those cases in which the spatial distribution of the trend magnitude is the result of a random spatial process (p -value greater than 0.1)

0.2 quantile									
	10 min	20 min	30 min	40 min	1 h	3 h	6 h	12 h	24 h
Moran's I	0.0442	-0.0368	0.0332	-0.4138	0.2722	-0.0475	-0.1668	0.1224	0.0202
Z-score	0.5108	0.0983	0.4965	-2.4335	1.6065	0.2671	-1.0277	0.8337	0.4338
p-value	0.6095	0.9217	0.6195	0.0150	0.1082	0.7894	0.3041	0.4045	0.6645
Sample Size	28	20	24	20	17	15	19	12	17
0.5 quantile									
	10 min	20 min	30 min	40 min	1 h	3 h	6 h	12 h	24 h
Moran's I	-0.0939	0.2174	0.0687	-0.2110	-0.5349	0.1059	<i>0.3401</i>	0.0665	-0.2730
Z-score	-0.4451	1.0868	0.7761	-0.0413	-1.4191	1.0091	<i>1.9193</i>	0.6519	-0.9623
p-value	0.6562	0.2771	0.4377	0.9670	0.1559	0.3129	<i>0.0549</i>	0.5145	0.3359
Sample Size	25	18	12	6	12	16	<i>22</i>	17	14
0.9 quantile									
	10 min	20 min	30 min	40 min	1 h	3 h	6 h	12 h	24 h
Moran's I	0.0854	0.0679	<i>0.3226</i>	<i>0.3245</i>	<i>0.1494</i>	<i>0.2432</i>	<i>0.2036</i>	<i>0.4244</i>	<i>0.6666</i>
Z-score	1.3501	1.3555	<i>3.0707</i>	<i>3.7794</i>	<i>2.1511</i>	<i>2.9731</i>	<i>1.9076</i>	<i>2.9303</i>	<i>3.5955</i>
p-value	0.1770	0.1753	<i>0.0021</i>	<i>0.0002</i>	<i>0.0315</i>	<i>0.0029</i>	<i>0.0564</i>	<i>0.0034</i>	<i>0.0003</i>
Sample Size	24	36	<i>37</i>	<i>37</i>	<i>28</i>	<i>23</i>	<i>18</i>	<i>17</i>	<i>15</i>
0.95 quantile									
	10 min	20 min	30 min	40 min	1 h	3 h	6 h	12 h	24 h
Moran's I	<i>0.2766</i>	<i>0.2718</i>	<i>0.1517</i>	<i>0.1777</i>	<i>0.1744</i>	0.0783	<i>0.1407</i>	<i>0.5767</i>	<i>0.4674</i>
Z-score	<i>2.9122</i>	<i>2.8582</i>	<i>2.1174</i>	<i>2.5842</i>	<i>1.7659</i>	0.8967	<i>1.8056</i>	<i>5.0331</i>	<i>2.8604</i>
p-value	<i>0.0036</i>	<i>0.0043</i>	<i>0.0342</i>	<i>0.0098</i>	<i>0.0774</i>	0.3699	<i>0.0710</i>	<i>0.0000</i>	<i>0.0042</i>
Sample Size	<i>44</i>	<i>46</i>	<i>36</i>	<i>34</i>	<i>26</i>	16	<i>15</i>	<i>16</i>	<i>17</i>
0.99 quantile									
	10 min	20 min	30 min	40 min	1 h	3 h	6 h	12 h	24 h
Moran's I	0.0501	<i>0.3047</i>	-0.0260	<i>0.2727</i>	-0.1462	-0.1967	<i>1.2306</i>	0.1711	0.3266
Z-score	1.0981	<i>2.7095</i>	0.1715	<i>1.8055</i>	-0.3092	-0.4255	<i>3.3606</i>	1.2302	0.8874
p-value	0.2722	<i>0.0067</i>	0.8638	<i>0.0710</i>	0.7571	0.6705	<i>0.0008</i>	0.2186	0.3749
Sample Size	43	<i>29</i>	25	<i>22</i>	14	13	<i>10</i>	5	5

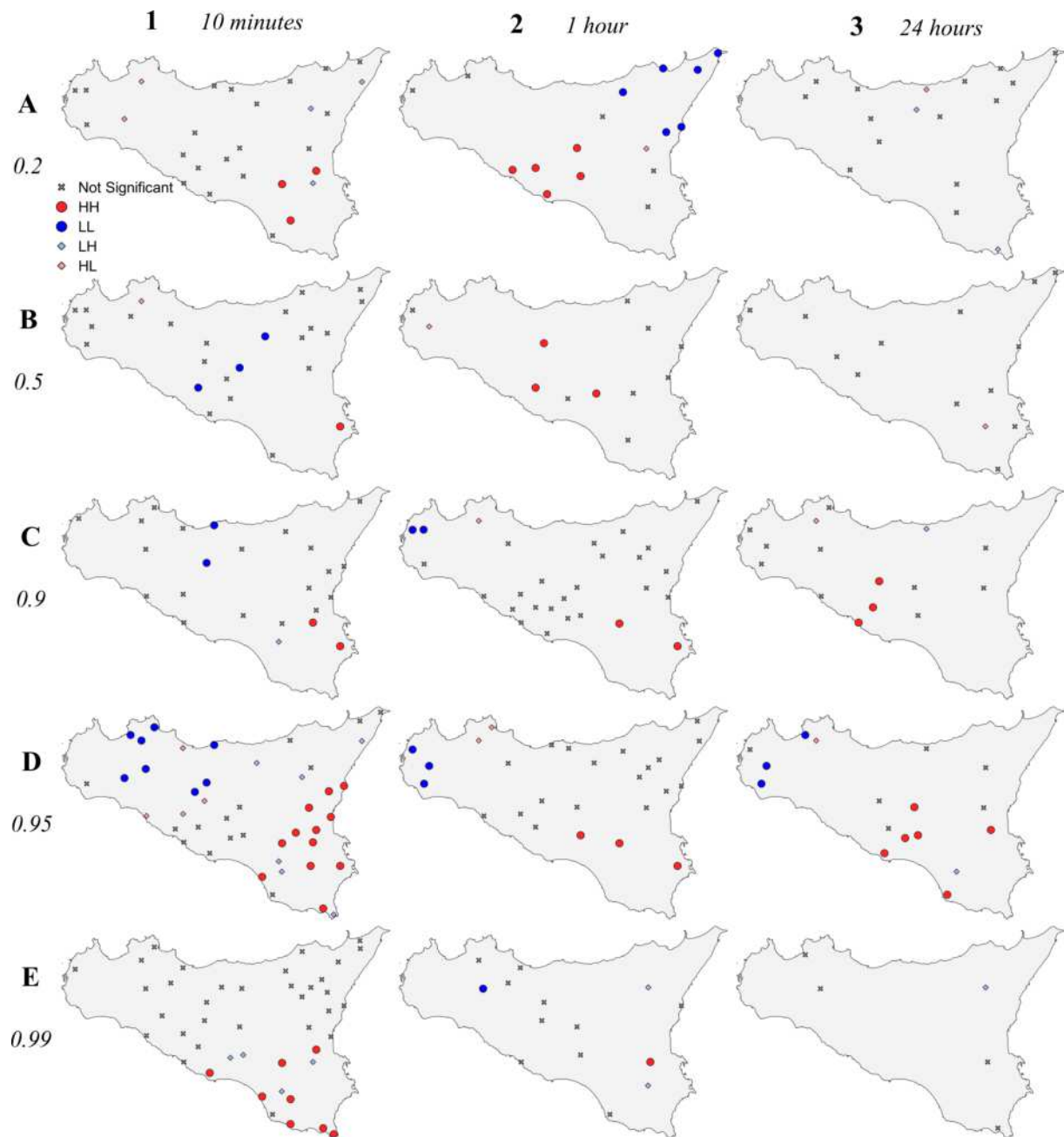


Figure A.5: Local Moran analysis at 0.2, 0.5, 0.9, 0.95, 0.99 quantiles for 10-minute, 1-hour and 23-hour durations. The bold letters, A-E, stand for the quantiles, while the bold numbers 1-3, indicate the durations. The LISA is applied to both the positive and negative trend magnitudes with a significance level of 0.1. Red and blue circles are relative to High-High (HH) and Low-Low (LL) clustering cases, respectively, and characterized by a p -value lower than 0.1. The significant outliers are marked with light blue and pink diamonds for Low-High (LH) and High-Low (HL) clustering cases, respectively. The crosses represent those locations in which the significance exceed the level of 0.1

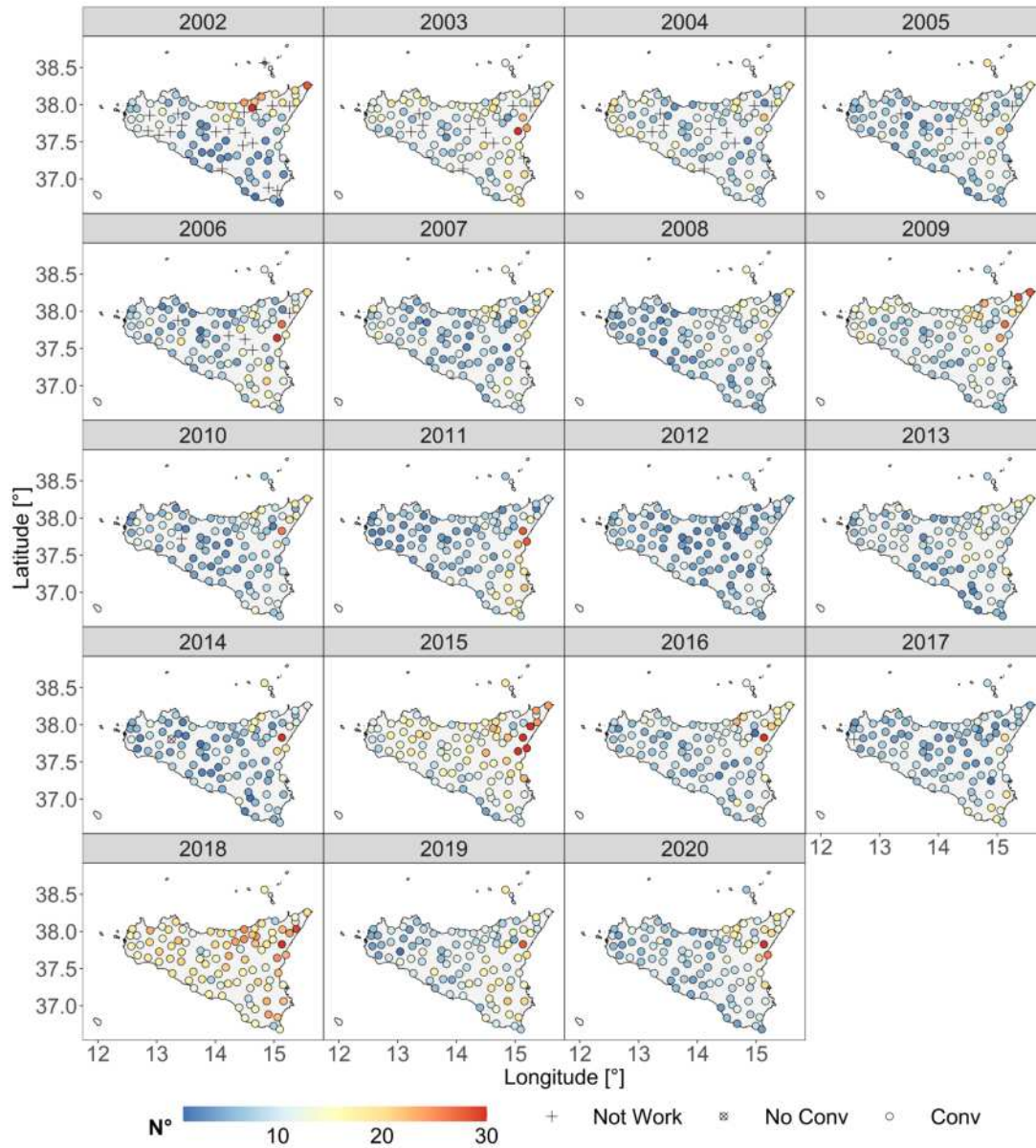


Figure A.6: Spatial distribution of the occurrence of convective events (expressed as number of convective events in a year) extracted by using the monthly median I_{cr} for $0.6 \text{ mm} \cdot 20\text{min}^{-1}$ and considering $\lambda=50\%$. Each panel is representative of a different year in the period 2002 – 2020. The colored points depict the gauges interested by at least one convective event, the circle-cross symbol stands for the working gauges where no convective events have been detected, while the plus sign symbolizes the not working stations in that year

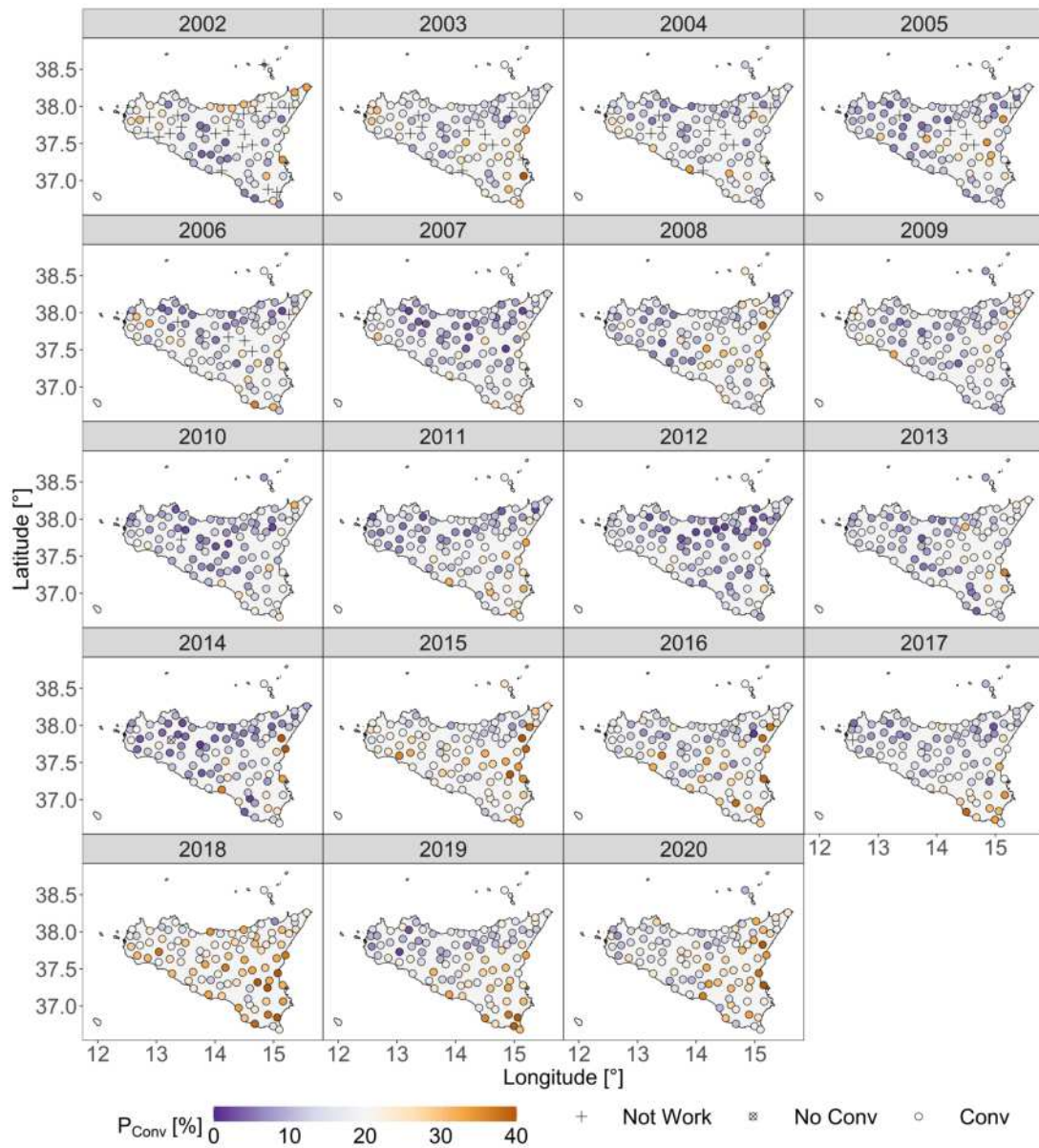


Figure A.7: Same of Figure A.6 but for the annual percentage of convective rainfall

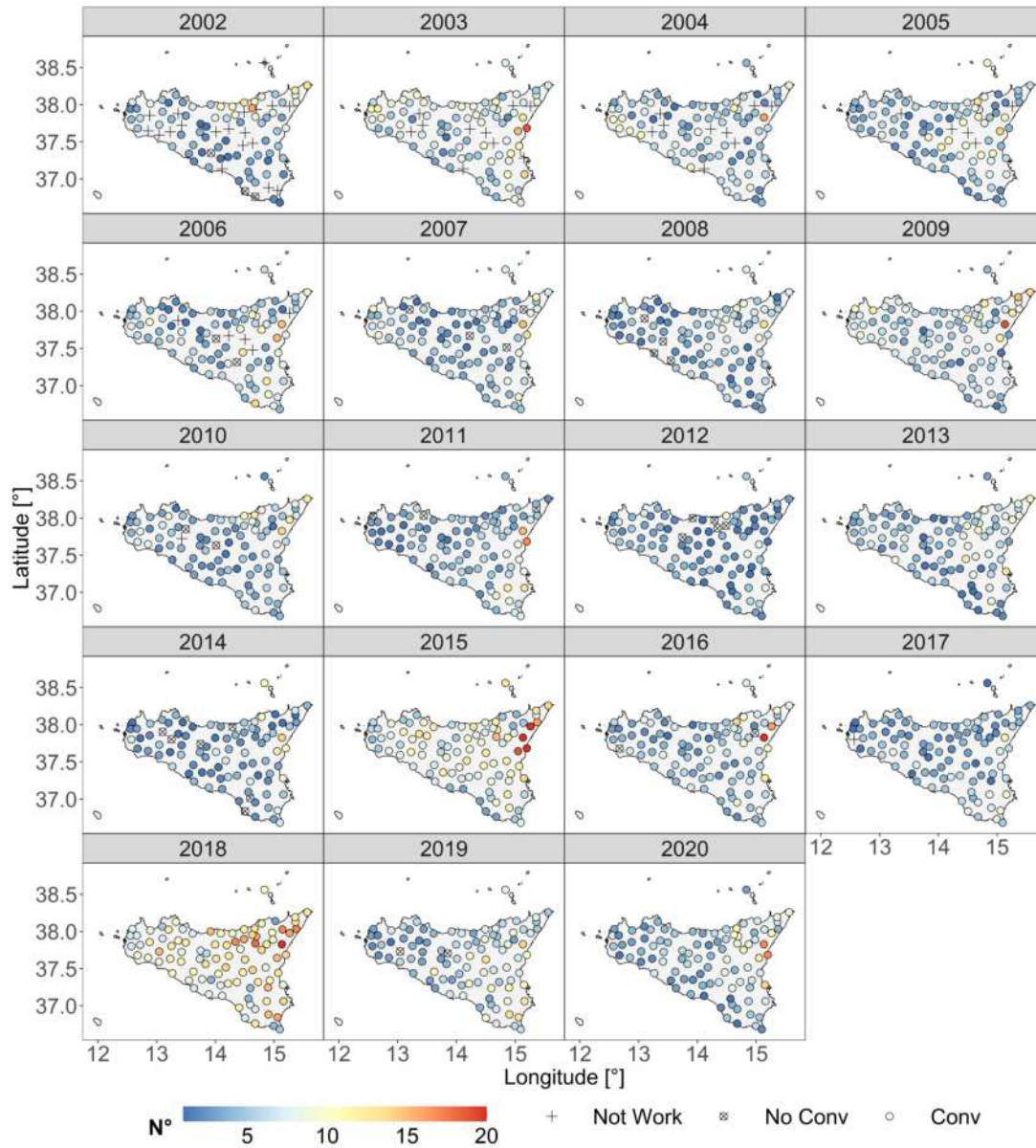


Figure A.8: Spatial distribution of the occurrence of convective events (expressed as number of convective events in a year) extracted by using the monthly median I_{cr} for $0.6 \text{ mm} \cdot 20 \text{ min}^{-1}$ and considering $\lambda=75\%$. Each panel is representative of a different year in the period 2002 – 2020. The colored points depict the gauges interested by at least one convective event, the circle-cross symbol stands for the working gauges where no convective events have been detected, while the plus sign symbolizes the not working stations in that year

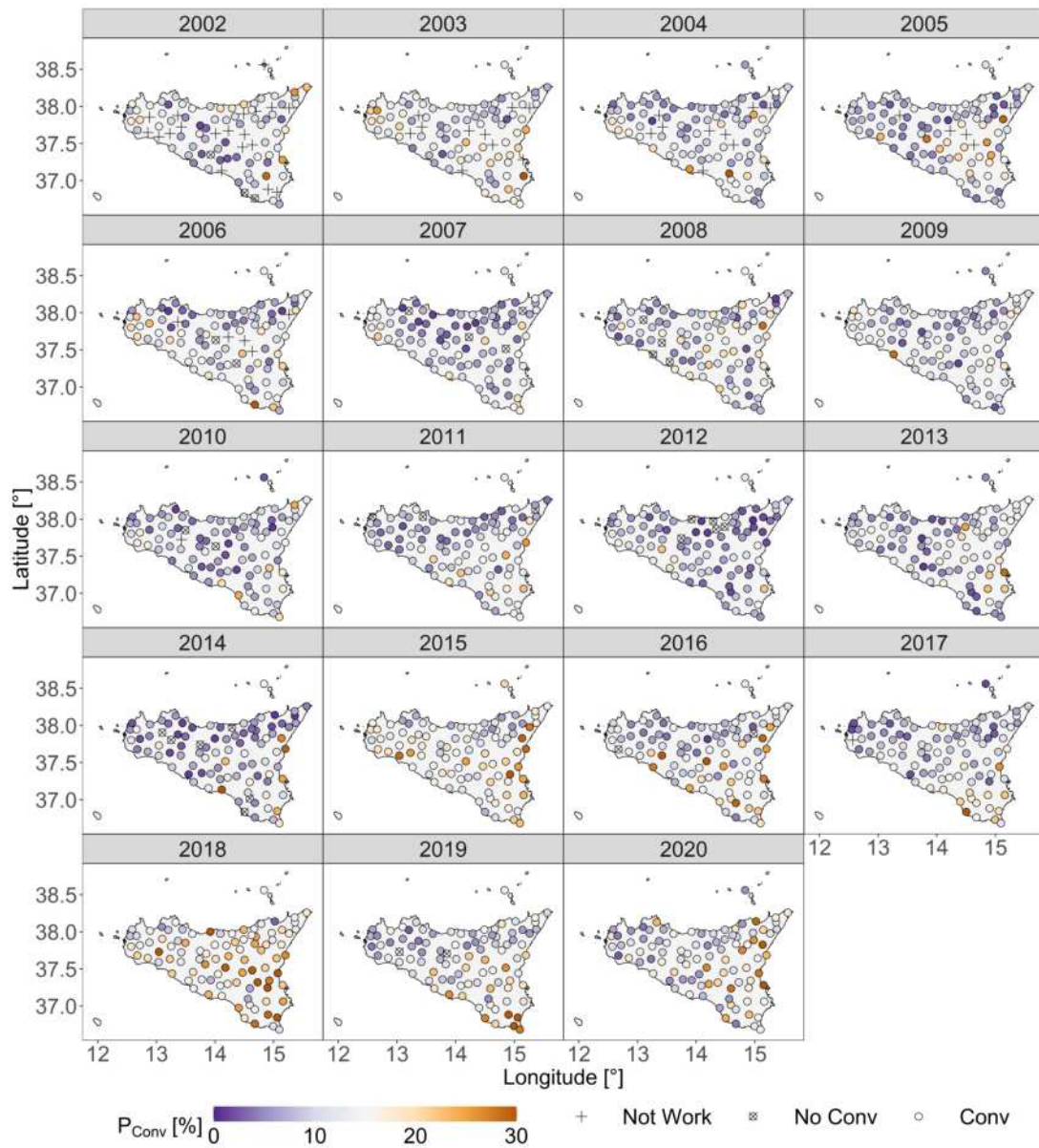


Figure A.9: Same of Figure A.8 but for the annual percentage of convective rainfall



B | Appendix: supplementary material for Chapter three

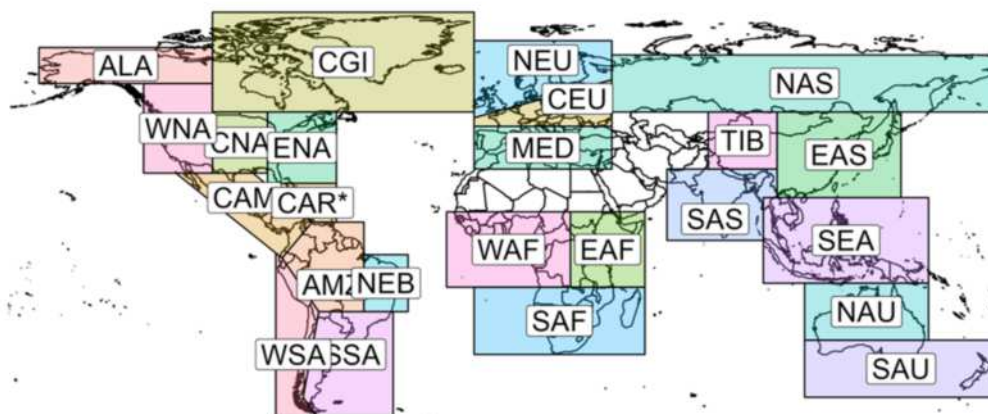


Figure B.1: Intergovernmental Panel on Climate Change WGI reference regions from the Fifth Assessment Report (AR5) (Stocker et al., 2014)



C | Appendix: supplementary material for Chapter four

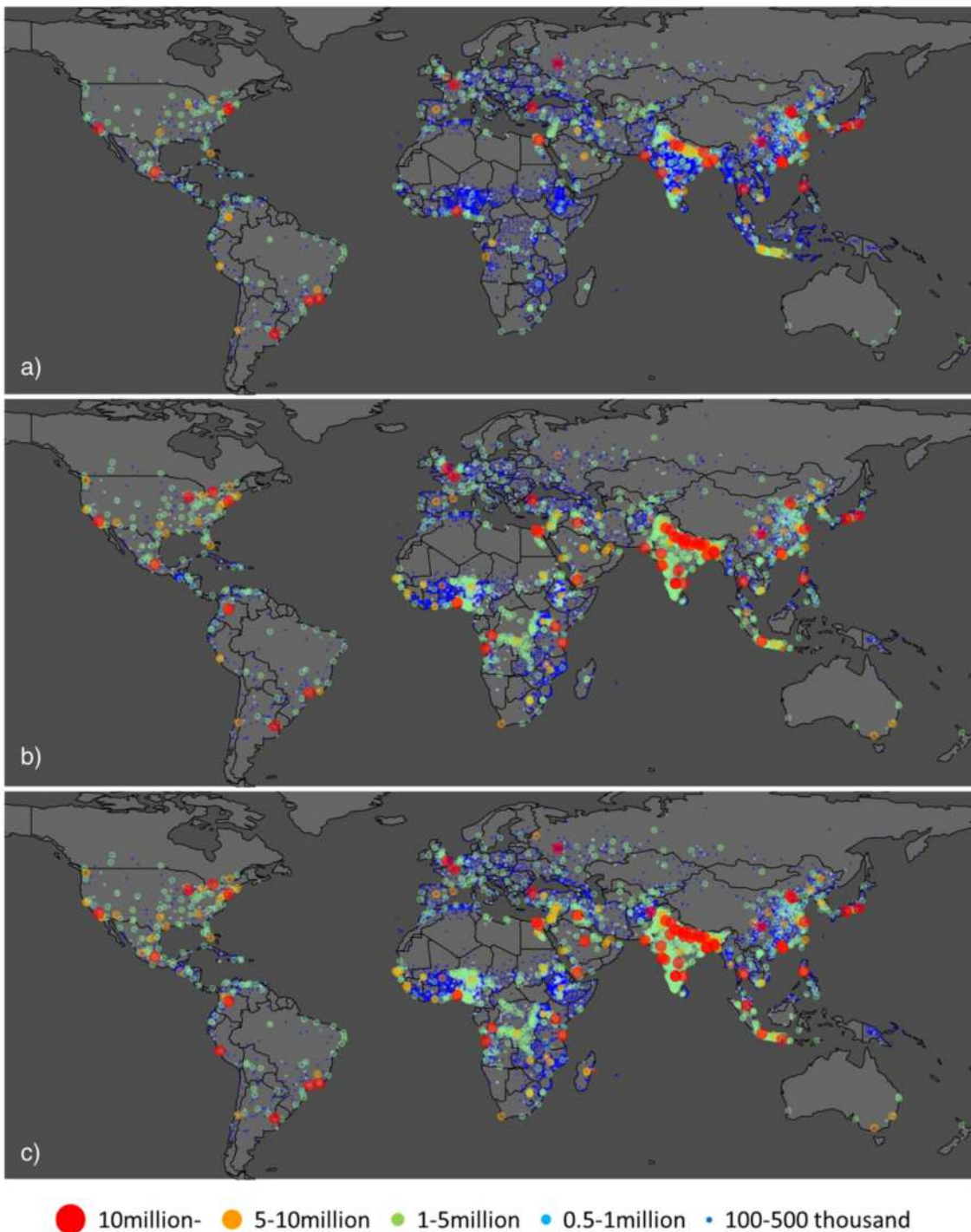


Figure C.1: From Kii (2021): Spatial distribution of urban agglomerations by the population scale for 2010 (a) and projections for 2100 under scenarios SSP1 (b) and SSP2 (c) respectively



Bibliography

- Abbate, A., Papini, M. and Longoni, L. (2022), ‘Orographic precipitation extremes: an application of lume (linear upslope model extension) over the alps and apennines in italy’, *Water* **14**(14), 2218.
- Abiodun, B. J., Adegoke, J., Abatan, A. A., Ibe, C. A., Egbebiyi, T. S., Engelbrecht, F. and Pinto, I. (2017), ‘Potential impacts of climate change on extreme precipitation over four african coastal cities’, *Climatic Change* **143**, 399–413.
- Adam, D. (2023), ‘What a 190-year-old equation says about rainstorms in a changing climate’, *Proceedings of the National Academy of Sciences* **120**(14), e2304077120.
- Adamowski, J., Adamowski, K. and Bougadis, J. (2010), ‘Influence of trend on short duration design storms’, *Water Resources Management* **24**, 401–413.
- Agostinelli, C. and Lund, U. (2023), *R package circular: Circular Statistics (version 0.5-0)*.
- Ahmadalipour, A., Moradkhani, H. and Kumar, M. (2019), ‘Mortality risk from heat stress expected to hit poorest nations the hardest’, *Climatic Change* **152**, 569–579.
- Ajjur, S. B. and Riffi, M. I. (2020), ‘Analysis of the observed trends in daily extreme precipitation indices in gaza strip during 1974–2016’, *International Journal of Climatology* **40**(14), 6189–6200.
- Alahmad, B., Vicedo-Cabrera, A. M., Chen, K., Garshick, E., Bernstein, A. S., Schwartz, J. and Koutrakis, P. (2022), ‘Climate change and health in kuwait: temperature and mortality projections under different climatic scenarios’, *Environmental Research Letters* **17**(7), 074001.
- Ali, E., Cramer, W., Carnicer, J., Georgopoulou, E., Hilmi, N., Cozannet, G. L. and Lionello, P. (2022), ‘Cross-chapter paper 4: Mediterranean region. in: Climate change 2022: Impacts, adaptation and vulnerability. contribution of working group ii to the sixth assessment report of the intergovernmental panel on climate change [h.-o. pörtner, d.c. roberts, m. tignor, e.s. poloczanska, k. mintenbeck, a. alegría, m. craig, s. langsdorf, s. löschke, v. möller, a. okem, b. rama (eds.)]’, *Ginevra, IPCC* pp. 2233—2272.
- Ali, H., Fowler, H. J., Lenderink, G., Lewis, E. and Pritchard, D. (2021), ‘Consistent large-scale response of hourly extreme precipitation to temperature variation over land’, *Geophysical Research Letters* **48**(4), e2020GL090317.

- Almeida, C., Oliveira-Júnior, J., Delgado, R., Cubo, P. and Ramos, M. (2017), ‘Spatiotemporal rainfall and temperature trends throughout the brazilian legal amazon, 1973–2013’, *International Journal of Climatology* **37**(4), 2013–2026.
- Alpert, P., Ben-Gai, T., Baharad, A., Benjamini, Y., Yekutieli, D., Colacino, M., Diodato, L., Ramis, C., Homar, V., Romero, R. et al. (2002), ‘The paradoxical increase of mediterranean extreme daily rainfall in spite of decrease in total values’, *Geophysical research letters* **29**(11), 31–1.
- Andimuthu, R., Kandasamy, P., Mudgal, B., Jeganathan, A., Balu, A. and Sankar, G. (2019), ‘Performance of urban storm drainage network under changing climate scenarios: Flood mitigation in indian coastal city’, *Scientific reports* **9**(1), 7783.
- Anselin, L. (1995), ‘Local indicators of spatial association—lisa’, *Geographical analysis* **27**(2), 93–115.
- Anselin, L., Syabri, I. and Kho, Y. (2009), Geoda: an introduction to spatial data analysis, in ‘Handbook of applied spatial analysis: Software tools, methods and applications’, Springer, pp. 73–89.
- Arnell, N. W. and Gosling, S. N. (2016), ‘The impacts of climate change on river flood risk at the global scale’, *Climatic Change* **134**, 387–401.
- Arnone, E., Dialynas, Y., Noto, L. and Bras, R. (2016), ‘Accounting for soil parameter uncertainty in a physically based and distributed approach for rainfall-triggered landslides’, *Hydrological Processes* **30**(6), 927–944.
- Arnone, E., Pumo, D., Viola, F., Noto, L. V. and La Loggia, G. (2013), ‘Rainfall statistics changes in sicily’, *Hydrology and Earth System Sciences* **17**(7), 2449–2458.
- Aronica, G. T., Brigandí, G. and Morey, N. (2012), ‘Flash floods and debris flow in the city area of messina, north-east part of sicily, italy in october 2009: the case of the giampileri catchment’, *Natural Hazards and Earth System Sciences* **12**(5), 1295–1309.
- Asseng, S., Ewert, F., Martre, P., Rötter, R. P., Lobell, D. B., Cammarano, D., Kimball, B. A., Ottman, M. J., Wall, G. W., White, J. W. et al. (2015), ‘Rising temperatures reduce global wheat production’, *Nature climate change* **5**(2), 143–147.
- Balaji, V., Couvreur, F., Deshayes, J., Gautrais, J., Hourdin, F. and Rio, C. (2022), ‘Are general circulation models obsolete?’, *Proceedings of the National Academy of Sciences* **119**(47), e2202075119.
- Ballester, J., Quijal-Zamorano, M., Méndez Turrubiates, R. F., Pegenaute, F., Herrmann, F. R., Robine, J. M., Basagaña, X., Tonne, C., Antó, J. M. and Achebak, H. (2023), ‘Heat-related mortality in europe during the summer of 2022’, *Nature medicine* pp. 1–10.
- Banerjee, A., Dhillon, I. S., Ghosh, J., Sra, S. and Ridgeway, G. (2005), ‘Clustering on the unit hypersphere using von mises-fisher distributions.’, *Journal of Machine Learning*

- Research* **6**(9).
- Bao, J., Sherwood, S. C., Alexander, L. V. and Evans, J. P. (2017), ‘Future increases in extreme precipitation exceed observed scaling rates’, *Nature Climate Change* **7**(2), 128–132.
- Barbosa, S., Scotto, M. and Alonso, A. (2011), ‘Summarising changes in air temperature over central europe by quantile regression and clustering’, *Natural Hazards and Earth System Sciences* **11**(12), 3227–3233.
- Barnes, P. W., Williamson, C. E., Lucas, R. M., Robinson, S. A., Madronich, S., Paul, N. D., Bornman, J. F., Bais, A. F., Sulzberger, B., Wilson, S. R. et al. (2019), ‘Ozone depletion, ultraviolet radiation, climate change and prospects for a sustainable future’, *Nature Sustainability* **2**(7), 569–579.
- Barriopedro, D., Fischer, E. M., Luterbacher, J., Trigo, R. M. and García-Herrera, R. (2011), ‘The hot summer of 2010: redrawing the temperature record map of europe’, *Science* **332**(6026), 220–224.
- Bartolini, G., Grifoni, D., Torrigiani, T., Vallorani, R., Meneguzzo, F. and Gozzini, B. (2014), ‘Precipitation changes from two long-term hourly datasets in tuscany, italy’, *International journal of climatology* **34**(15), 3977–3985.
- Bartolomeu, S., Carvalho, M., Marta-Almeida, M., Melo-Gonçalves, P. and Rocha, A. (2016), ‘Recent trends of extreme precipitation indices in the iberian peninsula using observations and wrf model results’, *Physics and Chemistry of the Earth, Parts A/B/C* **94**, 10–21.
- Beck, H. E., Van Dijk, A. I., Larraondo, P. R., McVicar, T. R., Pan, M., Dutra, E. and Miralles, D. G. (2022), ‘Mswx: Global 3-hourly 0.1 bias-corrected meteorological data including near-real-time updates and forecast ensembles’, *Bulletin of the American Meteorological Society* **103**(3), E710–E732.
- Beck, H. E., Wood, E. F., Pan, M., Fisher, C. K., Miralles, D. G., Van Dijk, A. I., McVicar, T. R. and Adler, R. F. (2019), ‘Mswep v2 global 3-hourly 0.1 precipitation: methodology and quantitative assessment’, *Bulletin of the American Meteorological Society* **100**(3), 473–500.
- Beck, H. E., Zimmermann, N. E., McVicar, T. R., Vergopolan, N., Berg, A. and Wood, E. F. (2018), ‘Present and future köppen-geiger climate classification maps at 1-km resolution’, *Scientific data* **5**(1), 1–12.
- Berg, P., Moseley, C. and Haerter, J. O. (2013), ‘Strong increase in convective precipitation in response to higher temperatures’, *Nature Geoscience* **6**(3), 181–185.
- Bevacqua, E., Maraun, D., Hobæk Haff, I., Widmann, M. and Vrac, M. (2017), ‘Multivariate statistical modelling of compound events via pair-copula constructions: analysis of floods in ravenna (italy)’, *Hydrology and Earth System Sciences* **21**(6), 2701–2723.

- Bevacqua, E., Maraun, D., Vousdoukas, M., Voukouvalas, E., Vrac, M., Mentaschi, L. and Widmann, M. (2019), ‘Higher probability of compound flooding from precipitation and storm surge in europe under anthropogenic climate change’, *Science advances* **5**(9), eaaw5531.
- Blanchet, J., Molinié, G. and Touati, J. (2018), ‘Spatial analysis of trend in extreme daily rainfall in southern france’, *Climate Dynamics* **51**, 799–812.
- Blenkinsop, S., Fowler, H. J., Barbero, R., Chan, S. C., Guerreiro, S. B., Kendon, E., Lenderink, G., Lewis, E., Li, X.-F., Westra, S. et al. (2018), ‘The intense project: using observations and models to understand the past, present and future of sub-daily rainfall extremes’, *Advances in Science and Research* **15**, 117–126.
- Blöschl, G., Hall, J., Viglione, A., Perdigão, R. A., Parajka, J., Merz, B., Lun, D., Arheimer, B., Aronica, G. T., Bilibashi, A. et al. (2019), ‘Changing climate both increases and decreases european river floods’, *Nature* **573**(7772), 108–111.
- Boergens, E., Güntner, A., Dobsław, H. and Dahle, C. (2020), ‘Quantifying the central european droughts in 2018 and 2019 with grace follow-on’, *Geophysical Research Letters* **47**(14), e2020GL087285.
- Bonaccorso, B., Cancelliere, A. and Rossi, G. (2005), ‘Detecting trends of extreme rainfall series in sicily’, *Advances in Geosciences* **2**, 7–11.
- Borga, M., Vezzani, C. and Fontana, G. D. (2005), ‘Regional rainfall depth–duration–frequency equations for an alpine region’, *Natural Hazards* **36**, 221–235.
- Bremond, P., Grelot, F. and Agenais, A.-L. (2013), ‘Economic evaluation of flood damage to agriculture–review and analysis of existing methods’, *Natural Hazards and Earth System Sciences* **13**(10), 2493–2512.
- Buffoni, L., Maugeri, M. and Nanni, T. (1999), ‘Precipitation in italy from 1833 to 1996’, *Theoretical and Applied Climatology* **63**, 33–40.
- Caccamo, M., Castorina, G., Colombo, F., Insinga, V., Maiorana, E. and Magazù, S. (2017), ‘Weather forecast performances for complex orographic areas: Impact of different grid resolutions and of geographic data on heavy rainfall event simulations in sicily’, *Atmospheric Research* **198**, 22–33.
- Caloiero, T., Coscarelli, R., Gaudio, R. and Leonardo, G. (2019), ‘Precipitation trend and concentration in the sardinia region’, *Theoretical and Applied Climatology* **137**, 297–307.
- Camuffo, D., della Valle, A. and Becherini, F. (2020), ‘A critical analysis of the definitions of climate and hydrological extreme events’, *Quaternary International* **538**, 5–13.
- Cannarozzo, M., D’asaro, F. and Ferro, V. (1995), ‘Regional rainfall and flood frequency analysis for sicily using the two component extreme value distribution’, *Hydrological Sciences Journal* **40**(1), 19–42.
- Cannarozzo, M., Noto, L. V. and Viola, F. (2006), ‘Spatial distribution of rainfall trends

- in sicily (1921–2000)’, *Physics and Chemistry of the Earth, Parts a/b/c* **31**(18), 1201–1211.
- Caracciolo, D., Francipane, A., Viola, F., Noto, L. V. and Deidda, R. (2018), ‘Performances of gpm satellite precipitation over the two major mediterranean islands’, *Atmospheric Research* **213**, 309–322.
- Casanueva, A., Rodríguez-Puebla, C., Frías, M. and González-Reviriego, N. (2014), ‘Variability of extreme precipitation over europe and its relationships with teleconnection patterns’, *Hydrology and Earth System Sciences* **18**(2), 709–725.
- Cassola, F., Iengo, A. and Turato, B. (2023), ‘Extreme convective precipitation in liguria (italy): a brief description and analysis of the event occurred on october 4, 2021’, *Bulletin of Atmospheric Science and Technology* **4**(1), 4.
- Ceccherini, G., Russo, S., Amezttoy, I., Marchese, A. F. and Carmona-Moreno, C. (2017), ‘Heat waves in africa 1981–2015, observations and reanalysis’, *Natural Hazards and Earth System Sciences* **17**(1), 115–125.
- Chapman, S., Birch, C. E., Marsham, J. H., Part, C., Hajat, S., Chersich, M. F., Ebi, K. L., Luchters, S., Nakstad, B. and Kovats, S. (2022), ‘Past and projected climate change impacts on heat-related child mortality in africa’, *Environmental Research Letters* **17**(7), 074028.
- Checkley, W., Epstein, L. D., Gilman, R. H., Figueroa, D., Cama, R. I., Patz, J. A. and Black, R. E. (2000), ‘Effects of ei niño and ambient temperature on hospital admissions for diarrhoeal diseases in peruvian children’, *The Lancet* **355**(9202), 442–450.
- Chen, H. and Sun, J. (2021), ‘Anthropogenic influence has increased climate extreme occurrence over china’, *Science bulletin* **66**(8), 749–752.
- Chen, X., Li, N., Liu, J., Zhang, Z., Liu, Y. and Huang, C. (2020), ‘Changes in global and regional characteristics of heat stress waves in the 21st century’, *Earth’s Future* **8**(11), e2020EF001636.
- Chen, X., Zhang, X., Church, J. A., Watson, C. S., King, M. A., Monselesan, D., Legresy, B. and Harig, C. (2017), ‘The increasing rate of global mean sea-level rise during 1993–2014’, *Nature Climate Change* **7**(7), 492–495.
- Chen, Y., Liao, Z., Shi, Y., Tian, Y. and Zhai, P. (2021), ‘Detectable increases in sequential flood-heatwave events across china during 1961–2018’, *Geophysical Research Letters* **48**(6), e2021GL092549.
- Cheng, L. and AghaKouchak, A. (2014), ‘Nonstationary precipitation intensity-duration-frequency curves for infrastructure design in a changing climate’, *Scientific reports* **4**(1), 7093.
- Choulakian, V. and Stephens, M. A. (2001), ‘Goodness-of-fit tests for the generalized pareto distribution’, *Technometrics* **43**(4), 478–484.

- Cioffi, F., Lall, U., Rus, E. and Krishnamurthy, C. K. B. (2015), ‘Space-time structure of extreme precipitation in europe over the last century’, *International Journal of Climatology* **35**(8), 1749–1760.
- Cipolla, G., Francipane, A. and Noto, L. V. (2020), ‘Classification of extreme rainfall for a mediterranean region by means of atmospheric circulation patterns and reanalysis data’, *Water Resources Management* **34**, 3219–3235.
- Clayton, D. G. (1978), ‘A model for association in bivariate life tables and its application in epidemiological studies of familial tendency in chronic disease incidence’, *Biometrika* **65**(1), 141–151.
- Coffel, E. D., Horton, R. M. and De Sherbinin, A. (2017), ‘Temperature and humidity based projections of a rapid rise in global heat stress exposure during the 21st century’, *Environmental Research Letters* **13**(1), 014001.
- Coll, M., Piroddi, C., Steenbeek, J., Kaschner, K., Ben Rais Lasram, F., Aguzzi, J., Ballesteros, E., Bianchi, C. N., Corbera, J., Dailianis, T. et al. (2010), ‘The biodiversity of the mediterranean sea: estimates, patterns, and threats’, *PloS one* **5**(8), e11842.
- Cook, L. M., McGinnis, S. and Samaras, C. (2020), ‘The effect of modeling choices on updating intensity-duration-frequency curves and stormwater infrastructure designs for climate change’, *Climatic change* **159**, 289–308.
- Costa, A. C. and Soares, A. (2009), ‘Trends in extreme precipitation indices derived from a daily rainfall database for the south of portugal’, *International Journal of Climatology: A Journal of the Royal Meteorological Society* **29**(13), 1956–1975.
- Crisci, A., Gozzini, B., Meneguzzo, F., Pagliara, S. and Maracchi, G. (2002), ‘Extreme rainfall in a changing climate: regional analysis and hydrological implications in tuscany’, *Hydrological Processes* **16**(6), 1261–1274.
- Curriero, F. C., Patz, J. A., Rose, J. B. and Lele, S. (2001), ‘The association between extreme precipitation and waterborne disease outbreaks in the united states, 1948–1994’, *American journal of public health* **91**(8), 1194–1199.
- Daramola, J. O., Abioja, M. O. and Onagbesan, O. M. (2012), ‘Heat stress impact on livestock production’, *Environmental stress and amelioration in livestock production* pp. 53–73.
- De Toffol, S., Laghari, A. and Rauch, W. (2009), ‘Are extreme rainfall intensities more frequent? analysis of trends in rainfall patterns relevant to urban drainage systems’, *Water Science and Technology* **59**(9), 1769–1776.
- Debortoli, N. S., Camarinha, P. I. M., Marengo, J. A. and Rodrigues, R. R. (2017), ‘An index of brazil’s vulnerability to expected increases in natural flash flooding and landslide disasters in the context of climate change’, *Natural hazards* **86**, 557–582.
- Deen, S. (2015), ‘Pakistan 2010 floods. policy gaps in disaster preparedness and response’,

- International journal of disaster risk reduction* **12**, 341–349.
- Delpla, I., Jung, A.-V., Baures, E., Clement, M. and Thomas, O. (2009), ‘Impacts of climate change on surface water quality in relation to drinking water production’, *Environment international* **35**(8), 1225–1233.
- Di Piazza, A., Conti, F. L., Noto, L., Viola, F. and La Loggia, G. (2011), ‘Comparative analysis of different techniques for spatial interpolation of rainfall data to create a serially complete monthly time series of precipitation for sicily, italy’, *International Journal of Applied Earth Observation and Geoinformation* **13**(3), 396–408.
- Diem, J. E., Konecky, B. L., Salerno, J. and Hartter, J. (2019), ‘Is equatorial africa getting wetter or drier? insights from an evaluation of long-term, satellite-based rainfall estimates for western uganda’, *International Journal of Climatology* **39**(7), 3334–3347.
- Do, H. X., Zhao, F., Westra, S., Leonard, M., Gudmundsson, L., Boulange, J. E. S., Chang, J., Ciais, P., Gerten, D., Gosling, S. N. et al. (2020), ‘Historical and future changes in global flood magnitude—evidence from a model–observation investigation’, *Hydrology and Earth System Sciences* **24**(3), 1543–1564.
- Donat, M., Alexander, L. V., Yang, H., Durre, I., Vose, R., Dunn, R. J., Willett, K. M., Aguilar, E., Brunet, M., Caesar, J. et al. (2013), ‘Updated analyses of temperature and precipitation extreme indices since the beginning of the twentieth century: The hadex2 dataset’, *Journal of Geophysical Research: Atmospheres* **118**(5), 2098–2118.
- Donat, M. G., Lowry, A. L., Alexander, L. V., O’Gorman, P. A. and Maher, N. (2016), ‘More extreme precipitation in the world’s dry and wet regions’, *Nature Climate Change* **6**(5), 508–513.
- Doney, S. C., Busch, D. S., Cooley, S. R. and Kroeker, K. J. (2020), ‘The impacts of ocean acidification on marine ecosystems and reliant human communities’, *Annual Review of Environment and Resources* **45**, 83–112.
- Douglas, E., Vogel, R. and Kroll, C. (2000), ‘Trends in floods and low flows in the united states: impact of spatial correlation’, *Journal of hydrology* **240**(1-2), 90–105.
- Dunn, R. (2019), ‘Hadisd version 3: monthly updates’, *Hadley centre technical note* **103**, 1–10.
- Dykstra, S. and Dzwonkowski, B. (2021), ‘The role of intensifying precipitation on coastal river flooding and compound river-storm surge events, northeast gulf of mexico’, *Water Resources Research* **57**(11), e2020WR029363.
- Easterling, D. R., Arnold, J., Knutson, T., Kunkel, K., LeGrande, A., Leung, L. R., Vose, R., Waliser, D. and Wehner, M. (2017), ‘Precipitation change in the united states’.
- Emanuel, K. (2005), ‘Increasing destructiveness of tropical cyclones over the past 30 years’, *Nature* **436**(7051), 686–688.
- Émile, M. and Gumbel, J. (1960), Distributions des valeurs extrêmes en plusieurs dimen-

- sions, *in* 'Annales de l'ISUP', Vol. 9, pp. 171–173.
- Eyring, V., Bony, S., Meehl, G. A., Senior, C. A., Stevens, B., Stouffer, R. J. and Taylor, K. E. (2016), 'Overview of the coupled model intercomparison project phase 6 (cmip6) experimental design and organization', *Geoscientific Model Development* **9**(5), 1937–1958.
- Fan, Y., Pei-Syuan, L., Im, E.-S. and Lo, M.-H. (2022), 'Regional disparities in the exposure to heat-related mortality risk under 1.5° c and 2° c global warming', *Environmental Research Letters* **17**(5), 054009.
- FAO (2011), 'FAO cuts wheat production forecast but considers supplies adequate — fao.org', <https://www.fao.org/newsroom/detail/FAO-cuts-wheat-production-forecast-but-considers-supplies-adequate/en>. [Accessed 02-10-2023].
- Feloni, E. G., Baltas, E. A., Nastos, P. T. and Matsangouras, I. T. (2019), 'Implementation and evaluation of a convective/stratiform precipitation scheme in attica region, greece', *Atmospheric Research* **220**, 109–119.
- Feng, H. and Zhang, M. (2015), 'Global land moisture trends: drier in dry and wetter in wet over land', *Scientific reports* **5**(1), 18018.
- Feng, X., Porporato, A. and Rodriguez-Iturbe, I. (2013), 'Changes in rainfall seasonality in the tropics', *Nature Climate Change* **3**(9), 811–815.
- Field, C. B. (2012), *Managing the risks of extreme events and disasters to advance climate change adaptation: special report of the intergovernmental panel on climate change*, Cambridge University Press.
- Findell, K. L., Keys, P. W., Van Der Ent, R. J., Lintner, B. R., Berg, A. and Krasting, J. P. (2019), 'Rising temperatures increase importance of oceanic evaporation as a source for continental precipitation', *Journal of Climate* **32**(22), 7713–7726.
- Fischer, E. M. and Knutti, R. (2013), 'Robust projections of combined humidity and temperature extremes', *Nature Climate Change* **3**(2), 126–130.
- Fischer, E. M. and Knutti, R. (2015), 'Anthropogenic contribution to global occurrence of heavy-precipitation and high-temperature extremes', *Nature climate change* **5**(6), 560–564.
- Fisher, N. I. (1995), *Statistical analysis of circular data*, cambridge university press.
- Forestieri, A., Lo Conti, F., Blenkinsop, S., Cannarozzo, M., Fowler, H. J. and Noto, L. V. (2018), 'Regional frequency analysis of extreme rainfall in sicily (italy)', *International Journal of Climatology* **38**(S1), e698–e716.
- Fowler, H. J., Lenderink, G., Prein, A. F., Westra, S., Allan, R. P., Ban, N., Barbero, R., Berg, P., Blenkinsop, S., Do, H. X. et al. (2021), 'Anthropogenic intensification of short-duration rainfall extremes', *Nature Reviews Earth & Environment* **2**(2), 107–122.

- Fowler, H. and Kilsby, C. (2003), ‘Implications of changes in seasonal and annual extreme rainfall’, *Geophysical Research Letters* **30**(13).
- Francipane, A., Pumo, D., Sinagra, M., La Loggia, G. and Noto, L. V. (2021), ‘A paradigm of extreme rainfall pluvial floods in complex urban areas: the flood event of 15 July 2020 in palermo (italy)’, *Natural Hazards and Earth System Sciences* **21**(8), 2563–2580.
- Frank, M. J. (1979), ‘On the simultaneous associativity of $f(x, y)$ and $x + y - f(x, y)$ ’, *Aequationes mathematicae* **19**, 194–226.
- Franzke, C. L. and Torelló i Sentelles, H. (2020), ‘Risk of extreme high fatalities due to weather and climate hazards and its connection to large-scale climate variability’, *Climatic Change* **162**(2), 507–525.
- Freychet, N., Hegerl, G. C., Lord, N. S., Lo, Y. E., Mitchell, D. and Collins, M. (2022), ‘Robust increase in population exposure to heat stress with increasing global warming’, *Environmental Research Letters* **17**(6), 064049.
- Frölicher, T. L., Winton, M. and Sarmiento, J. L. (2014), ‘Continued global warming after co2 emissions stoppage’, *Nature Climate Change* **4**(1), 40–44.
- Funari, E., Manganelli, M. and Sinisi, L. (2012), ‘Impact of climate change on waterborne diseases’, *Annali dell’Istituto superiore di sanita* **48**, 473–487.
- Garcia, R. R., Kinnison, D. E. and Marsh, D. R. (2012), ‘“world avoided” simulations with the whole atmosphere community climate model’, *Journal of Geophysical Research: Atmospheres* **117**(D23).
- Geirinhas, J. L., Russo, A., Libonati, R., Sousa, P. M., Miralles, D. G. and Trigo, R. M. (2021), ‘Recent increasing frequency of compound summer drought and heatwaves in southeast brazil’, *Environmental Research Letters* **16**(3), 034036.
- Gentilucci, M., Barbieri, M., D’Aprile, F. and Zardi, D. (2020), ‘Analysis of extreme precipitation indices in the marche region (central italy), combined with the assessment of energy implications and hydrogeological risk’, *Energy Reports* **6**, 804–810.
- Gillett, N. P., Arora, V. K., Zickfeld, K., Marshall, S. J. and Merryfield, W. J. (2011), ‘Ongoing climate change following a complete cessation of carbon dioxide emissions’, *Nature Geoscience* **4**(2), 83–87.
- Giorgi, F. (2006), ‘Climate change hot-spots’, *Geophysical research letters* **33**(8).
- Giorgi, F., Coppola, E. and Raffaele, F. (2014), ‘A consistent picture of the hydroclimatic response to global warming from multiple indices: Models and observations’, *Journal of Geophysical Research: Atmospheres* **119**(20), 11–695.
- Giorgi, F. and Lionello, P. (2008), ‘Climate change projections for the mediterranean region’, *Global and planetary change* **63**(2-3), 90–104.
- Gonzalez-Hidalgo, J. C., Brunetti, M. and de Luis, M. (2010), ‘Precipitation trends in spanish hydrological divisions, 1946–2005’, *Climate Research* **43**(3), 215–228.

- Griffith, D. A. (2010), ‘The moran coefficient for non-normal data’, *Journal of Statistical Planning and Inference* **140**(11), 2980–2990.
- Grimm, A. M. (2011), ‘Interannual climate variability in south america: impacts on seasonal precipitation, extreme events, and possible effects of climate change’, *Stochastic Environmental Research and Risk Assessment* **25**, 537–554.
- Gu, L., Chen, J., Yin, J., Slater, L. J., Wang, H.-M., Guo, Q., Feng, M., Qin, H. and Zhao, T. (2022), ‘Global increases in compound flood-hot extreme hazards under climate warming’, *Geophysical Research Letters* **49**(8), e2022GL097726.
- Guan, Y., Zhou, W., Jia, X., Zhang, Y. and Dong, R. (2023), ‘The synergistic impact of spod and enso on itcz: observation study’, *Climate Dynamics* **60**(5-6), 1297–1311.
- Güçlü, Y. S. (2018), ‘Multiple şen-innovative trend analyses and partial mann-kendall test’, *Journal of Hydrology* **566**, 685–704.
- Gumbel, E. J. (1941), ‘The return period of flood flows’, *The annals of mathematical statistics* **12**(2), 163–190.
- Hao, L. and Naiman, D. Q. (2007), *Quantile regression*, number 149, Sage.
- Hardwick Jones, R., Westra, S. and Sharma, A. (2010), ‘Observed relationships between extreme sub-daily precipitation, surface temperature, and relative humidity’, *Geophysical Research Letters* **37**(22).
- Harper, S. (2014), ‘Economic and social implications of aging societies’, *Science* **346**(6209), 587–591.
- Hasegawa, T., Sakurai, G., Fujimori, S., Takahashi, K., Hijioka, Y. and Masui, T. (2021), ‘Extreme climate events increase risk of global food insecurity and adaptation needs’, *Nature Food* **2**(8), 587–595.
- Helsel, D. R. and Frans, L. M. (2006), ‘Regional kendall test for trend’, *Environmental science & technology* **40**(13), 4066–4073.
- Hersbach, H., Bell, B., Berrisford, P., Hirahara, S., Horányi, A., Muñoz-Sabater, J., Nicolas, J., Peubey, C., Radu, R., Schepers, D. et al. (2020), ‘The era5 global reanalysis’, *Quarterly Journal of the Royal Meteorological Society* **146**(730), 1999–2049.
- Hirabayashi, Y., Mahendran, R., Koirala, S., Konoshima, L., Yamazaki, D., Watanabe, S., Kim, H. and Kanae, S. (2013), ‘Global flood risk under climate change’, *Nature climate change* **3**(9), 816–821.
- Hochman, A., Marra, F., Messori, G., Pinto, J. G., Raveh-Rubin, S., Yosef, Y. and Zittis, G. (2022), ‘Extreme weather and societal impacts in the eastern mediterranean’, *Earth System Dynamics* **13**(2), 749–777.
- Hodel, F. H. and Fieberg, J. R. (2021), ‘Cylcop: An r package for circular-linear copulae with angular symmetry’, *BioRxiv* pp. 2021–07.
- Hodel, F. H. and Fieberg, J. R. (2022), ‘Circular–linear copulae for animal movement

- data', *Methods in Ecology and Evolution* **13**(5), 1001–1013.
- Houghton, J. T., Ding, Y., Griggs, D. J., Noguer, M., van der Linden, P. J., Dai, X., Maskell, K., Johnson, C. A. et al. (2001), *Climate change 2001: the scientific basis*, Vol. 881, Cambridge university press Cambridge.
- Houze Jr, R. A. (1997), 'Stratiform precipitation in regions of convection: A meteorological paradox?', *Bulletin of the American Meteorological Society* **78**(10), 2179–2196.
- Houze Jr, R. A. (2014), *Cloud dynamics*, Academic press.
- Im, E.-S., Kang, S. and Eltahir, E. A. (2018), 'Projections of rising heat stress over the western maritime continent from dynamically downscaled climate simulations', *Global and Planetary Change* **165**, 160–172.
- Ingold, K. and Fischer, M. (2014), 'Drivers of collaboration to mitigate climate change: An illustration of swiss climate policy over 15 years', *Global environmental change* **24**, 88–98.
- Jetz, W., Wilcove, D. S. and Dobson, A. P. (2007), 'Projected impacts of climate and land-use change on the global diversity of birds', *PLoS biology* **5**(6), e157.
- Jiang, Y., Zhou, L., Roundy, P. E., Hua, W. and Raghavendra, A. (2021), 'Increasing influence of indian ocean dipole on precipitation over central equatorial africa', *Geophysical Research Letters* **48**(8), e2020GL092370.
- Jiménez Cisneros, B. E., Oki, T., Arnell, N. W., Benito, G., Cogley, J. G., Doll, P., Jiang, T. and Mwakalila, S. S. (2014), 'Freshwater resources'.
- Johnson, R. A. and Wehrly, T. E. (1978), 'Some angular-linear distributions and related regression models', *Journal of the American Statistical Association* **73**(363), 602–606.
- Jolly, W. M., Cochrane, M. A., Freeborn, P. H., Holden, Z. A., Brown, T. J., Williamson, G. J. and Bowman, D. M. (2015), 'Climate-induced variations in global wildfire danger from 1979 to 2013', *Nature communications* **6**(1), 7537.
- Joshi, M. K., Rai, A., Kulkarni, A. and Kucharski, F. (2020), 'Assessing changes in characteristics of hot extremes over india in a warming environment and their driving mechanisms', *Scientific Reports* **10**(1), 2631.
- Karagiannidis, A., Karacostas, T., Maheras, P. and Makrogiannis, T. (2009), 'Trends and seasonality of extreme precipitation characteristics related to mid-latitude cyclones in europe', *Advances in Geosciences* **20**, 39–43.
- Karwat, A. and Franzke, C. L. (2021), 'Future projections of heat mortality risk for major european cities', *Weather, climate, and society* **13**(4), 913–931.
- Katsafados, P., Papadopoulos, A., Varlas, G., Papadopoulou, E. and Mavromatidis, E. (2014), 'Seasonal predictability of the 2010 russian heat wave', *Natural Hazards and Earth System Sciences* **14**(6), 1531–1542.
- Katzenberger, A., Schewe, J., Pongratz, J. and Levermann, A. (2021), 'Robust increase

- of indian monsoon rainfall and its variability under future warming in cmip6 models', *Earth System Dynamics* **12**(2), 367–386.
- Khan, S. J., Deere, D., Leusch, F. D., Humpage, A., Jenkins, M. and Cunliffe, D. (2015), 'Extreme weather events: Should drinking water quality management systems adapt to changing risk profiles?', *Water research* **85**, 124–136.
- Khomsii, K., Mahe, G., Trambly, Y., Sinan, M. and Snoussi, M. (2015), 'Trends in rainfall and temperature extremes in morocco.', *Natural Hazards & Earth System Sciences Discussions* **3**(2).
- Kii, M. (2021), 'Projecting future populations of urban agglomerations around the world and through the 21st century', *npj Urban Sustainability* **1**(1), 10.
- Kim, H., Villarini, G., Jane, R., Wahl, T., Misra, S. and Michalek, A. (2023), 'On the generation of high-resolution probabilistic design events capturing the joint occurrence of rainfall and storm surge in coastal basins', *International Journal of Climatology* **43**(2), 761–771.
- King, A. D. and Harrington, L. J. (2018), 'The inequality of climate change from 1.5 to 2 c of global warming', *Geophysical Research Letters* **45**(10), 5030–5033.
- Koenker, R. (2004), 'Quantreg: An r package for quantile regression and related methods', *The Comprehensive R Archive Network website*.
- Koenker, R. (2005), *Quantile regression*, Vol. 38, Cambridge university press.
- Koenker, R. and Bassett Jr, G. (1978), 'Regression quantiles', *Econometrica: journal of the Econometric Society* pp. 33–50.
- Koenker, R. and Machado, J. A. (1999), 'Goodness of fit and related inference processes for quantile regression', *Journal of the american statistical association* **94**(448), 1296–1310.
- Kolios, S. and Feidas, H. (2010), 'A warm season climatology of mesoscale convective systems in the mediterranean basin using satellite data', *Theoretical and Applied Climatology* **102**, 29–42.
- Konrad, H., Shepherd, A., Gilbert, L., Hogg, A. E., McMillan, M., Muir, A. and Slater, T. (2018), 'Net retreat of antarctic glacier grounding lines', *Nature Geoscience* **11**(4), 258–262.
- Kornhuber, K., Coumou, D., Vogel, E., Lesk, C., Donges, J. F., Lehmann, J. and Horton, R. M. (2020), 'Amplified rossby waves enhance risk of concurrent heatwaves in major breadbasket regions', *Nature Climate Change* **10**(1), 48–53.
- Kothawale, D., Revadekar, J. V. and Rupa Kumar, K. (2010), 'Recent trends in pre-monsoon daily temperature extremes over india', *Journal of earth system science* **119**, 51–65.
- Kotz, M., Levermann, A. and Wenz, L. (2022), 'The effect of rainfall changes on economic

- production', *Nature* **601**(7892), 223–227.
- Kourtis, I. M. and Tsihrintzis, V. A. (2021), 'Adaptation of urban drainage networks to climate change: A review', *Science of the Total Environment* **771**, 145431.
- Kourtis, I. M. and Tsihrintzis, V. A. (2022), 'Update of intensity-duration-frequency (idf) curves under climate change: a review', *Water Supply* **22**(5), 4951–4974.
- Kovats, R. S. and Hajat, S. (2008), 'Heat stress and public health: a critical review', *Annu. Rev. Public Health* **29**, 41–55.
- Kumar, N., Poonia, V., Gupta, B. and Goyal, M. K. (2021), 'A novel framework for risk assessment and resilience of critical infrastructure towards climate change', *Technological Forecasting and Social Change* **165**, 120532.
- Kundzewicz, Z. W., Krysanova, V., Dankers, R., Hirabayashi, Y., Kanae, S., Hattermann, F., Huang, S., Milly, P. C., Stoffel, M., Driessen, P. et al. (2017), 'Differences in flood hazard projections in europe—their causes and consequences for decision making', *Hydrological Sciences Journal* **62**(1), 1–14.
- Kyselý, J., Rulfová, Z., Farda, A. and Hanel, M. (2016), 'Convective and stratiform precipitation characteristics in an ensemble of regional climate model simulations', *Climate dynamics* **46**, 227–243.
- Lang, M., Ouarda, T. B. and Bobée, B. (1999), 'Towards operational guidelines for over-threshold modeling', *Journal of hydrology* **225**(3-4), 103–117.
- Lausier, A. M. and Jain, S. (2018), 'Overlooked trends in observed global annual precipitation reveal underestimated risks', *Scientific reports* **8**(1), 16746.
- Lazoglou, G. and Anagnostopoulou, C. (2019), 'Joint distribution of temperature and precipitation in the mediterranean, using the copula method', *Theoretical and Applied Climatology* **135**, 1399–1411.
- Lee, K.-O., Aemisegger, F., Pfahl, S., Flamant, C., Lacour, J.-L. and Chaboureau, J.-P. (2019), 'Contrasting stable water isotope signals from convective and large-scale precipitation phases of a heavy precipitation event in southern italy during hymex iop 13: a modelling perspective', *Atmospheric Chemistry and Physics* **19**(11), 7487–7506.
- Legendre, P. and Fortin, M. J. (1989), 'Spatial pattern and ecological analysis', *Vegetatio* **80**, 107–138.
- Lenderink, G., Barbero, R., Loriaux, J. and Fowler, H. (2017), 'Super-clausius-clapeyron scaling of extreme hourly convective precipitation and its relation to large-scale atmospheric conditions', *Journal of Climate* **30**(15), 6037–6052.
- Lenderink, G., de Vries, H., Fowler, H. J., Barbero, R., van Uft, B. and van Meijgaard, E. (2021), 'Scaling and responses of extreme hourly precipitation in three climate experiments with a convection-permitting model', *Philosophical Transactions of the Royal Society A* **379**(2195), 20190544.

- Lenderink, G. and Van Meijgaard, E. (2008), ‘Increase in hourly precipitation extremes beyond expectations from temperature changes’, *Nature Geoscience* **1**(8), 511–514.
- Lenton, T. M. (2011), ‘Early warning of climate tipping points’, *Nature climate change* **1**(4), 201–209.
- Leonard, M., Westra, S., Phatak, A., Lambert, M., van den Hurk, B., McInnes, K., Risbey, J., Schuster, S., Jakob, D. and Stafford-Smith, M. (2014), ‘A compound event framework for understanding extreme impacts’, *Wiley Interdisciplinary Reviews: Climate Change* **5**(1), 113–128.
- Lesk, C., Rowhani, P. and Ramankutty, N. (2016), ‘Influence of extreme weather disasters on global crop production’, *Nature* **529**(7584), 84–87.
- Levy, K., Smith, S. M. and Carlton, E. J. (2018), ‘Climate change impacts on waterborne diseases: moving toward designing interventions’, *Current environmental health reports* **5**, 272–282.
- Lewis, E., Fowler, H., Alexander, L., Dunn, R., McClean, F., Barbero, R., Guerreiro, S., Li, X.-F. and Blenkinsop, S. (2019), ‘Gsd: a global sub-daily rainfall dataset’, *Journal of Climate* **32**(15), 4715–4729.
- Li, B., Beaudoin, H. and Rodell, M. (2018), ‘Nasa/gsfc/hsl, gldas catchment land surface model l4 daily 0.25 × 0.25 degree v2. 0, greenbelt, maryland, usa, goddard earth sciences data and information services center (ges disc)’.
- Li, X., Hu, Q., Wang, R., Zhang, D. and Zhang, Q. (2021), ‘Influences of the timing of extreme precipitation on floods in poyang lake, china’, *Hydrology Research* **52**(1), 26–42.
- Li, Y., Schubert, S., Kropp, J. P. and Rybski, D. (2020), ‘On the influence of density and morphology on the urban heat island intensity’, *Nature communications* **11**(1), 2647.
- Libertino, A., Ganora, D. and Claps, P. (2019), ‘Evidence for increasing rainfall extremes remains elusive at large spatial scales: The case of italy’, *Geophysical Research Letters* **46**(13), 7437–7446.
- Lionello, P. and Scarascia, L. (2018), ‘The relation between climate change in the mediterranean region and global warming’, *Regional Environmental Change* **18**, 1481–1493.
- Llasat, M.-C. (2001), ‘An objective classification of rainfall events on the basis of their convective features: application to rainfall intensity in the northeast of spain’, *International Journal of Climatology: A Journal of the Royal Meteorological Society* **21**(11), 1385–1400.
- Llasat, M. C., del Moral, A., Cortès, M. and Rigo, T. (2021), ‘Convective precipitation trends in the spanish mediterranean region’, *Atmospheric Research* **257**, 105581.
- Longobardi, A. and Villani, P. (2010), ‘Trend analysis of annual and seasonal rainfall time series in the mediterranean area’, *International journal of Climatology* **30**(10), 1538–1546.

- Luo, M. and Lau, N.-C. (2018), ‘Increasing heat stress in urban areas of eastern china: Acceleration by urbanization’, *Geophysical Research Letters* **45**(23), 13–060.
- Mach, K. J., Kraan, C. M., Adger, W. N., Buhaug, H., Burke, M., Fearon, J. D., Field, C. B., Hendrix, C. S., Maystadt, J.-F., O’Loughlin, J. et al. (2019), ‘Climate as a risk factor for armed conflict’, *Nature* **571**(7764), 193–197.
- Mallakpour, I. and Villarini, G. (2017), ‘A nalysis of changes in the magnitude, frequency, and seasonality of heavy precipitation over the contiguous us a’, *Theoretical and Applied Climatology* **130**, 345–363.
- Mantyka-Pringle, C. S., Visconti, P., Di Marco, M., Martin, T. G., Rondinini, C. and Rhodes, J. R. (2015), ‘Climate change modifies risk of global biodiversity loss due to land-cover change’, *Biological Conservation* **187**, 103–111.
- Mardia, K. V. (1975), ‘Statistics of directional data’, *Journal of the Royal Statistical Society Series B: Statistical Methodology* **37**(3), 349–371.
- Marelle, L., Myhre, G., Hodnebrog, Ø., Sillmann, J. and Samset, B. H. (2018), ‘The changing seasonality of extreme daily precipitation’, *Geophysical Research Letters* **45**(20), 11–352.
- Mariotti, A., Pan, Y., Zeng, N. and Alessandri, A. (2015), ‘Long-term climate change in the mediterranean region in the midst of decadal variability’, *Climate Dynamics* **44**, 1437–1456.
- Massey Jr, F. J. (1951), ‘The kolmogorov-smirnov test for goodness of fit’, *Journal of the American statistical Association* **46**(253), 68–78.
- Masson-Delmotte, V., Zhai, P., Pirani, A., Connors, S. L., Péan, C., Berger, S., Caud, N., Chen, Y., Goldfarb, L., Gomis, M. et al. (2021), ‘Climate change 2021: the physical science basis’, *Contribution of working group I to the sixth assessment report of the intergovernmental panel on climate change* **2**.
- Mazdiyasi, O. and AghaKouchak, A. (2015), ‘Substantial increase in concurrent droughts and heatwaves in the united states’, *Proceedings of the National Academy of Sciences* **112**(37), 11484–11489.
- Mazdiyasi, O., AghaKouchak, A., Davis, S. J., Madadgar, S., Mehran, A., Ragno, E., Sadegh, M., Sengupta, A., Ghosh, S., Dhanya, C. et al. (2017), ‘Increasing probability of mortality during indian heat waves’, *Science advances* **3**(6), e1700066.
- McGregor, G. R. and Vanos, J. K. (2018), ‘Heat: a primer for public health researchers’, *Public Health* **161**, 138–146.
- Mehrabi, Z., Delzeit, R., Ignaciuk, A., Levers, C., Braich, G., Bajaj, K., Amo-Aidoo, A., Anderson, W., Balgah, R. A., Benton, T. G. et al. (2022), ‘Research priorities for global food security under extreme events’, *One Earth* **5**(7), 756–766.
- Menon, A., Levermann, A., Schewe, J., Lehmann, J. and Frieler, K. (2013), ‘Consistent

- increase in indian monsoon rainfall and its variability across cmip-5 models', *Earth System Dynamics* **4**(2), 287–300.
- Merz, B., Blöschl, G., Vorogushyn, S., Dottori, F., Aerts, J. C., Bates, P., Bertola, M., Kemter, M., Kreibich, H., Lall, U. et al. (2021), 'Causes, impacts and patterns of disastrous river floods', *Nature Reviews Earth & Environment* **2**(9), 592–609.
- Michaelides, S., Karacostas, T., Sánchez, J. L., Retalis, A., Pytharoulis, I., Homar, V., Romero, R., Zanis, P., Giannakopoulos, C., Bühl, J. et al. (2018), 'Reviews and perspectives of high impact atmospheric processes in the mediterranean', *Atmospheric Research* **208**, 4–44.
- Milly, P. C. D., Wetherald, R. T., Dunne, K. and Delworth, T. L. (2002), 'Increasing risk of great floods in a changing climate', *Nature* **415**(6871), 514–517.
- Moftakhari, H. and AghaKouchak, A. (2019), 'Increasing exposure of energy infrastructure to compound hazards: cascading wildfires and extreme rainfall', *Environmental Research Letters* **14**(10), 104018.
- Monteiro, J. M. and Caballero, R. (2019), 'Characterization of extreme wet-bulb temperature events in southern pakistan', *Geophysical Research Letters* **46**(17-18), 10659–10668.
- Mora, C., Dousset, B., Caldwell, I. R., Powell, F. E., Geronimo, R. C., Bielecki, C. R., Counsell, C. W., Dietrich, B. S., Johnston, E. T., Louis, L. V. et al. (2017), 'Global risk of deadly heat', *Nature climate change* **7**(7), 501–506.
- Moran, P. A. (1950), 'Notes on continuous stochastic phenomena', *Biometrika* **37**(1/2), 17–23.
- Morbidelli, R. (2022), *Rainfall: Modeling, Measurement and Applications*, Elsevier.
- Morel, C. and Senesi, S. (2002), 'A climatology of mesoscale convective systems over europe using satellite infrared imagery. ii: Characteristics of european mesoscale convective systems', *Quarterly Journal of the Royal Meteorological Society: A journal of the atmospheric sciences, applied meteorology and physical oceanography* **128**(584), 1973–1995.
- Morrison, A., Villarini, G., Zhang, W. and Scoccimarro, E. (2019), 'Projected changes in extreme precipitation at sub-daily and daily time scales', *Global and planetary change* **182**, 103004.
- Mosley, L. M. (2015), 'Drought impacts on the water quality of freshwater systems; review and integration', *Earth-Science Reviews* **140**, 203–214.
- Mueller, V., Gray, C. and Kosec, K. (2014), 'Heat stress increases long-term human migration in rural pakistan', *Nature climate change* **4**(3), 182–185.
- Muñoz-Díaz, D. and Rodrigo, F. (2006), 'Seasonal rainfall variations in spain (1912–2000) and their links to atmospheric circulation', *Atmospheric Research* **81**(1), 94–110.
- Mutiibwa, D., Vavrus, S. J., McAfee, S. A. and Albright, T. P. (2015), 'Recent spatiotem-

- poral patterns in temperature extremes across conterminous united states', *Journal of Geophysical Research: Atmospheres* **120**(15), 7378–7392.
- Myhre, G., Alterskjær, K., Stjern, C. W., Hodnebrog, Ø., Marelle, L., Samset, B. H., Sillmann, J., Schaller, N., Fischer, E., Schulz, M. et al. (2019), 'Frequency of extreme precipitation increases extensively with event rareness under global warming', *Scientific reports* **9**(1), 16063.
- Nastos, P., Matsangouras, I. and Chronis, T. (2014), 'Spatio-temporal analysis of lightning activity over greece—preliminary results derived from the recent state precision lightning network', *Atmospheric Research* **144**, 207–217.
- Nastos, P. and Zerefos, C. (2008), 'Decadal changes in extreme daily precipitation in greece', *Advances in Geosciences* **16**, 55–62.
- Nelsen, R. B. (2006), *An introduction to copulas*, Springer.
- Nicholson, S. E. (2018), 'The itcz and the seasonal cycle over equatorial africa', *Bulletin of the American Meteorological Society* **99**(2), 337–348.
- Ning, G., Luo, M., Wang, S., Liu, Z., Wang, P. and Yang, Y. (2022), 'Dominant modes of summer wet bulb temperature in china', *Climate Dynamics* pp. 1–16.
- Nissen, K. M. and Ulbrich, U. (2017), 'Increasing frequencies and changing characteristics of heavy precipitation events threatening infrastructure in europe under climate change', *Natural Hazards and Earth System Sciences* **17**(7), 1177–1190.
- Noto, L. V., Cipolla, G., Francipane, A. and Pumo, D. (2023a), 'Climate change in the mediterranean basin (part i): Induced alterations on climate forcings and hydrological processes', *Water Resources Management* **37**(6-7), 2287–2305.
- Noto, L. V., Cipolla, G., Francipane, A. and Pumo, D. (2023b), 'Climate change in the mediterranean basin (part ii): A review of challenges and uncertainties in climate change modeling and impact analyses', *Water Resources Management* pp. 1–17.
- Noto, L. V. and La Loggia, G. (2009), 'Use of l-moments approach for regional flood frequency analysis in sicily, italy', *Water resources management* **23**, 2207–2229.
- Nouaceur, Z. (2010), 'Évaluation des changements climatiques au maghreb. étude du cas des régions du quart nord-est algérien', *Risques et changements climatiques* pp. 463–468.
- Nouaceur, Z. and Murărescu, O. (2016), 'Rainfall variability and trend analysis of annual rainfall in north africa', *International Journal of Atmospheric Sciences* **2016**.
- Oleson, K. W., Monaghan, A., Wilhelmi, O., Barlage, M., Brunsell, N., Feddema, J., Hu, L. and Steinhoff, D. (2015), 'Interactions between urbanization, heat stress, and climate change', *Climatic Change* **129**, 525–541.
- Oreskes, N., Shrader-Frechette, K. and Belitz, K. (1994), 'Verification, validation, and confirmation of numerical models in the earth sciences', *Science* **263**(5147), 641–646.
- Pal, I., Anderson, B. T., Salvucci, G. D. and Gianotti, D. J. (2013), 'Shifting season-

- ality and increasing frequency of precipitation in wet and dry seasons across the us', *Geophysical Research Letters* **40**(15), 4030–4035.
- Panda, D. K., Panigrahi, P., Mohanty, S., Mohanty, R. and Sethi, R. (2016), 'The 20th century transitions in basic and extreme monsoon rainfall indices in india: Comparison of the etccdi indices', *Atmospheric Research* **181**, 220–235.
- Pendergrass, A. G. (2018), 'What precipitation is extreme?', *Science* **360**(6393), 1072–1073.
- Perkins-Kirkpatrick, S. and Lewis, S. (2020), 'Increasing trends in regional heatwaves', *Nature communications* **11**(1), 3357.
- Perkins-Kirkpatrick, S., White, C., Alexander, L., Argüeso, D., Boschat, G., Cowan, T., Evans, J., Ekström, M., Oliver, E., Phatak, A. et al. (2016), 'Natural hazards in australia: heatwaves', *Climatic Change* **139**, 101–114.
- Persiano, S., Ferri, E., Antolini, G., Domeneghetti, A., Pavan, V. and Castellarin, A. (2020), 'Changes in seasonality and magnitude of sub-daily rainfall extremes in emilia-romagna (italy) and potential influence on regional rainfall frequency estimation', *Journal of Hydrology: Regional Studies* **32**, 100751.
- Pewsey, A., Neuhäuser, M. and Ruxton, G. D. (2013), *Circular statistics in R*, OUP Oxford.
- Pfahl, S., O'Gorman, P. A. and Fischer, E. M. (2017), 'Understanding the regional pattern of projected future changes in extreme precipitation', *Nature Climate Change* **7**(6), 423–427.
- Pfleiderer, P., Schleussner, C.-F., Kornhuber, K. and Coumou, D. (2019), 'Summer weather becomes more persistent in a 2 c world', *Nature Climate Change* **9**(9), 666–671.
- Philandras, C., Nastos, P., Kapsomenakis, J., Douvis, K., Tselioudis, G. and Zerefos, C. (2011), 'Long term precipitation trends and variability within the mediterranean region', *Natural Hazards and Earth System Sciences* **11**(12), 3235–3250.
- Piani, C. and Haerter, J. (2012), 'Two dimensional bias correction of temperature and precipitation copulas in climate models', *Geophysical Research Letters* **39**(20).
- Pörtner, H.-O., Roberts, D. C., Tignor, M., Poloczanska, E., Mintenbeck, K., Alegria, A., Craig, M., Langsdorf, S., Löschke, S., Möller, V. et al. (2022), 'Ippc 2022: Climate change 2022: impacts, adaptation and vulnerability: working group ii contribution to the sixth assessment report of the intergovernmental panel on climate change'.
- Posthumus, H., Morris, J., Hess, T., Neville, D., Phillips, E. and Baylis, A. (2009), 'Impacts of the summer 2007 floods on agriculture in england', *Journal of Flood Risk Management* **2**(3), 182–189.
- Pujol, N., Neppel, L. and Sabatier, R. (2007), 'Regional tests for trend detection in maximum precipitation series in the french mediterranean region', *Hydrological Sciences*

- Journal* **52**(5), 956–973.
- Pumo, D., Carlino, G., Blenkinsop, S., Arnone, E., Fowler, H. and Noto, L. V. (2019), ‘Sensitivity of extreme rainfall to temperature in semi-arid mediterranean regions’, *Atmospheric Research* **225**, 30–44.
- Rahimi, J., Mutua, J. Y., Notenbaert, A. M., Marshall, K. and Butterbach-Bahl, K. (2021), ‘Heat stress will detrimentally impact future livestock production in east africa’, *Nature Food* **2**(2), 88–96.
- Raleigh, C. and Kniveton, D. (2012), ‘Come rain or shine: An analysis of conflict and climate variability in east africa’, *Journal of peace research* **49**(1), 51–64.
- Raymond, C., Singh, D. and Horton, R. (2017), ‘Spatiotemporal patterns and synoptics of extreme wet-bulb temperature in the contiguous united states’, *Journal of Geophysical Research: Atmospheres* **122**(24), 13–108.
- Reudenbach, C., Heinemann, G., Heuel, E., Bendix, J. and Winiger, M. (2001), ‘Investigation of summertime convective rainfall in western europe based on a synergy of remote sensing data and numerical models’, *Meteorology and Atmospheric Physics* **76**, 23–41.
- Rhoades, A. M., Ullrich, P. A., Zarzycki, C. M., Johansen, H., Margulis, S. A., Morrison, H., Xu, Z. and Collins, W. D. (2018), ‘Sensitivity of mountain hydroclimate simulations in variable-resolution cesm to microphysics and horizontal resolution’, *Journal of Advances in Modeling Earth Systems* **10**(6), 1357–1380.
- Ribes, A., Thao, S., Vautard, R., Dubuisson, B., Somot, S., Colin, J., Planton, S. and Soubeyroux, J.-M. (2019), ‘Observed increase in extreme daily rainfall in the french mediterranean’, *Climate dynamics* **52**, 1095–1114.
- Ridder, N. N., Pitman, A. J., Westra, S., Ukkola, A., Do, H. X., Bador, M., Hirsch, A. L., Evans, J. P., Di Luca, A. and Zscheischler, J. (2020), ‘Global hotspots for the occurrence of compound events’, *Nature communications* **11**(1), 5956.
- Riemann-Campe, K., Fraedrich, K. and Lunkeit, F. (2009), ‘Global climatology of convective available potential energy (cape) and convective inhibition (cin) in era-40 re-analysis’, *Atmospheric Research* **93**(1-3), 534–545.
- Rigo, T. and Llasat, M. (2004), ‘A methodology for the classification of convective structures using meteorological radar: Application to heavy rainfall events on the mediterranean coast of the iberian peninsula’, *Natural Hazards and Earth System Sciences* **4**(1), 59–68.
- Rigo, T. and Llasat, M.-C. (2007), ‘Analysis of mesoscale convective systems in catalonia using meteorological radar for the period 1996–2000’, *Atmospheric Research* **83**(2-4), 458–472.
- Robine, J.-M., Cheung, S. L. K., Le Roy, S., Van Oyen, H., Griffiths, C., Michel, J.-P. and Herrmann, F. R. (2008), ‘Death toll exceeded 70,000 in europe during the summer

- of 2003', *Comptes rendus biologiques* **331**(2), 171–178.
- Rodell, M., Houser, P., Jambor, U., Gottschalk, J., Mitchell, K., Meng, C.-J., Arsenault, K., Cosgrove, B., Radakovich, J., Bosilovich, M. et al. (2004), 'The global land data assimilation system', *Bulletin of the American Meteorological society* **85**(3), 381–394.
- Rosen, A. M. (2015), 'The wrong solution at the right time: The failure of the kyoto protocol on climate change', *Politics & Policy* **43**(1), 30–58.
- Rosenzweig, C., Tubiello, F. N., Goldberg, R., Mills, E. and Bloomfield, J. (2002), 'Increased crop damage in the us from excess precipitation under climate change', *Global Environmental Change* **12**(3), 197–202.
- Rousi, E., Kornhuber, K., Beobide-Arsuaga, G., Luo, F. and Coumou, D. (2022), 'Accelerated western european heatwave trends linked to more-persistent double jets over eurasia', *Nature communications* **13**(1), 3851.
- Ruiz-Leo, A. M., Hernández, E., Queralt, S. and Maqueda, G. (2013), 'Convective and stratiform precipitation trends in the spanish mediterranean coast', *Atmospheric Research* **119**, 46–55.
- Rulfová, Z. and Kyselý, J. (2013), 'Disaggregating convective and stratiform precipitation from station weather data', *Atmospheric research* **134**, 100–115.
- Rulfová, Z., Kyselý, J. et al. (2014), 'Trends of convective and stratiform precipitation in the czech republic, 1982–2010', *Advances in Meteorology* **2014**.
- Sandford, C., Illingworth, A. and Thompson, R. (2017), 'The potential use of the linear depolarization ratio to distinguish between convective and stratiform rainfall to improve radar rain-rate estimates', *Journal of Applied Meteorology and Climatology* **56**(11), 2927–2940.
- Sauter, C., White, C. J., Fowler, H. J. and Westra, S. (2023), 'Temporally compound-ing heatwave-heavy rainfall events in australia', *International Journal of Climatology* **43**(2), 1050–1061.
- Scala, P., Cipolla, G., Treppiedi, D. and Noto, L. V. (2022), 'The use of gamlss framework for a non-stationary frequency analysis of annual runoff data over a mediterranean area', *Water* **14**(18), 2848.
- Schmidt, T. (2007), 'Coping with copulas', *Copulas-From theory to application in finance* **3**, 1–34.
- Schwarz, G. (1978), 'Estimating the dimension of a model', *The annals of statistics* pp. 461–464.
- Segan, D. B., Murray, K. A. and Watson, J. E. (2016), 'A global assessment of current and future biodiversity vulnerability to habitat loss-climate change interactions', *Global Ecology and Conservation* **5**, 12–21.
- Sen, P. K. (1968), 'Estimates of the regression coefficient based on kendall's tau', *Journal*

- of the American statistical association* **63**(324), 1379–1389.
- Seneviratne, S., Nicholls, N., Easterling, D., Goodess, C., Kanae, S., Kossin, J., Luo, Y., Marengo, J., McInnes, K., Rahimi, M. et al. (2012), ‘Changes in climate extremes and their impacts on the natural physical environment’.
- Shukla, P., Skea, J., Calvo Buendía, E., Masson-Delmotte, V., Pörtner, H.-O., Roberts, D., Zhai, P., Slade, R., Connors, Sarah van Diemen, R., Ferrat, M., Haughey, E., Luz, S., Neogi, S., Pathak, M., Petzold, J., Portugal Pereira, J., Vyas, P., Huntley, L., Kissick, K., Belkacemi, M. and Malley, J. (2019), ‘Climate change and land: an ipcc special report on climate change, desertification, land degradation, sustainable land management, food security, and greenhouse gas fluxes in terrestrial ecosystems’, *Ginevra, IPCC*.
- Sillmann, J., Kharin, V. V., Zwiers, F. W., Zhang, X. and Bronaugh, D. (2013), ‘Climate extremes indices in the cmip5 multimodel ensemble: Part 2. future climate projections’, *Journal of geophysical research: atmospheres* **118**(6), 2473–2493.
- Singh, B. K., Delgado-Baquerizo, M., Egidi, E., Guirado, E., Leach, J. E., Liu, H. and Trivedi, P. (2023), ‘Climate change impacts on plant pathogens, food security and paths forward’, *Nature Reviews Microbiology* pp. 1–17.
- Sklar, M. (1959), Fonctions de répartition à n dimensions et leurs marges, *in* ‘Annales de l’ISUP’, Vol. 8, pp. 229–231.
- Smith, T. T., Zaitchik, B. F. and Gohlke, J. M. (2013), ‘Heat waves in the united states: definitions, patterns and trends’, *Climatic change* **118**, 811–825.
- Sommer, C., Malz, P., Seehaus, T. C., Lippl, S., Zemp, M. and Braun, M. H. (2020), ‘Rapid glacier retreat and downwasting throughout the european alps in the early 21st century’, *Nature communications* **11**(1), 3209.
- Song, X., Song, S., Sun, W., Mu, X., Wang, S., Li, J. and Li, Y. (2015), ‘Recent changes in extreme precipitation and drought over the songhua river basin, china, during 1960–2013’, *Atmospheric Research* **157**, 137–152.
- Sottile, G., Francipane, A., Adelfio, G. and Noto, L. V. (2022), ‘A pca-based clustering algorithm for the identification of stratiform and convective precipitation at the event scale: an application to the sub-hourly precipitation of sicily, italy’, *Stochastic Environmental Research and Risk Assessment* **36**(8), 2303–2317.
- Spalding, M. D. and Brown, B. E. (2015), ‘Warm-water coral reefs and climate change’, *Science* **350**(6262), 769–771.
- Steiner, M., Houze Jr, R. A. and Yuter, S. E. (1995), ‘Climatological characterization of three-dimensional storm structure from operational radar and rain gauge data’, *Journal of Applied Meteorology and Climatology* **34**(9), 1978–2007.
- Stephenson, D. B., Diaz, H. and Murnane, R. (2008), ‘Definition, diagnosis, and origin of

- extreme weather and climate events', *Climate extremes and society* **340**, 11–23.
- Stocker, T. F., Qin, D., Plattner, G.-K., Tignor, M. M., Allen, S. K., Boschung, J., Nauels, A., Xia, Y., Bex, V. and Midgley, P. M. (2014), 'Climate change 2013: The physical science basis. contribution of working group i to the fifth assessment report of ipcc the intergovernmental panel on climate change'.
- Stone Jr, B. (2012), *The city and the coming climate: Climate change in the places we live*, Cambridge University Press.
- Stott, P. A., Christidis, N., Otto, F. E., Sun, Y., Vanderlinden, J.-P., van Oldenborgh, G. J., Vautard, R., von Storch, H., Walton, P., Yiou, P. et al. (2016), 'Attribution of extreme weather and climate-related events', *Wiley Interdisciplinary Reviews: Climate Change* **7**(1), 23–41.
- Stull, R. (2011), 'Wet-bulb temperature from relative humidity and air temperature', *Journal of applied meteorology and climatology* **50**(11), 2267–2269.
- Sun, Q., Miao, C., Hanel, M., Borthwick, A. G., Duan, Q., Ji, D. and Li, H. (2019), 'Global heat stress on health, wildfires, and agricultural crops under different levels of climate warming', *Environment international* **128**, 125–136.
- Sun, Q., Zhang, X., Zwiers, F., Westra, S. and Alexander, L. V. (2021), 'A global, continental, and regional analysis of changes in extreme precipitation', *Journal of Climate* **34**(1), 243–258.
- Sun, Y., Zhang, X., Zwiers, F. W., Song, L., Wan, H., Hu, T., Yin, H. and Ren, G. (2014), 'Rapid increase in the risk of extreme summer heat in eastern china', *Nature Climate Change* **4**(12), 1082–1085.
- Supari, Tangang, F., Juneng, L. and Aldrian, E. (2017), 'Observed changes in extreme temperature and precipitation over indonesia', *International Journal of Climatology* **37**(4), 1979–1997.
- Tabari, H. (2020), 'Climate change impact on flood and extreme precipitation increases with water availability', *Scientific reports* **10**(1), 13768.
- Teixeira, E. I., Fischer, G., Van Velthuisen, H., Walter, C. and Ewert, F. (2013), 'Global hot-spots of heat stress on agricultural crops due to climate change', *Agricultural and Forest Meteorology* **170**, 206–215.
- Thomas, K. M., Charron, D. F., Waltner-Toews, D., Schuster, C., Maarouf, A. R. and Holt, J. D. (2006), 'A role of high impact weather events in waterborne disease outbreaks in canada, 1975–2001', *International journal of environmental health research* **16**(03), 167–180.
- Toimil, A., Losada, I. J., Camus, P. and Díaz-Simal, P. (2017), 'Managing coastal erosion under climate change at the regional scale', *Coastal Engineering* **128**, 106–122.
- Tomio, J., Sato, H. and Mizumura, H. (2010), 'Interruption of medication among out-

- patients with chronic conditions after a flood', *Prehospital and disaster medicine* **25**(1), 42–50.
- Tramblay, Y., Neppel, L., Carreau, J. and Sanchez-Gomez, E. (2012), 'Extreme value modelling of daily areal rainfall over mediterranean catchments in a changing climate', *Hydrological Processes* **26**(25), 3934–3944.
- Tramblay, Y. and Somot, S. (2018), 'Future evolution of extreme precipitation in the mediterranean', *Climatic Change* **151**(2), 289–302.
- Tremblay, A. (2005), 'The stratiform and convective components of surface precipitation', *Journal of the atmospheric sciences* **62**(5), 1513–1528.
- Trenberth, K. E., Dai, A., Van Der Schrier, G., Jones, P. D., Barichivich, J., Briffa, K. R. and Sheffield, J. (2014), 'Global warming and changes in drought', *Nature Climate Change* **4**(1), 17–22.
- Treppiedi, D., Cipolla, G., Francipane, A. and Noto, L. (2021), 'Detecting precipitation trend using a multiscale approach based on quantile regression over a mediterranean area', *International Journal of Climatology* **41**(13), 5938–5955.
- Treppiedi, D., Cipolla, G. and Noto, L. V. (2023), 'Convective precipitation over a mediterranean area: From identification to trend analysis starting from high-resolution rain gauges data', *International Journal of Climatology* **43**(1), 293–313.
- Van de Vyver, H., Van Schaeybroeck, B., De Troch, R., Hamdi, R. and Termonia, P. (2019), 'Modeling the scaling of short-duration precipitation extremes with temperature', *Earth and Space Science* **6**(10), 2031–2041.
- Vargas Zeppetello, L. R., Raftery, A. E. and Battisti, D. S. (2022), 'Probabilistic projections of increased heat stress driven by climate change', *Communications Earth & Environment* **3**(1), 183.
- Varouchakis, E. A., Corzo, G. A., Karatzas, G. P. and Kotsopoulou, A. (2018), 'Spatio-temporal analysis of annual rainfall in crete, greece', *Acta Geophysica* **66**, 319–328.
- Veatch, W. and Villarini, G. (2020), 'Modeling the seasonality of extreme coastal water levels with mixtures of circular probability density functions', *Theoretical and Applied Climatology* **140**, 1199–1206.
- Veatch, W. and Villarini, G. (2022), 'Modeling riverine flood seasonality with mixtures of circular probability density functions', *Journal of Hydrology* **613**, 128330.
- Villarini, G. (2012), 'Analyses of annual and seasonal maximum daily rainfall accumulations for ukraine, moldova, and romania', *International Journal of Climatology* **32**(14), 2213–2226.
- Villarini, G., Smith, J. A., Baeck, M. L., Vitolo, R., Stephenson, D. B. and Krajewski, W. F. (2011b), 'On the frequency of heavy rainfall for the midwest of the united states', *Journal of Hydrology* **400**(1-2), 103–120.

- Villarini, G., Smith, J., Ntelekos, A. A. and Schwarz, U. (2011a), 'Annual maximum and peaks-over-threshold analyses of daily rainfall accumulations for austria', *Journal of Geophysical Research: Atmospheres* **116**(D5).
- Vizy, E. K. and Cook, K. H. (2012), 'Mid-twenty-first-century changes in extreme events over northern and tropical africa', *Journal of Climate* **25**(17), 5748–5767.
- Vogel, J., Paton, E., Aich, V. and Bronstert, A. (2021), 'Increasing compound warm spells and droughts in the mediterranean basin', *Weather and Climate Extremes* **32**, 100312.
- von Mises, R. (1918), 'Über die "ganzzahligkeit" der atomgewichte und verwandete fragen', *Physikalische Zeitschrift* **19**, 490.
- Von Storch, H. (1999), Misuses of statistical analysis in climate research, in 'Analysis of Climate Variability: Applications of Statistical Techniques Proceedings of an Autumn School Organized by the Commission of the European Community on Elba from October 30 to November 6, 1993', Springer, pp. 11–26.
- Wahl, T., Jain, S., Bender, J., Meyers, S. D. and Luther, M. E. (2015), 'Increasing risk of compound flooding from storm surge and rainfall for major us cities', *Nature Climate Change* **5**(12), 1093–1097.
- Wang, P., Leung, L. R., Lu, J., Song, F. and Tang, J. (2019), 'Extreme wet-bulb temperatures in china: the significant role of moisture', *Journal of Geophysical Research: Atmospheres* **124**(22), 11944–11960.
- Wehrli, K., Guillod, B. P., Hauser, M., Leclair, M. and Seneviratne, S. I. (2018), 'Assessing the dynamic versus thermodynamic origin of climate model biases', *Geophysical research letters* **45**(16), 8471–8479.
- Wei, W., Chen, L., Fu, B., Lü, Y. and Gong, J. (2009), 'Responses of water erosion to rainfall extremes and vegetation types in a loess semiarid hilly area, nw china', *Hydrological Processes: An International Journal* **23**(12), 1780–1791.
- Weltzin, J. F., Loik, M. E., Schwinning, S., Williams, D. G., Fay, P. A., Haddad, B. M., Harte, J., Huxman, T. E., Knapp, A. K., Lin, G. et al. (2003), 'Assessing the response of terrestrial ecosystems to potential changes in precipitation', *Bioscience* **53**(10), 941–952.
- Westra, S., Alexander, L. V. and Zwiers, F. W. (2013), 'Global increasing trends in annual maximum daily precipitation', *Journal of climate* **26**(11), 3904–3918.
- Westra, S., Fowler, H. J., Evans, J. P., Alexander, L. V., Berg, P., Johnson, F., Kendon, E. J., Lenderink, G. and Roberts, N. (2014), 'Future changes to the intensity and frequency of short-duration extreme rainfall', *Reviews of Geophysics* **52**(3), 522–555.
- W.H.O. (2018), *The state of food security and nutrition in the world 2018: building climate resilience for food security and nutrition*, Food & Agriculture Org.
- Wi, S., Valdés, J. B., Steinschneider, S. and Kim, T.-W. (2016), 'Non-stationary frequency

- analysis of extreme precipitation in south korea using peaks-over-threshold and annual maxima', *Stochastic environmental research and risk assessment* **30**, 583–606.
- Xie, H. and Wang, K. (2013), Joint-probability methods for precipitation and flood frequencies analysis, *in* '2013 Third International Conference on Intelligent System Design and Engineering Applications', IEEE, pp. 913–916.
- Yu, J., Qin, X., Chiew, Y. M., Min, R. and Shen, X. (2017), 'Stochastic optimization model for supporting urban drainage design under complexity', *Journal of Water Resources Planning and Management* **143**(9), 05017008.
- Yue, S. and Wang, C. Y. (2002), 'Applicability of prewhitening to eliminate the influence of serial correlation on the mann-kendall test', *Water resources research* **38**(6), 4–1.
- Yusoff, N. A., Shafii, H. and Omar, R. (2017), 'The impact of floods in hospital and mitigation measures: A literature review', *IOP Conference Series: Materials Science and Engineering* **271**(1), 012026.
- Zander, K. K., Botzen, W. J., Oppermann, E., Kjellstrom, T. and Garnett, S. T. (2015), 'Heat stress causes substantial labour productivity loss in australia', *Nature climate change* **5**(7), 647–651.
- Zeder, J. and Fischer, E. M. (2020), 'Observed extreme precipitation trends and scaling in central europe', *Weather and Climate Extremes* **29**, 100266.
- Zhang, W. and Villarini, G. (2020), 'Deadly compound heat stress-flooding hazard across the central united states', *Geophysical Research Letters* **47**(15), e2020GL089185.
- Zhao, L., Lee, X., Smith, R. B. and Oleson, K. (2014), 'Strong contributions of local background climate to urban heat islands', *Nature* **511**(7508), 216–219.
- Zhao, Y., Sultan, B., Vautard, R., Braconnot, P., Wang, H. J. and Ducharne, A. (2016), 'Potential escalation of heat-related working costs with climate and socioeconomic changes in china', *Proceedings of the National Academy of Sciences* **113**(17), 4640–4645.
- Zscheischler, J., Martius, O., Westra, S., Bevacqua, E., Raymond, C., Horton, R. M., van den Hurk, B., AghaKouchak, A., Jézéquel, A., Mahecha, M. D. et al. (2020), 'A typology of compound weather and climate events', *Nature reviews earth & environment* **1**(7), 333–347.
- Zscheischler, J. and Seneviratne, S. I. (2017), 'Dependence of drivers affects risks associated with compound events', *Science advances* **3**(6), e1700263.
- Zscheischler, J., Westra, S., Van Den Hurk, B. J., Seneviratne, S. I., Ward, P. J., Pitman, A., AghaKouchak, A., Bresch, D. N., Leonard, M., Wahl, T. et al. (2018), 'Future climate risk from compound events', *Nature Climate Change* **8**(6), 469–477.